

UCLA

UCLA Electronic Theses and Dissertations

Title

Reliability of Structural Wall Shear Design for Tall Reinforced Concrete Core Wall Buildings

Permalink

<https://escholarship.org/uc/item/2vv3w1nn>

Author

Kim, Sunai

Publication Date

2016

Peer reviewed|Thesis/dissertation

UNIVERSITY OF CALIFORNIA

Los Angeles

Reliability of Structural Wall Shear Design for
Tall Reinforced Concrete Core Wall Buildings

A dissertation in partial satisfaction of the
requirements for the degree Doctor of Philosophy
in Civil Engineering

by

Sunai Kim

2016

© Copyright by

Sunai Kim

2016

ABSTRACT OF THE DISSERTATION

Reliability of Structural Wall Shear Design for
Tall Reinforced Concrete Core Wall Buildings

by

Sunai Kim

Doctor of Philosophy in Civil Engineering

University of California, Los Angeles, 2016

Professor John Wright Wallace, Chair

Along the west coast of the United States, reinforced concrete core wall systems are commonly selected as seismic force resisting systems for tall buildings. During strong ground shaking, core wall systems are intended to dissipate energy by yielding of coupling beams, followed by flexural yielding at the wall base. Although the wall behavior is governed by flexure, the wall design is often governed by shear, as the walls experience high shear demands, usually up to the ACI318-11 code limiting shear stress of $8 \cdot \sqrt{f'_c}$ *psi* over a significant wall height. The high shear demands are due to a lack of redundancy in tall buildings, as the wall lengths are limited to the perimeter of the elevator core.

Design of tall buildings is typically conducted using performance-based design procedures recommended by Los Angeles Tall Buildings Structural Design Council (LATBSDC, 2014) or Pacific Earthquake Engineering Research Center Tall Buildings Initiative (PEER TBI, 2010). Provisions in these two documents recommend shear design per acceptance criterion

$$F_{uc} \leq \kappa_i \phi F_{n,e}$$

where F_{uc} is 1.5 times the mean shear demand resulting from a suite of ground motions, $F_{n,e}$ is the nominal strength computed from expected material properties, κ_i is the risk reduction factor based on risk categories, and ϕ is the uncertainty in $F_{n,e}$. The 1.5 factor applied to the mean shear demand is referred to as the demand factor, γ . Although shear failure can be fatal due to its sudden and brittle nature, the reliability of this shear design acceptance criterion has not yet been thoroughly researched.

To assess seismic reliability of structural wall shear design acceptance criterion, dispersion in structural responses, specifically for shear demands, must be quantified. Dispersion in structural responses (referred to as engineering demand parameters, EDPs) primarily results from three sources, namely, record-to-record (RTR) variability, modeling and/or model parameter uncertainties, and design uncertainties. To study how these uncertainties contribute to dispersion in tall building EDPs, eleven input random variables (expected to be the most relevant) were selected. Specifically, uncertainties in scaled ground motions, unconfined and confined concrete compressive strengths, reinforcing steel yield strength, shear modulus, coupling beam strength, seismic mass, dead and live gravity loads, damping, and shear wall design variations were considered. A series of 20 and 30-story nonlinear models for reinforced-concrete core wall systems were built and Monte Carlo simulations were utilized to assign values for random variables and to perform nonlinear response history analyses. Analyses were performed at five seismic hazard levels corresponding to return periods of 25, 43, 475, 2495, and 4975 years, until an adequate convergence in dispersion measure was reached. Selected EDPs (base shear, roof drifts, coupling beam rotations, and structural wall boundary element axial strains) were evaluated and statistical parameters were quantified. Results show that dispersion in EDPs was the largest for coupling beam rotations and shear wall axial strains. Total

dispersion, measured in coefficient of variation, ranged between 0.15 and 0.85, considering all EDPs at all five hazard levels. The relative contributions from RTR variability and model parameter/design uncertainties accounted for 72-98% and 2-28% of the total dispersion, respectively. Fitted probability distributions were either normal or lognormal for all EDPs and using correlated random variables for model parameter uncertainties resulted in changes in dispersion of -6% to 5% compared with using independent random variables.

Using the measured dispersion values, the current recommendations in Los Angeles Tall Buildings Structural Design Council (LATBSDC, 2014) were reviewed for shear design of structural walls in tall reinforced-concrete core wall buildings ($F_{uc} \leq \kappa_i \phi F_{n,e}$). Both closed-form solutions using full distribution methods and Monte Carlo simulation results were used to assess reliability of the current shear design acceptance criterion. Statistical parameters were established for shear demand by using measured dispersion values from nonlinear response history analyses of tall reinforced-concrete core wall buildings, and experimental test results from shear-controlled walls were used to establish statistical parameters for shear capacity. A range of reliability results were computed for various shear demand and capacity statistical parameters. The current shear design acceptance criterion using $\gamma=1.5$ and $\phi=1.0$ resulted in 94.2% reliability for structural walls with $f'_c < 8\text{ksi}$ and 96.5% reliability for structural walls with $f'_c \geq 8\text{ksi}$. Minimum values for the demand factor, γ , are tabulated for various risk categories defined per ASCE7-10.

Results suggest that the use of $\phi=1.0$, along with appropriate expected material properties, produce an acceptable probability of failure. Per Pacific Earthquake Engineering Center Tall Buildings Initiative (PEER TBI, 2010), the recommended use of $\phi=0.75$ appears excessively conservative. However, due to a lack of experimental tests on possible shear strength

degradation in walls that yield in flexure, limitations on curvature ductility or plastic rotation demands are recommended in the plastic hinge regions. Moreover, since this study is based on variations of results from two prototype tall core wall buildings; to reduce the potential conservatism in the current guidelines, a comprehensive reliability study including a larger population of tall buildings is further needed to calibrate γ and ϕ factors.

The dissertation of Sunai Kim is approved.

Scott Joseph Brandenburg

Joel Conte

Thomas A. Sabol

Jonathan Paul Stewart

John Wright Wallace, Committee Chair

University of California, Los Angeles

2016

TABLE OF CONTENTS

ABSTRACT.....	ii
LIST OF FIGURES.....	xv
LIST OF TABLES.....	xxv
ACKNOWLEDGEMENTS.....	xxix
VITA.....	xxxix
CHAPTER 1. INTRODUCTION.....	1
1.1. Background and Motivations	1
1.2. Objectives.....	5
1.3. Organization.....	6
CHAPTER 2. LITERATURE REVIEW.....	8
2.1. Tall Building Definition.....	8
2.2. Governing Codes.....	8
2.2.1. Selection of Seismic Force-Resisting System for Tall Buildings.....	9
2.2.2. Tall Building Design Comparison: Code-Based versus LATBSDC (2014)	11
2.3. Performance-Based Design Procedures per LATBSDC (2014)	13
2.3.1. Methodology.....	13
2.3.2. Analysis Procedure	15
2.3.3. SLE Level Analysis – Global Acceptance Criteria.....	16
2.3.4. SLE Level Analysis – Component Acceptance Criteria.....	16
2.3.5. MCE Level Analysis – Global Acceptance Criteria.....	17
2.3.6. MCE Level Analysis – Component Acceptance Criteria	18

2.4.	Design of Tall Reinforced Concrete Structural Walls	20
2.4.1.	Shear Design per LATBSDC (2014)	20
2.4.2.	Shear Demands	21
2.4.3.	Shear Capacity	22
2.4.4.	Reliability of Shear Design.....	23
2.5.	Changes to Tall Building Design and Analysis Procedures.....	25
2.5.1.	Proposed Changes in ASCE7-16 Chapter 16.....	25
2.5.2.	Number of Ground Motions.....	25
2.5.3.	Period Range.....	25
2.5.4.	Unacceptable Responses.....	26
2.5.5.	Element-Level Force-Controlled Acceptance Criteria	27
2.6.	Summary of Current and Proposed Shear Design Provisions.....	29
CHAPTER 3. GROUND MOTION SELECTION AND MODIFICATION		31
3.1.	Introduction	31
3.2.	Project Site	31
3.3.	Site Hazard Characterization.....	32
3.4.	Ground Motion Suites	35
3.5.	Ground Motion Record Selection and Modification.....	36
3.5.1.	Suite A – 15 Pairs of Scaled Ground Motions at 5 Hazard Levels.....	36
3.5.2.	Suite B – 30 Pairs of Scaled Ground Motions at DBE and MCE Hazard Levels...	41

3.5.3. Suites C and D – 30 Scaled Ground Motions at MCE Hazard Level for 2D Analysis.....	42
3.6. Methods Not Considered – Spectral Matching	43
3.7. Limitations and Future Work	48
 CHAPTER 4. DESIGN, MODELING, AND ANALYSIS OF TALL REINFORCED CONCRETE CORE WALL BUILDINGS.....	
4.1. Introduction	49
4.2. Description of the 30-Story Building	49
4.3. Loading Criteria	50
4.4. Governing Codes and Methodology	54
4.5. Development of Nonlinear Perform 3D Model.....	55
4.5.1. Overview of Perform 3D Model.....	55
4.5.2. Strength and Stiffness Properties	56
4.5.3. Inelastic Properties of Shear Wall Elements.....	58
4.5.4. Inelastic Properties of Coupling Beams.....	60
4.5.5. Embedded Beams.....	61
4.5.6. Inelastic Properties of the Slab Outrigger System	62
4.5.7. P-Delta Column	64
4.5.8. Damping.....	65
4.6. Nonlinear Response History Analysis Results.....	67

4.6.1.	Service Level (SLE43) Analysis Results	68
4.6.2.	Collapse Prevention Level (MCE) Analysis Results	70
4.7.	Development of Opensees 2D Model	80
4.7.1.	Overview of Opensees 2D Model.....	80
4.7.2.	Inelastic Properties of Shear Wall Elements.....	82
4.7.3.	Inelastic Properties of Coupling Beams.....	83
4.7.4.	Concrete Constitutive Model	84
4.7.5.	Reinforcing Steel Constitutive Model	85
4.7.6.	Damping.....	85
4.7.7.	Solution Strategy.....	85
4.8.	Conclusions	86
4.9.	Limitations and Future Work.....	87
CHAPTER 5. UNCERTAINTIES CONSIDERED AND SELECTION OF RANDOM VARIABLES		88
5.1.	Introduction	88
5.2.	Types of Uncertainties	89
5.3.	Sources of Uncertainty.....	89
5.4.	Random Variables	92
5.4.1.	Uniform Random Variable	94
5.4.2.	Normal Random Variable.....	95

5.4.3.	Lognormal Random Variable	96
5.4.4.	Gamma Random Variable.....	97
5.5.	Selection of Random Variables.....	98
5.6.	RTR Variability.....	99
5.7.	Model Parameter Uncertainties.....	100
5.7.1.	Concrete Compressive Strengths	100
5.7.2.	Reinforcing Steel Yield Strengths	103
5.7.3.	Coupling Beam Strengths	104
5.7.4.	Mass and Dead Loads	105
5.7.5.	Live Loads	105
5.7.6.	Damping.....	106
5.7.7.	Shear Modulus	106
5.8.	Design Uncertainties	107
5.8.1.	Shear Wall Boundary Element Design	107
5.9.	Correlation.....	108
5.10.	Uncertainties Not Considered	109
CHAPTER 6. QUANTIFICATION OF DISPERSION IN ENGINEERING DEMAND		
PARAMETERS USING MONTE CARLO SIMULATIONS.....		
6.1.	Methodology	113
6.2.	Random Number Generation	117

6.3.	Criteria for Outlier Data Removal.....	119
6.4.	3D Analysis: Quantification of Dispersion	120
6.4.1.	Base Shear Force.....	120
6.4.2.	Required Number of Simulations and Convergence	125
6.4.3.	Roof Drifts	126
6.4.4.	Coupling Beam Rotations.....	127
6.4.5.	Tensile and Compressive Axial Strains in Shear Walls.....	128
6.5.	2D Analysis: Quantification of Dispersion due to Correlation	130
6.5.1.	Challenges in Opensees Analysis	131
6.6.	Summary of EDP Dispersion Values.....	135
6.7.	Cumulative Distribution Functions	139
6.8.	Conclusions	144
6.9.	Limitations and Future Work.....	146
CHAPTER 7. UNCERTAINTIES IN STRUCTURAL WALL SHEAR CAPACITY		148
7.1.	Shear Capacity.....	148
7.2.	Structural Wall Failure Modes and Shear Capacity	149
7.3.	Statistical Parameters for Shear Capacity	151
7.3.1.	Structural Walls with $f'_c \geq 8\text{ksi}$	151
7.3.2.	Structural Walls with $f'_c < 8\text{ksi}$	152
7.3.3.	Probability Distribution Tests through Probability Papers	155

7.4.	Context in which Shear Controlled Wall Tests were Used	156
7.5.	Conclusions	158
7.6.	Limitations and Future Work	160
CHAPTER 8. STRUCTURAL WALL SHEAR DESIGN RELIABILITY		162
8.1.	Background	162
8.2.	Normal Distribution for Random Variables C and D	164
8.3.	Lognormal Distribution for Random Variables C and D	166
8.4.	Monte Carlo Simulations	168
8.5.	Component Reliability Methodology	169
8.6.	Shear Design Reliability MCE Hazard Level	171
8.6.1.	Structural Walls with $f'_c < 8\text{ksi}$	171
8.6.2.	Variations in Monte Carlo Probability of Failure Estimator	173
8.6.3.	Structural Walls with $f'_c \geq 8\text{ksi}$	174
8.6.4.	Summary	175
8.7.	Shear Design Reliability All Hazard Levels	176
8.8.	Conclusions	177
8.9.	Limitations and Future Work	178
CHAPTER 9. CONCLUSIONS		179
APPENDIX A		183
	Description of the 20-Story Building	183

Strength and Stiffness Properties	185
Coupling Beam and Structural Wall Designs	186
APPENDIX B	187
1. Embedded Beam Sensitivity Study.....	188
2. Rayleigh Damping versus Modal Damping.....	196
3. Shear Wall Axial Strains.....	202
4. Analysis of Core Wall Compressive Zones	205
APPENDIX C	210
Base Shear Force.....	210
Roof Drifts	212
Coupling Beam Rotations	215
Tensile Axial Strains.....	221
Compressive Axial Strains.....	236
REFERENCES	239

LIST OF FIGURES

Figure 1-1. (a) Typical elevation view of a tall reinforced concrete core wall building and (b) intended nonlinear behavior under seismic events	4
Figure 1-2. Typical plan view of a reinforced concrete core wall building.....	4
Figure 2-1. Inelastic force-deformation curve, SEAOC Blue Book (2008)	9
Figure 2-2. Isometric floor plan views of a tall building design using (a) dual system of reinforced concrete core walls and reinforced concrete moment frames and (b) reinforced concrete core walls. Image courtesy of Magnusson Klemencic Associates.....	12
Figure 2-3. Elevation of 40-story building, Moehle (2007).....	21
Figure 3-1. Project location, PEER TBI Task 12 (2011).....	32
Figure 3-2. PSH deaggregation for MCE hazard level with 2475-year return period at T=2.0 seconds, PEER TBI Task 12 (2011)	33
Figure 3-3. PSH deaggregation for MCE hazard level with 2475-year return period at T=3.0 seconds, PEER TBI Task 12 (2011)	34
Figure 3-4. Suite A – Geomean of 15 pairs of scaled ground motions and mean compared to target spectrum at hazard levels (a) SLE25, (b) SLE43, (c) DBE, (d) MCE, and (e) OVE	38
Figure 3-5. Suite B - Geomean of 30 pairs of scaled ground motions and mean compared to target spectrum at hazard levels (a) DBE and (b) MCE	41
Figure 3-6. (a) Suite C and (b) Suite D – 30 single-direction scaled ground motions and mean compared to target spectrum at MCE hazard level.....	42
Figure 3-7. 11 pairs of MCE hazard ground motions modified by (a) amplitude scaling and (b) spectral matching	44
Figure 4-1. 30-Story building, typical floor plan view: levels 1 through 29	51

Figure 4-2. 30-Story building, roof plan view	51
Figure 4-3. 30-Story building, Elevation A of south wall	52
Figure 4-4. 30-Story building, Detail 1 of coupling beam diagonal reinforcement	53
Figure 4-5. 30-Story building, Detail 2 of coupling beam full section confinement.....	53
Figure 4-6. Stress-strain relationships for (a) unconfined concrete based on modified Hognestad, (b) confined concrete based on Razvi and Saatcioglu (1999), and (c) A706 reinforcing steel	58
Figure 4-7. Boundary element dimensions on level 1.	59
Figure 4-8. A partial elevation view of Perform 3D model.....	59
Figure 4-9. Rigid-plastic shear hinge, CSI (2011).....	60
Figure 4-10. Diagonally reinforced coupling beam test results by Naish et al (2013b), ½ scale test results are shown as dotted lines.....	61
Figure 4-11. Perform 3D trilinear force-displacement relationship.....	61
Figure 4-12. (a) Schematic drawing of a coupled wall system, (b) Perform 3D modeling of shear walls, coupling beams and embedded beams	61
Figure 4-13. (a) Typical floor plan view showing effective slab widths for east-west direction (b) simplified (lumped) slab-column outrigger system with lumped gravity columns and slab widths	63
Figure 4-14. (a) Test specimen of post-tensioned slab connection to gravity column and core wall (b) Total lateral force versus drift ratio, Klemencic et al. (2006).....	64
Figure 4-15. Rayleigh damping	66
Figure 4-16. SLE43 interstory drifts for (a) H1 direction and (b) H2 direction	68
Figure 4-17. SLE43 coupling beam rotations for (a) North coupling beam, (b) South coupling beam, (c) West coupling beam, and (d) East coupling beam.....	69

Figure 4-18. MCE interstory drifts for (a) H1 direction, (b) H2 direction, and MCE residual interstory drifts for (c) H1 direction, and (d) H2 direction	72
Figure 4-19. MCE coupling beam rotations for (a) North coupling beam, (b) South coupling beam, (c) West coupling beam, and (d) East coupling beam.....	73
Figure 4-20. MCE shear demand for (a) H1 direction, (b) H2 direction, and MCE shear demand versus ACI318 limit for (c) H1 direction, and (d) H2 direction	74
Figure 4-21. MCE relative floor acceleration for (a) H1 direction and (b) H2 direction	75
Figure 4-22. MCE moment demand for (a) H1 direction and (b) H2 direction.....	75
Figure 4-23. MCE north shear wall boundary element extreme fiber compressive and tensile strains, at (a) Location 1, (b) Location 2, (c) Location 3, and (d) Location 4	76
Figure 4-24. MCE south shear wall boundary element extreme fiber compressive and tensile strains, at (a) Location 5, (b) Location 6, (c) Location 7, and (d) Location 8	77
Figure 4-25. MCE west shear wall boundary element extreme fiber compressive and tensile strains, at (a) Location A and (b) Location B	78
Figure 4-26. MCE east shear wall boundary element extreme fiber compressive and tensile strains, at (a) Location C and (b) Location D	78
Figure 4-27. MCE shear wall (a) maximum mean tensile strains and (b) minimum mean compressive strains in the plastic hinge regions	79
Figure 4-28. A 3-Dimensional reinforced concrete core wall system to an idealized 2-dimensional Opensees model using centerline modeling	81
Figure 4-29. Partial elevation view of 2D 30-story Opensees model overlaid with a schematic drawing of shear walls and coupling beams. The plastic hinges and springs are zeroLength elements.	82

Figure 4-30. (a) MVLEM element (b) MVLEM rotations and displacements (Orakcal et al., 2004)	83
.....	83
Figure 4-31. Basic parameters of the modified Ibarra-Medina-Krawinkler deterioration model with Peak-Oriented hysteretic response, Lignos and Krawinkler (2012)	83
.....	83
Figure 4-32. Concrete constitutive model by Chang and Mander (1994) (a) hysteretic constitutive model and (b) compression and tension envelop curves	85
.....	85
Figure 5-1. Probability mass function for a random variable X	94
.....	94
Figure 5-2. PDF and CDF of a normal random variable, X	95
.....	95
Figure 5-3. PDF of a lognormal random variable	96
.....	96
Figure 5-4. PDFs of gamma random variables	97
.....	97
Figure 5-5. Probabilistic models for (a) confined and unconfined concrete compressive strengths and (b) diagonally reinforced concrete coupling beam strengths	99
.....	99
Figure 5-6. CDF for high strength concrete (a) $f'_c = 7,000$ psi, (b) $f'_c = 8,000$ psi, (c) $f'_c = 9,000$ psi, (d) $f'_c = 10,000$ psi, and (e) $f'_c = 12,000$ psi (Nowak et al, 2008)	102
.....	102
Figure 6-1. Flowchart of Monte Carlo simulations procedure, Perform 3D analysis	115
.....	115
Figure 6-2. Flowchart of Monte Carlo simulations procedure, Opensees 2D analysis	116
.....	116
Figure 6-3. 30-Story building base shear normalized by $A_{cv} \cdot f'_c$, mean and dispersion at 5 hazard levels for (a) H1 and (b) H2 directions	120
.....	120
Figure 6-4. RTR variability in DBE hazard level response spectra (a) Suite A and (b) Suite B	123
.....	123
Figure 6-5. RTR variability in MCE hazard level response spectra (a) Suite A and (b) Suite B	123
.....	123
Figure 6-6. Convergence test for dispersion measure: COV versus number of runs for normalized base shear, in (a) H1 and (b) H2 directions	125
.....	125

Figure 6-7. 30-Story building roof drift mean and dispersion at 5 hazard levels for (a) H1 and (b) H2 directions	126
Figure 6-8. 30-Story building 20 th floor coupling beam rotations, mean and dispersion at 5 hazard levels for (a) North and (b) East coupling beams.....	127
Figure 6-9. Shear wall boundary element strain gage locations	128
Figure 6-10. 30-Story building structural wall boundary element strains. Mean and dispersion at 5 hazard levels for BE #1 (a) tensile and (b) compressive strains, BE #3 (c) tensile and (d) compressive strains	129
Figure 6-11. Frequency and dispersion in 30 ground motions randomly selected 1000 times through uniform distribution.....	133
Figure 6-12. Frequency and dispersion in the first 1000 converged ground motions for the 20-story Opensees analyses using (a) correlated and (b) independent random variables	133
Figure 6-13. Frequency and dispersion in the first 1000 converged ground motions for the 30-story Opensees analyses using (a) correlated and (b) independent random variables	134
Figure 6-14. 30-story building Suite A analyses: cumulative distribution function for (a) normalized base shear, (b) roof drift, and (c) CB rotations	141
Figure 6-15. 30-story building Suite A analyses: cumulative distribution function for Corner BE (a) tensile strains and (b) compressive strains, as well as End BE (c) tensile strains and (d) compressive strains	142
Figure 7-1. Structural wall shear capacity ($V_{max}/V_{ne,ACI}$) versus curvature ductility, Wallace et al (2013).....	150
Figure 7-2. Variation in measured shear strength to nominal shear strength ratio versus reinforcement per (a) Wallace (1998) (b) Wood (1990).....	154

Figure 7-3. Histogram of $V_{max}/V_{n,e}$ using data by (a) Wallace (1998) (b) Wood (1990).....	154
Figure 7-4. Probability distribution tests of $V_{max}/V_{n,e}$ using (a) Wallace (1998) (b) Wood (1990)	154
Figure 7-5. General sequence of tall reinforced concrete core wall building behavior during a hazard and the context in which shear controlled wall tests were used. All strain limits shown are for plastic hinge regions.....	157
Figure 8-1. Flowchart of component reliability assessment using closed form solutions.....	170
Figure 8-2. Shear design reliability MCE hazard for structural walls with $f'_c < 8\text{ksi}$ (a) per closed-form solutions and (b) comparative results between closed-form solutions and Monte Carlo simulations	172
Figure 8-3. Variations in Monte Carlo probability of failure estimator versus required number of runs.....	173
Figure 8-4. Shear design reliability MCE hazard for structural walls with $f'_c \geq 8\text{ksi}$ (a) per closed-form solutions and (b) comparative results between closed-form solutions and Monte Carlo simulations	174
Figure 8-5. Shear design reliability at various ground motion intensities for structural walls with (a) $f'_c < 8\text{ksi}$ (b) $f'_c \geq 8\text{ksi}$	176

APPENDIX A

Figure A-1. 20-Story building, typical floor plan view	184
Figure A-2. 20-Story building, Elevation A of south wall	185

APPENDIX B

Figure B-1. Embedded beams with a stiffness of $E = 20 \cdot E_{cb}$ and $EI/L = 10$ for coupling beams (a) North (b) South (c) West (d) East	190
---	-----

Figure B-2. Embedded beams with a stiffness of $E = 20 \cdot E_{cb}$ and $EI/L = 20$ for coupling beams (a) North (b) South (c) West (d) East	190
Figure B-3. Varied stiffness values for embedded beams with span of 20ft for coupling beams (a) North (b) South (c) West (d) East	194
Figure B-4. Varied stiffness values for embedded beams with span of 10ft for coupling beams (a) North (b) South (c) West (d) East	194
Figure B-5. 30-story building interstory drift comparison between Rayleigh damping and modal damping for (a) H1 direction (b) H2 direction and (c) % difference	197
Figure B-6. 30-story building coupling beam rotations comparison between Rayleigh damping and modal damping for (a) North (b) South (c) West and (d) East coupling beams	198
Figure B-7. 30-story building coupling beam rotations comparison (% difference) between Rayleigh damping and modal damping in (a) positive rotations and (b) negative rotations	199
Figure B-8. 30-story building base shear comparison between Rayleigh damping and modal damping for (a) H1 direction (b) H2 direction and (c) % difference	200
Figure B-9. Axial strains are plotted from the lowest row of shear wall elements.	204
Figure B-10. Axial strains are plotted from strain gages over the height of each story	204
Figure B-11. Minimum core wall boundary element lengths, per common practice	205
Figure B-12. Core wall axial strains plotted for GM #14 at 8.4, 10.1, 12.4, 14.0, 18.0, 19.3, 29.7, and 31.3 seconds.	209

APPENDIX C

Figure C-1. Normalized base shear histogram and fitted distribution for H1 direction (a) SLE25 (b) SLE43 (c) DBE(15) (d) DBE(30) (e) MCE(15) (f) MCE(30) and (g) OVE hazard levels ..	210
---	-----

Figure C-2. Normalized base shear histogram and fitted distribution for H2 direction (a) SLE25 (b) SLE43 (c) DBE(15) (d) DBE(30) (e) MCE(15) (f) MCE(30) and (g) OVE hazard levels ..	211
Figure C-3. Convergence test for dispersion measure: COV versus number of runs for roof drifts, in (a) H1 and (b) H2 directions	212
Figure C-4. Roof drift histogram and fitted distribution for H1 direction (a) SLE25 (b) SLE43 (c) DBE(15) (d) DBE(30) (e) MCE(15) (f) MCE(30) and (g) OVE hazard levels	213
Figure C-5. Roof drift histogram and fitted distribution for H2 direction (a) SLE25 (b) SLE43 (c) DBE(15) (d) DBE(30) (e) MCE(15) (f) MCE(30) and (g) OVE hazard levels	214
Figure C-6. 30-Story building 20 th floor coupling beam rotations, mean and dispersion at 5 hazard levels for (a) North (b) East (c) South and (d) West coupling beams	215
Figure C-7. Convergence test for dispersion measure: COV versus number of runs for (a) North (b) East (c) South and (d) West coupling beams	216
Figure C-8. North coupling beam histogram and fitted distribution for (a) SLE25 (b) SLE43 (c) DBE(15) (d) DBE(30) (e) MCE(15) (f) MCE(30) and (g) OVE hazard levels	217
Figure C-9. East coupling beam histogram and fitted distribution for (a) SLE25 (b) SLE43 (c) DBE(15) (d) DBE(30) (e) MCE(15) (f) MCE(30) and (g) OVE hazard levels	218
Figure C-10. South coupling beam histogram and fitted distribution for (a) SLE25 (b) SLE43 (c) DBE(15) (d) DBE(30) (e) MCE(15) (f) MCE(30) and (g) OVE hazard levels	219
Figure C-11. West coupling beam histogram and fitted distribution for (a) SLE25 (b) SLE43 (c) DBE(15) (d) DBE(30) (e) MCE(15) (f) MCE(30) and (g) OVE hazard levels	220
Figure C-12. 30-Story building structural wall boundary element tensile axial strains, mean and dispersion at 5 hazard levels for BE (a) #1 (b) #4 (c) #5 and (d) #8	221

Figure C-13. Boundary element tensile axial strain (#1) histogram and fitted distribution (a) SLE25 (b) SLE43 (c) DBE(15) (d) DBE(30) (e) MCE(15) (f) MCE(30) and (g) OVE hazard levels	222
Figure C-14. Boundary element tensile axial strain (#4) histogram and fitted distribution (a) SLE25 (b) SLE43 (c) DBE(15) (d) DBE(30) (e) MCE(15) (f) MCE(30) and (g) OVE hazard levels	223
Figure C-15. Boundary element tensile axial strain (#5) histogram and fitted distribution (a) SLE25 (b) SLE43 (c) DBE(15) (d) DBE(30) (e) MCE(15) (f) MCE(30) and (g) OVE hazard levels	224
Figure C-16. Boundary element tensile axial strain (#8) histogram and fitted distribution (a) SLE25 (b) SLE43 (c) DBE(15) (d) DBE(30) (e) MCE(15) (f) MCE(30) and (g) OVE hazard levels	225
Figure C-17. 30-Story building structural wall boundary element tensile axial strains, mean and dispersion at 5 hazard levels for BE (a) #2 (b) #3 (c) #6 (d) #7 (e) #9 (f) #10 (g) #11 and (h) #12	227
Figure C-18. Boundary element tensile axial strain (#2) histogram and fitted distribution (a) SLE25 (b) SLE43 (c) DBE(15) (d) DBE(30) (e) MCE(15) (f) MCE(30) and (g) OVE hazards	228
Figure C-19. Boundary element tensile axial strain (#3) histogram and fitted distribution (a) SLE25 (b) SLE43 (c) DBE(15) (d) DBE(30) (e) MCE(15) (f) MCE(30) and (g) OVE hazard levels	229

Figure C-20. Boundary element tensile axial strain (#6) histogram and fitted distribution (a) SLE25 (b) SLE43 (c) DBE(15) (d) DBE(30) (e) MCE(15) (f) MCE(30) and (g) OVE hazard levels	230
Figure C-21. Boundary element tensile axial strain (#7) histogram and fitted distribution (a) SLE25 (b) SLE43 (c) DBE(15) (d) DBE(30) (e) MCE(15) (f) MCE(30) and (g) OVE hazard levels	231
Figure C-22. Boundary element tensile axial strain (#9) histogram and fitted distribution (a) SLE25 (b) SLE43 (c) DBE(15) (d) DBE(30) (e) MCE(15) (f) MCE(30) and (g) OVE hazard levels	232
Figure C-23. Boundary element tensile axial strain (#10) histogram and fitted distribution (a) SLE25 (b) SLE43 (c) DBE(15) (d) DBE(30) (e) MCE(15) (f) MCE(30) and (g) OVE hazard levels	233
Figure C-24. Boundary element tensile axial strain (#11) histogram and fitted distribution (a) SLE25 (b) SLE43 (c) DBE(15) (d) DBE(30) (e) MCE(15) (f) MCE(30) and (g) OVE hazard levels	234
Figure C-25. Boundary element tensile axial strain (#12) histogram and fitted distribution (a) SLE25 (b) SLE43 (c) DBE(15) (d) DBE(30) (e) MCE(15) (f) MCE(30) and (g) OVE hazard levels	235
Figure C-26. 30-Story building structural wall boundary element compressive axial strains, mean and dispersion at 5 hazard levels for BE (a) #1 (b) #4 (c) #5 and (d) #8	236
Figure C-27. 30-Story building structural wall boundary element compressive axial strains, mean and dispersion at 5 hazard levels for BE (a) #2 (b) #3 (c) #6 (d) #7 (e) #9 (f) #10 (g) #11 and (h) #12	238

LIST OF TABLES

Table 2-1. Design coefficients and factors for seismic force-resisting systems, a partial list of ductile systems from ASCE7-10 Table 12.2-1	10
Table 2-2. Summary of basic requirements for tall building analysis, LATBSDC (2014)	14
Table 2-3. Expected material strengths, LATBSDC (2014).....	14
Table 2-4. Reinforced concrete stiffness properties, LATBSDC (2014).....	15
Table 2-5. SLE Elastic response spectrum analysis – component acceptance criteria.....	16
Table 2-6. Risk reduction factor per risk categories	18
Table 2-7. Acceptance criteria for key structural responses from a reinforced concrete core wall building, under MCE level analysis.....	19
Table 2-8. Summary of 40-story building nonlinear dynamic analysis results, Moehle (2007) ..	21
Table 2-9. Reliability of rectangular wall shear design (Wallace et al, 2013).....	24
Table 2-10. Importance factors and probabilities of failure by Risk Category of buildings for earthquake loads, ASCE7-10	27
Table 2-11. Load factors for force-controlled behaviors, ASCE7-16	27
Table 2-12. Assumed demand dispersion for general and well-defined cases (ASCE7-16)	28
Table 2-13. Assumed capacity dispersion for general and well-defined cases (ASCE7-16)	28
Table 2-14. Required ratios of λ/ϕ to achieve 10% probability of collapse	29
Table 2-15. Comparison of current and proposed shear demand load factors for MCE level shear design of tall reinforced-concrete buildings	30
Table 3-1. A summary of five seismic hazard levels.....	33
Table 3-2. Summary of ground motion Suites A, B, C, and D.....	35
Table 3-3. Weighted errors for scale factor calculation.....	37
Table 3-4. Suite A – Earthquake information for 15 scaled ground motions at 5 hazard levels ..	39

Table 3-5. Suite A – Scale factors for 15 ground motions at 5 hazard levels.....	40
Table 3-6. MCE level ground motions considered for amplitude scaling and spectral matching	44
Table 3-7. Suite B – 30 scaled ground motions for DBE hazard level.....	45
Table 3-8. Suite B – 30 scaled ground motions for MCE hazard level	46
Table 4-1. Dimensions of structural members for 30-story building.....	50
Table 4-2. Loading Criteria.....	50
Table 4-3. ASCE7-10 Seismic parameters	54
Table 4-4. Concrete member strength and stiffness.....	56
Table 4-5. Reinforcing strength	57
Table 4-6. Stiffness assumptions	57
Table 4-7. Details of Perform 3D shear wall element	59
Table 4-8. Shear displacement hinge – modeling and cyclic degradation parameters	61
Table 4-9. Effective slab widths, corresponding stiffness factors (α), and normalized effective stiffness factors, $\alpha \cdot \beta$ for actual and lumped cases	63
Table 4-10. Slab-beams – modeling and cyclic degradation parameters.....	64
Table 4-11. 30-Story building modal properties.....	67
Table 4-12. MCE level key structural responses	70
Table 4-13. MCE shear wall design and transverse reinforcement	71
Table 4-14. Opensees dynamic analysis solution strategy.....	86
Table 5-1. Uncertainties in collapse capacity estimates (Haselton et al, 2007).....	90
Table 5-2. A summary of input random variables	98
Table 5-3. Statistical parameters for compressive strengths of high strength concrete.....	101

Table 5-4. Statistical parameters for yield and tensile strengths of A706 Grade 60 reinforcement (Bournonville et al, 2004).....	103
Table 5-5. Summary of reinforced concrete beam test results (Naish et al, 2013a).....	104
Table 5-6. Summary of periods associated with first five Ritz vectors for “MA” and “3D” models (Naeim et al, 2010).....	111
Table 5-7. Primary causes of structural failures, Melchers (1999).....	112
Table 6-1. Total number of Monte Carlo simulations	114
Table 6-2. Summary of Matlab syntax for random variable generations	117
Table 6-3. Mean and dispersion measured in logarithmic standard deviation for Suites A and B at DBE and MCE hazard levels	124
Table 6-4. Variation in base shear dispersion measure, using a sample size of 1000	125
Table 6-5. 20 and 30-Story building modal properties (Opensees)	130
Table 6-6. Summary of Opensees convergence rates	132
Table 6-7. Summary of EDP dispersion values.....	136
Table 6-8. Summary of minimum and maximum EDP dispersion values and relative percentage contributions from RTR variability and model parameter/design uncertainties.....	138
Table 6-9. Summary of EDP means, standard deviations, and probability distributions	140
Table 6-10. Summary of EDP values at standard z-scores 0, ± 1 , and ± 2 , for 30-story building Suite A analyses	143
Table 7-1. Shear-controlled wall tests separated into two bins by ACI318-11 limiting shear stress (Wallace et al, 2013).....	152
Table 8-1. Anticipated reliability and corresponding reliability indexes,	163
Table 8-2. Summary of all reliability methodology and parameters considered.....	170

Table 8-3. Summary of MCE level Monte Carlo simulations	172
Table 8-4. Summary of variations in Monte Carlo probability of failure estimator	173
Table 8-5. Comparison of minimum required γ to achieve anticipated reliability versus current γ	175
Table 8-6. Shear design reliability (%) MCE hazard based on various values of γ , ρ_D , and ρ_C	175

APPENDIX A

Table A-1. Dimensions of structural members for 20-story building	183
---	-----

APPENDIX B

Table B-1. Summary of coupling beam rotations and errors for $EI/L=10$ and 20	191
Table B-2. Summary of tensile and compressive axial strains and errors	204

ACKNOWLEDGEMENTS

First of all, I would like to thank my advisor, Professor John Wallace, for all his guidance and support in the past 4 years while completing my doctoral studies. I have gained valuable technical knowledge and an idea of what a full and well-rounded career looks like: a career that combines meaningful research, impactful teaching, fascinating consulting projects, and leadership within our industry to serve a greater community. I am thankful that our working relationship has opened so many doors to new opportunities.

I am grateful for my doctoral committee members, Professor Stewart, Professor Sabol, Professor Conte, and Professor Brandenburg; I learned a lot from their expertise and I found their insightful and timely feedback to be very helpful. It was a great pleasure to work with Professor Sabol as his teaching assistant; I learned so much from his immensely knowledgeable and meticulous teaching styles and from his wisdom in balancing his teaching/consulting careers. I am also grateful for his generous support and encouragement throughout my graduate studies. I would also like to thank Professor Burton who spent numerous hours in advising and discussing structural reliability and his input greatly improved this research.

My special thanks go to Professor Youssef Hashash from University of Illinois at Urbana-Champaign, who has been an integral part in my personal and professional endeavors. He has been a great mentor who has continuously encouraged me to make the best decisions and become the best version of myself since I was an undergraduate research assistant in his group. I'd like to thank him for always being there to shed light on my journey and for our conversations that have truly expanded my views beyond academia.

Over the years, I have collaborated with several master of science and doctoral students and this thesis would not be complete today without their contributions. Jackson English was particularly helpful with building modeling in the beginning stages of this research and Yu Zhang was very diligent in optimizing my Opensees code that significantly increased the productivity of my work.

I'd also like to thank former Ph.D. students Anne Lemnitzer and Kristijan Kolozvari; they both have been extremely open and generous in sharing their resources and it was always uplifting to hear their honest experiences.

My acknowledgement extends to my fellow graduate student researchers Chris Segura, Thien Tran, Sofia Gavridou, and Negin Aryaee for their friendship and the times we shared in our offices exchanging enjoyable conversations and discussing the progress of our work. I'd also like to thank my friends outside of academia for their friendship and encouragement; having a great network of friends helped me move past the research roadblocks.

Last but not least, I'd like to thank my parents and my sister Ok-Kyung for their continuous support throughout all of my personal and professional goals.

VITA

2006 B.S., Civil Engineering
University of Illinois at Urbana-Champaign
Urbana, IL

2006 – 2007 Transportation Design Engineer, P.E.
CTE | AECOM
Chicago, IL

2007 – 2008 M.S., Structural and Earthquake Engineering
University of California Los Angeles
Los Angeles, CA

2008 – 2012 Structural Design Engineer, S.E.
John A. Martin & Associates, Inc.
Los Angeles, CA

Summer, 2014 Forensics Engineering Intern / Tall Buildings Researcher
Thornton Tomasetti
New York, NY

2012 – 2016 Graduate Student Researcher & Teaching Assistant
Department of Civil and Environmental Engineering
University of California, Los Angeles
Los Angeles, CA

CHAPTER 1. INTRODUCTION

This chapter first provides background, motivations, and objectives of the research, and then the overview of the dissertation is presented.

1.1. Background and Motivations

Along the west coast of the United States, reinforced concrete core wall systems are commonly selected as seismic force resisting systems for tall buildings. During strong ground shaking, core wall systems are intended to dissipate energy by yielding of coupling beams, followed by flexural yielding at the wall base (Figure 1-1). Although the wall behavior is governed by flexure, the wall design is often governed by shear, as the walls experience high shear demands (usually up to the ACI318-11 code limiting shear stress of $8 \cdot \sqrt{f'_c}$ psi) over a significant height of the core. The high shear demands are due to a lack of redundant walls in tall buildings, as the lengths of the walls are limited to the perimeter of the elevator core, as shown on Figure 1-2.

The design procedures for tall buildings are typically conducted using performance-based design procedures recommended by Los Angeles Tall Buildings Structural Design Council (LATBSDC, 2014) or Pacific Earthquake Engineering Research Center Tall Buildings Initiative (PEER TBI, 2010). Provisions in the two documents recommend shear design per acceptance criterion

$$F_{uc} \leq \kappa_i \phi F_{n,e}$$

where F_{uc} is 1.5 times the mean shear demand resulting from a suite of ground motions, $F_{n,e}$ is the nominal strength computed from expected material properties, κ_i is the risk reduction factor based on risk categories, and ϕ is the uncertainty in $F_{n,e}$. The 1.5 factor applied to the mean

shear demand is referred to as the demand factor, γ . Although shear failure can be fatal due to its sudden and brittle nature, the reliability of this shear design acceptance criterion has not yet been thoroughly researched. Moreover, there is a lack of consensus in the governing codes and tall building guidelines regarding the use of γ , κ_i , and ϕ factors. Given the importance of structural walls (as the main seismic force resisting system, along with coupling beams) in tall reinforced concrete core wall buildings, these issues have served as a motivation to pursue this research. The limitations of the current shear design acceptance criterion are summarized as follows.

1. The demand factor, $\gamma=1.5$, is an empirical factor established to achieve conservatism in shear design (PEER TBI, 2010).
2. There are discrepancies in ϕ recommendations, where LATBSDC (2014) recommends $\phi =1.0$ and PEER TBI (2010) recommends $\phi =0.75$.
3. There are discrepancies in applications of κ_i ; κ_i is generally not applied for force-controlled actions under MCE analysis per LATBSDC (2014) recommendations. On the other hand, the proposed changes in ASCE7-16 Chapter 16 apply an equivalent factor (seismic importance factor applied to shear demands) to force-controlled actions.
4. The proposed changes in ASCE7-16 Chapter 16 *Nonlinear Response History Analysis* recommend significantly higher factors for γ . For critical actions, the proposed γ range between 2.0 and 3.0 (depending on risk categories), for ordinary actions, the proposed γ range between 1.5 and 2.25, and for noncritical actions, the proposed γ range between 1.0 and 1.50. Structural wall shear design correspond to critical actions; thus, $\gamma=2.0$ is recommended for risk categories I and II, $\gamma=2.5$ is recommended for risk category III, and $\gamma=3.0$ is recommended for risk category IV. This is a significant increase from the current recommendations set forth in LATBSDC (2014). The proposed factors are high

for two main reasons; first, because seismic importance factors were applied to demands, and also because reliabilities were estimated using conservative assumptions of shear capacities (code nominal shear strengths using expected material properties, no reserve strengths shown per experimental tests were used).

Thus, it is evident from the aforementioned shortcomings and discrepancies that there is a need to conduct reliability studies for the current shear design acceptance criterion. It would be important to quantify and incorporate all uncertainties that contribute to shear demand and capacity to predict reliability of shear designs, and to establish γ and ϕ factors for various risk categories and ground motion intensities.

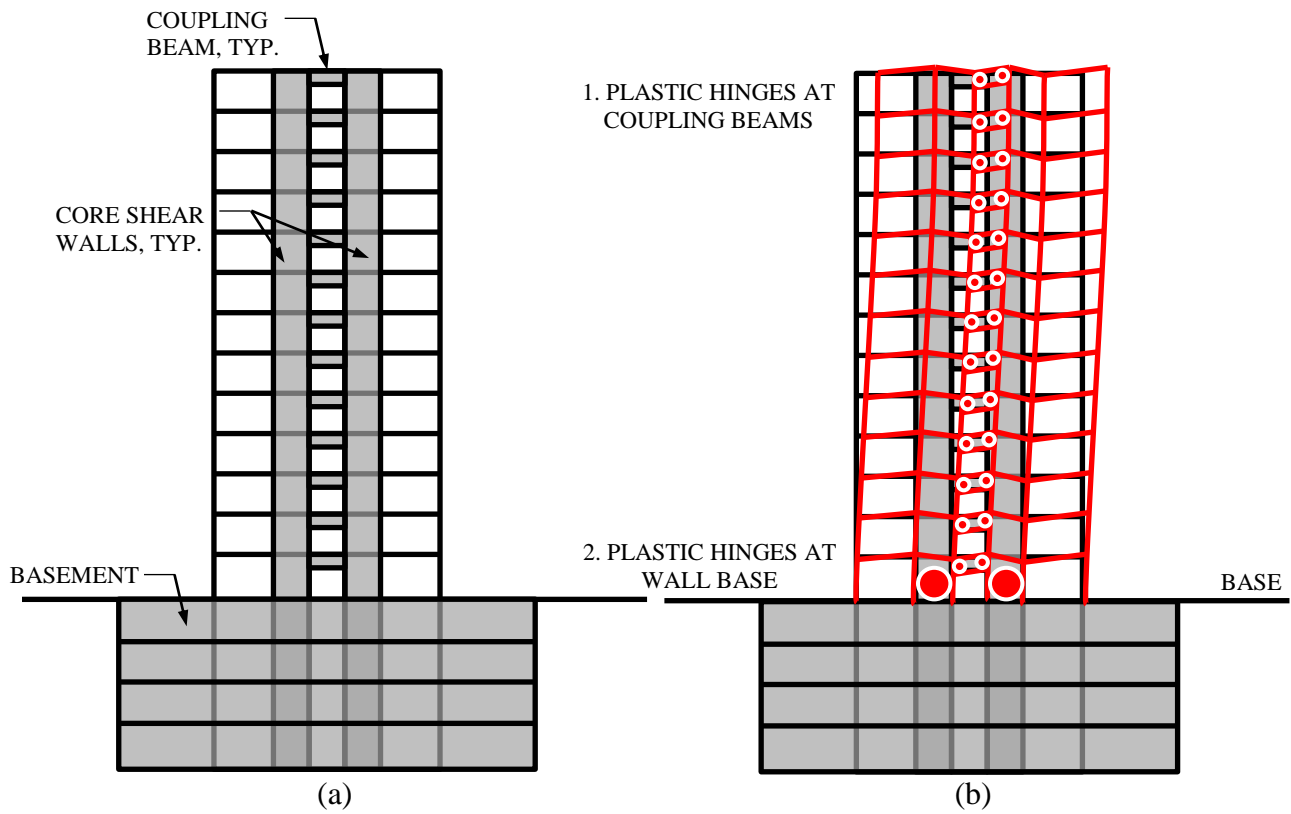


Figure 1-1. (a) Typical elevation view of a tall reinforced concrete core wall building and (b) intended nonlinear behavior under seismic events

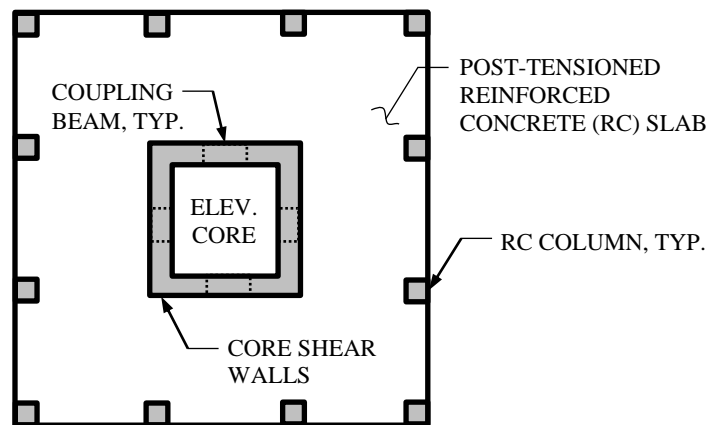


Figure 1-2. Typical plan view of a reinforced concrete core wall building

1.2. Objectives

Given the shortcomings of the current structural wall shear design acceptance criterion, a methodology was developed to compute reliability of structural wall shear design. Statistical parameters for shear demand were quantified through 20 and 30-story building nonlinear response history analyses performed through Monte Carlo simulations, and statistical parameters for shear capacity were measured through available shear controlled wall test results. Given the statistical parameters for shear demand and capacity, closed form solutions and Monte Carlo simulations were utilized to evaluate reliability of the current shear design acceptance criterion. Reliabilities were computed for various risk categories and ground motion intensities. In all, the primary objectives of the study are:

1. to compute reliability of structural wall shear design for risk categories I, II, III, and IV, conditioned upon a seismic hazard;
2. to provide minimum required γ and ϕ factors for each risk category, conditioned upon a seismic hazard;
3. to establish a framework for tall building component reliability studies, not only for shear design acceptance criterion but also for other components;
4. to quantify statistical parameters (mean and dispersion) for tall building engineering demand parameters, such as shear force demands, drifts, coupling beam rotations, and core wall axial strains;
5. to examine structural wall failure modes and quantify statistical parameters (mean and dispersion) for shear controlled wall capacities; and
6. to provide insightful sensitivity studies that address common modeling issues for tall buildings.

1.3. Organization

This dissertation is organized into nine chapters; a brief summary of the organization is provided below.

- Chapter 2 summarizes tall building design and analysis procedures currently used in the United States. Relevant building codes and design guidelines for tall building designs are introduced. Subsequently, the current state for shear design of tall reinforced-concrete core walls is discussed. Lastly, the proposed changes to ASCE7-16 that will affect various aspects of nonlinear response history analysis are reviewed.
- Chapter 3 summarizes the ground motion selection and modification process for the design and analysis of tall buildings.
- Chapter 4 describes the design, modeling, and analysis procedures for the 20 and 30-story reinforced concrete core wall buildings. The two buildings were designed to satisfy the performance criteria set forth in LATBSDC (2014).
- Chapter 5 provides a description of all input uncertainties considered to quantify dispersion in various structural responses (referred to as engineering demand parameters, EDPs).
- Chapter 6 presents Monte Carlo simulation methodology used to quantify dispersion in selected EDPs and presents findings on tall building EDP dispersions and means.
- Chapter 7 reviews current procedures used to calculate nominal shear strength of structural walls and uncertainties in shear capacity were evaluated using experimental test results of shear-controlled walls.
- Chapter 8 reviews various component reliability methodologies and describes the procedures used to compute reliability of structural wall shear design for tall buildings.

Reliability of structural wall shear design is presented for various risk categories and ground motion intensities.

- Chapter 9 presents a brief summary of this study and the conclusions.

CHAPTER 2. LITERATURE REVIEW

This chapter summarizes tall building design and analysis procedures currently used in the United States. The chapter begins by introducing relevant building codes and design guidelines applicable for tall building designs. Next, the current state for shear design of tall reinforced-concrete core walls is discussed. Lastly, the proposed changes to ASCE7-16 that will affect various aspects of nonlinear response history analysis are reviewed.

2.1. Tall Building Definition

The definition of tall buildings is adopted from Los Angeles Tall Buildings Structural Design Council (LATBSDC, 2014). Tall buildings are defined as those with height, h_n , greater than 160-ft above the base. This height, h_n , is measured to the top of level n , which represents the roof of the structure excluding the heights of mechanical penthouses and nonstructural elements. The base is taken as the average ground elevation adjacent to the structure.

2.2. Governing Codes

The governing building code for this tall building study is based on 2012 International Building Code (IBC) and 2013 California Building Code (CBC), which adopts ASCE7-10 Minimum Design Loads for Buildings and Other Structures.

2.2.1. Selection of Seismic Force-Resisting System for Tall Buildings

Under the governing codes, there are two options for tall building designs in Seismic Design Categories D or above. The first option is to follow linear procedures outlined in ASCE7-10 Chapter 12 *Seismic Design Requirements for Building Structures*. Linear analysis is performed using three factors, response modification factor (R), overstrength factor (Ω_0), and deflection amplification factor (C_d) to adjust linear responses to nonlinear responses, as shown on Figure 2-1.

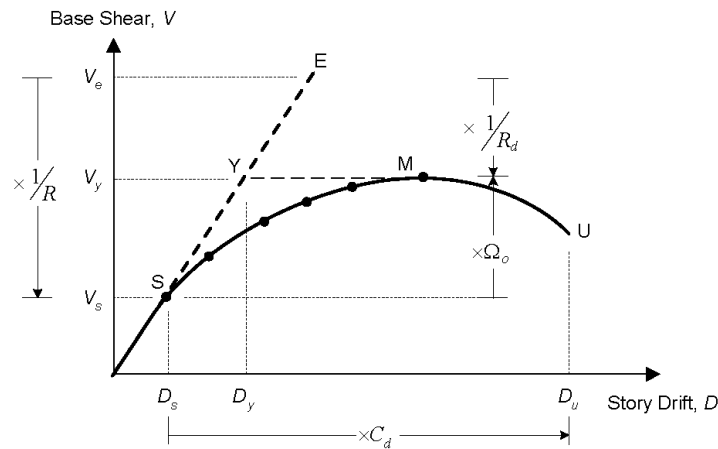


Figure 2-1. Inelastic force-deformation curve, SEAOC Blue Book (2008)

With basic seismic parameters computed from linear analysis, a ductile seismic force-resisting system is selected for seismic design categories D or above. A partial list of ductile systems from ASCE7-10 is shown on Table 2-1. However, for ductile bearing wall systems and building frame systems, the building codes limit structural heights to 160-ft, thereby prohibiting the use of these seismic force-resisting systems for tall buildings. Provisions in the building codes are primarily based on understanding of low to mid-rise structures; therefore, when these provisions are applied to tall buildings, an optimal design may not result, both in terms of cost and safety. For other ductile seismic force-resisting systems that do not have height limitations, steel special moment-resisting frame systems and steel special dual systems tend to be too flexible to meet

drift requirements for tall buildings. Thus, a commonly selected system with no height limitations and enough stiffness to meet the drift requirements is the dual system with special reinforced concrete shear walls and special moment frames capable of resisting at least 25% of prescribed seismic forces.

Table 2-1. Design coefficients and factors for seismic force-resisting systems, a partial list of ductile systems from ASCE7-10 Table 12.2-1

Seismic Force-Resisting System	R	Ω_0	C_d	Structural system limitations including structural height, h_n (ft)				
				Seismic Design Category				
				B	C	D	E	F
A. Bearing wall systems								
1. Special reinforced concrete shear walls	5	2.5	5	NL ¹	NL	160	160	160
B. Building frame systems								
1. Steel eccentrically braced frames	8	2	4	NL	NL	160	160	160
2. Steel special concentrically braced frames	6	2	5	NL	NL	160	160	100
C. Moment-resisting frames								
1. Steel special moment frames	8	3	5.5	NL	NL	NL	NL	NL
D. Dual systems with special moment frames capable of resisting at least 25% of prescribed seismic forces								
1. Steel eccentrically braced frames	8	2.5	4	NL	NL	NL	NL	NL
2. Steel special concentrically braced frames	7	2.5	5.5	NL	NL	NL	NL	NL
3. Special reinforced concrete shear walls	7	2.5	5.5	NL	NL	NL	NL	NL

¹NL = no limit

The second option for tall building designs is to follow alternative lateral-force procedures stated in 2012 IBC Section 104.11 and ASCE7-10 Section 12.6. Section 104.11 of 2012 IBC reads:

“The provisions of this code are not intended to prevent the installation of any material or to prohibit any design or method of construction not specifically prescribed by this code, provided that such alternative method has been approved. An alternative material, design, or method of construction shall be approved where the building official finds that the proposed design is satisfactory and complies with the intent of the provisions of this code, and that the material,

method or work offered is, for the purpose intended, at least the equivalent of that prescribed in this code in quality, strength, effective, fire resistance, durability and safety.”

Following this alternative approach, structural engineers are allowed to use performance-based design procedures for tall buildings. The intent of the non-prescriptive approach is to allow more accurate and reliable design based on linear response spectrum and nonlinear response history analyses. For tall building designs in Los Angeles, ‘An Alternative Procedure for Seismic Analysis and Design of Tall Buildings Located in the Los Angeles Region’ is used (LATBSDC, 2014). In other western regions of the United States, either the LATBSDC (2014) approach is used, or the Pacific Earthquake Engineering Research Center Tall Buildings Initiative Guidelines (PEER TBI, 2010), along with region-specific city codes are used. For the past ten to fifteen years, reinforced concrete core wall systems have been the most widely selected seismic force-resisting system for tall buildings (PEER Task 12, 2011).

2.2.2. Tall Building Design Comparison: Code-Based versus LATBSDC (2014)

In the previous section, two procedures used for the design of tall buildings were introduced. Based on the two procedures, the following seismic force-resisting systems were selected:

- Code-based: a dual system with special reinforced concrete shear walls and special moment frames capable of resisting at least 25% of prescribed seismic forces
- Alternate lateral-force procedures per LATBSDC (2014): reinforced concrete core wall systems

The comparisons of the two seismic force-resisting systems are shown on Figure 2-2. Although either system can be used to design tall buildings that will demonstrate satisfactory seismic performance, there are major disadvantages in selecting a dual system as shown on Figure 2-2(a). The dual systems have reinforced concrete moment frames along the perimeter of

the building where the depths of these moment frame beams obstruct window spaces and have the potential to increase floor to floor heights. On the other hand, the core wall only system as shown on Figure 2-2(b) maximizes the window spaces which in turn minimizes the floor-to-floor heights. This can potentially create more floors for a given building height, and increase revenue. Thus, the reinforced concrete core wall systems have been the most popular and efficient structural systems for tall building designs so far (PEER Task 12, 2011).

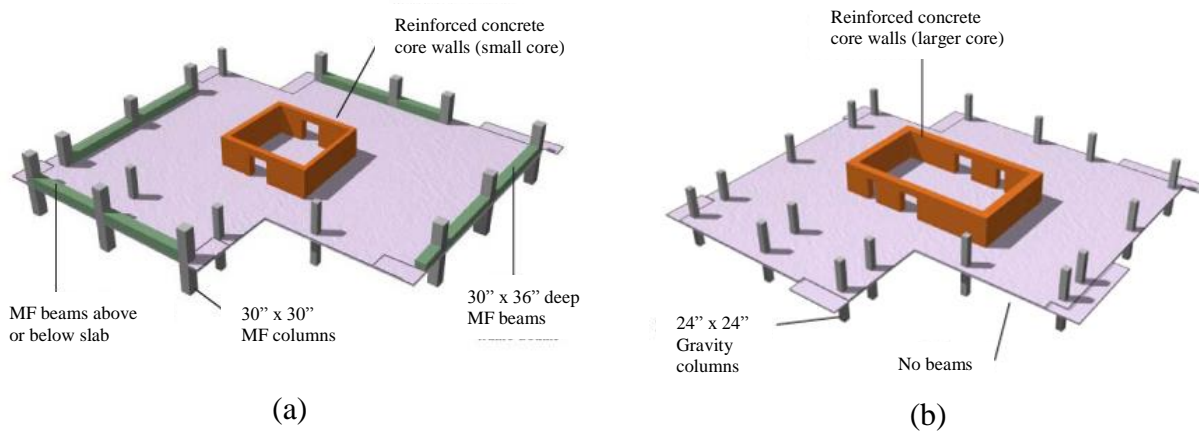


Figure 2-2. Isometric floor plan views of a tall building design using (a) dual system of reinforced concrete core walls and reinforced concrete moment frames and (b) reinforced concrete core walls. Image courtesy of Magnusson Klemencic Associates.

Since the reinforced concrete core wall buildings are the most widely used, relative to dual systems, the core system was chosen as a prototype tall building for this study.

2.3. Performance-Based Design Procedures per LATBSDC (2014)

2.3.1. Methodology

Performance-based design of tall, reinforced concrete core wall buildings is commonly achieved in three stages, as recommended by Los Angeles Tall Buildings Structural Design Council (Table 2-2; LATBSDC, 2014). First, an initial design is created based on experience to proportion members and apply capacity design concepts. In this step, the height limitations set forth by ASCE 7, either 160 ft or 240 ft depending on the system, are ignored. Next, the adequacy of the initial design is demonstrated by evaluating the performance of the building at both service and collapse prevention hazard levels using acceptance criteria established in an approved, project-specific “Basis of Design.” It is common to conduct the service-level assessment first using linear response spectrum analysis, and then adjust the member proportions based on experience prior to conducting the MCE analysis. The MCE analysis requires developing a three-dimensional nonlinear model subjected to seven or more pairs of earthquake records. In recent years, it has become more common to use 11 pairs of horizontal ground motion records for MCE and use of three pairs and maximum response is not generally accepted. Typical adjustments might involve designing for a wall shear stress of 2.0 to 2.5 times the wall shear force obtained in the SLE evaluation, and modifying coupling beam strengths to be more uniform over the building height.

Table 2-2. Summary of basic requirements for tall building analysis, LATBSDC (2014)

Design/ Evaluation Step	Ground Motion Intensity	Type of Analysis	Type of Mathematical Model	Accidental Torsion Considered	Material Reduction Factors	Material Strength
1	Nonlinear behavior defined / Capacity design					
2	SLE RP ¹ 43 years	LDP ² or NDP ³	3D ⁴	Yes	$\phi = 1.0$	Expected properties
3	MCE RP 2475 years	NDP	3D	Yes, if flagged from Step 2 No, otherwise	$\phi = 1.0$	Expected properties

¹ RP: return period

² LDP: linear dynamic procedure

³ NDP: nonlinear dynamic procedure

⁴ 3D: three-dimensional

The structural models are recommended to incorporate realistic estimates of strength and stiffness properties for all materials and components. Thus, expected material properties are utilized instead of nominal properties (Table 2-3) and various reinforced concrete stiffness parameters are recommended for SLE and MCE hazard levels (Table 2-4). Although the current recommendation of using $1.3 \cdot f'_c$ for expected concrete compressive strength is generally appropriate for normal strength concrete; a factor of $1.1 \cdot f'_c$ has been shown to be more appropriate for $6\text{ksi} < f'_c \leq 12\text{ksi}$ based on studies conducted by Nowak et al (2008) on over 2000 concrete samples. The lower expected concrete strengths are typically a result of the softer aggregate used, which also has been shown to produce lower than expected values of Modulus of Elasticity (LATBSDC, 2014).

Table 2-3. Expected material strengths, LATBSDC (2014)

Material	Expected strength
Yield strength for reinforcing steel	$1.17 \cdot f_y$
Ultimate compressive strength for concrete	$1.3 \cdot f'_c$

Table 2-4. Reinforced concrete stiffness properties, LATBSDC (2014)

Element	SLE and wind	MCE
Structural walls	Flexural – $0.75 \cdot I_g$ Shear – $1.0 \cdot A_g$	Flexural – $1.0 \cdot E_c$ Shear – $0.5 \cdot A_g$
Basement walls	Flexural – $1.0 \cdot I_g$ Shear – $1.0 \cdot A_g$	Flexural – $0.8 \cdot I_g$ Shear – $0.5 \cdot A_g$
Coupling beams	Flexural – $0.3 \cdot I_g$ Shear – $1.0 \cdot A_g$	Flexural – $0.2 \cdot I_g$ Shear – $1.0 \cdot A_g$
Diaphragms (in-plane only)	Flexural – $0.5 \cdot I_g$ Shear – $0.8 \cdot A_g$	Flexural – $0.25 \cdot I_g$ Shear – $0.25 \cdot A_g$
Moment frame beams	Flexural – $0.7 \cdot I_g$ Shear – $1.0 \cdot A_g$	Flexural – $0.35 \cdot I_g$ Shear – $1.0 \cdot A_g$
Moment frame columns	Flexural – $0.9 \cdot I_g$ Shear – $1.0 \cdot A_g$	Flexural – $0.7 \cdot I_g$ Shear – $1.0 \cdot A_g$

2.3.2. Analysis Procedure

When response spectrum analysis is used, the structure is evaluated using the following load combinations:

$$1.0 \cdot D + L_{exp} + 1.0 \cdot E_x + 0.3 \cdot E_y$$

$$1.0 \cdot D + L_{exp} + 1.0 \cdot E_y + 0.3 \cdot E_x$$

where D is the service dead load, L_{exp} is the expected service live load taken as 25% of the unreduced live load, and E_x and E_y represent the earthquake loads in X and Y directions. To calculate responses for each horizontal direction, at least 90 percent of the participating mass of the structure should be included, and the Complete Quadratic Combination (CQC) is recommended for modal response calculations. When nonlinear response history analysis is performed, the following load combination for each horizontal ground motion pair is used:

$$1.0 \cdot D + L_{exp} + 1.0 \cdot E$$

where E represents dynamic earthquake loads.

2.3.3. SLE Level Analysis – Global Acceptance Criteria

For global responses at the SLE level, story drift is limited to 0.5% of story height in any story.

2.3.4. SLE Level Analysis – Component Acceptance Criteria

Acceptance criteria for all actions at the component level (forces, moments, strains, displacements, or other deformations) are defined as force-controlled or deformation-controlled actions. Force-controlled actions are those in which inelastic deformation capacity cannot be assured and deformation-controlled actions are those in which reliable inelastic deformation capacity is achievable without critical strength degradation.

Under elastic response spectrum analysis, the component responses must meet acceptance criteria provided in Table 2-5. Careful attention should be paid when increasing the strength of deformation-controlled elements as it may adversely affect the performance of the building during the MCE level analysis.

Table 2-5. SLE Elastic response spectrum analysis – component acceptance criteria

Component Response	Risk Category	Demand to Capacity Ratio
Deformation-controlled action	I and II	1.50
	III	1.20
	IV	< 1.20, as determined by seismic peer review panel (SPRP)
Force-controlled action	-	0.70

Under nonlinear response history analysis, when less than seven pairs of ground motions are used, maximum responses shall be evaluated, otherwise, the mean of the maximum responses can be used. In lieu of providing specific guidelines, LATBSDC refers to acceptance criteria for Immediate Occupancy performance per ASCE41-13, Seismic Evaluation and Retrofit of Existing Buildings, as a measure of component evaluation. Project-specific acceptance criteria are typically developed by the design team (Engineer-of-Record), as each project tends to have

unique attributes, and approved by an independent peer-review panel appointed by the jurisdiction in consultation with the design team.

2.3.5. MCE Level Analysis – Global Acceptance Criteria

At the MCE level, the global responses include story drift, residual drift, and check for loss of story strength. For peak transient drift, the following criteria must be met:

$$\bar{\Delta} \leq 0.03 \cdot \kappa_i$$

$$\Delta \leq 0.045 \cdot \kappa_i$$

where $\bar{\Delta}$ is the mean of the absolute values of the peak transient drift ratios from the suite of analyses, Δ is the absolute value of the maximum story drift ratio from any analysis, and κ_i is the risk reduction factor derived from risk categories in ASCE7-10, as shown on Table 2-6. For residual drift, the following criteria must be met:

$$\bar{\Delta}_r \leq 0.01 \cdot \kappa_i$$

$$\Delta_r \leq 0.015 \cdot \kappa_i$$

where $\bar{\Delta}_r$ is the mean of the absolute values of residual drift ratios from the suite of analyses and Δ_r is the maximum residual story drift ratio from any analysis. In any nonlinear response history analysis, deformations shall not result in a loss of any story strength that exceeds 20% of the initial strength. Modeling story strength loss for reinforced concrete core wall buildings using commercial computer programs often leads to non-convergence; therefore, actual modeling of strength loss is rare.

Table 2-6. Risk reduction factor per risk categories

Risk Category from ASCE7-10 Table 1.5-1	Seismic importance factor, I_e (ASCE7-10)	$1/I_e$	Risk reduction factor, κ_i (LATBSDC, 2014)
I	1.0	1.0	1.00
II	1.0	1.0	1.00
III	1.25	0.80	0.80
IV	1.50	0.67	Value to be established by SPRP

2.3.6. MCE Level Analysis – Component Acceptance Criteria

For force-controlled actions, the following design acceptance criterion applies:

$$F_{uc} \leq \kappa_i \phi F_{n,e}$$

where F_{uc} is 1.5 times the mean demand resulting from a suite of ground motions, $F_{n,e}$ is the nominal strength computed from expected material properties, ϕ is the uncertainty in $F_{n,e}$, taken as 1.0, and κ_i is the risk reduction factor from Table 2-6. Per LATBSDC Section C3.5.4.1.1(a), κ_i is applied for deformation-controlled acceptance criteria but states that κ_i is not necessary for force-controlled actions. However, this approach is not necessarily widely accepted. This is because the nonlinear procedures set forth in the proposed ASCE7-16 Chapter 16 applies seismic importance factors to shear demands (equivalent to risk reduction factors applied to shear capacity, see Table 2-6) to both force-controlled and deformation-controlled actions. This will be addressed later in Chapter 2.5.5.

For deformation-controlled actions, the mean responses or member deformations are evaluated against project specific acceptable criteria (Basis of Design) multiplied by κ_i . The project specific acceptance criteria are usually established by referencing appropriate publications (journal papers or technical reports), material specific codes, or Primary Collapse

Prevention values published in ASCE41 (2013) for nonlinear response procedures. A summary of MCE level analysis acceptance criteria for key structural responses from a reinforced concrete core wall building is provided in Table 2-7.

Table 2-7. Acceptance criteria for key structural responses from a reinforced concrete core wall building, under MCE level analysis

Structural response	Response type	Acceptance criteria
Story drift	Global	0.03·κ _i - maximum mean from suite of analyses 0.045·κ _i - maximum from any single analysis κ _i = risk reduction factor, Table 2-6
Residual story drift	Global	0.01·κ _i - maximum mean from suite of analyses 0.015·κ _i - maximum from any single analysis
Coupling beam rotations	Component Def-controlled	0.06·κ _i - maximum mean from suite of analyses
Shear wall		
A. Shear force	Component Force-controlled	$1.5 \cdot F_{uc} \leq \kappa_i \cdot \phi \cdot F_{n,e}$ F _{uc} = mean value of demand F _{n,e} = nominal strength computed from expected material properties κ _i = 1.0 for force-controlled action φ = 1.0
B. Compressive strain*	Component Force-controlled	Within plastic hinge: 0.0075 - 1.5 times maximum mean from suite of analyses Outside of plastic hinge: 0.003 - 1.5 times maximum mean from suite of analyses
C. Tensile strain*	Component Def-controlled	Within plastic hinge: 0.01 - maximum mean from suite of analyses Outside of plastic hinge: 2·ε _y - maximum mean from suite of analyses

* Higher strain values may be allowed for the plastic hinge region, e.g., 0.01 in compression and 0.03 in tension; however, in this case, the φ-factor on wall shear may be reduced from 1.0 to 0.75 due to the uncertainty of greater nonlinear flexural deformations on wall shear strength. This is further described in Chapter 7.4.

2.4. Design of Tall Reinforced Concrete Structural Walls

While the component-level acceptance criteria for the design of tall structural walls are set forth in LATBSDC (2014), specific strength calculations and detailing provisions are referred to American Concrete Institute Building Code Requirements for Structural Concrete (ACI318-11) Sections 21.9.1 through 21.9.6. Design for flexure and axial loads are accomplished using plane-section analysis per Section 21.9.5, whereas requirements for development and splicing of longitudinal reinforcement over the wall height are contained in Section 21.9.2. More stringent requirements may be incorporated into the design depending on available information. The procedures for shear design are explained in the following.

2.4.1. Shear Design per LATBSDC (2014)

Per LATBSDC (2014), shear design of a tall structural wall is evaluated per force-controlled acceptance criterion. It is summarized using $\kappa_i=1.0$ and $\phi = 1.0$ as:

$$1.5 \cdot F_{uc} \leq F_{n,e}$$

where, F_{uc} is the mean shear demand and $F_{n,e}$ is the nominal strength computed from expected material properties (shear capacity). Although not noted in LATBSDC (2014), the footnote to Table 2-7 is commonly enforced, and a reduced ϕ is sometimes used. In contrast, PEER TBI (2010) recommends shear design using the same acceptance criterion but with $\phi = 0.75$. This is a significant difference that warrants further examination of this shear design acceptance criterion and to determine which factors are appropriate based on reliability studies. The background on shear demands (F_{uc}) and capacities ($F_{n,e}$) are further explained in the subsections below.

2.4.2. Shear Demands

The mean shear demand, F_{uc} , is determined from nonlinear response history analysis (NLRHA) using a suite of ground motions. The shear demand is not set to the mean demand determined from the NLRHA responses because half of the ground motions exceeding the mean design will imply a significant probability of failure for a brittle response. Moreover, shear demand corresponding to the mean plus one standard deviation value is also not recommended, since the dispersion in shear demand is not only influenced by processing of ground motions (i.e., record-to-record variability) but also due to other factors that impact dispersion that are not typically considered (e.g., uncertainties in modeling, model parameters, design, materials, and etc; see FEMA P695, 2009).

These issues are highlighted by Moehle (2007) using a case study of a 40-story building. Figure 2-3 shows elevation of the 40-story building and Table 2-8 shows a summary of nonlinear dynamic analysis results from 14 pairs of scaled earthquake ground motions matched to the target response spectrum.

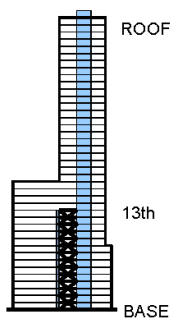


Figure 2-3. Elevation of 40-story building, Moehle (2007)

Table 2-8. Summary of 40-story building nonlinear dynamic analysis results, Moehle (2007)

	Roof Drift (ft)	Wall Base Shear (kips)	Wall moment at 13 th floor (k·ft)
Minimum	2.1	7,600	513,000
Maximum	6.7	29,700	1,080,000
Mean, μ	4.2	15,500	900,000
$\mu + \sigma$.4	22, 00	1,090,000
C.O.V.	0.23	0. 3	0.21

Table 2-8 shows that the mean base shear demand is 15,500 kips and mean plus one standard deviation is 22,200 kips. Thus, if the shear demand is defined at one standard deviation above

the mean, it results in a 43% increase in base shear but also achieves greater conservatism in design. On one hand, this may seem like a significant increase in shear demands that results in large cost and design implications; however, from another perspective there are benefits in that the probability of shear failure is greatly reduced. It is noted that the dispersion in structural responses due to ground motion variation (commonly referred to as record-to-record, or RTR variability), is not the only source of uncertainty.

Although determining appropriate shear demands in tall reinforced concrete core walls is an important process, this topic has not yet been thoroughly researched. As structural walls are the main seismic force-resisting system in a tall core wall building and shear failure can be fatal due to its sudden and brittle nature, examining the reliability of current core wall shear design is crucial. The current 1.5 factor applied to F_{uc} is an empirical factor intended to achieve a greater conservatism in shear design and it represents dispersion in shear responses resulting from nonlinear response history analysis including record-to-record variability, modeling uncertainties, and design uncertainties (PEER TBI, 2010). A systematic study is needed to better understand sources of uncertainty in wall shear demands and to better assess demand and capacity, to assess the reliability of structural wall shear design for tall reinforced concrete core wall buildings.

2.4.3. Shear Capacity

Shear capacity of a structural wall is determined from the nominal shear strength equation as specified in ACI318-11:

$$V_n = A_{cv} \left[\alpha_c \lambda \sqrt{f'_c} + \rho_t f_y \right]$$

where A_{cv} is the cross-sectional area of shear wall, f'_c is the concrete compressive strength, ρ_t is the horizontal reinforcement ratio, f_y is the reinforcing steel yield strength, and α_c varies linearly

from 3.0 for walls with aspect ratio h_w/l_w (height to length of wall) less than 1.5, to 2.0 for walls with aspect ratio greater than 2.0. Per ACI318-11, the maximum shear stress on any one wall is limited to $A_{cv}\left[10\sqrt{f'_cPsi}\right]$ and the average shear stress on all walls is limited to $A_{cv}\left[8\sqrt{f'_cPsi}\right]$. Using the nominal shear strength equation, the expected shear strength ($F_{n,e}$) can be calculated using expected material properties.

However, the ACI318 nominal shear strength equation is rather simple and does not include factors that are known to have an impact on shear strength, namely, axial loads and quantity of boundary longitudinal and transverse reinforcement (Orakcal et al, 2009). Moreover, this equation has shown to produce a low strength estimate compared to the actual shear strengths achieved through laboratory tests, and this ensures a low probability of failure (Wood, 1990; Orakcal et al 2009; Wallace et al, 2013).

To better assess the reliability of wall shear design, a thorough study is needed to compare demand and capacity, as well as sources of uncertainty, to ensure current practice includes an appropriate margin of safety. Moreover, there is a need to determine appropriate demands factors for various risk categories.

2.4.4. Reliability of Shear Design

Wallace et al (2013) conducted preliminary studies to assess reliability of structural wall shear design acceptance criteria by extending works by Hamburger (2011). In studies by Wallace et al (2013), reliability of a rectangular, reinforced concrete wall was assessed using four design cases. The wall had the following properties: $f'_c = 8\text{ksi}$, $f_y = 60\text{ksi}$, $\rho_t = 0.011$, and $A_{cv} = 30'' \times 360'' = 10,800 \text{ in}^2$. The four design cases were assessed with Monte Carlo simulations using statistical parameters for random variables established from test results. All random variables were

assumed to be normally distributed, and variations in cross-section properties were assumed to be negligible. The overstrength in shear-controlled structural walls was evaluated for two cases using nominal and expected properties, and the means and coefficients of variation (COV) are summarized as follows:

Nominal Properties: $\text{Mean}[V_{\text{max,test}} / V_n] = 1.73$, $\text{COV} = 0.22$

Expected Properties: $\text{Mean}[V_{\text{max,test}} / V_{n,e}] = 1.57$, $\text{COV} = 0.20$

For material properties, an expected mean of 1.13 and coefficient of variation of 0.10 were used for concrete (Nowak et al, 2008), and an expected mean of 1.13 and coefficient of variation of 0.02 were used for reinforcing steel. The preliminary reliability results are summarized in Table 2-9. This study is a continuation of works by Wallace et al (2013).

Table 2-9. Reliability of rectangular wall shear design (Wallace et al, 2013)

Parameter	Design Case			
	I	II	III	IV
Criteria	$\phi \cdot F_n = 1.5 \cdot F_u$	$\phi \cdot F_{n,e} = 1.5 \cdot F_u$	$\phi \cdot F_n = 1.5 \cdot F_u$	$\phi \cdot F_{n,e} = 1.5 \cdot F_u$
f'_c (psi)	8,000	9,040	8,000	9,040
f_y (psi)	60,000	67,800	60,000	67,800
Φ	0.75	0.75	1.0	1.0
F_u (kips)	4563	5091	6084	6788
Reliability (%)	98.7	97.7	96.9	94.0

2.5. Changes to Tall Building Design and Analysis Procedures

2.5.1. Proposed Changes in ASCE7-16 Chapter 16

This section reviews the proposed changes in ASCE7-16 that will impact performance-based design of tall buildings. This information is based on a draft of ASCE7-16 received on January 27, 2016 for research purposes. The major changes in ASCE7-16 Chapter 16 *Nonlinear Response History Analysis* include: the number of ground motions required for nonlinear response history analysis, period range for ground motion modification process, unacceptable responses, and element level force-controlled acceptance criteria. Although there are other important changes, only the aforementioned topics are summarized here.

2.5.2. Number of Ground Motions

Before the 2016 edition, ASCE7 Chapter 16 required a minimum of three or seven pairs of ground motions for nonlinear response history analysis. When three pairs of ground motions were used, maximum results were evaluated and when seven pairs of ground motions were used, mean results were evaluated. The ASCE7-16 standard now requires at least eleven pairs of ground motions for nonlinear response history analysis. This number was increased to obtain more reliable estimates of mean structural responses.

2.5.3. Period Range

In ASCE7-10, modified ground motions were required to be scaled or spectrally matched so that the mean of ground motions matched to target response spectrum between periods $0.2 \cdot T$ and $1.5 \cdot T$, where T represents the fundamental period of the building. The lower bound reflects contributions from higher mode responses and the upper bound captures period elongation effects once the building was damaged and softened. In ASCE7-16, this range has changed to

0.2·T to 2.0·T where T is redefined as the maximum fundamental period of the building. Previous research has shown that the upper bound of 1.5·T was not long enough for assessing softening effects of ductile frame buildings (ASCE7-16). The lower bound also has another requirement that it must capture all periods needed for 90% mass participation in analyzing both directions of the building.

2.5.4. Unacceptable Responses

In the 2016 edition of ASCE7, using unacceptable responses are now prohibited for examining the global acceptance criteria. An unacceptable response is defined as any of the following: (1) analytical solutions fails to converge, (2) predicted demands on deformation-controlled elements exceeds the valid range of modeling, (3) predicted demands on critical or ordinary force-controlled elements exceeds element capacity, or (4) predicted deformation demands on elements not explicitly modeled exceeds the deformation limits at which the members are no longer able to carry their gravity loads. For Risk Category I and II structures, where spectral matching of ground motions is not used, maximum of one ground motion is permitted to produce unacceptable response. If 20 or more ground motions are used, a maximum of two unacceptable responses are permitted and if 30 or more ground motions are used, a maximum of three unacceptable responses are permitted. For Risk Category III and IV structures, no ground motions shall produce unacceptable responses. When a ground motion produces unacceptable responses, 120% of the median value, and no less than the mean value, should be used for evaluation.

2.5.5. Element-Level Force-Controlled Acceptance Criteria

Lastly, a significant change comes from increases in element level, force-controlled acceptance criteria. Force-controlled actions shall satisfy the following equation:

$$\gamma I_e(Q_u - Q_{ns}) + Q_{ns} \leq Q_e$$

where I_e is the importance factor as shown on Table 2-10, Q_{ns} is the demand caused by loads other than seismic, Q_e is the expected component strength, and γ is the load factor shown on Table 2-11.

Table 2-10. Importance factors and probabilities of failure by Risk Category of buildings for earthquake loads, ASCE7-10

Risk Category from ASCE7-10 Table 1.5-1	Seismic importance factor, I_e	Probability of failure for MCE hazard level
I	1.00	10%
II	1.00	10%
III	1.25	6%
IV	1.50	3%

Table 2-11. Load factors for force-controlled behaviors, ASCE7-16

Action type	Load factor, γ
Critical	2.0
Ordinary	1.5
Noncritical	1.0

This acceptance criterion was established from examining the force-controlled acceptance criterion defined by PEER TBI (2010) guidelines:

$$\lambda F_u \leq \phi F_{n,e}$$

where F_u is the mean demand resulting from a suite of ground motions, $F_{n,e}$ is the nominal strength computed from expected material properties, ϕ is the uncertainty in $\bar{F}_{n,e}$, taken as 1.0, and λ is a calibration parameter. To determine the calibration parameter, λ , a few assumptions

were made. First, the component demand and capacity were assumed to follow lognormal distributions. Then λ was calibrated to achieve probability of collapse goals as stated in Table 2-10. Here, a conservative assumption was made so that the failure of a single critical force-controlled component would result in a total or partial structural collapse of the building. This calibration process is highly dependent on the uncertainties in component demand and capacity; thus, two cases for higher dispersion (general) and lower dispersion (well-defined mechanism) were examined. The dispersion values for demand and capacity are presented in Table 2-12 and Table 2-13 as logarithmic standard deviations.

Table 2-12. Assumed demand dispersion for general and well-defined cases (ASCE7-16)

Demand dispersion, β_D		Variability and uncertainties in the demand
General	Well-defined mechanism	
0.40	0.20	Record-to-record variability (for MCE_R ground motions)
0.20	0.20	Uncertainty from estimating demands using structural model
0.13	0.06	Variability from estimating demands from mean of only 11 ground motions
0.46	0.29	$\beta_{D-Total}$

Table 2-13. Assumed capacity dispersion for general and well-defined cases (ASCE7-16)

Capacity dispersion, β_C		Variability and uncertainties in the capacity
General	Well-defined mechanism	
0.30	0.30	Typical variability in strength equation for $F_{n,e}$ (from available data)
0.10	0.10	Typical uncertainty in strength equation for $F_{n,e}$ (extrapolation beyond available data)
0.20	0.20	Uncertainty in as-built strength because of construction quality and possible errors
0.37	0.37	$\beta_{C-Total}$

In the calibration process, both demand and capacity lognormal means were normalized to 1.0. The computed values to achieve 10% probability of collapse are as reported in Table 2-14. The

same procedures were used to compute λ for 6% and 3% probabilities of collapse, and these values were simplified as shown on Table 2-11.

Table 2-14. Required ratios of λ/ϕ to achieve 10% probability of collapse

Required ratio of λ/ϕ	
General	Well-defined mechanism
2.1	1.9

The factors shown on Table 2-11 are high because a conservative assumption was made about the component reserve capacity, $F_{n,e}$, and no reserve strength factor was used. When there is conservatism in the component strength equations as shown in experimental tests, $F_{n,e}$ can be multiplied by a component reserve strength factor. Thus, the correct use of shear reserve strength factor would be between $1.57 \cdot F_{n,e}$ and $1.67 \cdot F_{n,e}$ (these factors are later introduced in Chapter 7).

2.6. Summary of Current and Proposed Shear Design Provisions

In this chapter, two methods for tall building design and analysis procedures (code-based and performance-based) were introduced, with a focus on performance-based design procedures per LATBSDC (2014). Furthermore, the main issues with structural wall shear design acceptance criteria were addressed. In the structural wall shear design criterion shown below,

$$1.5 \cdot F_{uc} \leq \kappa_i \phi F_{n,e}$$

several issues are noted, where (1) the 1.5 factor is an empirical factor established to achieve conservatism in shear design, (2) there is discrepancy between LATBSDC (2014) and PEER TBI (2010) recommendations for ϕ , where 1.0 and 0.75 are recommended, respectively, (3) there is a discrepancy in the use of κ_i , as it is generally not applied force-controlled actions under MCE analysis per LATBSDC (2014) recommendations, whereas the proposed changes in ASCE7-16

Chapter 16 apply an equivalent factor (seismic importance factor applied to shear demands) to force-controlled actions, and (4) the proposed changes for shear demand factors are significantly higher in ASCE7-16 Chapter 16 (in lieu of 1.5). The current and proposed demand factors for structural wall shear design of tall reinforced-concrete buildings are summarized in Table 2-15. The proposed shear demand factors per ASCE7-16 are shown to be high due to the use of seismic importance factors and from using conservative assumptions on shear capacities; adjustments are recommended.

Table 2-15. Comparison of current and proposed shear demand load factors for MCE level shear design of tall reinforced-concrete buildings

Risk Category, ASCE7-10 Table 1.5-1	Current ¹ LATBSDC (2014)	Proposed based on action type ASCE7-16 draft ²		
		Critical	Ordinary	Noncritical
I	1.5	2.0	1.5	1.0
II	1.5	2.0	1.5	1.0
III	1.5	2.5	1.875	1.25
IV	-	3.0	2.25	1.5

¹ does not include risk reduction factor, κ_i (refer to Chapter 2.3.6)

² includes load factor, γ , and seismic importance factor, I_e

CHAPTER 3. GROUND MOTION SELECTION AND MODIFICATION

This chapter summarizes the ground motion selection and modification process for the design and analysis of tall buildings.

3.1. Introduction

There are currently many ground motion selection and modification methods available for nonlinear response history analysis of structures. In this study, amplitude scaling was used to modify ground motions and the mean of ground motions were matched to the target Uniform Hazard Spectrum. Five hazard levels were selected to examine structural responses at various hazards. The details of this process are explained in the following sections and some of the limitations of this method are also presented.

3.2. Project Site

The project location was chosen as downtown Los Angeles, California; it represents an urban area that is densely populated with tall buildings. A specific location, at longitude -118.25 and latitude 34.05, was chosen because a case study of 42-story building was previously conducted at this site by Pacific Earthquake Engineering Research Center Tall Buildings Initiative (PEER TBI) Task 12 (2011), and the site-specific response spectra and the ground motions at five hazard levels were available.

As shown on Figure 3-1, this project site is 0.9 miles from Puente Hills fault, 4.5 miles from Hollywood fault, 5.5 miles from Raymond fault, 7.1 miles from Santa Monica fault, 15.2 miles from Elsinore fault, 24.9 miles from Sierra Madre fault, and 34.8 miles from San Andreas fault. The soil conditions correspond to site class C, very dense soil and soft rock, per ASCE7-

10 Chapter 11 with an average shear wave velocity of $V_{s30} = 1180$ ft/s (PEER TBI Task 12, 2011).



Figure 3-1. Project location, PEER TBI Task 12 (2011)

3.3. Site Hazard Characterization

To identify dominant seismic events in various hazard levels, PEER TBI Task 12 (2011) performed probabilistic seismic hazard (PSH) deaggregation. Five selected hazard levels, ranging from low intensity/frequent ground motions to high intensity/extreme event ground motions, were evaluated. Refer to Table 3-1 for descriptions of the five hazard levels. The probabilistic seismic hazard deaggregation at the five hazard levels identified which seismic events dominated the project site, and this information was used in selecting and modifying ground motions. See Figure 3-2 and Figure 3-3 for PSHA deaggregation for MCE hazard level, at periods 2.0 and 3.0 seconds, respectively. For rare events and long periods, the hazards were dominated by relatively large magnitude-small distance event, or an extremely large magnitude-long distance event. Due to scarcity of real ground motion recordings that match the dominant

seismic events, ground motions were modified by amplitude scaling to create new recordings for the project site.

Table 3-1. A summary of five seismic hazard levels

Name	Hazard	Earthquake	Probability	Return Period
SLE25	Service	Service Level Earthquake	70% in 30 years	25 years
SLE43	Service	Service Level Earthquake	50% in 30 years	43 years
DBE	Life Safety	Design Basis Earthquake	10% in 50 years	475 years
MCE	Collapse Prevention	Maximum Considered Eq.	2% in 50 years	2475 years
OVE	-	-	1% in 50 years	4975 years

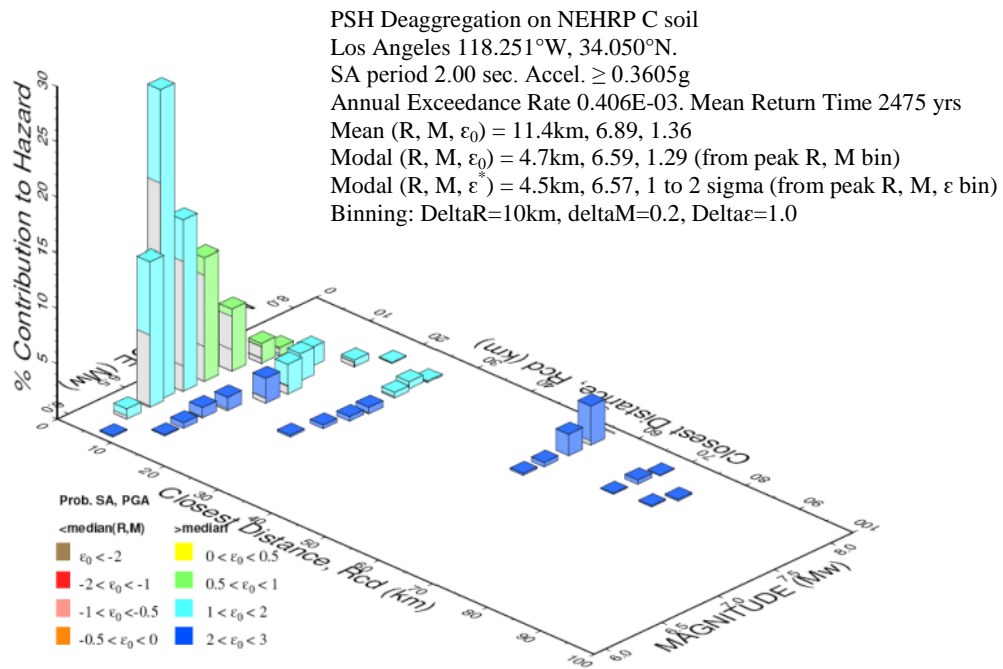


Figure 3-2. PSH deaggregation for MCE hazard level with 2475-year return period at T=2.0 seconds, PEER TBI Task 12 (2011)

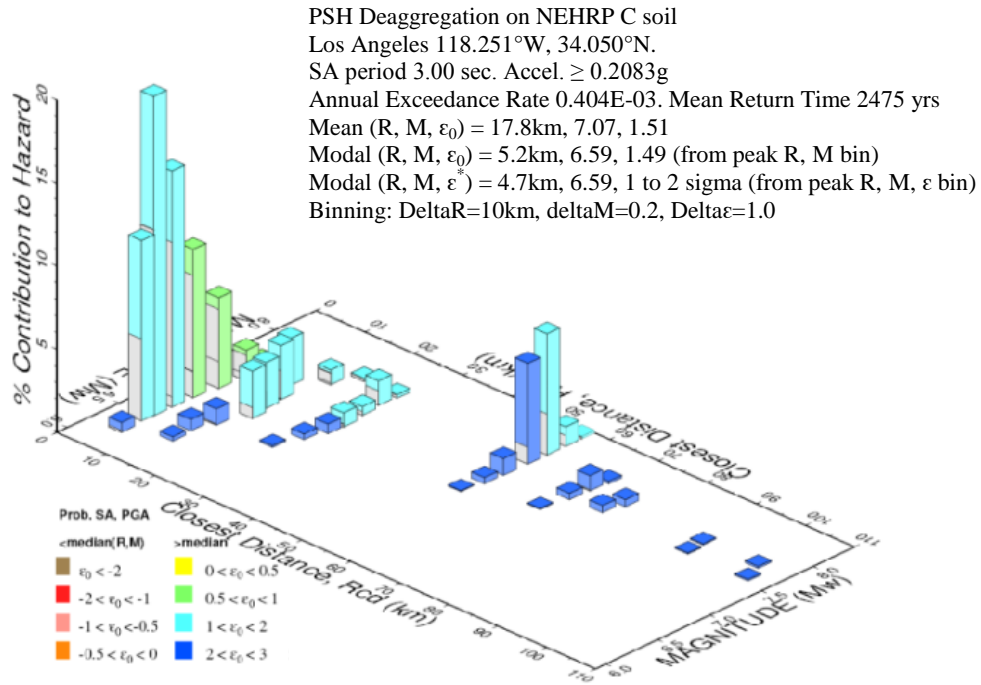


Figure 3-3. PSH deaggregation for MCE hazard level with 2475-year return period at T=3.0 seconds, PEER TBI Task 12 (2011)

3.4. Ground Motion Suites

Four suites of ground motions were created for various design and assessment purposes. The first suite, Suite A, consists of 15 pairs of scaled ground motions at all five hazard levels. The SLE43 and MCE hazard levels within Suite A were used to design tall buildings and all five hazard levels were used to examine dispersion of structural responses. The second suite, Suite B, was expanded from Suite A and consists of 30 pairs of scaled ground motions at DBE and MCE hazard levels. The purpose of this suite was to create a sufficiently large database of ground motions to measure dispersion in structural responses. Suites C and D consist of 30 ground motions at MCE hazard level and they were created for a two-dimensional model analysis, thus, the ground motions are in a single direction (versus pairs). Refer to Table 3-2 for a summary of the ground motion suites.

Table 3-2. Summary of ground motion Suites A, B, C, and D

GM Suite		Suite A	Suite B	Suite C	Suite D
Analysis		Perform 3D		Opensees 2D	
Analysis Model		30-Story	30-Story	20-Story	30-Story
GM Modification		Scaled	Scaled	Scaled	Scaled
Hazard	SLE25	15 pairs	-	-	-
	SLE43	15 pairs	-	-	-
	DBE	15 pairs	30 pairs	-	-
	MCE	15 pairs	30 pairs	30 single	30 single
	OVE	15 pairs	-	-	-

3.5. Ground Motion Record Selection and Modification

The ground motions at all five hazard levels were selected from PEER Next Generation Attenuation (NGA) strong motion database. This database contains 7075 records from 175 earthquakes. The selected ground motions do not include records of aftershocks and foreshocks or near-fault effects. For the OVE hazard level, only 7 pairs of ground motions were selected from the NGA database and 8 pairs of ground motions were created from simulations.

Next, the selected ground motions were modified by amplitude scaling to match uniform hazard target spectrum at each hazard level. All target spectra were created for 5% critically damped single-degree-of-freedom systems. Details on this process are discussed in the following subsections.

3.5.1. Suite A – 15 Pairs of Scaled Ground Motions at 5 Hazard Levels

The process of selecting and scaling ground motions for Suite A is summarized as follows:

1. Ground motion time histories were selected from NGA database with maximum source distance of 100 km (62 miles) and maximum shear wave velocity between 180 to 1200 m/sec (590 to 3940 ft/s).
2. Low-pass filter was used with cutoff frequencies less than 0.1 Hz; this ensured long-period frequency content necessary for tall building design and analysis.
3. Response spectra for the two horizontal components of a single ground motion were computed for 5% critically damped single-degree-of-freedom system. A geometric mean of the two horizontal components of a single ground motion was considered as a single recording.

4. The scale factor was computed as the smallest error between the target spectrum and the geometric mean of a single ground motion. This calculation is shown below, and the maximum scale factor was set to 5.0.

$$PSa(T)_{target} \cong SF \cdot PSa(T)_{geomean\ time\ series}$$

$$\text{where } SF = \sum_{[T_i-T_j]} \frac{[PSa(T)]_{target}}{[PSa(T)]_{geomean\ time\ series}} \cdot wt$$

SF = scale factor
wt = weighted error
T_i = 0.5 seconds
T_j = 10.0 seconds

The errors were computed for a range of periods to account for higher mode effects and softening of the building. Furthermore, errors were weighted to ensure a better match in the longer periods as summarized in Table 3-3.

Table 3-3. Weighted errors for scale factor calculation

Period range (seconds)	Weighted error
$0.5 \leq T \leq 3.0$	10%
$3.0 < T \leq 7.0$	60%
$7.0 < T \leq 10.0$	30%

5. The scaled recordings were sorted by smallest error and the first 15 ground motions were selected for Suite A.
6. The selected and scaled ground motions were down-sampled from the original sampling rate to 25 samples per second (dt = 0.04 seconds) for a faster analysis time.

Response spectra for all five hazard levels are shown on Figure 3-4. Refer to Table 3-4 for earthquake information and Table 3-5 for scale factors.

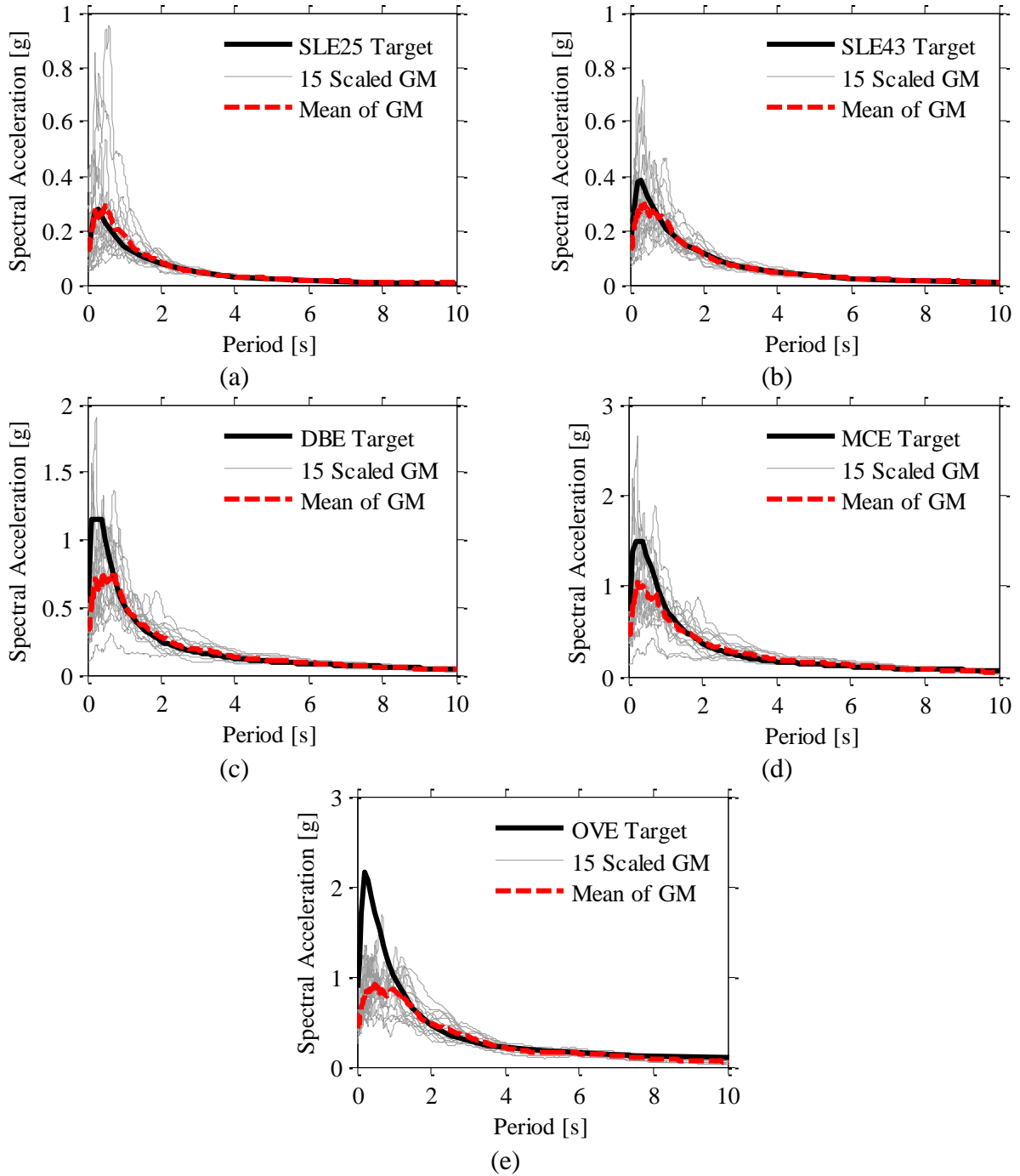


Figure 3-4. Suite A – Geomean of 15 pairs of scaled ground motions and mean compared to target spectrum at hazard levels (a) SLE25, (b) SLE43, (c) DBE, (d) MCE, and (e) OVE

Table 3-4. Suite A – Earthquake information for 15 scaled ground motions at 5 hazard levels

GM No.	Earthquake name (NGA Seq.)				
	SLE25	SLE43	DBE	MCE	OVE
1	Chi-Chi, Taiwan (1317)	Chi-Chi, Taiwan (1420)	Chi-Chi, Taiwan (1223)	Chi-Chi, Taiwan (1436)	Landers (838)
2	Chi-Chi, Taiwan (1420)	Loma Prieta (757)	Chi-Chi, Taiwan (1423)	Chi-Chi, Taiwan (1504)	Chi-Chi, Taiwan (1546)
3	Loma Prieta (757)	Chi-Chi, Taiwan (1317)	Landers (838)	Landers (838)	Landers (900)
4	Denali, Alaska (2111)	Hector Mine (1816)	Hector Mine (1810)	Landers (900)	Chi-Chi, Taiwan (1515)
5	Hector Mine (1816)	Denali, Alaska (2111)	Kocaeli, Turkey (1155)	Kocaeli, Turkey (1155)	Kocaeli, Turkey (1163)
6	Hector Mine (1787)	Hector Mine (1810)	Landers (900)	Denali, Alaska (2114)	Kocaeli, Turkey (1155)
7	Landers (832)	Landers (832)	Kocaeli, Turkey (1177)	Kocaeli, Turkey (1163)	Denali, Alaska (2114)
8	Cape Mendocino (827)	Cape Mendocino (827)	Denali, Alaska (2114)	Imperial Valley-06 (169)	Hector Mine (1792)
9	Landers (850)	Denali, Alaska (2114)	Imperial Valley-06 (169)	Hector Mine (1792)	SIMULATION 1 (-)
10	Denali, Alaska (2114)	Imperial Valley-06 (169)	Cape Mendocino (827)	Cape Mendocino (827)	SIMULATION 2 (-)
11	Imperial Valley-06 (169)	Landers (850)	St Elias, Alaska (1629)	St Elias, Alaska (1629)	SIMULATION 3 (-)
12	Kobe, Japan (1109)	Kobe, Japan (1113)	Tabas, Iran (143)	Tabas, Iran (143)	SIMULATION 4 (-)
13	Kocaeli, Turkey (1155)	Kocaeli, Turkey (1155)	Hector Mine (1811)	Duzce, Turkey (1605)	SIMULATION 5 (-)
14	Kobe, Japan (1104)	Kobe, Japan (1104)	Duzce, Turkey (1605)	Loma Prieta (757)	SIMULATION 6 (-)
15	Duzce, Turkey (1602)	Loma Prieta (804)	Loma Prieta (757)	Duzce, Turkey (1619)	SIMULATION 7 (-)

Table 3-5. Suite A – Scale factors for 15 ground motions at 5 hazard levels

GM No.	Scale factors				
	SLE25	SLE43	DBE	MCE	OVE
1	0.49	1.16	4.06	3.84	4.28
2	0.80	0.99	4.16	1.29	2.04
3	0.68	0.72	2.33	3.24	2.51
4	1.74	1.70	3.66	1.9	1.69
5	1.17	2.52	2.65	3.68	4.91
6	0.58	1.09	1.36	1.00	4.86
7	0.63	0.92	3.65	3.71	1.33
8	0.55	0.80	0.72	2.35	4.88
9	1.05	0.21	1.69	3.69	1.00
10	0.15	0.50	2.69	3.73	1.00
11	0.35	1.52	1.25	1.74	1.00
12	4.59	1.08	0.56	0.78	1.00
13	0.54	0.79	4.84	0.96	1.00
14	0.35	0.51	0.69	4.62	1.00
15	0.44	2.62	3.33	4.96	1.00

3.5.2. Suite B – 30 Pairs of Scaled Ground Motions at DBE and MCE Hazard Levels

Suite B was created to measure dispersion in structural responses using Monte Carlo simulations. Thirty pairs of ground motions were selected and scaled at DBE and MCE hazard levels. The ground motion selection and modification procedures were the same as Suite A, as stated in the previous section. Figure 3-5 shows the response spectrum for Suite B and Table 3-7 and Table 3-8 outline detailed earthquake information for DBE and MCE hazard levels, respectively.

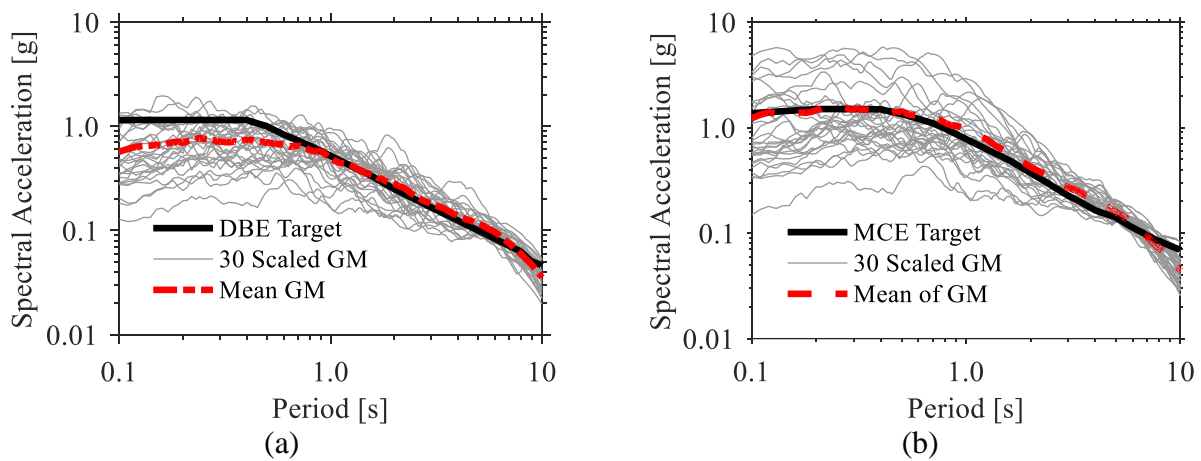


Figure 3-5. Suite B - Geomean of 30 pairs of scaled ground motions and mean compared to target spectrum at hazard levels (a) DBE and (b) MCE

3.5.3. Suites C and D – 30 Scaled Ground Motions at MCE Hazard Level for 2D Analysis

Suites C and D were created to measure dispersion in structural responses in 2-dimensional Opensees models. From Suite B, subsets of thirty ground motions were selected for the MCE hazard level, and single-direction ground motions were considered as follows.

Suite C for 20-story building:

- GM1 direction: 3, 7, 10, 12, 14, 15, 18, 19, 21, 22, 24, 25, 26, 27, 29 (15 selected)
- GM2 direction: 2, 4, 5, 7, 8, 9, 10, 13, 19, 20, 23, 24, 26, 27, 28 (15 selected)

Suite D for 30-story building:

- GM1 direction: 3, 4, 6, 7, 10, 12, 13, 15, 18, 21, 23, 24, 25, 26, 27 (15 selected)
- GM2 direction: 4, 7, 13, 14, 15, 16, 17, 19, 20, 21, 23, 24, 26, 29, 30 (15 selected)

Response spectra for the two suites are shown on Figure 3-6.

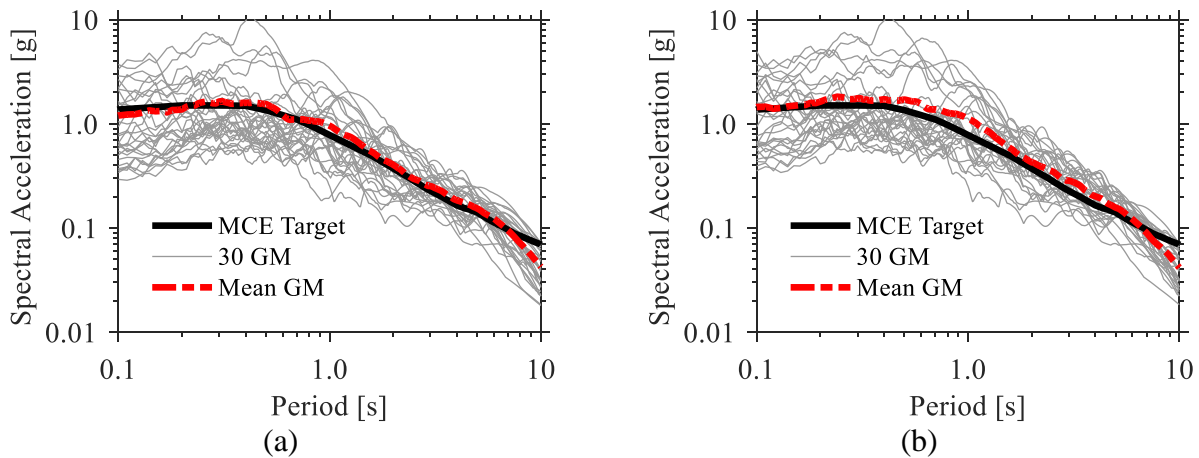


Figure 3-6. (a) Suite C and (b) Suite D – 30 single-direction scaled ground motions and mean compared to target spectrum at MCE hazard level

3.6. Methods Not Considered – Spectral Matching

Other than amplitude scaling methods introduced in the previous sections, another ground motion modification method that was not considered in this study was the ground motion spectral matching method (Abrahamson and Al Atik, 2010). A corresponding software program, RSPMatch09 (Abrahamson and Al Atik, 2010), performs time-domain spectral matching by adding adjustment wavelets to an initial acceleration time series, which produces a response spectrum that closely matches target response spectrum. The spectral matching is performed over the required period range; however, since the short period spectral accelerations are influenced by long period wavelets, time series adjustment is typically performed in multiple passes, starting with short periods, then progressively adjusting longer periods. During the spectral matching process, consideration of ground motion spectral shapes is important to ensure that the long period content necessary for tall building evaluation is present. Furthermore, once ground motions are spectrally matched, the acceleration, velocity, and displacement time series are plotted and checked for unstable solutions, and any ground motions that result in drifting are discarded.

Although preliminary studies were conducted to evaluate the effects of using spectrally matched ground motions (Kim and Wallace, 2014), this topic was not considered in the overall reliability study. The reason for this was because spectral matching artificially reduces dispersion in ground motions and using this suite of ground motions will most likely produce lower dispersion in structural responses and higher reliability results. Studies by Bazzurro and Luco (2006) have shown that using spectrally matched ground motions reduce record-to-record variability by 60% to 80% compared to non-processed ground motions. However, higher

reliability results computed by using spectrally matched ground motions will not be accurate due to unrealistically small dispersion introduced in the ground motions.

The preliminary studies with 11 ground motions are summarized on Table 3-6, and the results of modifying the ground motions by the two methods, amplitude scaling and spectral matching, are shown on Figure 3-7. Graphically, it is evident that spectral matching reduces the dispersion in the ground motions drastically, and using these ground motions will considerably bias the reliability results.

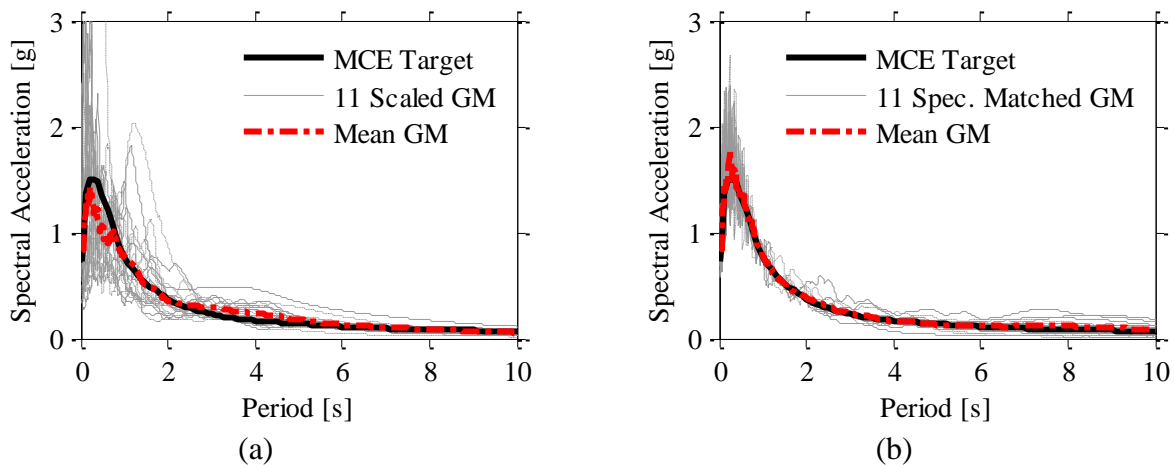


Figure 3-7. 11 pairs of MCE hazard ground motions modified by (a) amplitude scaling and (b) spectral matching

Table 3-6. MCE level ground motions considered for amplitude scaling and spectral matching

GM No.	MCE GM No. from Suite B	Name of Ground Motion (NGA Seq.)
1	2	Chi-Chi, Taiwan (1504)
2	3	Landers (838)
3	5	Kocaeli, Turkey (1155)
4	8	Imperial Valley-06 (169)
5	12	Tabas, Iran (143)
6	17	Chi-Chi, Taiwan (1546)
7	20	Landers (879)
8	21	Hector Mine (1787)
9	23	Kocaeli, Turkey (1176)
10	24	Hector Mine (1762)
11	27	Kobe, Japan (1100)

Table 3-7. Suite B – 30 scaled ground motions for DBE hazard level

GM No.	NPTS	Dt (sec)	NGA Seq.	EQ Name	Station	M	R _{jb} (km)	Mechanism	Lowest usable freq.	Soil	V _{s30} (km/s)	Scale Factor	GM1 in NGA	GM2 in NGA
1	49,980	0.004	1223	Chi-Chi, Taiwan	CHY067	7.62	83.6	Reverse Oblique	0.0375	D	228.0	4.06	CHICHI/CHY067-N.at2	CHICHI/CHY067-W.at2
2	26,800	0.005	1423	Chi-Chi, Taiwan	TAP026	7.62	95.9	Reverse Oblique	0.0375	D	215.0	4.16	CHICHI/TAP026-N.at2	CHICHI/TAP026-E.at2
3	2,000	0.02	838	Landers	Barstow	7.28	34.9	Strike Slip	0.07	C	370.8	2.33	LANDERS/BRS000.at2	LANDERS/BRS090.at2
4	6,000	0.01	1810	Hector Mine	Mecca - CVWD Yard	7.13	92.0	Strike Slip	0.091	D	345.4	3.66	HECTOR/11625090.at2	HECTOR/11625180.at2
5	27,711	0.005	1155	Kocaeli, Turkey	Bursa Tofas	7.51	60.4	Strike Slip	0.1	D	274.5	2.65	KOCAELI/BUR000.at2	KOCAELI/BUR090.at2
6	2,200	0.02	900	Landers	Yermo Fire Station	7.28	23.6	Strike Slip	0.07	D	353.6	1.36	LANDERS/YER270.at2	LANDERS/YER360.at2
7	25,856	0.005	1177	Kocaeli, Turkey	Zeytinburnu	7.51	52.0	Strike Slip	0.075	D	274.5	3.65	KOCAELI/ZYT000.at2	KOCAELI/ZYT090.at2
8	18,000	0.005	2114	Denali, Alaska	TAPS Pump Station #10	7.90	0.2	Strike Slip	0.025	D	329.4	0.72	DENALI/ps10047.at2	DENALI/ps10317.at2
9	9,992	0.01	169	Imperial Valley-06	Delta	6.53	22.0	Strike Slip	0.0625	D	274.5	1.69	IMPVALL/H-DLT262.at2	IMPVALL/H-DLT352.at2
10	2,200	0.02	827	Cape Mendocino	Fortuna - Fortuna Blvd	7.01	16.0	Reverse	0.07	C	457.1	2.69	CAPEMEND/FOR000.at2	CAPEMEND/FOR090.at2
11	16,594	0.005	1629	St Elias, Alaska	Yakutat	7.54	80.0	Reverse	0.04	D	274.5	1.25	STELIAS/059v2009.at2	STELIAS/059v2279.at2
12	1,642	0.02	143	Tabas, Iran	Tabas	7.35	1.8	Reverse	0.0625	B	766.8	0.56	TABAS/TAB-LN.at2	TABAS/TAB-TR.at2
13	11,800	0.005	1811	Hector Mine	Mentone Fire Station #9	7.13	91.2	Strike Slip	0.026	D	271.4	4.84	HECTOR/1417a180.at2	HECTOR/1417c270.at2
14	5,177	0.005	1605	Duzce, Turkey	Duzce	7.14	0.0	Strike Slip	0.1	D	276.0	0.69	DUZCE/DZC180.at2	DUZCE/DZC270.at2
15	3,250	0.02	757	Loma Prieta	Dumbarton Bridge West End FF	6.93	35.3	Reverse Oblique	0.0625	D	274.5	3.33	LOMAP/DUMB267.at2	LOMAP/DUMB357.at2
16	2,500	0.02	832	Landers	Amboy	7.28	69.2	Strike Slip	0.1	C	382.9	3.22	LANDERS_AB Y000.AT2	LANDERS_A BY090.AT2
17	2,000	0.02	855	Landers	Fort Irwin	7.28	63.0	Strike Slip	0.07	C	367.4	4.94	LANDERS_FT I000.AT2	LANDERS_F TI090.AT2
18	3,000	0.02	862	Landers	Indio - Coachella Canal	7.28	54.3	Strike Slip	0.1	D	339.0	4.71	LANDERS_IN D000.AT2	LANDERS_I ND090.AT2
19	6,000	0.005	1148	Kocaeli, Turkey	Arcelik	7.51	10.6	Strike Slip	0.0875	C	523.0	2.34	KOCAELI_AR E000.AT2	KOCAELI_A RE090.AT2
20	26,624	0.005	1149	Kocaeli, Turkey	Atakoy	7.51	56.5	Strike Slip	0.0375	D	310.0	3.95	KOCAELI_AT K000.AT2	KOCAELI_A TK090.AT2

21	21,323	0.005	1163	Kocaeli, Turkey	Hava Alani	7.51	58.3	Strike Slip	0.025	D	354.4	2.73	KOCAELI_DH M000.AT2	KOCAELI_D HM090.AT2
22	5,765	0.005	1619	Duzce, Turkey	Mudurnu	7.14	34.3	Strike Slip	0.1	C	535.2	3.85	DUZCE_MDR 000.AT2	DUZCE_MDR 090.AT2
23	3,000	0.02	1762	Hector Mine	Amboy	7.13	41.8	Strike Slip	0.08	C	382.9	2.08	HECTOR_AB Y090.AT2	HECTOR_AB Y360.AT2
24	10,000	0.01	1792	Hector Mine	Indio - Riverside Co Fair Grnds	7.13	74.0	Strike Slip	0.1	D	282.1	2.75	HECTOR_IRF 360.AT2	HECTOR_IRF 090.AT2
25	18,200	0.005	3783	Hector Mine	Beaumont - 6th & Maple	7.13	89.7	Strike Slip	0.025	D	315.2	2.28	HECTOR_B6 M090.AT2	HECTOR_B6 M360.AT2
26	14,592	0.005	1786	Hector Mine	Heart Bar State Park	7.13	61.2	Strike Slip	0.0299	C	624.9	4.74	HECTOR_HBS 090.AT2	HECTOR_HB S180.AT2
27	12,000	0.01	888	Landers	San Bernardino E & Hospitality	7.28	79.8	Strike Slip	0.1	D	297.0	4.07	LANDERS_H OS090.AT2	LANDERS_H OS180.AT2
28	5,437	0.005	1158	Kocaeli, Turkey	Duzce	7.51	13.6	Strike Slip	0.1	D	281.9	1.18	KOCAELI_DZ C180.AT2	KOCAELI_D ZC270.AT2
29	18,000	0.005	1224	Chi-Chi, Taiwan	CHY069	7.62	86.0	Reverse Oblique	0.025	D	224.4	4.89	CHICHI_CHY 069-E.AT2	CHICHI_CHY 069-N.AT2
30	18,000	0.005	1226	Chi-Chi, Taiwan	CHY071	7.62	78.7	Reverse Oblique	0.0375	D	203.0	2.59	CHICHI_CHY 071-E.AT2	CHICHI_CHY 071-N.AT2

Table 3-8. Suite B – 30 scaled ground motions for MCE hazard level

GM No.	NPTS	Dt (sec)	NGA Seq.	EQ Name	Station	M	R _{jb} (km)	Mechanism	Lowest usable freq.	Soil	V _{s30} (km/s)	Scale Factor	GM1 in NGA	GM2 in NGA
1	17,601	0.005	1436	Chi-Chi, Taiwan	TAP052	7.62	98.5	Reverse Oblique	0.03	C	473.9	3.84	CHICHI/ TAP052-E.at2	CHICHI/ TAP052-N.at2
2	18,000	0.005	1504	Chi-Chi, Taiwan	TCU067	7.62	0.64	Reverse Oblique	0.04	C	433.6	1.29	CHICHI/ TCU067-E.at2	CHICHI/ TCU067-N.at2
3	2,000	0.02	838	Landers	Barstow	7.28	34.86	Strike Slip	0.07	C	370.7	3.24	LANDERS/ BRS000.at2	LANDERS/ BRS090.at2
4	2,200	0.02	900	Landers	Yermo Fire Station	7.28	23.6	Strike Slip	0.07	D	353.6	1.90	LANDERS/ YER270.at2	LANDERS/ YER360.at2
5	27,711	0.005	1155	Kocaeli, Turkey	Bursa Tofas	7.51	60.4	Strike Slip	0.1	D	274.5	3.68	KOCAELI/ BUR000.at2	KOCAELI/ BUR090.at2
6	18,000	0.005	2114	Denali, Alaska	TAPS Pump Station #10	7.90	0.18	Strike Slip	0.03	D	329.4	1.00	DENALI/ ps10047.at2	DENALI/ ps10317.at2
7	21,323	0.005	1163	Kocaeli, Turkey	Hava Alani	7.51	58.3	Strike Slip	0.09	C	424.8	3.71	KOCAELI/ DHM000.at2	KOCAELI/ DHM090.at2
8	9,992	0.01	169	Imperial Valley-06	Delta	6.53	22.0	Strike Slip	0.06	D	274.5	2.35	IMPVALL/ H-DLT262.at2	IMPVALL/ H-DLT352.at2
9	10,000	0.01	1792	Hector Mine	Indio - Riverside Co Fair Grnds	7.13	74.0	Strike Slip	0.1	D	207.4	3.69	HECTOR/ 12543360.at2	HECTOR/ 12543090.at2

10	2,200	0.02	827	Cape Mendocino	Fortuna - Fortuna Blvd	7.01	15.9	Reverse	0.07	C	457.0	3.73	CAPEMEND/ FOR000.at2	CAPEMEND/ FOR090.at2
11	16,594	0.005	1629	St Elias, Alaska	Yakutat	7.54	80.0	-	-	D	274.5	1.74	STELIAS/ 059v2009.at2	STELIAS/ 059v2279.at2
12	1,642	0.02	143	Tabas, Iran	Tabas	7.35	1.7	Reverse	0.06	B	766.7	0.78	TABAS/ TAB-LN.at2	TABAS/ TAB-TR.at2
13	5,177	0.005	1605	Duzce, Turkey	Duzce	7.14	0.0	Strike Slip	0.1	D	276.0	0.96	DUZCE/ DZC180.at2	DUZCE/ DZC270.at2
14	3,250	0.02	757	Loma Prieta	Dumbarton Bridge West End FF	6.93	35.3	Reverse Oblique	0.06	D	274.5	4.62	LOMAP/ DUMB267.at2	LOMAP/ DUMB357.at2
15	5,765	0.005	1619	Duzce, Turkey	Mudurnu	7.14	34.3	Strike Slip	0.1	C	659.6	4.96	DUZCE/ MDR000.at2	DUZCE/ MDR090.at2
16	28,000	0.005	1422	Chi-Chi, Taiwan	TAP024	7.62	94.8	Reverse Oblique	0.025	D	194.9	4.54	CHICHI/ TAP024-S.at2	CHICHI/ TAP024- W.at2
17	18,000	0.005	1546	Chi-Chi, Taiwan	TCU122	7.62	9.3	Reverse Oblique	0.025	C	475.4	1.54	CHICHI/ TCU122-E.at2	CHICHI/ TCU122-N.at2
18	6,000	0.005	1148	Kocaeli, Turkey	Arcelik	7.51	10.5	Strike Slip	0.0875	C	523.0	3.11	KOCAELI/ ARC000.at2	KOCAELI/ ARC090.at2
19	1,800	0.02	829	Cape Mendocino	Rio Dell Overpass - FF	7.01	7.8	-	0.07	D	311.7	4.68	CAPEMEND/ RIO270.at2	CAPEMEND/ RIO360.at2
20	9,625	0.005	879	Landers	Lucerne	7.28	2.1	Strike Slip	0.1	C	684.9	1.5	LANDERS/ LCN260.at2	LANDERS/ LCN345.at2
21	4,531	0.01	1787	Hector Mine	Hector	7.13	10.3	Strike Slip	0.0375	C	684.9	3.94	HECTOR/ HEC000.at2	HECTOR/ HEC090.at2
22	2,500	0.02	832	Landers	Amboy	7.28	69.2	Strike Slip	0.1	D	271.4	4.29	LANDERS/ ABY000.at2	LANDERS/ ABY090.at2
23	7,000	0.005	1176	Kocaeli, Turkey	Yarimca	7.51	1.3	Strike Slip	0.0875	D	297.0	0.97	KOCAELI/ YPT060.at2	KOCAELI/ YPT330.at2
24	3,000	0.02	1762	Hector Mine	Amboy	7.13	41.8	Strike Slip	0.08	D	271.4	2.73	HECTOR/ 21081090.at2	HECTOR/ 21081360.at2
25	8,000	0.01	1104	Kobe, Japan	Fukushima	6.90	17.8	Strike Slip	0.1	D	256.0	2.4	KOBE/ FKS000.at2	KOBE/ FKS090.at2
26	5,590	0.01	1602	Duzce, Turkey	Bolu	7.14	12.0	Strike Slip	0.0625	D	326.0	2.98	DUZCE/ BOL000.at2	DUZCE/ BOL090.at2
27	14,000	0.01	1100	Kobe, Japan	Abeno	6.90	24.8	Strike Slip	0.0625	D	256.0	4.15	KOBE/ ABN000.at2	KOBE/ ABN090.at2
28	8,000	0.005	319	Westmorland	Westmorland Fire Sta	5.90	6.1	Strike Slip	0.1	D	193.6	4.82	WESTMORL/ WSM090.at2	WESTMORL/ WSM180.at2
29	19,806	0.01	1110	Kobe, Japan	Morigawachi	6.90	24.7	Strike Slip	0.1	D	256.0	4.04	KOBE/ MRG000.at2	KOBE/ MRG090.at2
30	1,500	0.02	825	Cape Mendocino	Cape Mendocino	7.01	0.0	Reverse	0.07	C	513.7	2.37	CAPEMEND/ CPM000.at2	CAPEMEND/ CPM090.at2

3.7. Limitations and Future Work

Limitations and future work are listed as follows.

1. All target spectra in this chapter were created using uniform hazard spectra (UHS) which assumes equal probability of occurrence at all periods. In Southern California, short period ordinates are generally influenced by moderate magnitude events at close distances while longer period ordinates are generally influenced by large magnitude events at longer distances. Although the two ordinates in the UHS have the same probability of occurrence, they are unlikely to happen during the same earthquake and this makes UHS unrealistic. To address this issue, the use of conditional mean spectrum (Baker, 2011) is recommended to supplement future studies; conditional mean spectrum represents a more realistic response spectral shape for a single earthquake event, conditioned upon a key period of interest.
2. For ground motion Suites B through D, 30 ground motions were selected and modified for various hazard levels. However, to reduce possible bias, it would be worthwhile to expand this study with a greater number of ground motions in the future.
3. Spectral matching procedures for ground motion modifications were not explored in this study. The proposed changes for ASCE7-16 Chapter 16 limit the use of spectral matching procedures for near-fault sites unless the pulse characteristics of the ground motions are retained after the completion of matching process. It might be helpful to compare the results from spectrally matched ground motions, which meet the ASCE7 requirements, in future studies.

CHAPTER 4. DESIGN, MODELING, AND ANALYSIS OF TALL REINFORCED CONCRETE CORE WALL BUILDINGS

This chapter describes the design, modeling, and analysis procedures for the 20 and 30-story reinforced concrete core wall buildings. The two buildings were designed to satisfy the performance criteria set forth in LATBSDC (2014).

4.1. Introduction

This study was conducted using 20 and 30-story prototype reinforced-concrete core wall buildings. The two buildings were designed using realistic floor plan layouts and typical ratios between floor areas and elevator core areas. The design, modeling, and analysis procedures are explained in detail using the 30-story building example and differences in the 20-story building designs and modeling criteria are included in Appendix A.

4.2. Description of the 30-Story Building

The 30-story reinforced-concrete office building is located in downtown Los Angeles, California. The lateral force-resisting system of the 30-story building consists of centrally located core shear wall with four coupling beams at each level, with one on each face (Figure 2); core walls are 34-inch thick and diagonally-reinforced coupling beams are 42-inch deep. The floor plan area is 17,956 square feet with a typical story height of 11-feet. The ratio of wall cross-sectional area in one direction versus floor plan area is approximately 1.3%.

The gravity system consist of 11-inch two-way, post-tensioned concrete slabs on levels 1 through 29, and a 10-inch two-way concrete slab at the roof level. Figure 4-1 and Figure 4-2 show typical plan views of levels 1 through 29 and the roof, respectively. Figure 4-3 shows an elevation view of the south core walls. The two-way slabs are supported on 36-inch by 36-inch

concrete columns at the exterior of the building and on the concrete shear walls at the interior of the building. Table 4-1 provides a summary of structural system and element sizes over the height of the building.

Table 4-1. Dimensions of structural members for 30-story building

Element	Level	Structural system & size
Shear walls	1-15	34-in. thick reinforced concrete
	16-Roof	24-in. thick reinforced concrete
Coupling beams	1-15	36-in x 42-in. deep reinforced concrete
	16-Roof	24-in x 42-in. deep reinforced concrete
Slabs	1-29	11-in. thick post-tensioned concrete
	Roof	10-in. thick reinforced concrete
Columns	1-15	36-in. x 36-in. reinforced concrete
	16-Roof	24-in. x 24-in. reinforced concrete

4.3. Loading Criteria

The criteria for superimposed gravity loads are shown in Table 4-2. These loads are in addition to the self-weight of the structure; minimum loading requirements were specified from Table 4-1 of ASCE7-10.

Table 4-2. Loading Criteria

Use	Location	Superimposed dead load (psf)	Live load (psf)
Office	Levels 1-29	22	50 reducible + 15 partition
Roof	Roof	35	20 reducible
Cladding	Perimeter of building	15 vertical	-

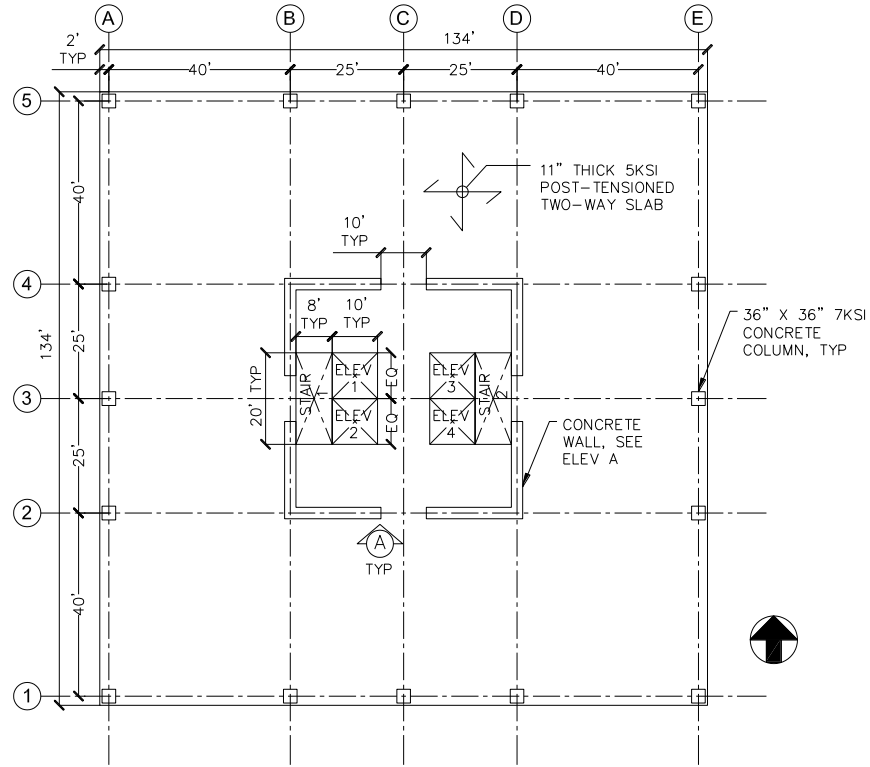


Figure 4-1. 30-Story building, typical floor plan view: levels 1 through 29

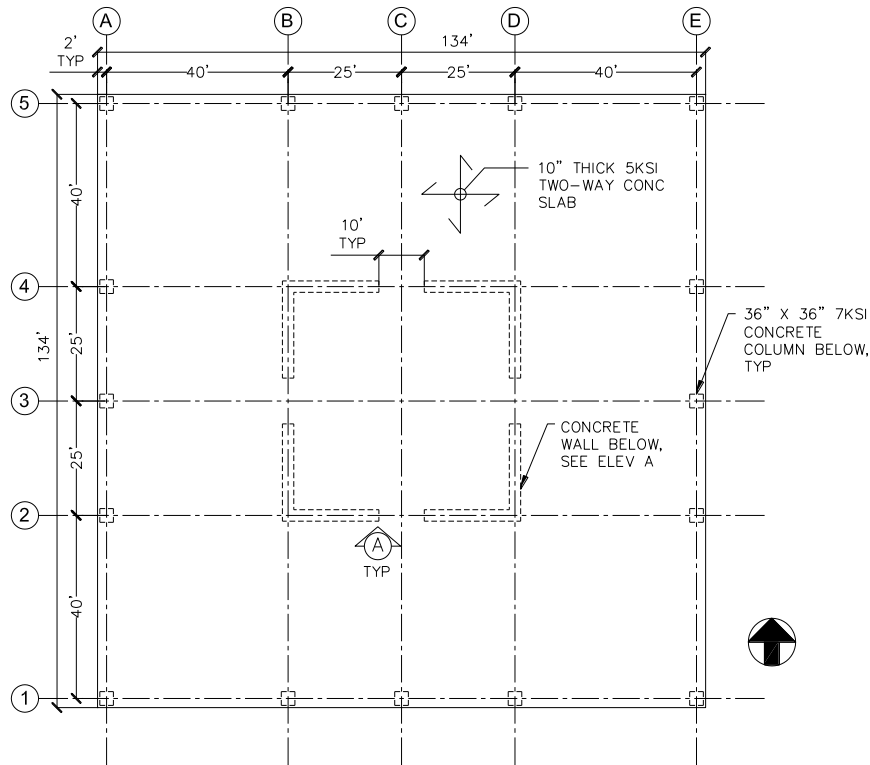


Figure 4-2. 30-Story building, roof plan view

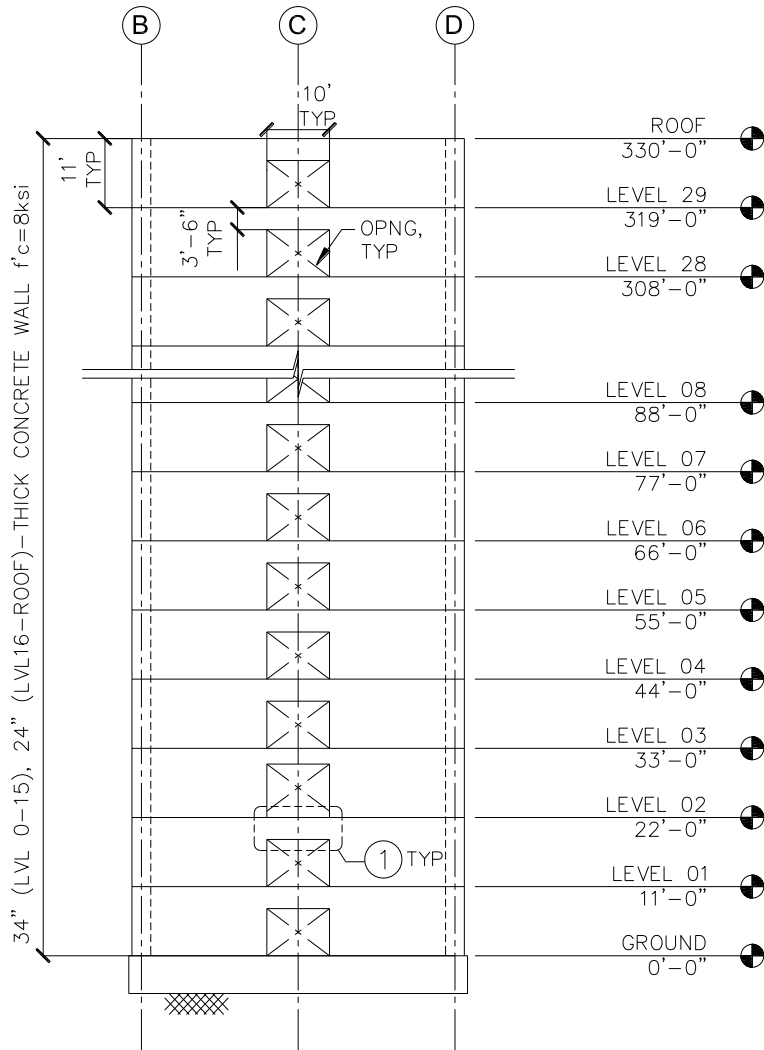


Figure 4-3. 30-Story building, Elevation A of south wall

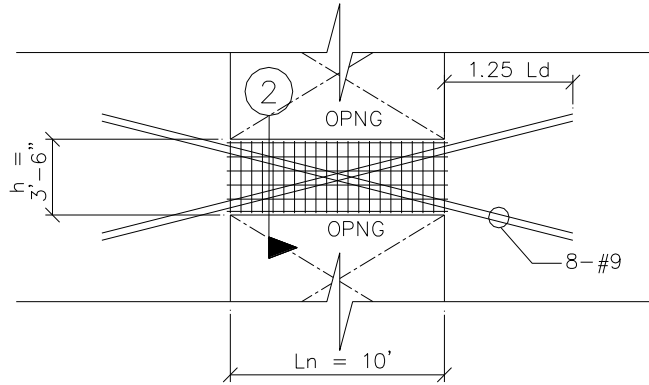


Figure 4-4. 30-Story building, Detail 1 of coupling beam diagonal reinforcement

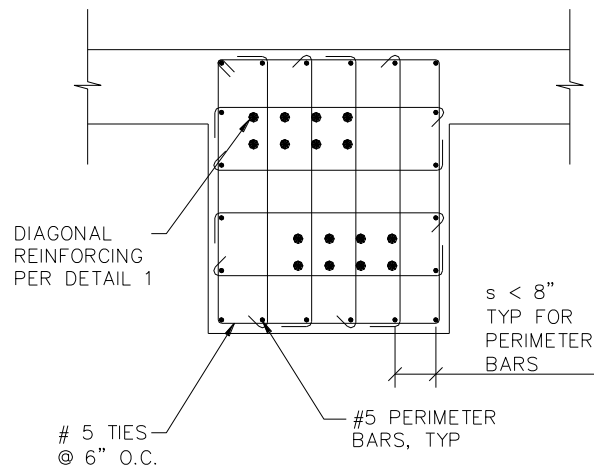


Figure 4-5. 30-Story building, Detail 2 of coupling beam full section confinement

4.4. Governing Codes and Methodology

The governing building code for this study is based on 2012 International Building Code (IBC) and 2013 California Building Code (CBC) which adopts ASCE7-10, Minimum Design Loads for Buildings and Other Structures. A summary of seismic parameters pertinent to this building are provided in Table 4-3.

Table 4-3. ASCE7-10 Seismic parameters

Seismic parameter	Value
Project location, Latitude/Longitude	34.05° N /118.25° W
Occupancy category	II
Importance factor, I_e	1.0
Mapped spectral acceleration (g)	$S_S = 2.147, S_1 = 0.720$
Site class	C
Seismic design category	D

Following the alternative lateral-force procedures stated in Section 104.11 of 2012 IBC and Section 12.6 of ASCE7-10, ‘An Alternative Procedure for Seismic Analysis and Design of Tall Buildings Located in the Los Angeles Region’ guidelines published by LATBSDC (2014) were used for the performance-based design of tall buildings.

4.5. Development of Nonlinear Perform 3D Model

Nonlinear response history analyses (NLRHA) are currently the best tool available to predict structural responses at different hazard levels. Although there are limitations, NLRHA aims to capture all significant modes of deformation and deterioration from the onset of damage to failure. In this study, two nonlinear models were built for the 30-story building using Perform 3D and Opensees, and a nonlinear model for the 20-story building was built in Opensees. Various aspects of Perform 3D nonlinear modeling are discussed in this section.

4.5.1. Overview of Perform 3D Model

A 3-dimensional, nonlinear model of the 30-story building was developed using CSI Perform 3D (2011) to represent the lateral force-resisting system of the building. Gravity system was excluded from the model, except for the slab-outrigger system at the four corners of the core walls where effective slab widths and lumped columns were modeled to capture the outrigger effects (PEER/ATC 72-1, 2010). The translational seismic mass was calculated using dead loads and mass moment of inertia (rotational mass) was calculated per equation below:

$$\text{Mass moment of inertia} = \sum(m \cdot I_c + m \cdot d^2) = \sum\left(m \cdot \left(\frac{B^2 + L^2}{12}\right) + m \cdot d^2\right)$$

where m = mass of floor [in weight or mass units]

B, L = floor dimensions [in]

d = distance to center of mass [in]

All lumped seismic masses were assigned to the center of mass at each floor. A rigid diaphragm was incorporated by slaving the horizontal degrees of freedom at each floor. The foundation of the building was modeled as pinned connections at the base of wall elements at the ground level. The P-delta effects were taken into account as a lumped gravity column at the center of the building with no lateral stiffness. Detailed examination of component modeling is documented in the following sections.

4.5.2. Strength and Stiffness Properties

In nonlinear response history analysis, it is common to use expected properties of materials and components rather than nominal or minimum specified properties that are typically used for code-level designs. Expected properties of concrete and reinforcing steel are shown on Table 4-4 and Table 4-5, respectively, and expected stiffness assumptions are presented in Table 4-6. It is important to use expected properties to best predict structural responses. However, it is noted that expected strength and modulus of elasticity for concrete mixes used in Los Angeles may not achieve these values because the aggregates commonly used in southern California are usually softer than those in eastern United States (LATBSDC, 2014).

The compressive concrete strength of column was limited to 1.4 times that of the slab system so that no special precautions need to be taken for concrete placement. If this ratio is greater than 1.4, special concrete placement procedures and additional inspection services must be considered per ACI318-11 Section 10.12.

Table 4-4. Concrete member strength and stiffness

Concrete Member	Nominal f'_c	Expected f'_c ¹	Nominal E ²	Expected E
Shear walls	8.0 ksi	10.4 ksi	4578 ksi	5080 ksi
Coupling beams	8.0 ksi	10.4 ksi	4578 ksi	5080 ksi
Post-tensioned slab	5.0 ksi	6.5 ksi	4415 ksi	4595 ksi
Non-post-tensioned slab	5.0 ksi	6.5 ksi	4415 ksi	4595 ksi
Columns	7.0 ksi	9.1 ksi	4347 ksi	4858 ksi

¹ Expected concrete material strength is taken as $1.3 \cdot f'_c$

² Modulus of elasticity is based on:

$$E_c = 57,000\sqrt{f'_c} \text{ for } f'_c \leq 6000 \text{ psi}$$

$$E_c = 40,000\sqrt{f'_c} + 10^6 \text{ for } f'_c > 6000 \text{ psi}$$

Table 4-5. Reinforcing strength

Reinforcing Member	Nominal	Expected yield ¹	Expected ultimate
ASTM A706 Grade 60	$F_y = 60$ ksi	$F_y = 70$ ksi	$F_u = 105$ ksi
0.5-in. diameter, 7-wire strand	$F_{pu} = 270$ ksi	N/A	N/A

¹ Expected reinforcing steel strength is $1.17 \cdot F_y$

Table 4-6. Stiffness assumptions

Element	SLE	MCE
Shear walls	Flexural: Fiber Section Shear: $1.0 GA_g$	Flexural: Fiber Section Shear: $0.5 GA_g$
Coupling beams	Flexural: $0.5 EI_g$ ¹ Shear: infinite ²	Flexural: $0.2 EI_g$ Shear: infinite
Slabs	Flexural: $\alpha \cdot \beta EI_g$ ³ Shear: $1.0 GA_g$	Flexural: $\alpha \cdot \beta EI_g$ Shear: $0.25 GA_g$
Columns	Flexural: $0.9 EI_g$ Shear: $1.0 GA_g$	Flexural: $0.7 EI_g$ Shear: $1.0 GA_g$

¹ Per LATBSDC (2014), $0.3 EI_g$ is commonly used

² All deformations in coupling beams are assumed to be associated with bending

³ α and β cracking factors are presented in the slab outrigger section

The material stress-strain relations for unconfined concrete, confined concrete and A706 reinforcing steel are shown on Figure 4-6. For unconfined concrete, modified Hognestad stress versus strain relations (Hognestad et al, 1955) were used as follows:

$$\text{Prior to peak stress (i) } 0 \leq \varepsilon_c \leq \varepsilon_0 \quad f_c = f'_c \left[\frac{2\varepsilon_c}{\varepsilon_0} - \left(\frac{\varepsilon_c}{\varepsilon_0} \right)^2 \right]$$

$$\text{Linear descending branch (ii) } \varepsilon_0 \leq \varepsilon_c \leq 0.0046 \quad f_c = f'_c \left(1 - 0.15 \frac{\varepsilon_c - \varepsilon_0}{0.0046 - \varepsilon_0} \right) \geq 0$$

$$\text{Zero stress (iii) } \varepsilon_c = 0.0046 \quad f_c = 0 \text{ ksi}$$

where $\varepsilon_0 = 0.0037$

f_c = concrete compressive strength [ksi]

f'_c = expected concrete compressive strength [ksi], defined per Table 4-4

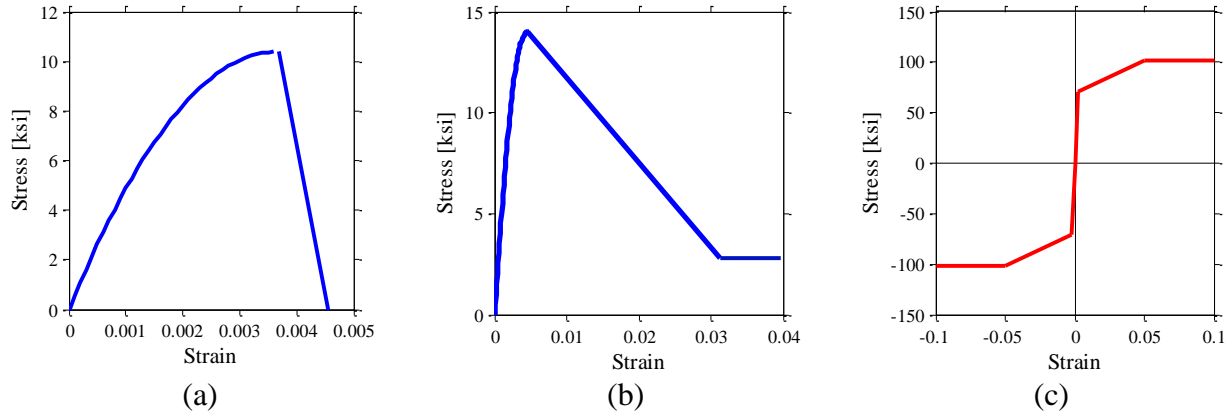


Figure 4-6. Stress-strain relationships for (a) unconfined concrete based on modified Hognestad, (b) confined concrete based on Razvi and Saatcioglu (1999), and (c) A706 reinforcing steel

4.5.3. Inelastic Properties of Shear Wall Elements

The axial and bending interaction of reinforced concrete shear walls was modeled using inelastic fiber shear wall elements. Each fiber is defined by its location, area, and stress-strain relationship as defined in the previous section. The in-plane shear responses were uncoupled from the axial and bending responses and elastic shear stiffness was modeled as:

$$\text{Cracked shear stiffness, } G_{eff} = \frac{G_c A}{2} = \frac{E_c}{4(1+\nu)} A = 0.2 \cdot E_c A$$

where E_c = expected elastic modulus, defined in Table 4-4
 A = cross-sectional area of the web
 ν = Poisson's ratio, 0.25

The boundary elements were modeled using reinforcing ratios specified per Table 4-7; boundary element lengths were chosen after analyzing shear wall compressive zones as documented in Appendix B. Although in-plane axial-bending behavior is nonlinear, out-of-plane bending behavior is elastic using Perform-3D, and was modeled at 25 percent of the gross concrete section elastic stiffness.

Table 4-7. Details of Perform 3D shear wall element

Levels	BE ¹ length	BE reinforcing ratio	BE material	Web reinforcing	Web material	Transverse reinforcing
1	78-in.	2%	Confined concrete ²	0.9%	Unconfined concrete ³	0.9%
2-5	70-in.	2%	Confined concrete	0.9%	Unconfined concrete	0.9%
6-10	50-in.	2%	Confined concrete	0.9%	Unconfined concrete	0.9%
11-15	38-in.	2%	Confined concrete	0.9%	Unconfined concrete	0.9%
16-20	30-in.	2%	Confined concrete	0.9%	Unconfined concrete	0.9%
21-Roof	-	-	-	0.9%	Unconfined concrete	0.9%

¹ Boundary element, refer to Figure 4-7

² Refer to Figure 4-6 (b)

³ Refer to Figure 4-6 (a)

The shear wall elements were modeled with one element per story, except for the first story where two elements were used. To capture shear wall element rotations and strains, a strain gage was modeled over the height of the plastic hinge length, which was calculated as the story height (common practice). The benefits of modeling a strain gage over the plastic hinge length is discussed through sensitivity study results in Appendix B. See Figure 4-8 for modeling details.

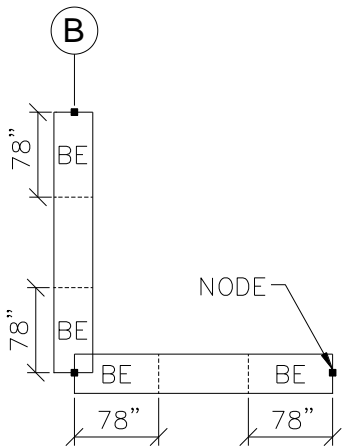


Figure 4-7. Boundary element dimensions on level 1.

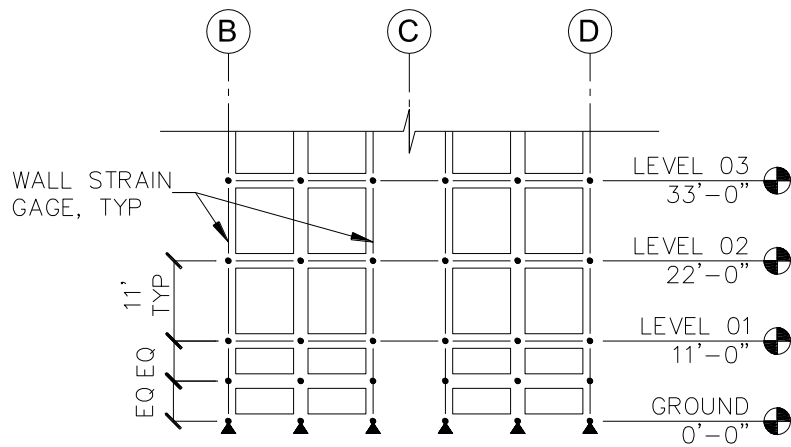


Figure 4-8. A partial elevation view of Perform 3D model

4.5.4. Inelastic Properties of Coupling Beams

Diagonally reinforced coupling beams were modeled using three components: a nonlinear rigid-plastic shear displacement hinge at the center of the beam and two elastic beam sections on both sides of the hinge, as shown on Figure 4-9.

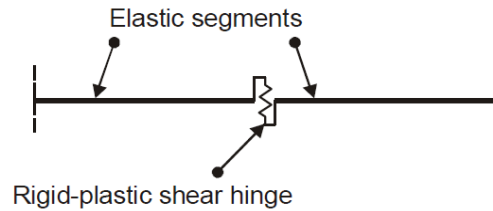


Figure 4-9. Rigid-plastic shear hinge, CSI (2011)

To establish force-displacement relationship, expected yield and ultimate shear strengths were calculated per equations below, and displacement values were based on diagonally reinforced coupling beam test results from Naish et al (2013a, b), as shown on Figure 4-10. Flexural stiffness was defined as $EI_{\text{eff}} = 0.2 \cdot EI_g$, and cyclic degradation parameters were based on calibrated values per Naish et al (2013b). All modeling parameters are shown in Table 4-8 and Figure 4-11.

$$F_Y = 2 \cdot A_{vd} \cdot (1.17 \cdot f_y) \cdot \sin(\alpha)$$

$$F_U = 1.4 \cdot F_Y$$

$$\delta_\theta = \theta \cdot L_b$$

where α = angle between diagonal reinforcing bars and longitudinal axis of coupling beam, 16°

A_{vd} = area of diagonal reinforcing bars

θ = rotation of coupling beam [radians]

δ = equivalent displacement of shear hinge at rotation θ [inch]

L_b = length of coupling beam [inch]

Table 4-8. Shear displacement hinge – modeling and cyclic degradation parameters

Component	F_Y (k)	F_U (k)	DY	DU	DL	DR	DX
Shear displacement hinge	309.6	433.4	-	1%	6.5%	9%	12%
Cyclic degradation factors	-	-	0.50	0.45	0.40	0.35	0.35

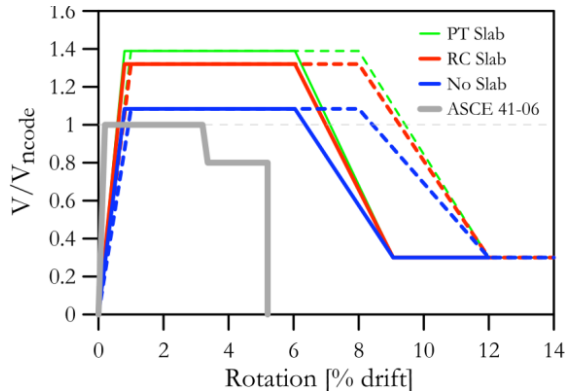


Figure 4-10. Diagonally reinforced coupling beam test results by Naish et al (2013b), 1/2 scale test results are shown as dotted lines

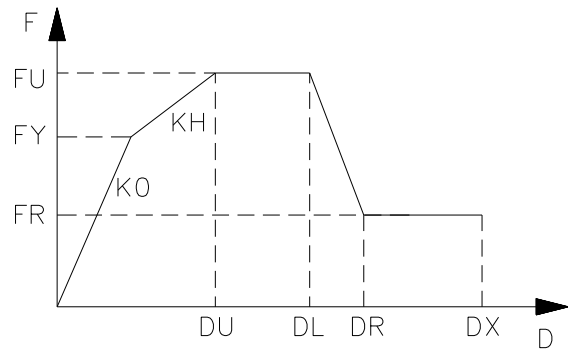


Figure 4-11. Perform 3D trilinear force-displacement relationship

4.5.5. Embedded Beams

In Perform3D, embedded beams are needed to connect coupling beams to shear wall elements because wall nodes do not have rotational stiffness. Based on sensitivity studies shown in Appendix B and Powell (2007), use of embedded beams with stiffness that is 20 times stiffer than the coupling beam section with negligible axial stiffness were used for the connection (refer to Figure 4-12). The embedded beams do not have a substantial impact on the stiffness of shear wall elements.



Figure 4-12. (a) Schematic drawing of a coupled wall system, (b) Perform 3D modeling of shear walls, coupling beams and embedded beams

4.5.6. Inelastic Properties of the Slab Outrigger System

Coupling between perimeter gravity columns and core walls was modeled using a simplified slab outrigger system model. The slabs were modeled with wide, shallow beams connecting the perimeter gravity columns to the core shear walls at the four corners of the building (see Figure 4-13). The effective slab widths were calculated for exterior slab conditions as

$$\alpha \cdot l_2 = c_1 + \frac{l_1}{6}$$

where $\alpha \cdot l_2$ is the elastic effective slab width, c_1 is the column dimension parallel to slab-beam element, and l_1 is the center-to-center span length in the direction under consideration (PEER/ATC 72-1, 2010). As shown on Table 4-9, the actual dimensions of elastic effective slab widths were first determined, and then the lumped parameters were determined. Once α was established, stiffness values were further reduced by $\beta = 0.5$ (Kang and Wallace 2005) to account for concrete cracking. Thus, the effective flexural stiffness of the slab was calculated as

$$E_c I_{effective} = E_c \cdot \beta \left[\frac{\alpha \cdot l_2 \cdot h^3}{12} \right]$$

where $\alpha \cdot \beta$ is the normalized effective stiffness, l_2 is the tributary width of the beam under consideration, and h is the slab thickness. All computed values from actual and lumped dimensions are summarized in Table 4-9.

Table 4-9. Effective slab widths, corresponding stiffness factors (α), and normalized effective stiffness factors, $\alpha \cdot \beta$ for actual and lumped cases

	Column-end	Wall-end
Actual	$l_1 = 40.0', l_{2E} = 32.5', l_{2M} = 25.0'$	
	$\alpha_a \cdot l_{2E} = 3' + \frac{32.5'}{6} = 8.42' (\alpha_a = 0.26)$ $\alpha_b \cdot l_{2M} = 3' + \frac{25.0'}{6} = 7.17' (\alpha_b = 0.29)$	$\alpha_c \cdot l_{2E} = 13.9' + \frac{32.5'}{6} = 19.3' (\alpha_c = 0.60)$ $\alpha_d \cdot l_{2M} = 25.0' (\alpha_d = 1.0)$
Lumped	$l_1 = 40.0', l_2 = 45.0'$	
	<u>Beam LB1</u> $\alpha = 0.28$ $\alpha \cdot \beta = (0.28) \cdot (0.50) = 0.14$	<u>Beam LB2</u> $\alpha = 1.0$ was used for simplicity (0.80 would be more accurate) $\alpha \cdot \beta = (1.0) \cdot (0.50) = 0.50$

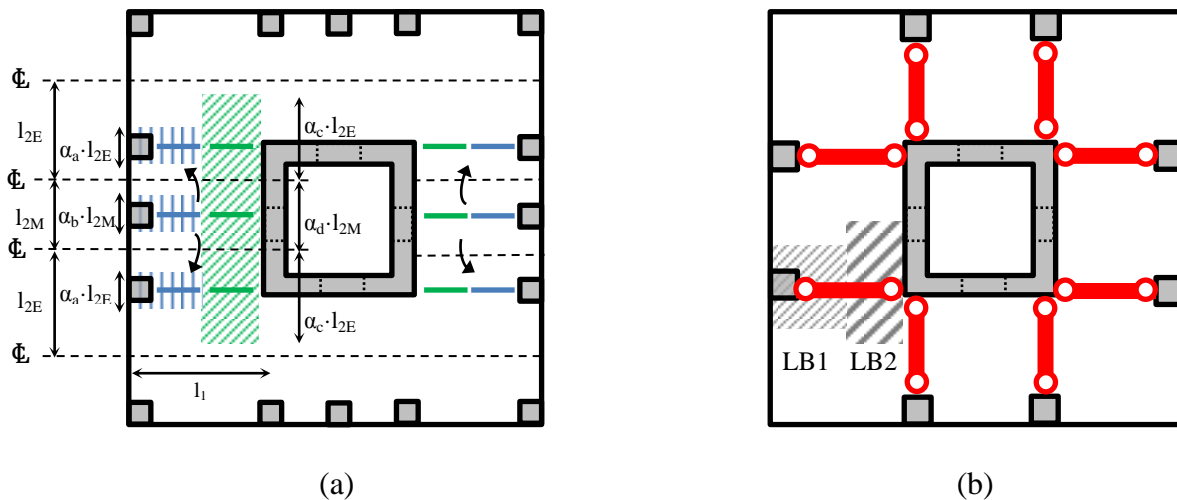
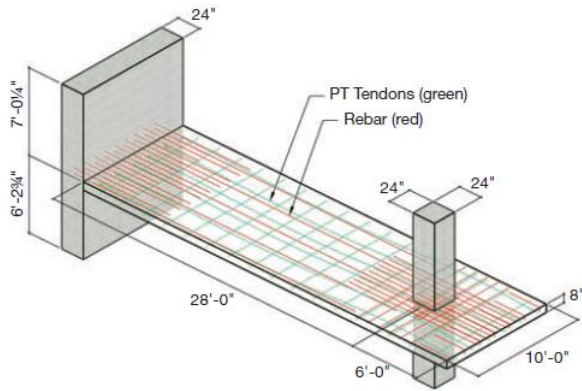


Figure 4-13. (a) Typical floor plan view showing effective slab widths for east-west direction (b) simplified (lumped) slab-column outrigger system with lumped gravity columns and slab widths

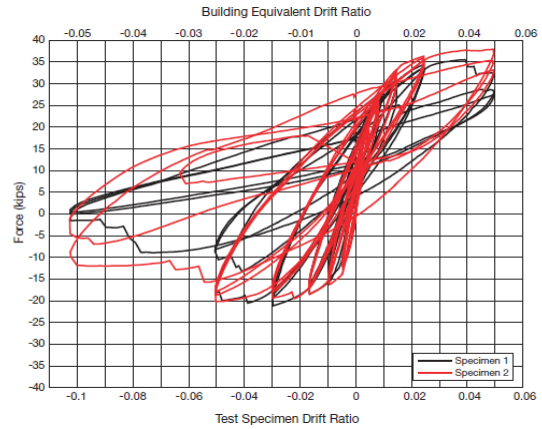
The modeling parameters for the slab-outrigger system were determined for the plastic hinges located at the ends of beam LB1 and LB2, as shown on Figure 4-13. The flexural strengths of the beams were determined per post-tensioned slab strength calculations per English (2013) and rotation parameters were defined per slab outrigger system test results shown in Klemencic et al. (2006); refer to Figure 4-14. Cyclic degradation parameters were also calibrated to match test results per Klemencic et al. (2006). See Table 4-10 for a summary of modeling and cyclic degradation parameters.

Table 4-10. Slab-beams – modeling and cyclic degradation parameters

Component	$F_Y +$ (k·in)	$F_U +$ (k·in)	$F_Y -$ (k·in)	$F_U -$ (k·in)	-
Slab-beam at wall	7,880	8,668	14,236	15,660	-
Slab-beam at column	4,043	4,447	4,043	4,447	-
-	DY	DU	DL	DR	DX
Cyclic degradation factors	0.50	0.20	0.20	0.20	0.20



(a)



(b)

Figure 4-14. (a) Test specimen of post-tensioned slab connection to gravity column and core wall
(b) Total lateral force versus drift ratio, Klemencic et al. (2006)

4.5.7. P-Delta Column

Global P-Delta effects of gravity loads acting on displaced nodes were incorporated into the analysis model through a P-Delta column. All gravity loads that were not accounted for in the model were assigned to the P-Delta column, and the P-Delta column was modeled as a linear elastic bar with zero flexural stiffness at the center of mass at all levels.

4.5.8. Damping

Two different damping models were used for design and analysis. Rayleigh damping was used for the performance-based design of the 30-story building (Chapter 4.6), whereas modal damping coupled with a small amount of Rayleigh damping was used for Monte Carlo simulations (Chapter 6). In the following subsections, modeling procedures, potential issues, and sensitivity studies for the two models are presented.

Rayleigh Damping

Energy dissipation of two inelastic elements, diagonally reinforced concrete coupling beams and slab-outrigger systems, were captured explicitly through cyclic degradation in the analysis model. For damping effects of structural, nonstructural, and foundation elements that were not incorporated in the analysis model, Rayleigh damping was used to represent equivalent viscous damping. Rayleigh damping uses a combination of stiffness and mass proportional damping, as

$$C = \alpha \cdot M + \beta \cdot K$$

where C is damping matrix, M is mass matrix, K is initial elastic stiffness matrix, and α and β are Rayleigh damping coefficients. Using Rayleigh damping results in essentially constant damping over a significant range of periods. In this study, 3% damping was assigned at $0.33 \cdot T_1$ and $1.5 \cdot T_1$, which resulted in approximately 2.5% damping at the first mode period. Refer to Figure 4-15.

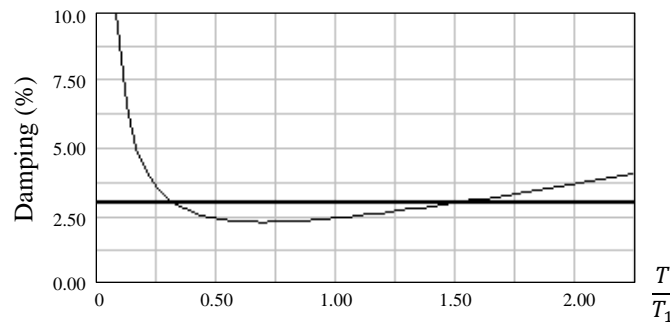


Figure 4-15. Rayleigh damping

Modal Damping

In performing Monte Carlo simulations (Chapter 6), modal damping of 2.5% (varies, see Chapter 5) along with 0.1% Rayleigh damping were used to address potential over-damping of higher modes that may occur with the use of only Rayleigh damping. When Rayleigh damping is used, the βK damping coefficients for coupling beams are based on the initial elastic bending and shear stiffness, which can be quite large. When the coupling beams yield, the βK damping coefficients stay constant; this can overestimate the βK energy dissipation whereas the deformations of the coupling beams can be underestimated (CSI, 2011). For modal damping, this is not a potential issue. However, when modal damping is used, the damping matrix is only based on the modes where mode shapes have been calculated. Since in a real structure, the number of degrees of freedom is much larger than the number of modes generally considered in analysis, many displaced shapes will be undamped. Thus, a small amount of Rayleigh damping is used in conjunction with modal damping to ensure that the higher modes are damped.

Sensitivity Studies

To address the differences in the use of Rayleigh versus modal damping, sensitivity studies were conducted. The details of the sensitivity study and comparative results are presented in Appendix B, whereas the impacts of these differences are later discussed in Chapter 6.4.

4.6. Nonlinear Response History Analysis Results

Nonlinear response history analysis was performed at service (SLE43) and collapse prevention (MCE) hazard levels, for ground motion Suite A. Load criteria per Table 4-2 were applied, and the following load combination was used to analyze the buildings, $1.0 \cdot D + L_{exp} \pm E$, where D, L_{exp} and E represent dead load, 25% of unreduced live load and effects of ground motions, respectively. The modal properties of the 30-story building are summarized on Table 4-11.

Table 4-11. 30-Story building modal properties

Vibration mode	Period (sec)	Mass participation		Dominant direction
		H1 (East-West)	H2 (North-South)	
1	2.48	33.7%	33.7%	Translation, H1 & H2
2	2.48	33.7%	33.7%	Translation, H1 & H2
3	2.17	0%	0%	Torsion

4.6.1. Service Level (SLE43) Analysis Results

At the SLE43 hazard level, the structure remains essentially elastic. Selected key structural responses, namely, interstory drifts and coupling beam rotations are shown on Figure 4-16 and Figure 4-17. Mean interstory drift ratios are less than the limit of 0.5% and the mean coupling beam rotations are approximately 0.3% which is less than yielding rotations of 1%, as shown by Naish et al (2013b). The coupling beam rotations represent total rotations, which include elastic and plastic rotations. All components satisfied the elastic demand to capacity ratios. H1 direction refers to the east-west direction, and H2 refers to the north-south direction.

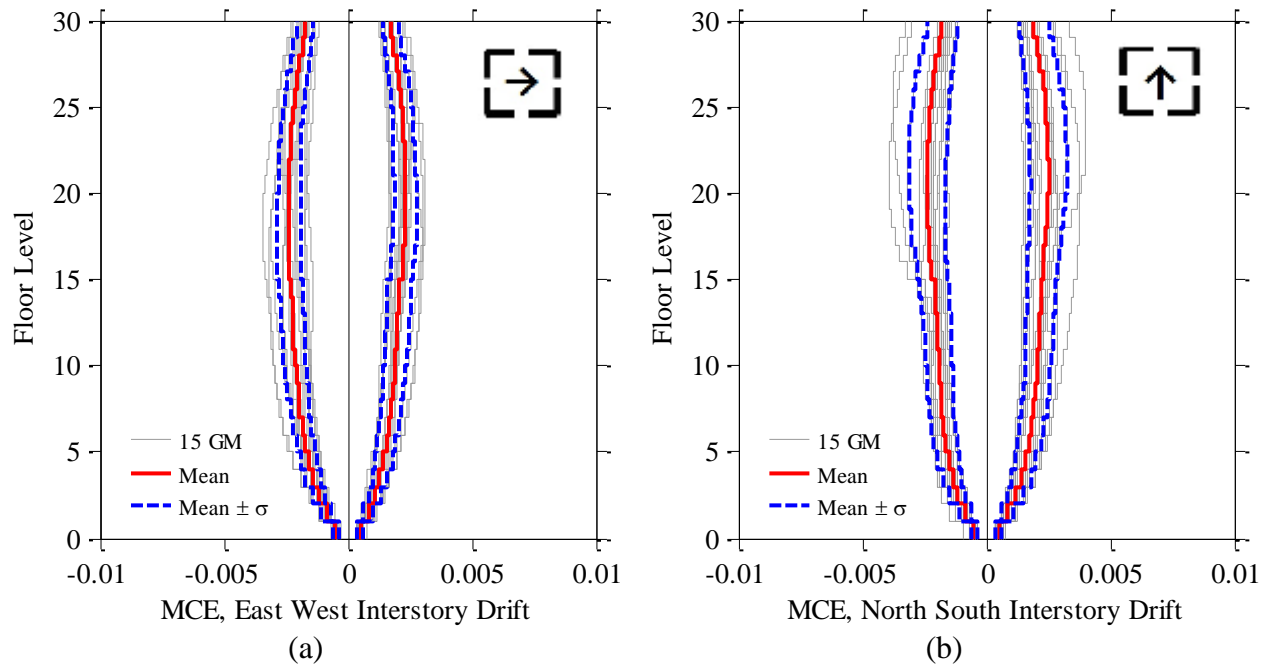


Figure 4-16. SLE43 interstory drifts for (a) H1 direction and (b) H2 direction

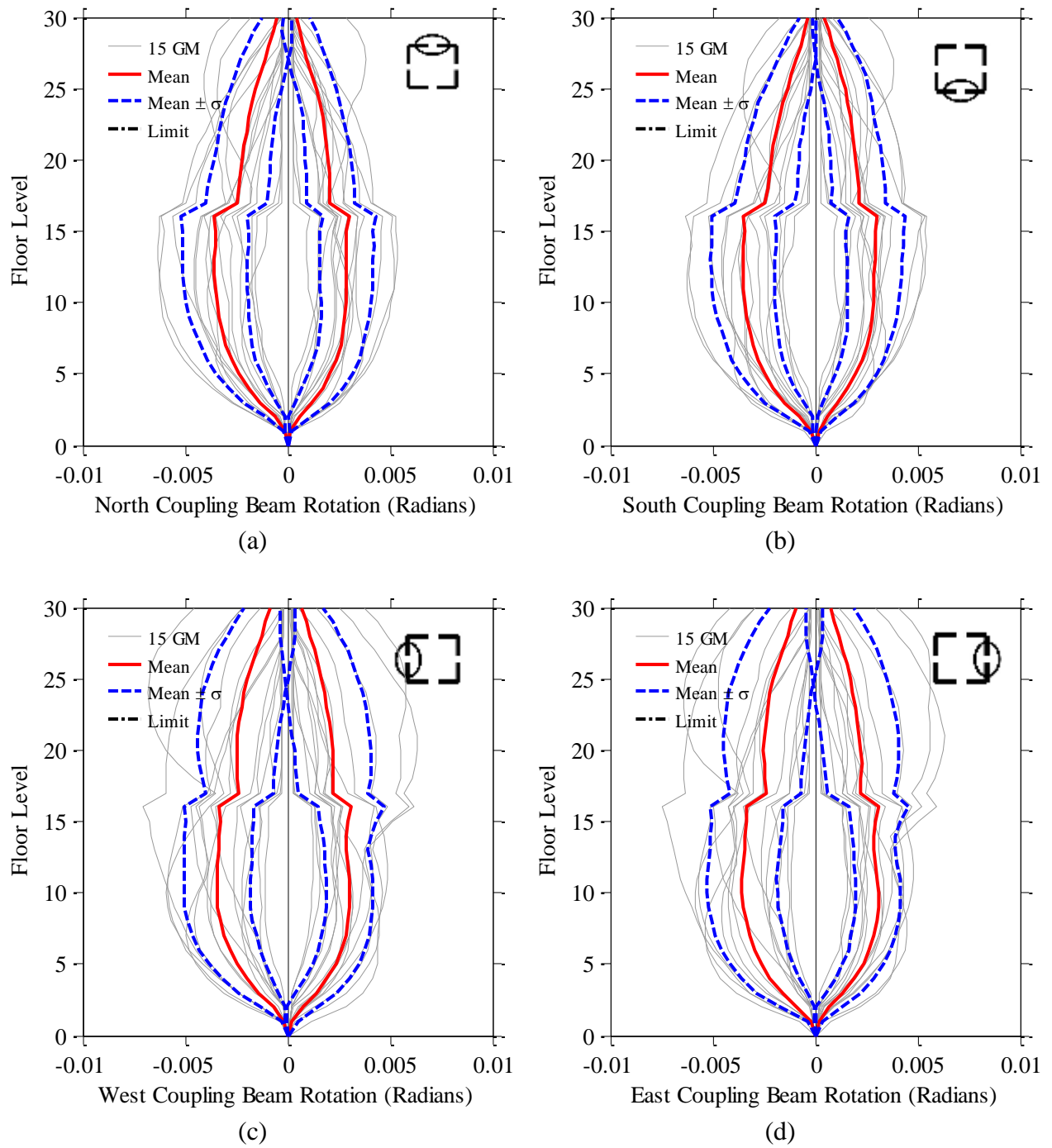


Figure 4-17. SLE43 coupling beam rotations for (a) North coupling beam, (b) South coupling beam, (c) West coupling beam, and (d) East coupling beam

4.6.2. Collapse Prevention Level (MCE) Analysis Results

At the MCE hazard level, the structure dissipates energy by yielding of the coupling beams first, and then through flexural yielding of the shear walls. Slab outriggers also typically yield due to differential deformations between the core and the gravity columns. Key structural responses were plotted and checked against criteria shown on Table 2-7. A summary of key responses are provided in Table 4-12.

Table 4-12. MCE level key structural responses

Structural response	Figures
Interstory drifts	Figure 4-18
Residual interstory drifts	
Coupling beam rotations	Figure 4-19
Structural wall shear force	Figure 4-20
Relative floor acceleration	Figure 4-21
Structural wall flexural moment	Figure 4-22
Strains in north shear walls	Figure 4-23
Strains in south shear walls	Figure 4-24
Strains in west shear walls	Figure 4-25
Strains in east shear walls	Figure 4-26
Maximum and minimum strains	Figure 4-27

The coupling beam rotations represent plastic rotations at the MCE hazard level; the contributions from elastic rotations were negligible at less than 1% of the total rotations.

Based on the structural wall shear forces, wall transverse reinforcement was designed per Chapter 2.4.3 and the results are shown on Table 4-13. All normalized shear demands (shear demands divided by $A_{cv} \cdot \sqrt{f'_c}$ using expected material properties) were less than the ACI318-11 recommended value of 8.

Table 4-13. MCE shear wall design and transverse reinforcement

Levels	1.5·Shear force (kips)	ρ_t	Normalized shear
1-5	26,130	0.0085	7.85
6-10	20,600	0.0061	6.19
11-15	16,110	0.0041	4.84
16-25	13,710	0.0056	4.12
26-30	10,750	0.0037	3.23

The axial strain values are initially presented by boundary element locations, and a summary of maximum mean tensile and minimum compressive strains are later presented on Figure 4-27 for the plastic hinge regions. It can be seen that the maximum mean tensile strain (0.0051) is less than the limit of 0.01 and that 1.5 times the minimum mean compressive strain (-0.002) is less than the limit of $-0.0075/1.5 = -0.005$; all limits are shown on Table 2-7.

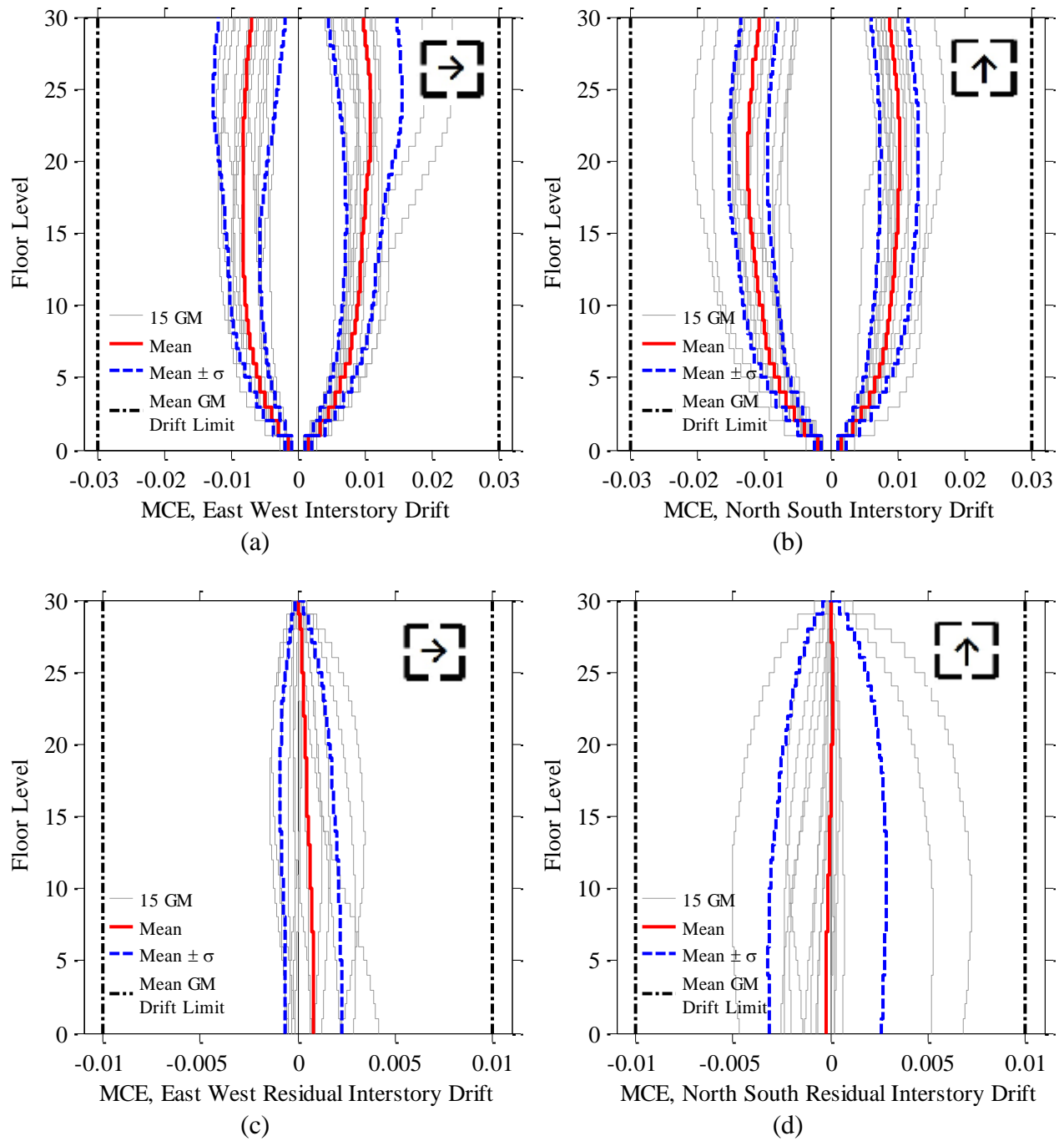


Figure 4-18. MCE interstory drifts for (a) H1 direction, (b) H2 direction, and MCE residual interstory drifts for (c) H1 direction, and (d) H2 direction

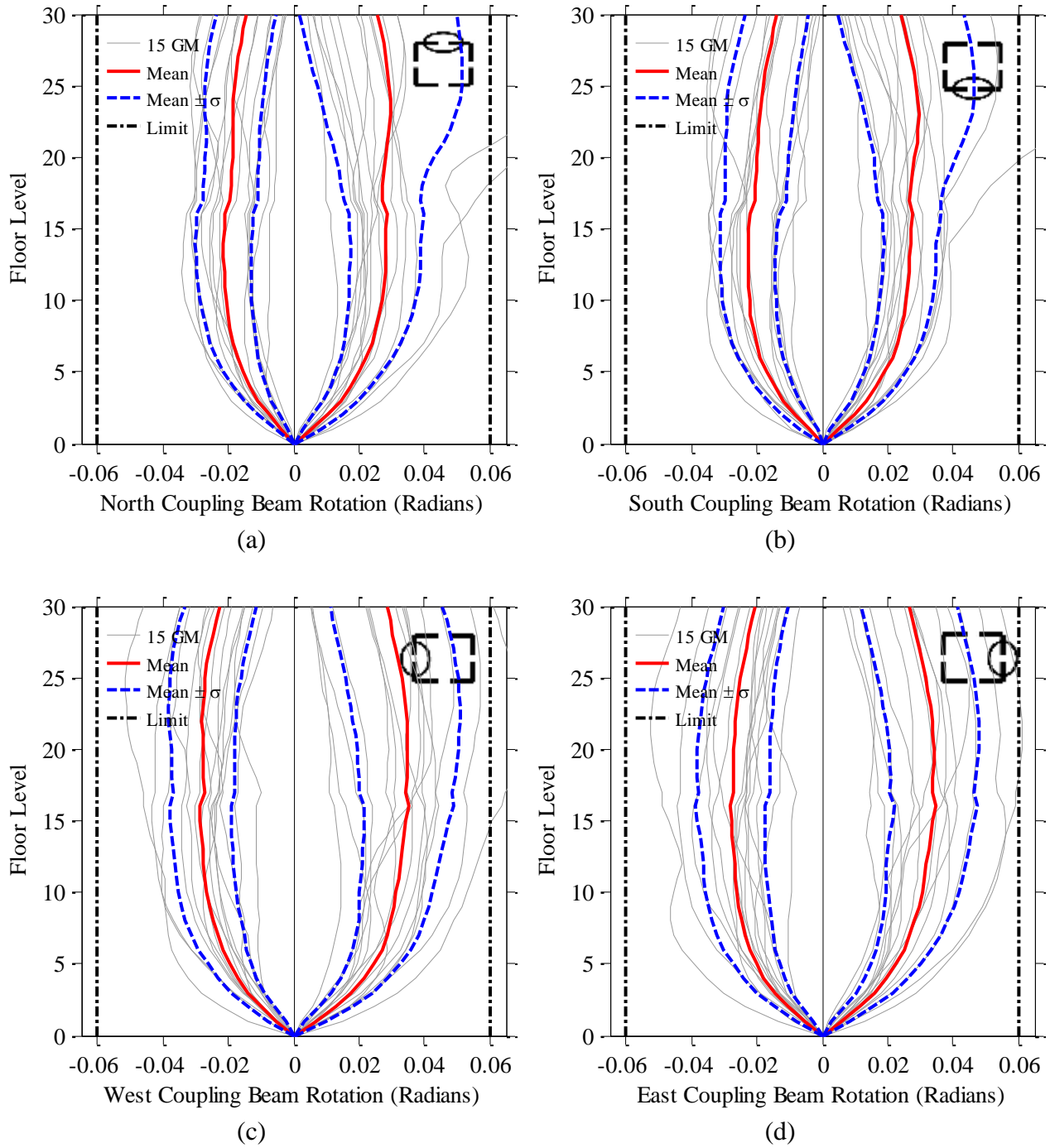


Figure 4-19. MCE coupling beam rotations for (a) North coupling beam, (b) South coupling beam, (c) West coupling beam, and (d) East coupling beam

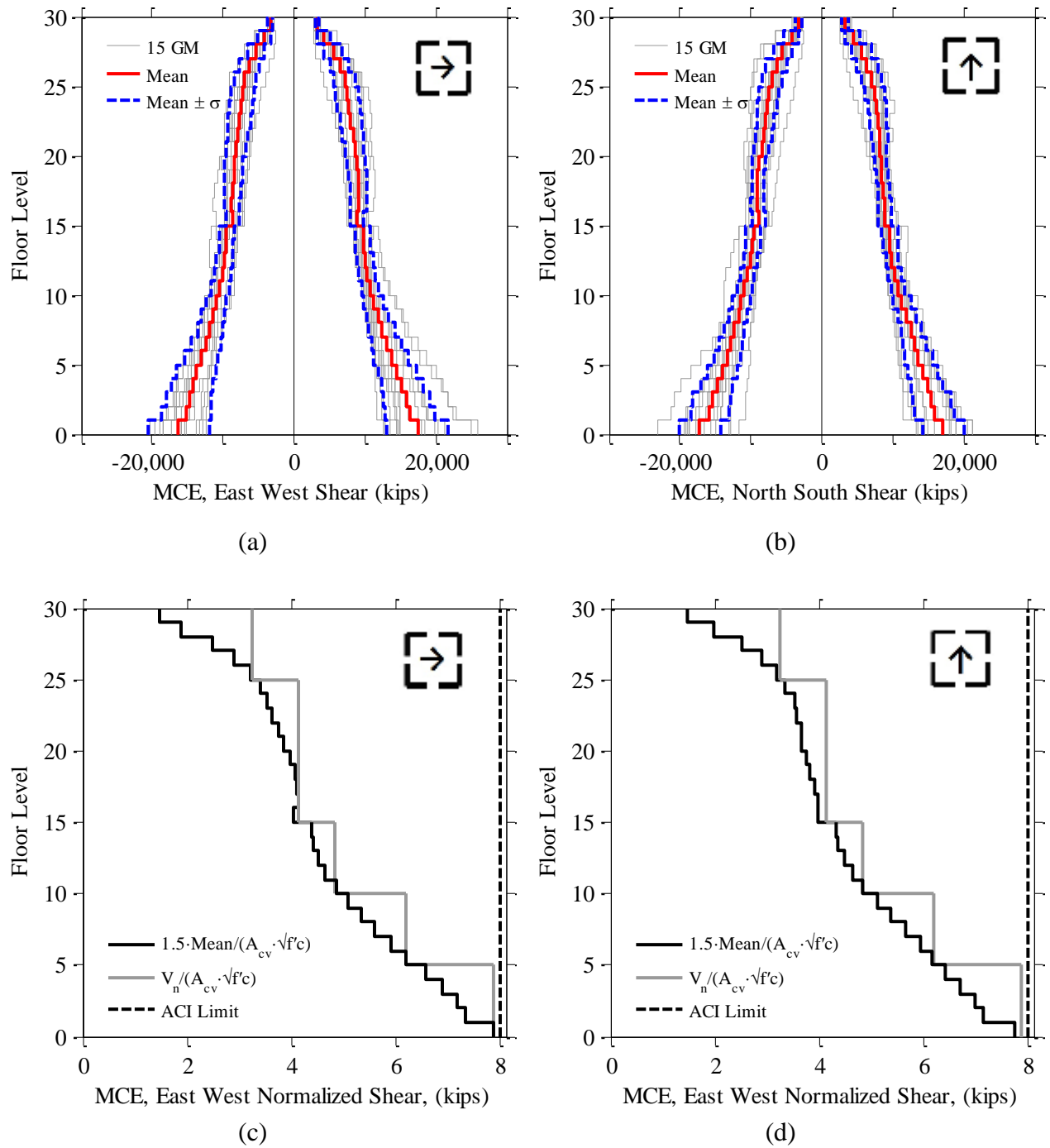


Figure 4-20. MCE shear demand for (a) H1 direction, (b) H2 direction, and MCE shear demand versus ACI318 limit for (c) H1 direction, and (d) H2 direction

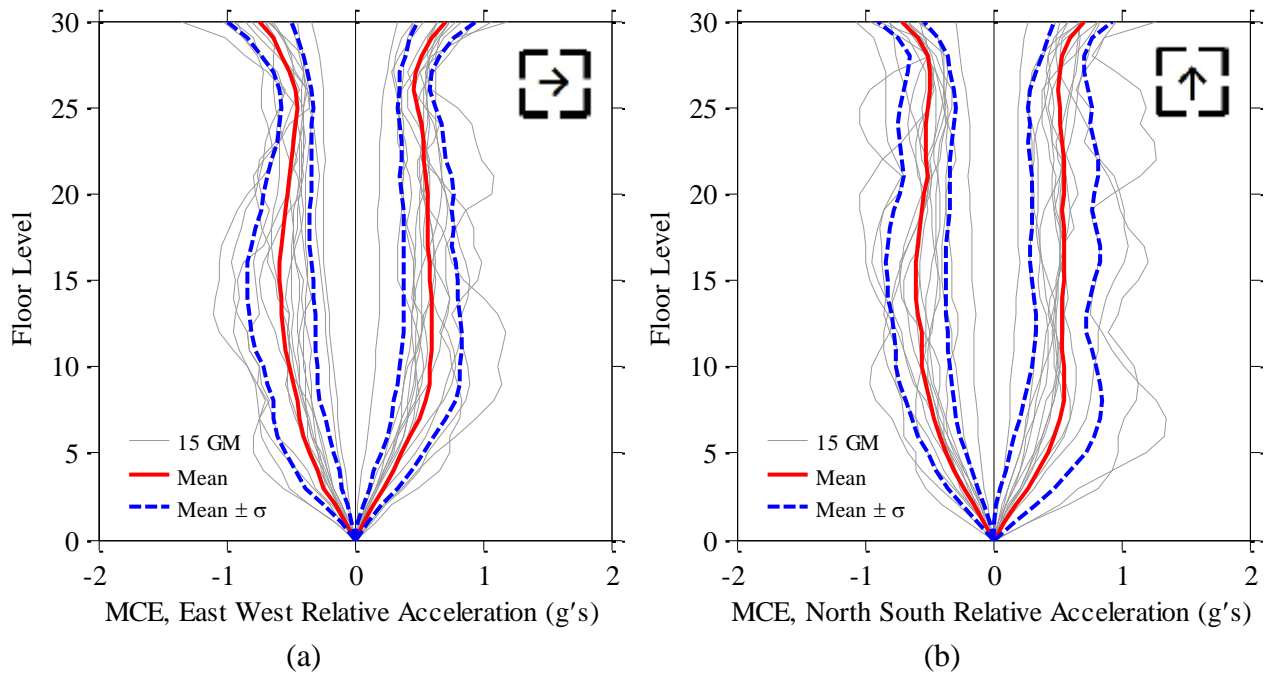


Figure 4-21. MCE relative floor acceleration for (a) H1 direction and (b) H2 direction

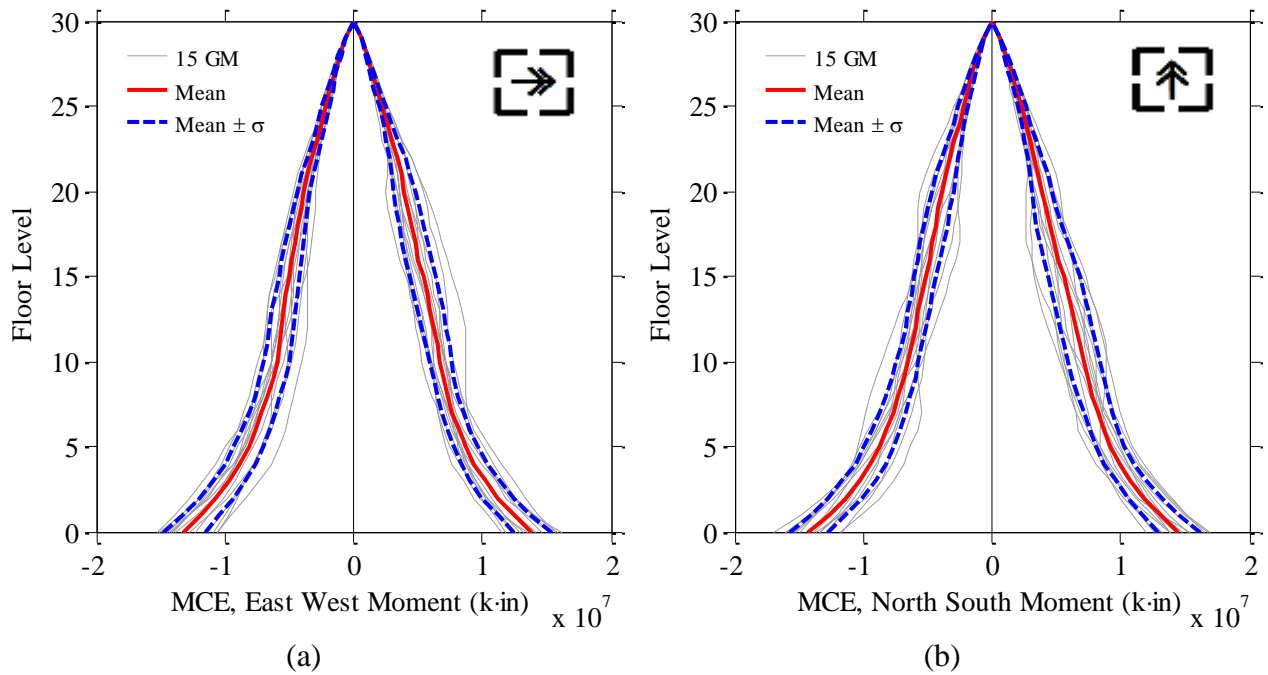


Figure 4-22. MCE moment demand for (a) H1 direction and (b) H2 direction

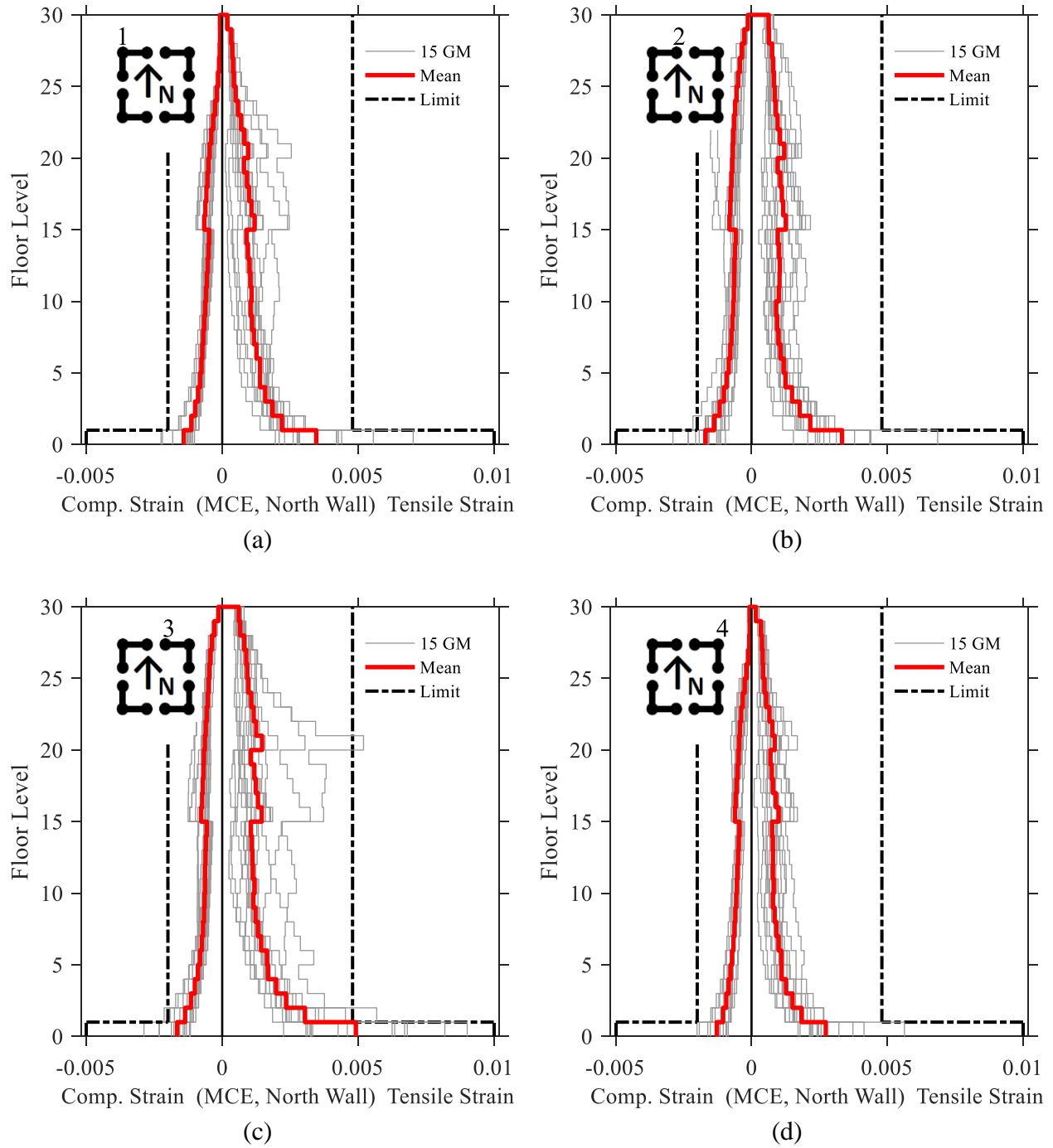


Figure 4-23. MCE north shear wall boundary element extreme fiber compressive and tensile strains, at (a) Location 1, (b) Location 2, (c) Location 3, and (d) Location 4

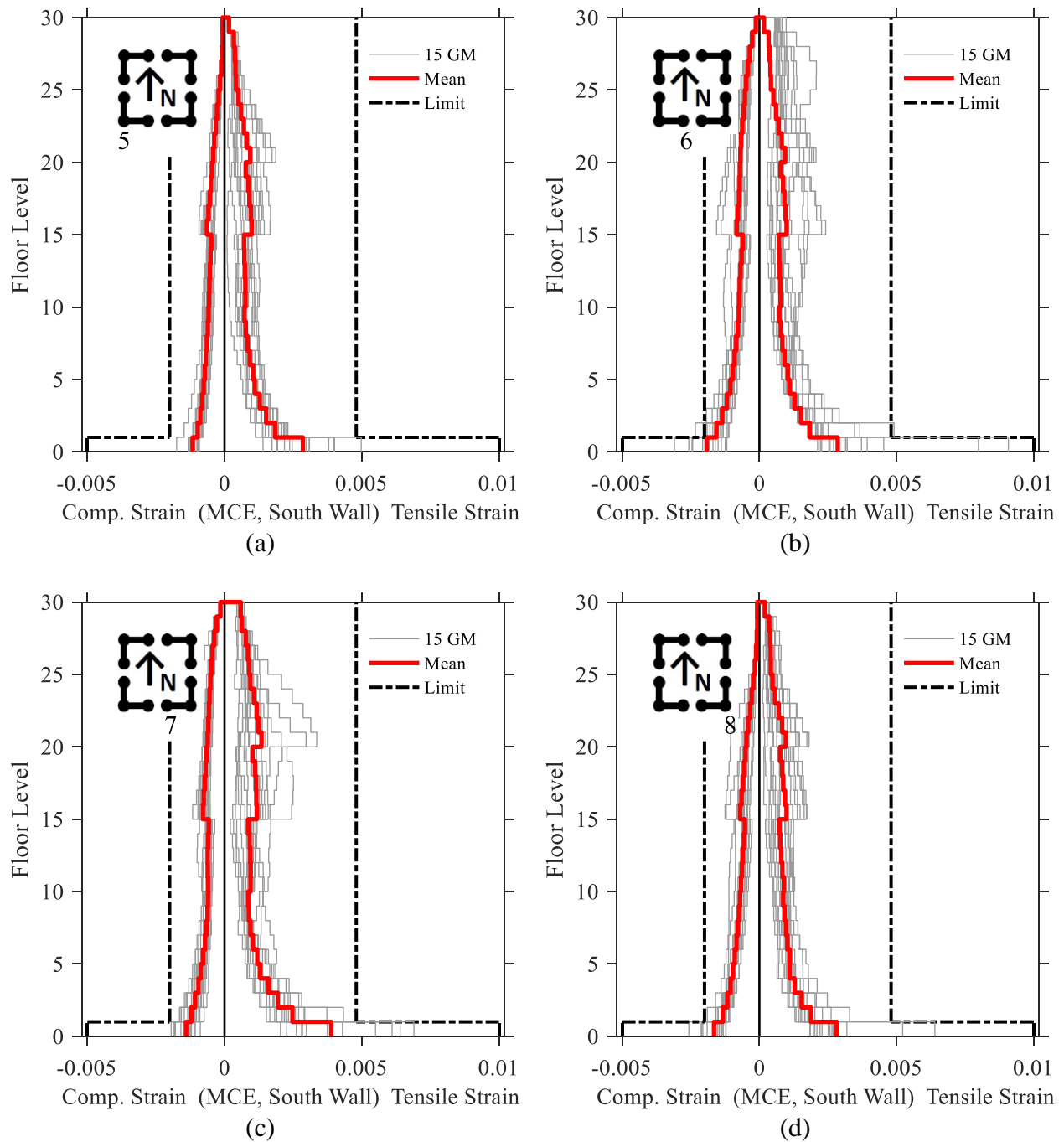


Figure 4-24. MCE south shear wall boundary element extreme fiber compressive and tensile strains, at (a) Location 5, (b) Location 6, (c) Location 7, and (d) Location 8

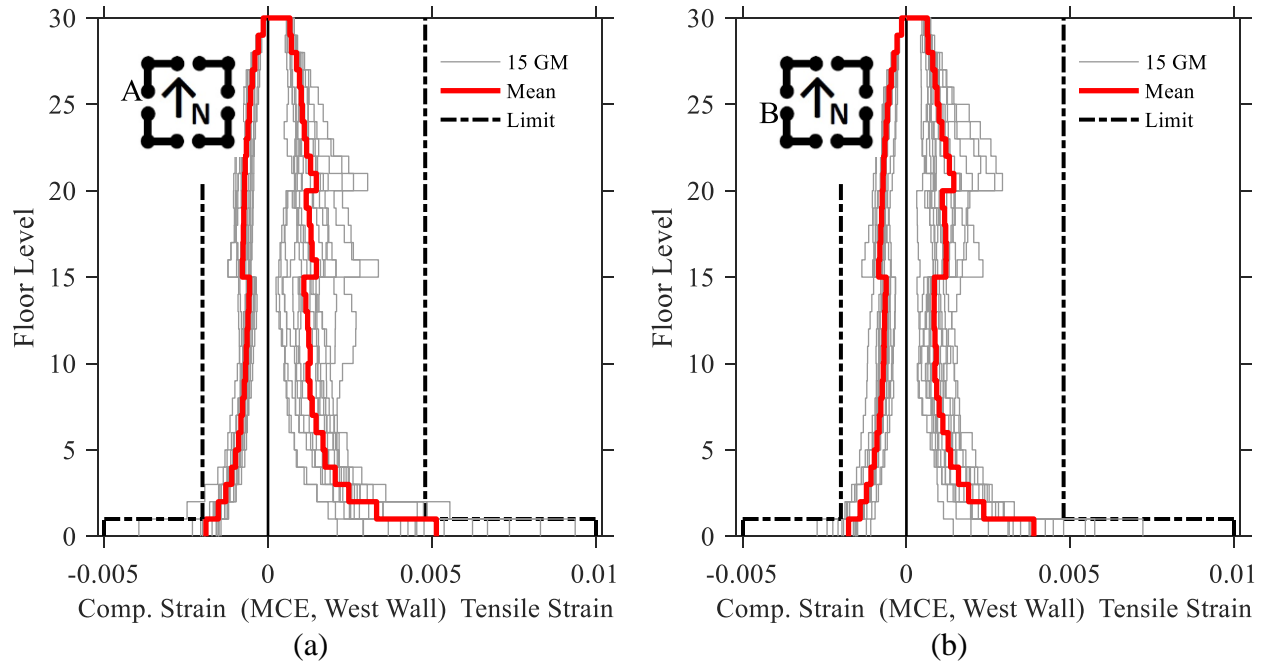


Figure 4-25. MCE west shear wall boundary element extreme fiber compressive and tensile strains, at (a) Location A and (b) Location B

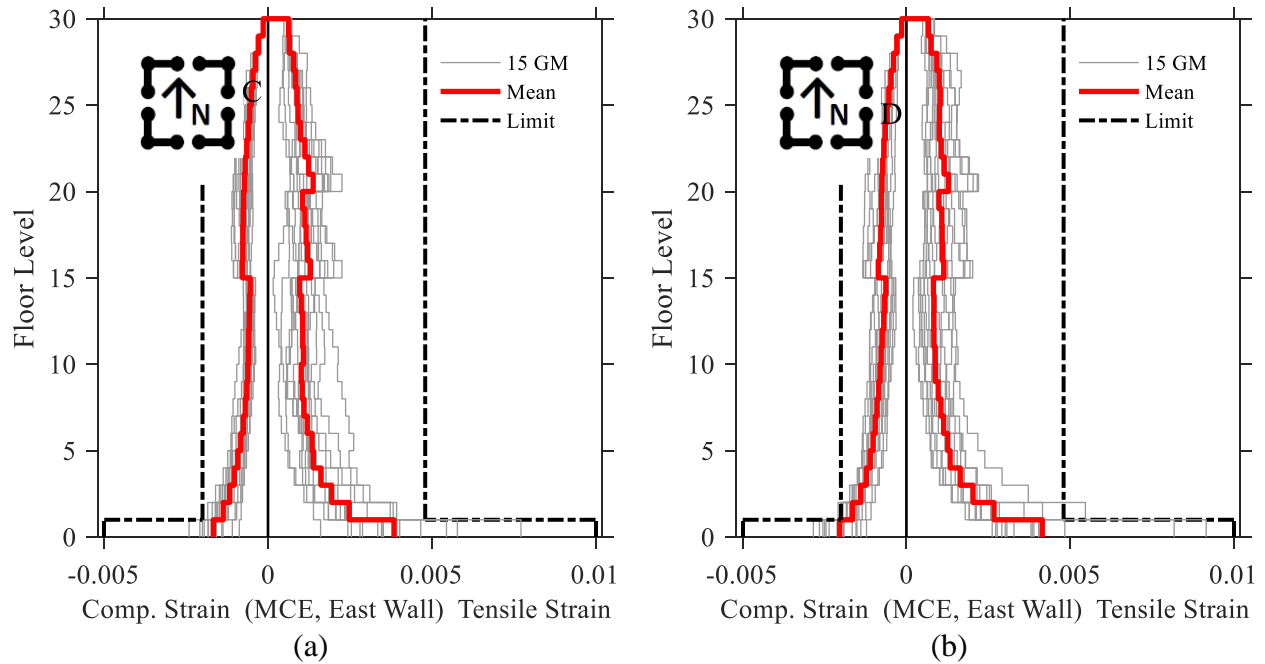


Figure 4-26. MCE east shear wall boundary element extreme fiber compressive and tensile strains, at (a) Location C and (b) Location D

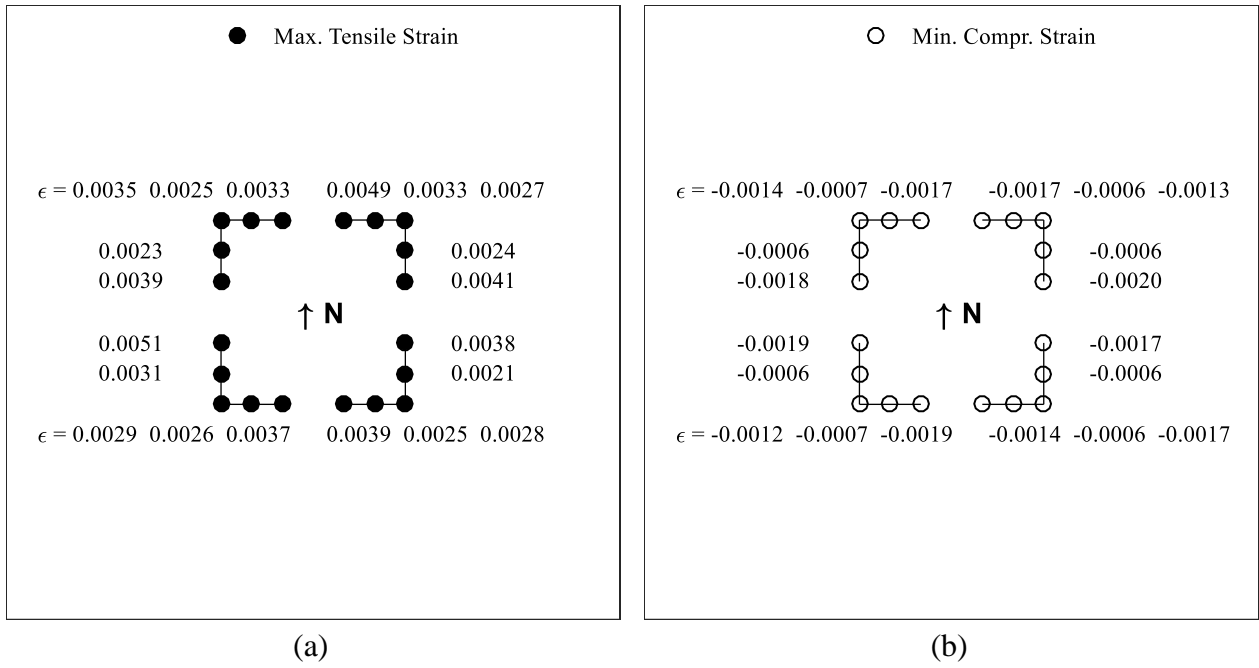


Figure 4-27. MCE shear wall (a) maximum mean tensile strains and (b) minimum mean compressive strains in the plastic hinge regions

4.7. Development of Opensees 2D Model

To overcome the challenges of high input and output processing times and computational costs faced in Perform 3D, Opensees (Open System for Earthquake Engineering Simulation, 2015) was adopted to supplement automated Monte Carlo simulations for the 20 and 30-story models. The main advantages of Opensees are its versatility and an open source platform; the software platform incorporates numerous types of materials, elements, components, and solution algorithms that can be scripted to automate dynamic analyses.

4.7.1. Overview of Opensees 2D Model

A two-dimensional, nonlinear model was developed in Opensees to represent the lateral force-resisting system of the 20 and 30-story buildings. To idealize the 3D core wall system to a 2D system, half of the core wall system was modeled with equivalent area and stiffness, as shown on Figure 4-28. The wall piers were modeled using the Multiple-Vertical-Line-Element-Model (MVLEM) and coupling beams were modeled using a linear elastic beam along the length of the beam, along with zero-length, nonlinear springs at beam ends. Rigid links were modeled to connect the coupling beams to the wall piers. P-delta effects were modeled using an elastic column with negligible lateral stiffness, and horizontal truss elements were used to connect the P-delta columns to the coupled wall piers. Translational seismic masses were lumped to the center of wall piers at all levels. All elements were fixed at the base, except for the P-delta column, which was pinned at the base. Detailed examination of component modeling is documented in the following sections and a partial elevation view of 2D Opensees model is illustrated in Figure 4-29.

Although there were benefits in implementing the Opensees models, there were also important limitations with using 2D models. Specifically, the biaxial bending of wall elements

was not considered, and although slab-outrigger effects could have been considered for one direction, this was excluded to simplify the models. While implementing 3D Opensees models would have been preferable, currently, the most widely used shear wall models (namely, force-based beam column models, MVLEM models, and shear-flexure interaction MVLEM models) do not have biaxial bending capabilities. In the recent years, various researchers have been working on developing 3D shear wall models; this is further discussed in Chapter 6.9.

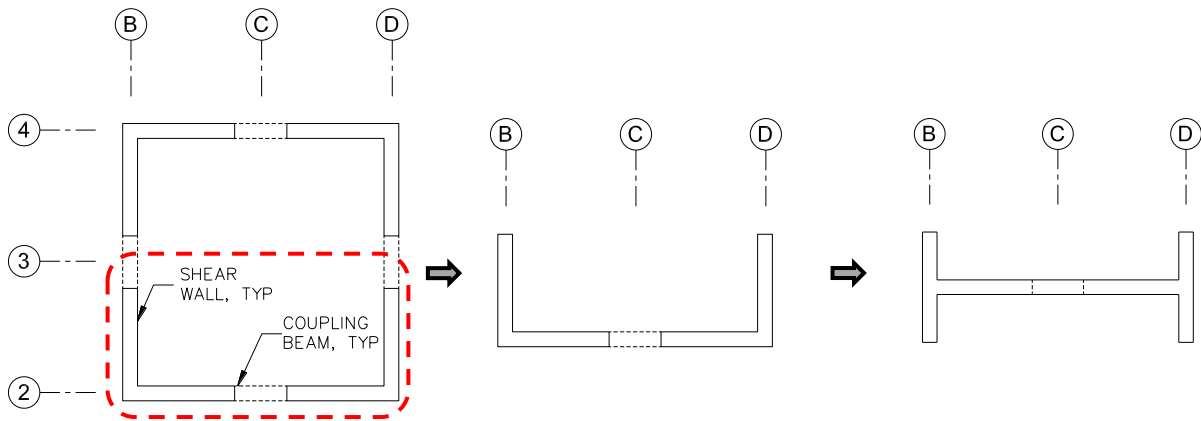


Figure 4-28. A 3-Dimensional reinforced concrete core wall system to an idealized 2-dimensional Opensees model using centerline modeling

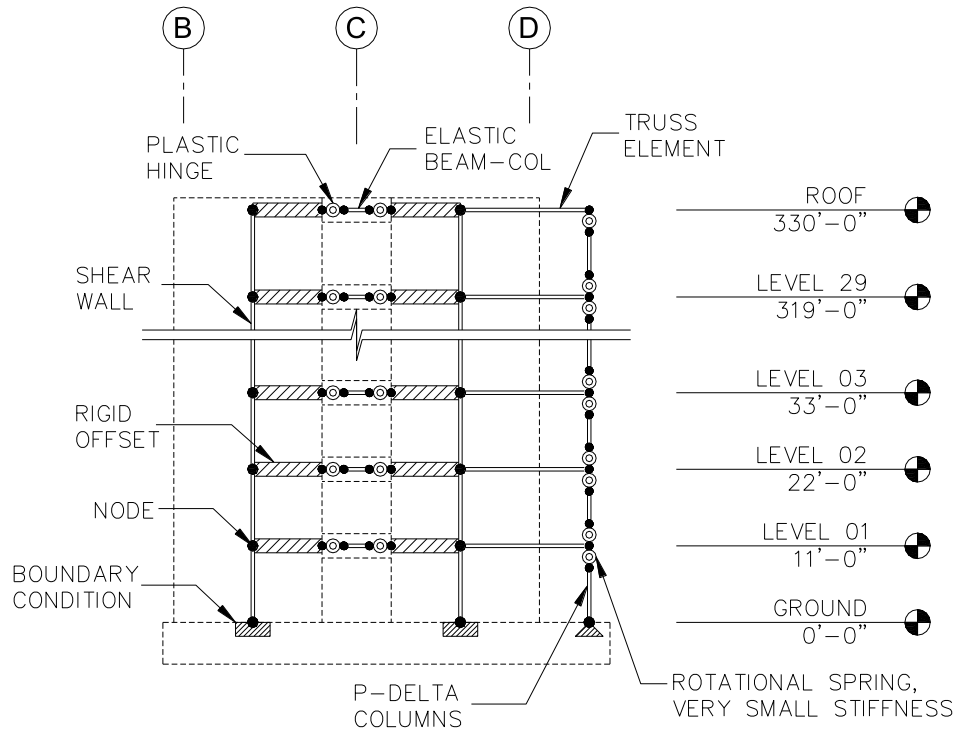


Figure 4-29. Partial elevation view of 2D 30-story Opensees model overlaid with a schematic drawing of shear walls and coupling beams. The plastic hinges and springs are zeroLength elements.

4.7.2. Inelastic Properties of Shear Wall Elements

All shear walls were modeled using MVLE approach described by Orakcal et al (2004) and implemented by Kolozvari et al (2015a, 2015b). MVLEM is a two-dimensional model where inelastic flexural and axial responses are simulated by a series of uniaxial elements connected to infinitely rigid beams at the top and the bottom. The elastic shear response is captured by a horizontal spring located at a distance ch from the element base (refer to Figure 4-30) and the shear response is uncoupled from flexural and axial responses. The wall rotations are concentrated at the center of rotation, at height ch above the wall base, assuming a uniform distribution of wall curvature over the height of each element. A value of $c=0.4$ was used based

on recommendations by Vulcano et al (1988). Wall piers were modeled with one element per story and eight uniaxial elements per element.

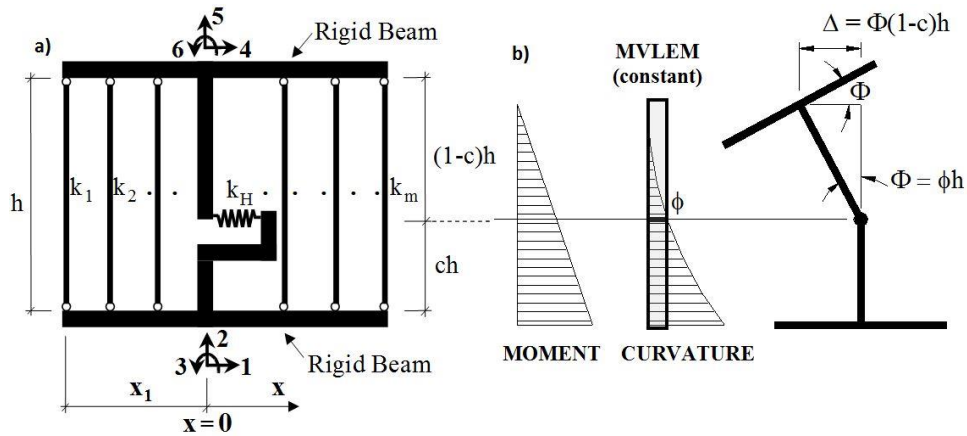


Figure 4-30. (a) MVLEM element (b) MVLEM rotations and displacements (Orakcal et al., 2004)

4.7.3. Inelastic Properties of Coupling Beams

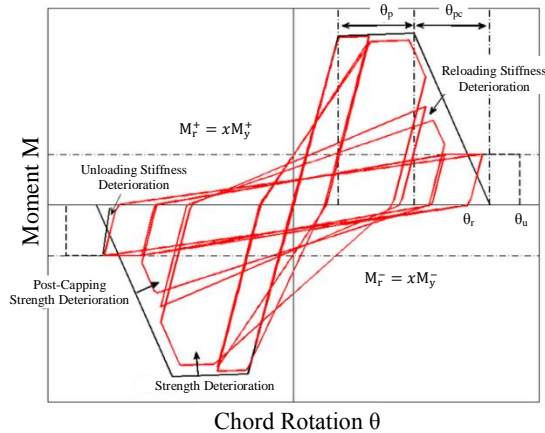


Figure 4-31. Basic parameters of the modified Ibarra-Medina-Krawinkler deterioration model with Peak-Oriented hysteretic response, Lignos and Krawinkler (2012)

Coupling beams were modeled using a linear elastic model along the beam length, compounded with zero-length inelastic springs at beam ends. Linear elastic beams were modeled with “elasticBeamColumn” elements by defining the beams’ cross-sectional area, Young’s Modulus,

and moment of inertia. A cracked section was utilized by assigning a factor of 0.20 to the concrete gross section moment of inertia. Zero-length plastic hinges were modeled using “ModIMKPeakOriented” materials developed by Lignos and Krawinkler (2012), which is based on calibration with test data from 200 experiments on reinforced concrete beams; the tri-linear backbone curve is described by seven main parameters for both positive and negative loading directions, namely, elastic stiffness (K_0), strain hardening ratio, effective yield strength (M_y), pre-capping rotation (θ_p), post-capping rotation (θ_{pc}), residual strength (M_{yres}), and deterioration parameter (Figure 4-31). To connect coupling beams to the wall elements, “elasticBeamColumn” elements were modeled with rigid flexural and axial properties (from the edge of the wall to the centerline of the vertical element).

4.7.4. Concrete Constitutive Model

For unconfined and confined concrete, a uniaxial hysteretic constitutive model developed by Chang and Mander (1994) was used. This material is called “ConcreteCM,” and it simulates hysteretic behavior of unconfined and confined concrete in cyclic compression and tension as shown on Figure 4-32 (Orakcal and Wallace, 2006).

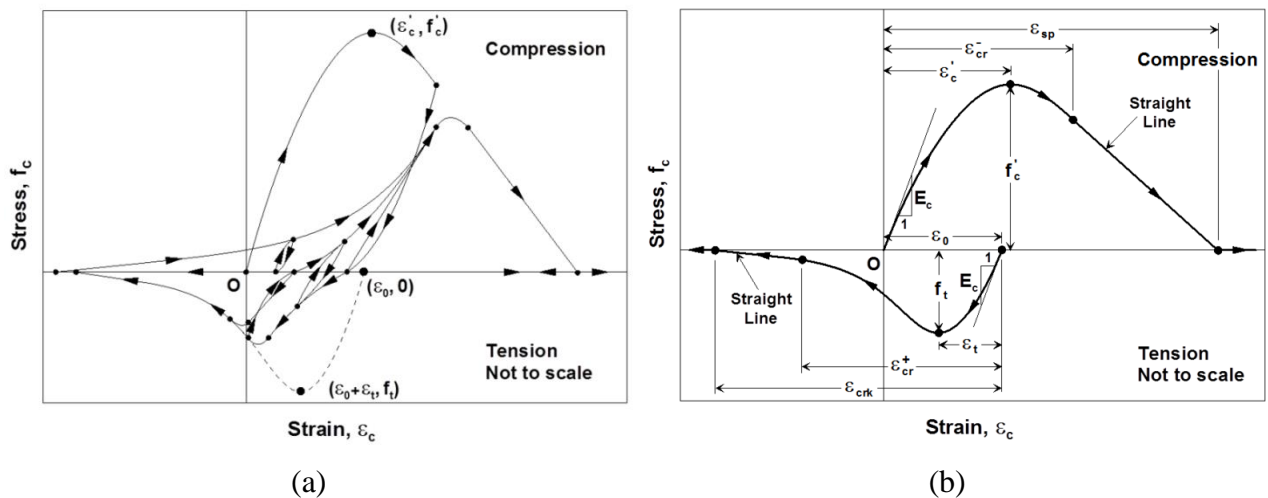


Figure 4-32. Concrete constitutive model by Chang and Mander (1994) (a) hysteretic constitutive model and (b) compression and tension envelop curves

4.7.5. Reinforcing Steel Constitutive Model

For reinforcing steel, a uniaxial nonlinear hysteretic material model, “SteelMPF,” developed by Menegotto and Pinto (1973) and extended by Filippou et al. (1993) to include isotropic strain hardening effects, was used. The implementation by Kolozvari et al (2015) was used, as it corrected several errors in the original coding.

4.7.6. Damping

The damping characteristics of the building were modeled using mass and stiffness proportional Rayleigh damping. Rayleigh damping coefficients were assigned so that 2.5% damping was achieved at first and third modes of vibration.

4.7.7. Solution Strategy

Static gravity analysis was first conducted and the gravity loads were held constant throughout nonlinear dynamic analysis. For each ground motion, a nonlinear solution was initially attempted using Newton algorithm with an analysis step (dt) of 0.04 seconds, and the global convergence was tested using Energy Increment with a tolerance of $1e-6$. If convergence was not achieved during a time step, the solution algorithm, analysis time step, and global convergence test parameters were subsequently changed until convergence was achieved. The following solution strategy, as shown on Table 4-14, was used for each non-converged time step. Once convergence was achieved, the solution strategy returned to step 1. Although there are various solution algorithms and convergence tests available in Opensees, the most effective solution algorithms and convergence tests were selected to reduce the computational time. The

most effective solutions were chosen after testing an exhaustive list of algorithms for convergence (counted when the full length of the earthquake record was successfully analyzed) over a large number of trial runs.

Table 4-14. Opensees dynamic analysis solution strategy

Step	Solution algorithm	Analysis step	Convergence test	Convergence tolerance
1	(a) Newton	dt	Energy Increment	1e-6
	(b) Newton with Initial Tangent	dt	Energy Increment	1e-6
	(c) Modified Newton	dt	Energy Increment	1e-6
	(d) Modified LineSearch	dt	Energy Increment	1e-6
	(e) Krylov Newton	dt	Energy Increment	1e-6
2	(a) through (e)	dt/2	Energy Increment	1e-2
3	(a) through (e)	dt/4	Energy Increment	1e-2
4	(a) through (e)	dt/8	Energy Increment	1e-2
5	(a) through (e)	dt/16	Energy Increment	1e-2
6	(a) through (e)	dt/32	Energy Increment	1e-2
7	(a) through (e)	dt/64	Energy Increment	1e-2
8	(a) through (e)	dt/64	Norm Displacement Inc.	1e-2

4.8. Conclusions

Nonlinear models were created for the 20 and 30-story prototype buildings. For the 30-story building, both 3D and 2D models were built using CSI Perform 3D and Opensees, respectively.

For the 20-story building, a 2D model was built using Opensees.

4.9. Limitations and Future Work

Limitations and future work are listed as follows.

1. In this study, only the tower portions of tall buildings were analyzed as part of the two-stage design and soil-structure interaction (SSI) effects were ignored. It would be helpful to model the basement and include the SSI effects in the future. This is further discussed in Chapter 5.
2. Shear-flexure interaction was not modeled for nonlinear modeling of structural walls. To capture accurate responses of structural walls, it will be essential to model the coupled effects of shear and axial/flexure responses in the future. Currently, shear-flexure interaction models are not available in Perform 3D, and in Opensees, there were challenges and convergence issues in implementing shear-flexure interaction models (“SFI_MVLEM”) for tall buildings. However, researchers are working on the SFI_MVLEM model to improve convergence and to extend applications to tall buildings for future studies.
3. It is important to note that this study was conducted with 20 and 30-story reinforced-concrete core wall building designs that were symmetric in geometry and did not require additional lateral systems to augment the core walls. For future work, it would be important to include various types of reinforced-concrete tall buildings, with irregular vertical and horizontal geometries and taller heights up to 70 stories that will require additional lateral systems around the perimeter of the building.

CHAPTER 5. UNCERTAINTIES CONSIDERED AND SELECTION OF RANDOM VARIABLES

This chapter summarizes all input uncertainties considered to quantify dispersion in various structural responses (referred to as engineering demand parameters, EDPs).

5.1. Introduction

Dispersion in tall building EDPs under nonlinear response history analyses are known to result from three major uncertainties, namely, (1) record-to-record (RTR) variability, (2) modeling and model parameter uncertainties, and (3) design uncertainties (FEMA P695, 2009). Record-to-record variability refers to uncertainty in structural responses resulting from selected and modified ground motion properties. Modeling uncertainties refer to the various selections of component models that may affect EDPs; for example, whether the shear walls were modeled using fiber elements or MVLEM elements can result in differences in EDPs. Model parameter uncertainties refer to a range of accepted values for force-deformation and other parameters used for modeling structural materials, components, and systems. Design uncertainties come from designer preferences, e.g., conservatism or conventions used for proportioning and detailing that lead to variations in member strengths and deformation capacities. To represent the RTR variability, model parameter and design uncertainties, eleven input random variables were selected, and statistical parameters such as mean, coefficient of variation (COV), and probability distribution were established for the selected random variables.

First, background is provided on different types of uncertainties, sources of uncertainties, and random variables, and then all input random variables are explained in detail.

5.2. Types of Uncertainties

Formally, all uncertainties can be categorized as aleatory or epistemic. Aleatory uncertainty refers to a phenomenon that is intrinsically random in nature. For example, the rate of earthquakes is an aleatory uncertainty because the rate of occurrence varies over time. In contrast, epistemic uncertainty arises from a lack of knowledge or limitations in data measurement. Thus, epistemic uncertainties can be reduced by further research or by gaining a better understanding of the issue. Following these definitions, record-to-record variability is defined as an aleatory uncertainty, and model parameter and design uncertainties, as well as uncertainties in shear capacity (Chapter 7) are defined as epistemic uncertainties.

5.3. Sources of Uncertainty

In Quantification of Building Seismic Performance Factors (FEMA P695, 2009), sources of uncertainties were categorized and quantified based on available research and case studies of example buildings. Although FEMA P695 was written in context of collapse assessment, the same uncertainties apply to component reliability assessment. The following sources of uncertainties were documented:

- Record-to-Record Uncertainty (RTR): Variability in RTR is defined as the combined effects of variations in frequency content and characteristics of various records, and variability in hazard characterization as reflected in the Far-Field ground motion record set. The dispersion measured in logarithmic standard deviation typically ranges from 0.35 to 0.45. A typical value of 0.40 is used in evaluation of structures with significant period elongation. A minimum value of 0.20 is recommended for RTR variability. These values were relatively consistent among studies conducted by various researchers (Haselton et al, 2007; Ibarra and Krawinkler, 2005a and 2005b; Zareian, 2006).

- **Modeling Uncertainty:** Modeling uncertainty describes the full range of structural responses associated with variations in computational models. It reflects how well the computational model captures structural behaviors.
- **Design Requirements Uncertainty:** Design requirements represent how complete and robust the design is, compared to the design requirements.
- **Test Data Uncertainty:** Test data uncertainty refers to the quality of experimental test data used to define the modeling parameters.

Furthermore, Haselton et al (2007) have examined collapse probabilities (as a function of intensity measure) for 4-story reinforced-concrete frame structures that were designed in compliance to 2003 International Building Code. To represent the likely variations in design, eight different design variations (labeled A through H in Table 5-1) were considered. Some of these variations include beam design strength factors, ratio of positive to negative beam flexural capacity, and slab steel. The uncertainties in collapse capacity estimates, including uncertainties from record-to-record variability and structural modeling uncertainties, are summarized as logarithmic standard deviations in Table 5-1.

Table 5-1. Uncertainties in collapse capacity estimates (Haselton et al, 2007)

Design	Median ($S_{a,col}$) [g]	Record-to- record-variability $\sigma_{LN,RTR}(S_{a,col})$	Modeling uncertainty $\sigma_{LN,model}(S_{a,col})$	Total uncertainty $\sigma_{LN,Total}(S_{a,col})$
A	2.19	0.36	0.45	0.58
B	2.08	0.31	0.35	0.47
C	2.35	0.46	0.45	0.64
D	0.95	0.39	0.35	0.52
E	1.95	0.32	0.35	0.47
F	1.86	0.38	0.35	0.52
G	1.88	0.34	0.35	0.49
H	1.92	0.30	0.35	0.46

In this study, dispersion in EDPs due to RTR variability, model parameter uncertainties, and design uncertainties were measured in Chapter 6, and test data uncertainties were quantified for shear-controlled walls in Chapter 7.

5.4. Random Variables

Statistical analysis with random variables involves random sampling to simulate a large number of experiments and to evaluate results. This means each random variable X_i is randomly sampled to give a sample value, x_i . When the range of a random variable is restricted to a countable number, the random variable is called discrete and its probability distribution is presented in the form of a probability mass function (PMF):

$$p_X(x) = P[X = x]$$

where p_X is the probability mass function and P represents probability. Another way to describe the probability distribution of a random variable is through a cumulative distribution function (CDF). The CDF is defined as the probability of the event that the random variable takes on is equal to or less than the argument, $F_X(x) = P[X \leq x]$, also noted as:

$$F_X(x) = \int_{-\infty}^x f_X(u) du$$

where F_X is the cumulative distribution function. The variable u is used as a dummy variable of integration to avoid confusion with the limit integration of x . When a random variable is free to take on any value on the real axis, the random variable is called continuous, and its probability distribution is presented in the form of a probability density function (PDF), where

$$f_X(x) \geq 0$$

$$\int_{-\infty}^{\infty} f_X(x) dx = 1$$

The probability density function is the first derivative of the cumulative distribution function, where

$$f_X(x) = \frac{d}{dx}F_X(x)$$

The probability distributions of random variables used in this study follow uniform, normal, lognormal, and gamma distributions and they are briefly described in the following sections.

5.4.1. Uniform Random Variable

If a random variable X is equally likely to take on any value in the interval a to b , its probability mass function (PMF) is constant over that range, where

$$f_X(x) = \begin{cases} \frac{1}{b-a}, & a \leq x \leq b \\ \text{elsewhere,} & 0 \end{cases}$$

and this is shown graphically on Figure 5-1. The cumulative distribution function (CDF) of the uniform variable is triangular, where

$$F_X(x) = \begin{cases} 0, & x < a \\ x, & a \leq x \leq b \\ b, & x > b \end{cases}$$

The mean and variance are represented as

$$m_X = a + \frac{b-a}{2}$$

$$\sigma_X^2 = \frac{(b-a)^2}{12}$$

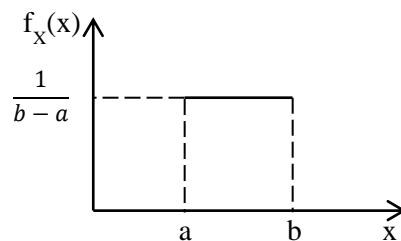


Figure 5-1. Probability mass function for a random variable X

5.4.2. Normal Random Variable

A probability distribution function (PDF) for a normal random variable X is:

$$f_X(x) = \frac{1}{\sigma_X \sqrt{2\pi}} \exp \left[-\frac{1}{2} \left(\frac{x - \mu_X}{\sigma_X} \right)^2 \right]$$

where μ_X and σ_X are the mean and standard deviation, respectively. Figure 5-2 shows the general shapes of PDF and CDF of a normal random variable. Although there is no closed-form solution for the CDF of a normal random variable, CDF tables are available for a special case where $\mu_X = 0$ and $\sigma_X = 1$. In this case, the PDF for a standard normal variable z is denoted by $\phi(z)$ and the CDF for a standard normal variable z is denoted as $\Phi(z)$ where

$$\phi(z) = \frac{1}{\sigma_X \sqrt{2\pi}} \exp \left[-\frac{1}{2} \left(\frac{x - \mu_X}{\sigma_X} \right)^2 \right]$$

$$\Phi(z) = 1 - \Phi(-z)$$

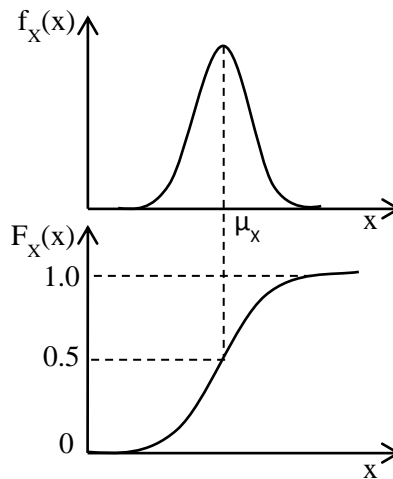


Figure 5-2. PDF and CDF of a normal random variable, X

5.4.3. Lognormal Random Variable

A random variable X is a lognormal random variable if $Y = \ln(X)$ follows a normal distribution.

A lognormal random variable is defined for positive values only, and Figure 5-3 shows the general shape for the PDF of a lognormal variable. A lognormal variable X has the following properties:

$$\mu_Y = \mu_{\ln(X)} = \ln(\mu_X) - \frac{1}{2} \sigma_{\ln(X)}^2$$

$$\sigma_Y = \sigma_{\ln(X)} = \ln(V_X^2 + 1)$$

where if V_X is less than 0.2, then $\sigma_{\ln(X)}^2 \approx V_X^2$ and $\mu_{\ln(X)} \approx \ln(\mu_X)$.

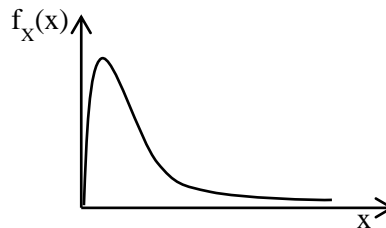


Figure 5-3. PDF of a lognormal random variable

5.4.4. Gamma Random Variable

The PDF of a gamma random variable is typically used for modeling sustained live load in buildings. The PDF of a gamma random variable is defined by

$$f_X(x) = \frac{\lambda(\lambda x)^{k-1} e^{-\lambda x}}{\Gamma(k)} \text{ for } x \geq 0$$

where $\Gamma(k) = \int_0^{\infty} e^{-u} \cdot u^{k-1} du$ and k and λ are shape and scale parameters, respectively.

Figure 5-4 shows various PDFs using different shape parameters. For the gamma distribution,

the mean can be calculated as $\mu_X = \frac{k}{\lambda}$ and the variance can be calculated as $\sigma_X^2 = \frac{k}{\lambda^2}$.

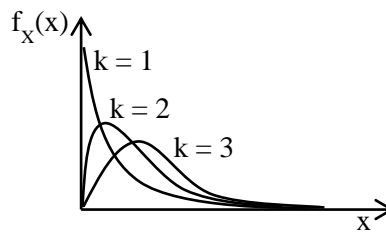


Figure 5-4. PDFs of gamma random variables

5.5. Selection of Random Variables

Although numerous random variables can be selected for tall buildings, only the most relevant ones were chosen to study propagation of uncertainties to dispersion in EDPs. Specifically, the uncertainties in ground motions, material strengths, shear modulus, coupling beam strengths, mass, loads, damping, and shear wall boundary element designs were considered. Detailed descriptions of each random variable are provided in the following subsections and Table 5-2 provides a summary of statistical parameters and probability distributions. Schematic representations of the probabilistic models are presented in Figure 5-5.

Table 5-2. A summary of input random variables

Demand Random Variables	Mean	COV, ρ_D	Distribution	Reference
1. Record-to-record variability				
15 or 30 Scaled ground motions	-	-	Uniform	This study
2a. Uncertainties in model parameters - element level				
Unconfined concrete compressive strength, f'_c	1.09·(8ksi)	0.09	Normal	Nowak et al. (2008)
Confined concrete compressive strength, f'_c	1.34·(1.09·8ksi)	0.09	Normal	Nowak et al. (2008)
Reinforcing steel yield strength, f_y	1.16·(60ksi)	0.04	Normal	Bournonville et al. (2004)
Shear Modulus, G	0.2·(E_c)	0.30	Normal	This study
Coupling beam strength, V_y	1.29·(V_y)	0.12	Normal	Naish et al. (2013a, b)
2b. Uncertainties in model parameters - system level				
Mass	1.0·(Mass)	0.10	Normal	Ellingwood et al. (1980)
Dead Load (axial load on walls & CB)	1.0·(DL)	0.10	Normal	Ellingwood et al. (1980)
Live Load (axial load on wall & CB)	0.25·(LL)	0.55	Gamma	Corotis and Doshi (1977)
Damping	0.025	0.30	Normal	Porter et al. (2002)
3. Uncertainties in design				
Shear wall boundary element design, r_{yb}	1.05	0.03	Normal	This study

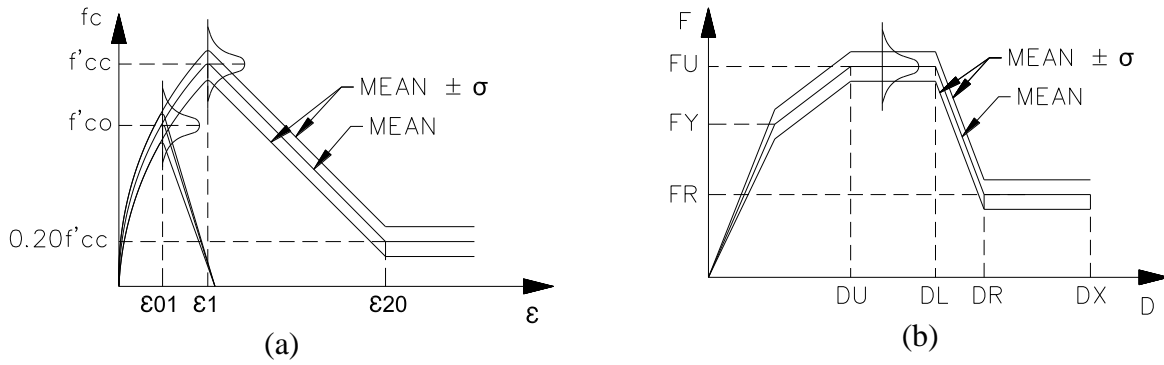


Figure 5-5. Probabilistic models for (a) confined and unconfined concrete compressive strengths and (b) diagonally reinforced concrete coupling beam strengths

5.6. RTR Variability

To measure the effects of RTR variability on dispersion of EDPs, ground motions from Suites A through D were utilized. Suites A and B were used for 3D nonlinear response history analyses, and Suites C and D were used for the 2D nonlinear response history analyses. All ground motions were selected randomly per a uniform distribution.

5.7. Model Parameter Uncertainties

5.7.1. Concrete Compressive Strengths

The test data for concrete compressive strength were obtained from Nowak et al (2008), which provide an extensive database for ordinary and high-strength ready mix and plant-cast concrete compressive strengths. For 8,000 psi concrete, statistical parameters were calculated from 753 samples, and mean value of 8,740 psi and coefficient of variation of 0.09 were calculated. As shown on Figure 5-6, although the upper 50% of the cumulative distribution function curve falls below the normal distribution test for 8,000 psi concrete, most of high strength concrete data were well represented with normal distribution. Thus, normal distribution was chosen. Since Young's modulus is a function of concrete compressive strength, stiffness was varied accordingly.

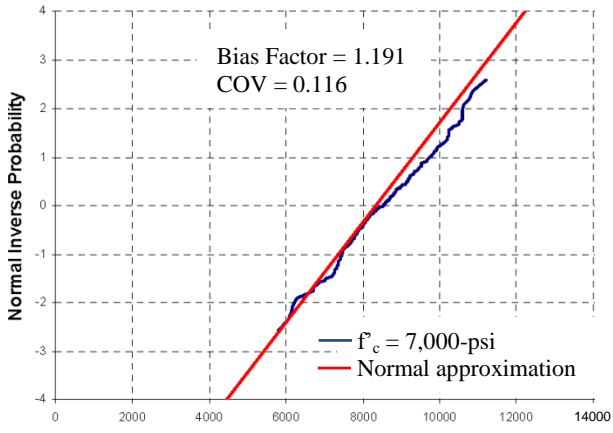
$$E_c = 40,000\sqrt{f'_c} + 1 \cdot 10^6 \text{ for } f'_c > 6000 \text{ psi}$$

The statistical parameters for high strength concrete are summarized in Table 5-3. The mean bias factor for high strength concrete between 7,000 psi $\leq f'_c \leq$ 12,000 psi is 1.12; thus, the current expected strength factor of $1.3 \cdot f'_c$ from ASCE41 and LATBSDC appears to be too high for high-strength concrete.

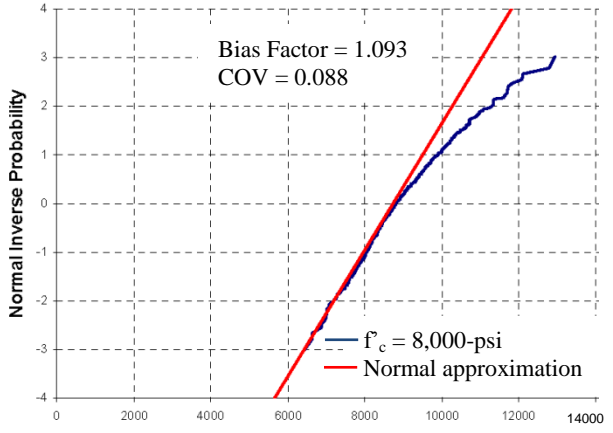
The actual concrete strength in the structure can vary from project to project; however, these variances are included in the fabrication and professional factors per Nowak et al (2008). Moreover, this data on concrete strength was obtained from many different sources (different concrete mix plants and construction sites), thus, it includes the batch-to-batch variation that is higher than within-test variation. Lastly, it also includes variation caused by different testing methods, different mix, and different ingredients.

Table 5-3. Statistical parameters for compressive strengths of high strength concrete
(Nowak et al, 2008)

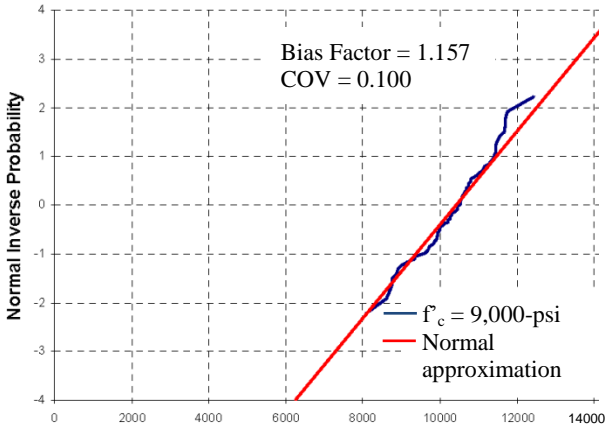
f'_c	Number of samples	Compressive strength at 28 days		
		Mean f'_c	Bias factor	COV
7,000 psi	210	8,430 psi	1.191	0.116
8,000 psi	753	8,740 psi	1.093	0.088
9,000 psi	73	10,410 psi	1.157	0.100
10,000 psi	635	11,280 psi	1.128	0.115
12,000 psi	381	12,440 psi	1.037	0.109
		Mean =	1.121	0.106



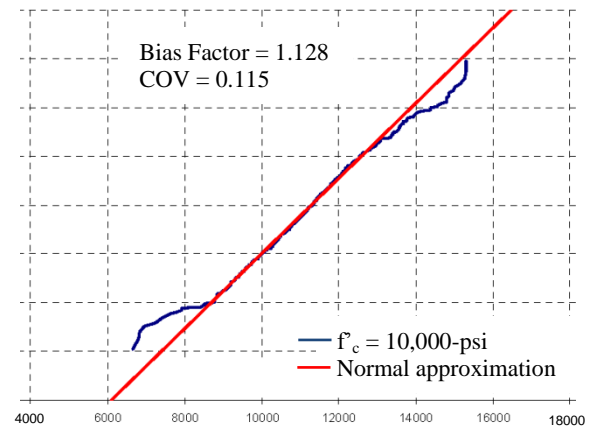
(a)



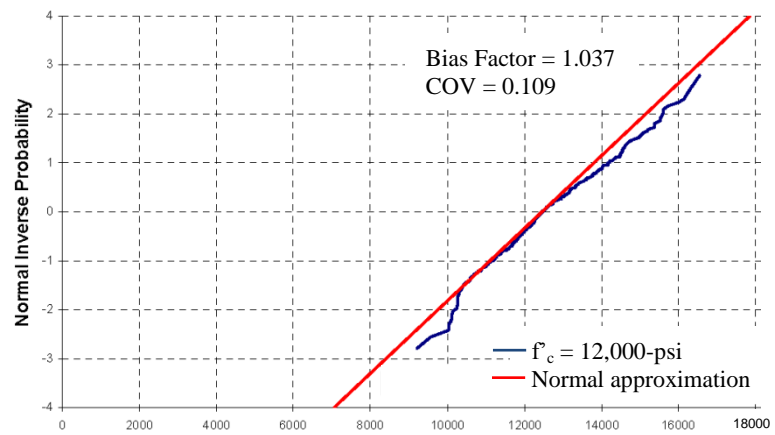
(b)



(c)



(d)



(e)

Figure 5-6. CDF for high strength concrete (a) $f_c = 7,000$ psi, (b) $f_c = 8,000$ psi, (c) $f_c = 9,000$ psi, (d) $f_c = 10,000$ psi, and (e) $f_c = 12,000$ psi (Nowak et al, 2008)

5.7.2. Reinforcing Steel Yield Strengths

Variations in reinforcing yield strength were examined from Bournonville et al (2004), where 3947 reinforcing bars from 13 sources were analyzed. For A706 Grade 60 reinforcing steel, average yield strength for all reinforcement sizes was 69.1 ksi, and coefficient of variation varied between 0.036 and 0.061, as shown on Table 5-4. A #11 reinforcement was chosen as a representative longitudinal reinforcement for shear wall boundary element designs and the corresponding mean of 70.0 ksi and coefficient of variation of 0.04 was used. The distribution for A706 Grade 60 reinforcing steel was tested to be well represented by either normal or beta distribution. A normal distribution was selected due to its versatility and ease of use.

Table 5-4. Statistical parameters for yield and tensile strengths of A706 Grade 60 reinforcement (Bournonville et al, 2004)

A706 Grade 60	Bar Size #11		All Bar Sizes	
	Yield	Tensile	Yield	Tensile
Mean (psi)	69,521	96,161	69,144	95,197
Median (psi)	69,000	95,500	69,000	95,000
Minimum (psi)	63,500	86,300	60,000	80,000
Maximum (psi)	78,000	107,000	85,400	116,000
Std. dev. (psi)	2,984	3,725	3,678	4,925
C.O.V.	0.0429	0.0387	0.0532	0.0517
5% Fractile	65,000	91,440	63,500	87,000
Kurtosis	-0.055	0.637	-0.276	0.211
Skewness	0.356	0.677	0.255	0.137
No. of heats	115	115	1,568	1,568

5.7.3. Coupling Beam Strengths

The mean and coefficient of variation for diagonally reinforced concrete beam strengths were calculated from test results attained from the University of California, Los Angeles (Naish et al, 2013a) where seven coupling beam designs were tested using various diagonal and transverse reinforcement configurations. The test data for coupling beams are not as widely available as those for columns or shear walls, and among the available tests, majority were performed at low aspect ratios (clear span to height ratio of 2.0 or less) with detailing that did not conform to modern construction standards per ACI 318-99, or later versions. Thus, all coupling beam test data were attained from Naish et al (2013a). The test specimens were constructed at half-scale, with an aspect ratio of 2.4 or 3.33, and had reinforced concrete slab, post-tensioned concrete slab, or no slab. As shown on Table 5-5, the mean ratio between the shear strength achieved in tests versus shear strength calculated from ACI318-11 (Chapter 2.4.3) was 1.29 and coefficient of variation was $\delta_1=0.116$. Due to a small sample size, uncertainty from sampling error was found to be $\delta_2 = \frac{\delta_1}{\sqrt{n}} = \frac{0.12}{\sqrt{7}} = 0.044$ and the total coefficient of variation was calculated as $\delta = \sqrt{\delta_1^2 + \delta_2^2} = \sqrt{0.116^2 + 0.044^2} = 0.12$. Due to a small sample size, an accurate probability distribution was difficult to fit, thus, a normal distribution was assumed.

Table 5-5. Summary of reinforced concrete beam test results (Naish et al, 2013a)

No.	Specimen Name	V_n (ACI) kips	$V_{\max, \text{test}}$ (kips)	$V_{\max, \text{test}}/V_n$
1	CB24F	136.3	171.0	1.255
2	CB24D	136.3	159.2	1.168
3	CB24F-RC	136.3	190.8	1.400
4	CB24F-PT	136.3	211.8	1.554
5	CB24F-1/2-PT	136.3	189.6	1.391
6	CB33F	107.8	124.0	1.150
7	CB33D	107.8	120.6	1.119
			Mean =	1.291

5.7.4. Mass and Dead Loads

Measurement in variability of mass and dead loads were referenced from Ellingwood et al (1980). The variability in mass and dead loads depends on many factors, including as-built members deviating from construction documents (also known as geometric variations), extra weight being added during the service life of the building, and difficulty in obtaining accurate unit weights of construction materials. Ellingwood summarizes the consensus obtained from several researchers in that the mass and dead loads were best described by a normal distribution, a mean of 1.0 was appropriate to account for total loads, and a typical coefficient of variation of 0.10 was recommended.

5.7.5. Live Loads

Determining an accurate representation of live load criteria is difficult due to its intrinsically variable nature. Thus, surveyed live loads from Corotis and Doshi (1977) were assessed for a realistic estimation. A comprehensive discussion on what types of buildings and the number of rooms surveyed is detailed in this study. For office spaces, live loads were surveyed from 580 rooms. A mean of 12.56 psf and coefficient of variation of 0.55 were calculated and a gamma distribution was fitted to the data by the method of moments. Since ASCE7-10 recommends 50 psf live load for offices, this mean is represented as 0.25·50 psf.

5.7.6. Damping

Experimental data on viscous damping were referenced from Porter et al (2002). Porter documents the estimates of viscous damping mean and coefficient of variation from three different studies. Upon examining the experimental data, Porter suggests that an appropriate coefficient of variation to be in the order of 0.3 to 0.4. For the mean and distribution, assumptions had to be made due to a small number of data available for reinforced concrete shear wall buildings. In this study, a mean of 2.5%, coefficient of variation of 0.30, and a normal distribution were assumed.

5.7.7. Shear Modulus

Per LATBSDC (2014) recommendations, a mean effective shear modulus of $G_{\text{eff}} = 0.2E_c \cdot A$ (refer to Chapter 4.5.3) was used. A coefficient of variation of 0.3 was chosen so that 96% of the effective shear modulus values are between $0.08E_c \cdot A$ and $0.32E_c \cdot A$.

Recent studies by Kolozvari and Wallace (2016) showed that using uncoupled shear wall models (nonlinear beam-column models) with an effective shear modulus of $0.2E_c \cdot A$ resulted in reasonable estimates for some, but not all, global and local responses in comparison with predictions obtained with coupled models (shear interaction model, as known as SFI-MVLEM, which captures interaction among axial/flexural and shear responses). For example, the use of $0.2E_c \cdot A$ in the uncoupled models provided a reasonable estimate of roof displacement responses, whereas $0.1E_c \cdot A$ provided a better estimate of shear force demands in plastic hinge regions. The sensitivity studies revealed that both global and local responses are considerably sensitive to the respective element models used for shear wall modeling, as well as the selection of effective shear modulus. Thus, a mean of $0.2E_c \cdot A$, with a coefficient of variation of 0.3, was used to consider a range of values for effective shear modulus, and a normal distribution was assumed.

5.8. Design Uncertainties

5.8.1. Shear Wall Boundary Element Design

Since the effort required to collect and examine variations in shear wall design data, e.g, from engineering firms, is prohibitive, practical assumptions were made. The mean, coefficient of variation, and distribution of shear wall design was made through variations in boundary element longitudinal reinforcing steel; mean of 1.03, coefficient of variation of 0.03 and a normal distribution was assumed. A mean of 1.03 was chosen because for either prescriptive-design or performance-based design, overdesign is discouraged because additional flexural strength is a potential source for increased shear and foundation demands and added cost. The coefficient of variation of 0.03 assumes that approximately 96% of designers will design boundary element longitudinal reinforcing steel in shear walls with a demand to capacity ratio between 0.97 and 1.09.

5.9. Correlation

Another important issue to consider is correlation between random variables. Correlation coefficients between two random variables can range from -1 to 1, where 0 represents independent random variables and ± 1 represents perfect positive or negative correlation. In this study, binary cases were examined with and without correlation, and the effects in EDPs were compared. Three sets of correlation were considered from the following pairs of random variables:

1. Unconfined and confined concrete compressive strength and shear modulus: f'_c & G
2. Reinforcing steel yield strength and coupling beam strength: f_y and V_y
3. Mass and dead load

Since perfect correlation would tend to produce more extreme EDPs, perfect positive correlations were assumed for all correlated random variables.

5.10. Uncertainties Not Considered

There are other important uncertainties that were not assessed in this study. Some of these include modeling uncertainties, variations in coupling beam stiffness factors, soil-structure interaction (SSI) effects, and human error. As potentially important as these are in affecting tall building structural responses, they are excluded from this study and are discussed in the following.

Modeling Uncertainties

Modeling uncertainties refer to different selection of component models that may affect EDPs; for example, whether the shear walls were modeled using fiber elements or MVLEM elements can result in differences in tall building EDPs. Although these differences in modeling were not examined as part of uncertainties that contribute to dispersion in tall building EDPs; binary cases of modeling uncertainties were examined and the results are documented in Appendix B. These include effects of shear wall element meshing and the use of Rayleigh damping versus modal damping.

Coupling Beam Stiffness Factors

For the MCE analysis, coupling beams flexural stiffness was defined as $0.2 EI_g$. This stiffness factor considers all deformations resulting from flexure, pullout, and shear. Although further experimental tests are needed to quantify the variations in this stiffness factor, it would be important to include coupling beam stiffness variations in the future. Lower stiffness factors will tend to delay the yielding of coupling beams, whereas higher factors will tend to yield coupling beams earlier. These differences in the onset of yielding will influence tall building responses

and it will be important to examine these variations. However, the impact on tall building EDP dispersion due to adding another model parameter random variable is assumed to be nominal.

Soil-Structure Interaction

Furthermore, uncertainties from SSI effects were not assessed. A recent case study by Naeim et al (2010) examined how modeling or omitting SSI effects, for a 54-story office building in Los Angeles, California, can impact structural responses. This study was performed by generating a three-dimensional, “most accurate” (MA) model in ETABS that accounts for SSI effects in the vertical and horizontal directions including rocking. The SSI effects were represented with a series of no tension springs and dampers reflecting site soil properties. The MA model was first calibrated to match the responses interpreted from the recorded ground motions, and then modifications were made with simplifications that were common in structural engineering practice. A few structural responses, namely, vibrational periods, story drifts, as well as maximum drifts, were compared and the errors were assessed. The MA model was compared with a modified model where the below ground portions of the building were ignored and the superstructure was fixed at the ground level (referred to as model “3D”). The comparisons showed that the first mode period was found to be 7% shorter for model 3D; the comparative results from the first five vibrational periods were shown on Table 5-6. Since the vibrational periods were altered, although peak roof displacements were similar in amplitude, they occurred at different times during the response. The error in peak roof displacement was reported to be less than 20%. The SSI effects on other important structural responses, such as shear demands, coupling beam deformations, or structural wall strains, were not examined.

Table 5-6. Summary of periods associated with first five Ritz vectors for “MA” and “3D” models (Naeim et al, 2010)

Model	Reported vibrations for first five Ritz vectors (sec)				
	1	2	3	4	5
“Most Accurate” (MA) Model with SSI effects	6.06	5.18	2.76	1.92	1.81
Modified model, “3D”	5.63	4.90	2.74	1.89	1.80

Since SSI effects have shown to influence tall building EDPs, it would be worthwhile to examine binary cases of structural models with and without SSI effects in the future. To include SSI effects as a random variable, statistical parameters of SSI effects should be quantified first from a large number of tall building studies.

Human Error

Another important uncertainty that was not assessed in this study was human error. A study by Melchers (1999) reviewed over 100 documented cases of structural failures before 1980 and summarized the primary causes of each failure, as shown on Table 5-7. Although not all failures were seismically induced, human error has been a primary contributor to recorded structural failures in the past. Unfortunately, because the understanding of human error is limited and much of that understanding is qualitative, the human error factor was excluded from this study. Nonetheless, it is an important factor that contributes to structural failures and may be considered in future work.

Table 5-7. Primary causes of structural failures, Melchers (1999)

Cause of structural failures	%
Inadequate appreciation of loading conditions or structural behavior	43
Inadequate execution of erection procedure	13
Random variations in loading, structure, materials, workmanship, etc	10
Contravention of requirements in contract documents or instructions	9
Mistakes in drawings or calculations	7
Unforeseeable misuse, abuse, and/or sabotage, catastrophe, deterioration	7
Inadequate information in contract documents or instructions	4
Others	7

CHAPTER 6. QUANTIFICATION OF DISPERSION IN ENGINEERING DEMAND PARAMETERS USING MONTE CARLO SIMULATIONS

This chapter presents (1) methodology used to quantify dispersion in selected engineering demand parameters (EDPs) and (2) findings on tall building EDP dispersions and means.

6.1. Methodology

To understand propagation of major uncertainties and to measure dispersion in tall building EDPs, Monte Carlo simulation techniques were used to perform nonlinear response history analyses on 20 and 30-story buildings. Monte Carlo simulation technique involves running a large number of random experiments to observe impacts. The basic concepts behind Monte Carlo simulations were described in the two flowcharts shown in Figure 6-1 and Figure 6-2.

Figure 6-1 shows Monte Carlo techniques used to perform nonlinear analysis in Perform 3D. The process starts with generating values for selected random variables and assigning these values and deterministic parameters to structural materials, components, and elements. Once the components and elements were defined, a nonlinear model was built. The loads were assigned once random values were generated for mass and vertical static loads and ground motions were randomly selected for applicable hazard levels. Subsequently, a random value for damping was selected and assigned to the structural system. Once the structural model was complete, nonlinear response history analyses were performed at all five hazard levels and selected engineering demand parameters (EDP) were examined. This procedure was repeated for 1000 simulations, and the required number of simulations was chosen so that the variation in the EDP dispersion measure was less than 0.10. The number of required simulations and variations in the EDP dispersion measure are further explained in later sections.

In contrast, Figure 6-2 shows Monte Carlo techniques used to conduct nonlinear analysis in Opensees. The process is similar to the one used for Perform 3D with the exception that all random variables were generated in Matlab (2016) and stored prior to nonlinear model generations to automate the Monte Carlo simulations. The total number of Monte Carlo simulations performed is summarized in Table 6-1.

Table 6-1. Total number of Monte Carlo simulations

Analysis Type		Perform 3D	Opensees	
Analysis Model		30-Story	20-Story	30-Story
No. of Simulations	Suite A	1000 x 5 hazards	-	-
	Suite B	1000 x 2 hazards	-	-
	Suite C	-	1000 x 1 hazard x 2 RV	-
	Suite D	-	-	1000 x 1 hazard x 2 RV
	Total	7000	2000	2000

Once Monte Carlo simulations were completed, probabilistic models were established for five selected EDPs. Shear demand was selected as a main EDP of interest, roof drift was selected as a global EDP, and coupling beam rotations as well as tensile and compressive axial strains in the shear wall boundary elements were selected as local EDPs.

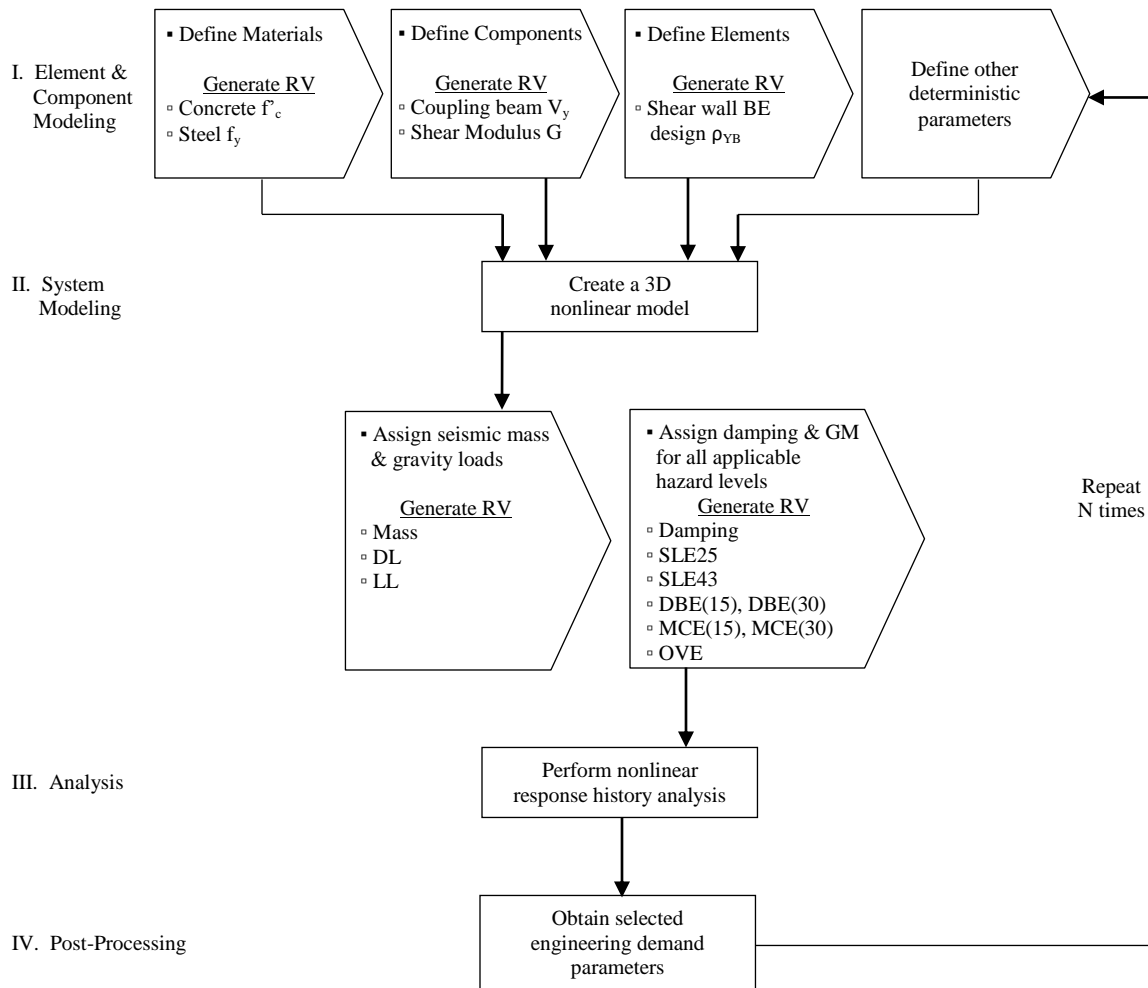


Figure 6-1. Flowchart of Monte Carlo simulations procedure, Perform 3D analysis

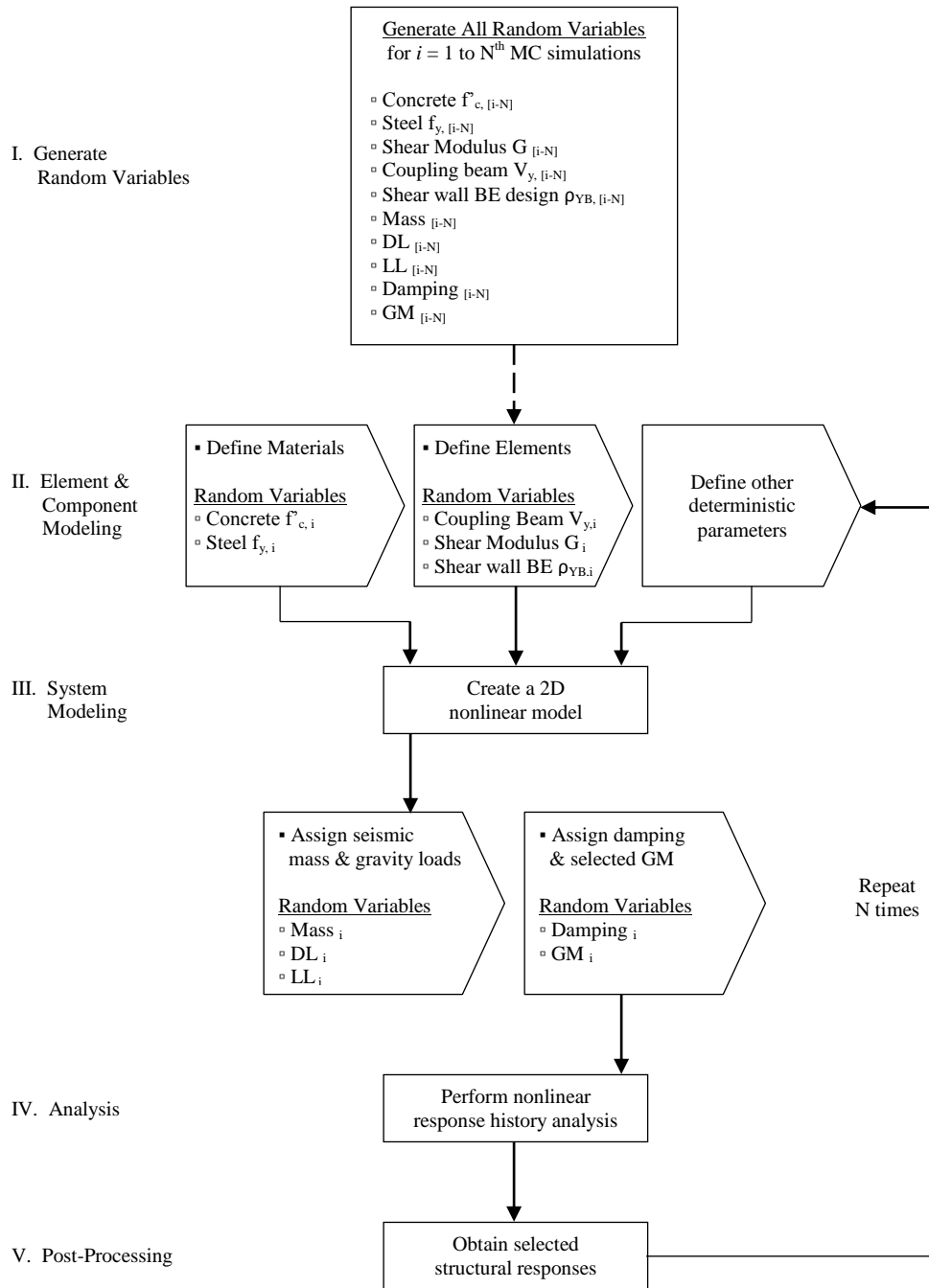


Figure 6-2. Flowchart of Monte Carlo simulations procedure, Opensees 2D analysis

6.2. Random Number Generation

Using the mean, coefficient of variation, and probability distribution information established in Chapter 5, random numbers for uniformly distributed random variables were generated in Matlab (2016) using Multiplicative Congruential Algorithm (Lehmer, 1951). This algorithm generates random numbers based on three integer parameters, a , c , and m , and an initial seed value, x_0 as

$$x_{k+1} = a \cdot x_k + c \pmod{m}$$

where the operation ‘mod m ’ takes the remainder after division by m , and k is the current step. Although this random number generator captures important statistical properties of true random sequences, because the sequence is generated by a deterministic algorithm, this generator is often referred to as pseudorandom. Random numbers from other probability distributions were also generated in Matlab; certain random number generation algorithms are based on transformations of the algorithm described above. The Matlab syntax used to generate random numbers are summarized in Table 6-2 below.

Table 6-2. Summary of Matlab syntax for random variable generations

Probability Distribution of a Random Variable	Matlab Syntax
Uniform	<code>randi([imin, imax], m, n)</code> Returns random integers from a discrete uniform distribution on the interval [imin, imax], in m-by-n array.
Normal	<code>normrnd(mu, sigma, [m, n])</code> Generates random numbers from a normal distribution with mean parameter μ and standard deviation parameter σ , in m-by-n array.
Lognormal	<code>lognrnd(mu, sigma, [m, n])</code> Generates random numbers from a lognormal distribution with lognormal mean μ and lognormal standard deviation σ , in m-by-n array.
Gamma	<code>gamrnd(A, B, [m, n])</code> Generates random numbers from a gamma distribution with shape parameter A and scale parameter B , in m-by-n array.

For lognormal distributions with mean m and variance v , the following equations were used to convert m and v to logarithmic units:

$$\mu_{LN} = \log\left(\frac{m^2}{\sqrt{v + m^2}}\right)$$
$$\sigma_{LN} = \sqrt{\log\left(\frac{v}{m^2} + 1\right)}$$

where μ_{LN} is logarithmic mean and σ_{LN} is logarithmic standard deviation. Often, random variables used in structural engineering modeling and analysis are assumed to be lognormally distributed; there are advantages in using lognormal distributions in that they produce non-negative outcomes. For normal distributions, negative numbers were checked and no negative numbers were encountered. For gamma distributions with mean m and standard deviation σ , the shape parameter A and scale parameter B were calculated as:

$$A \text{ (k per Chapter 5.4.4)} = \frac{m^2}{\sigma^2}$$

$$B \left(\frac{1}{\lambda} \text{ per Chapter 5.4.4}\right) = \frac{\sigma^2}{m}$$

6.3. Criteria for Outlier Data Removal

In the process of examining EDPs and establishing probabilistic distributions, some outliers were removed. Outliers are atypical, infrequent realizations that indicate behavior that are not consistent with expected response of the structure. A possible cause for outliers may be due to convergence issues from dynamic analysis which can result in drifting of EDPs. To remove outliers, a lack of homogeneity was examined and outliers outside the range of ± 2 standard deviations were removed. For drifts and coupling beam rotations at the MCE hazard level, outliers beyond the +2 standard deviation range were removed but in all cases no more than 5% of the data points were removed.

6.4. 3D Analysis: Quantification of Dispersion

All Perform 3D Monte Carlo simulations were performed with independent random variables for the 30-story model. Although these procedures were computationally expensive and required extensive post-processing, they were more robust than 2D Opensees analyses due to high convergence rates (over 95%).

6.4.1. Base Shear Force

Base shear was evaluated in two directions: H1 and H2 which represent X and Y directions, respectively. In each simulation, base shear was recorded as the maximum of positive and the absolute value of negative responses. These values, excluding outliers, were used to establish probabilistic distributions. For all five hazard levels, the means, standard deviations, and coefficients of variation are graphically noted on Figure 6-3.

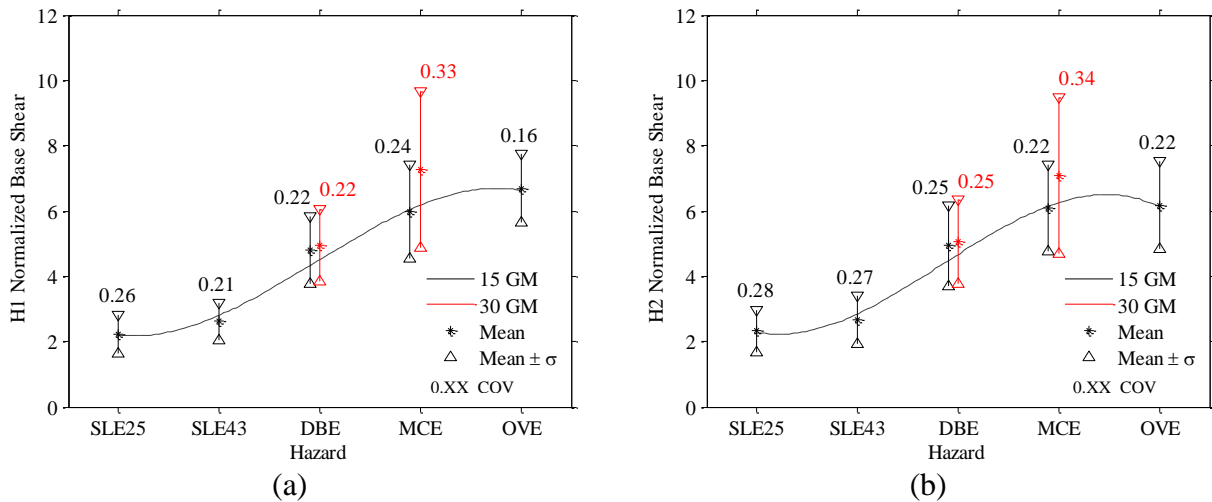


Figure 6-3. 30-Story building base shear normalized by $A_{cv} \cdot \sqrt{f'_c}$, mean and dispersion at 5 hazard levels for (a) H1 and (b) H2 directions

Coefficient of variation (COV) was used as a dispersion measure for all EDPs, and the COV measured from Monte Carlo simulations represent total dispersion resulting from record-to-record variability, model parameter uncertainties, and design uncertainties. For shear demand, COV varied from 0.16 to 0.28 for simulations performed with ground motions Suite A, and from 0.22 to 0.34 for simulations performed with ground motions Suite B. To further examine the base shear data, histogram with 30 bins were plotted and probability density functions were fitted, as shown in Appendix C. The data from all 5 hazard levels were observed to follow either normal or lognormal distribution with no clear trend specific to hazard levels.

In comparing the dispersion values from Suites A and B per Figure 6-3, it can be seen that the dispersion values were similar at the DBE level, whereas the values were significantly different at the MCE hazard level. This was due to variability that originates from the ground motions (RTR variability); it is apparent from Figure 6-4 that the variability in Suites A and B were similar at the DBE hazard level, whereas the variability in Suites A and B varied considerably at the MCE hazard level, as shown on Figure 6-5. This can also be seen from the tabulated ground motion dispersion values (measured in logarithmic standard deviation) shown in Table 6-3.

It is important to note the differences in 30-story building base shear forces obtained from performance-based design procedures as shown in Chapter 4 versus base shear forces obtained from Monte Carlo simulations in this chapter. When the 30-story building was designed per LATBSDC (2014) guidelines, the normalized base shear demand per MCE level analysis was 5.23 (noted as $1.5 \cdot 5.23 = 7.85$ in Chapter 4.6.2). This is within the ACI318-11 recommended value for normalized base shear of $\frac{8 \cdot A_{cv} \cdot \sqrt{f'_c}}{1.5} = 5.33$. Per MCE level Monte Carlo simulations

(MCS), the normalized base shear demand was 6.04. This increase resulted from two major changes that were implemented in 3D models when MCS were performed: (1) the buildings were initially designed with expected concrete strength of $1.3 \cdot f'_c$ in Chapter 4 but MCS were performed with expected strengths of $1.09 \cdot f'_c$ per Nowak et al (2008) and (2) damping was originally modeled with Rayleigh damping in Chapter 4 but this was later corrected; during MCS, modal damping with a small amount of Rayleigh damping (0.1%) was used. See Appendix B for sensitivity studies between Rayleigh damping and modal damping. As demonstrated in Appendix B, Rayleigh damping has shown to underestimate base shear demands by approximately 14%, compared to modal damping; thus base shear demands increased during MCS. Moreover, when the base shear forces were normalized by $A_{cv} \cdot \sqrt{1.09 \cdot f'_c}$, the shear demands increased by a factor of $\sqrt{1.3}/\sqrt{1.09} = 1.09$. Both of these factors have contributed to the increase in shear demands. In a real design project, some of the designs would have been iterated to meet the ACI318 maximum shear stress requirements; however, since the focus of this chapter was to quantify shear demand dispersion, the designs were not iterated.

In examining the mean values, there were differences in EDP means resulting from Suites A and B. For example, the base shear forces resulting from Suites A and B were similar for the DBE hazard level but significantly different for the MCE hazard level, as shown on Figure 6-3. For the DBE hazard level, the mean base shear forces resulting from Suites A and B were 4.87 and 5.00, respectively. The changes in the mean values were minor ($< 3\%$) because RTR variability and the mean response spectra for both Suites A and B were similar at the first mode period, as well as for higher modes (shorter periods)—refer to Figure 6-4 and Table 6-3. For the MCE hazard level, mean base shear force resulting from Suites A and B were 6.04 and 7.19,

respectively. This change was significant (19%) because RTR variability and the mean response spectrum were higher for Suite B at higher modes—refer to Figure 6-5 and Table 6-3.

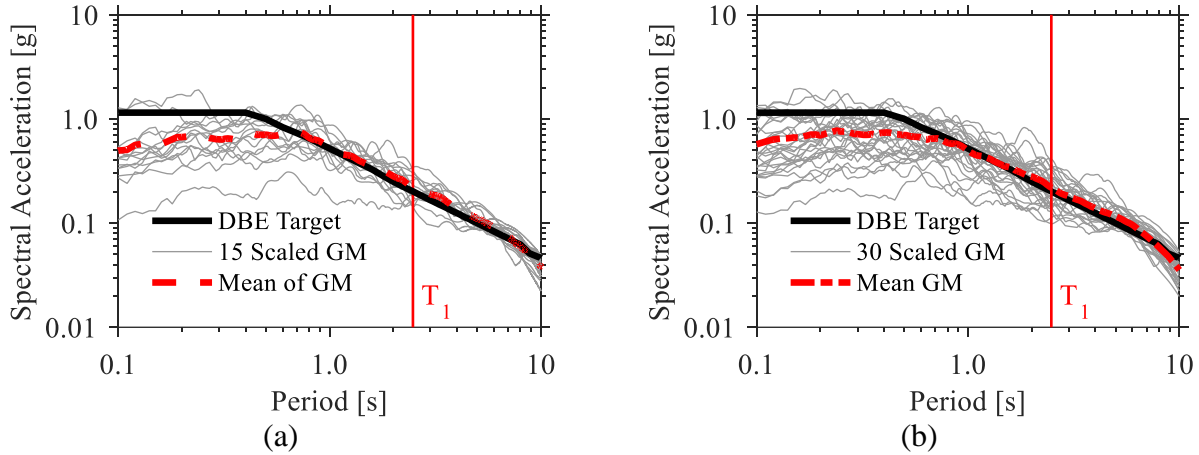


Figure 6-4. RTR variability in DBE hazard level response spectra (a) Suite A and (b) Suite B

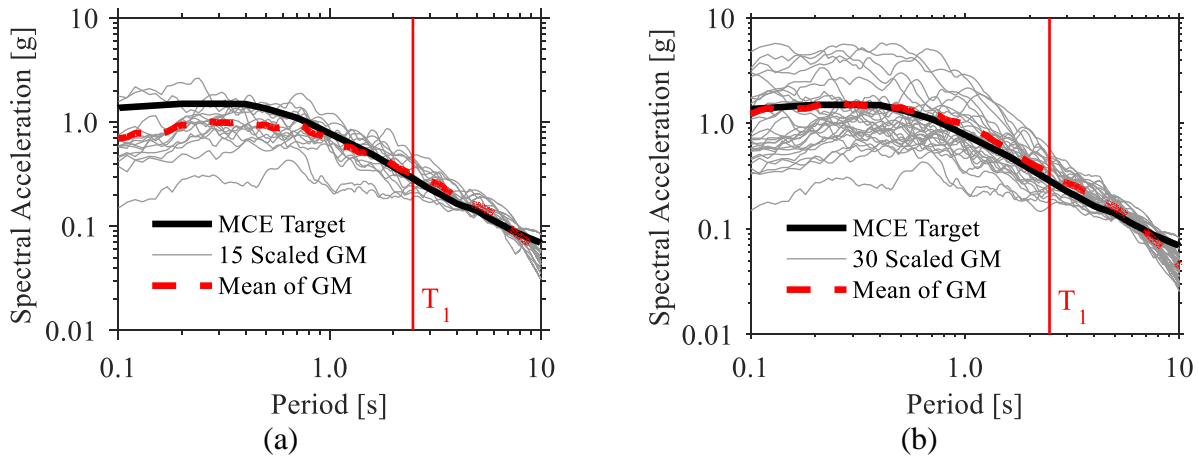


Figure 6-5. RTR variability in MCE hazard level response spectra (a) Suite A and (b) Suite B

Table 6-3. Mean and dispersion measured in logarithmic standard deviation for Suites A and B at DBE and MCE hazard levels

Hazard	Stat.	GM Suite	Period (sec)									
			0.2	0.4	0.6	0.8	1.0	2.0	3.0	4.0	5.0	10.0
DBE	Mean Sa (g)	A	0.66	0.70	0.70	0.65	0.51	0.28	0.19	0.13	0.11	0.04
		B	0.69	0.74	0.66	0.59	0.49	0.28	0.18	0.14	0.12	0.04
		(% diff)	5.0%	5.5%	-4.9%	-8.6%	-3.7%	1.1%	-3.7%	4.5%	7.3%	-1.6%
	σ_{LN}	A	0.50	0.39	0.36	0.36	0.31	0.37	0.26	0.22	0.18	0.22
		B	0.46	0.42	0.38	0.37	0.37	0.45	0.28	0.30	0.21	0.25
		(% diff)	-8.9%	8.7%	6.1%	1.1%	17.2%	22.7%	7.4%	36.2%	17.8%	16.0%
MCE	Mean Sa (g)	A	0.92	1.00	0.85	0.79	0.66	0.38	0.26	0.19	0.16	0.05
		B	1.50	1.48	1.33	1.14	0.99	0.43	0.28	0.21	0.17	0.05
		(% diff)	63.8%	47.5%	55.8%	43.6%	50.1%	13.3%	7.3%	13.7%	5.9%	-1.9%
	σ_{LN}	A	0.50	0.36	0.33	0.38	0.36	0.37	0.25	0.19	0.17	0.27
		B	0.72	0.76	0.74	0.67	0.63	0.40	0.23	0.23	0.18	0.30
		(% diff)	45.6%	109.9%	120.9%	78.1%	76.9%	8.1%	-7.7%	16.8%	6.9%	11.6%

6.4.2. Required Number of Simulations and Convergence

A sample size of 1000 simulations was used for Monte Carlo simulations. This sample size was chosen so that the variation in the EDP dispersion measure was less than 0.10. Thus, COV of each EDP was progressively examined with added number of runs; an example is shown on Figure 6-6. Graphically, it is evident that 1000 simulations were adequate for convergence of base shear dispersion measure. Variations in base shear dispersion measure using a sample size of 1000 are summarized in Table 6-4; variations were less than the specified value of 0.10 at all hazard levels.

Table 6-4. Variation in base shear dispersion measure, using a sample size of 1000

	SLE25	SLE43	DBE(15)	DBE(30)	MCE(15)	MCE(30)	OVE
δ^1 in H1 base shear COV	0.066	0.067	0.051	0.051	0.065	0.042	0.086
δ in H2 base shear COV	0.073	0.045	0.049	0.047	0.082	0.051	0.060

¹ total variation in EDP dispersion measure

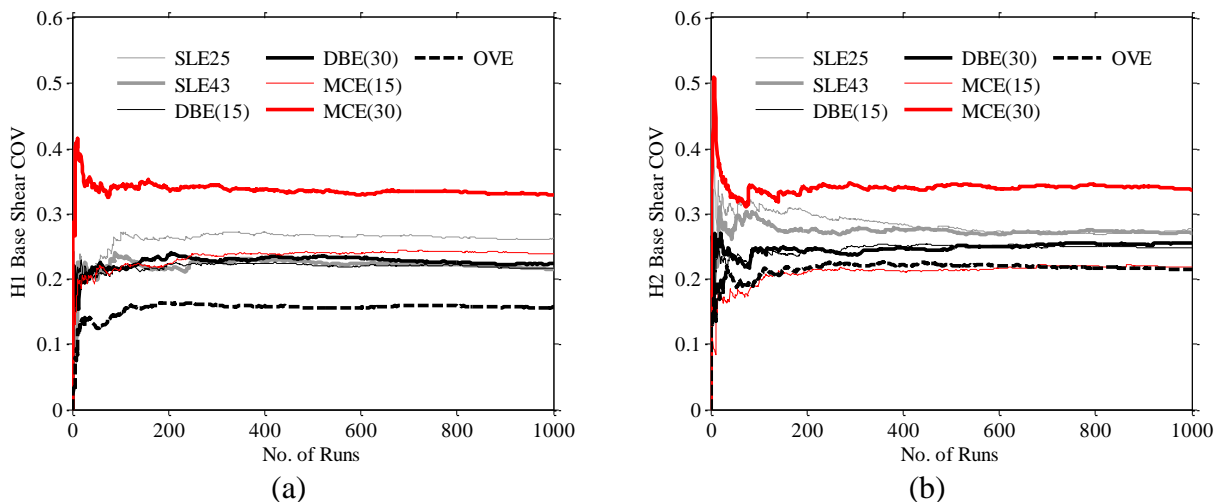


Figure 6-6. Convergence test for dispersion measure: COV versus number of runs for normalized base shear, in (a) H1 and (b) H2 directions

6.4.3. Roof Drifts

The same aforementioned procedures were used to evaluate drifts, and the results are shown on Figure 6-7. The COV varied from 0.19 to 0.34 for simulations performed with ground motions Suite A, and from 0.37 to 0.40 for simulations performed with ground motions Suite B. The data from all 5 hazard levels followed either normal or lognormal distributions. Refer to Appendix C additional plots on convergence tests and histograms overlaid with probability distribution functions.

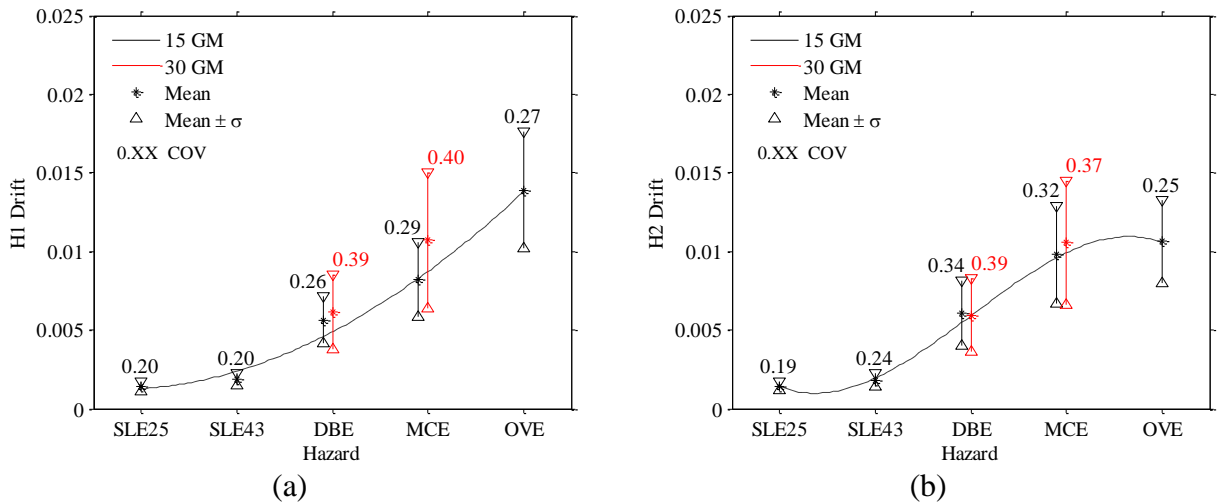


Figure 6-7. 30-Story building roof drift mean and dispersion at 5 hazard levels for (a) H1 and (b) H2 directions

6.4.4. Coupling Beam Rotations

Figure 6-8 shows results for coupling beam rotations at north and east sides of the building. Since the building is symmetric, responses were similar in north/south coupling beams and also in east/west coupling beams. The responses were collected from the 20th level, approximately where the maximum mean values were observed. For the two service hazard levels, total rotations were evaluated including elastic and plastic rotations. For all other hazard levels, only plastic rotations were evaluated since the contribution of elastic rotations were negligible at less than 1% of the total rotations. The COV varied between 0.36 and 0.85 for simulations performed with ground motions Suite A, and between 0.52 and 0.59 for simulations performed with ground motions Suite B. Data from all 5 hazard levels followed either normal or lognormal distributions. Refer to Appendix C additional plots on convergence tests and histograms overlaid with probability distribution functions.

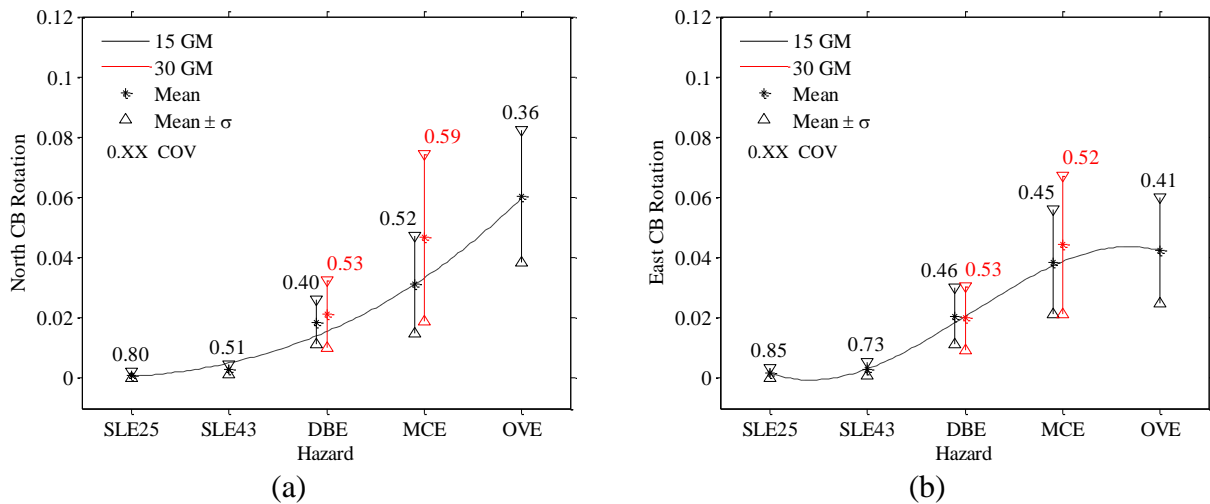


Figure 6-8. 30-Story building 20th floor coupling beam rotations, mean and dispersion at 5 hazard levels for (a) North and (b) East coupling beams

6.4.5. Tensile and Compressive Axial Strains in Shear Walls

Tensile and compressive axial strains were evaluated at all shear wall boundary elements, labeled as #1 through #16 shown on Figure 6-9. Representative results for boundary elements #1 and #3 are graphically shown on Figure 6-10. On average, the tensile axial strain COV varied between 0.37 and 0.60 for simulations performed with ground motions Suite A, and between 0.38 and 0.57 for simulations performed with ground motions Suite B. The average compressive axial strain COV varied between 0.14 and 0.40 for simulations performed with ground motions Suite A, and between 0.21 and 0.43 for simulations performed with ground motions Suite B. Data from all 5 hazard levels followed either normal or lognormal distributions. Refer to Appendix C additional plots on convergence tests and histograms overlaid with probability distribution functions. For all EDPs, summaries of dispersion values are provided in Chapter 6.6.

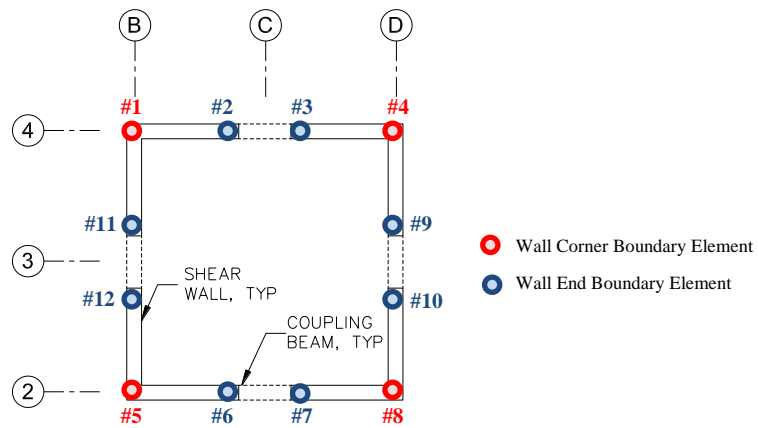


Figure 6-9. Shear wall boundary element strain gage locations

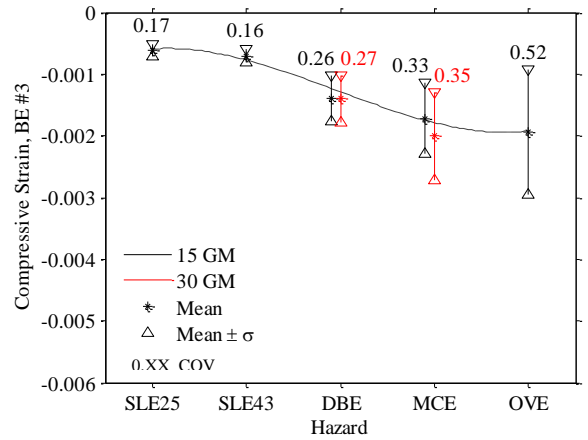
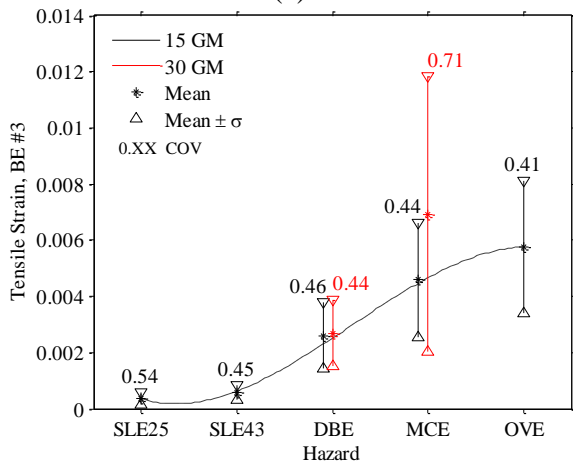
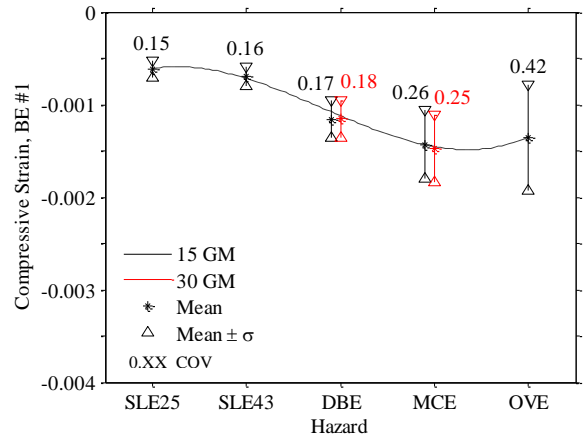
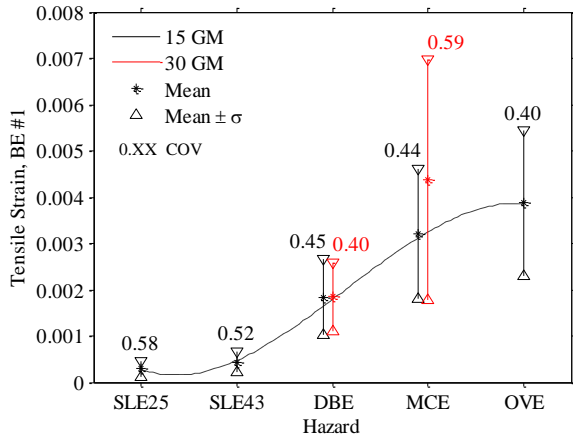


Figure 6-10. 30-Story building structural wall boundary element strains. Mean and dispersion at 5 hazard levels for BE #1 (a) tensile and (b) compressive strains, BE #3 (c) tensile and (d) compressive strains

6.5. 2D Analysis: Quantification of Dispersion due to Correlation

The modal properties of 2D 20 and 30-story buildings are noted on Table 6-5.

Table 6-5. 20 and 30-Story building modal properties (Opensees)

Model/Ht	Period (sec) based on vibrational modes		
	1	2	3
20-Story	1.55	0.36	0.16
30-Story	2.47	0.63	0.28

Monte Carlo simulations were performed for 2D 20 and 30-story models at the MCE hazard level, with correlated and independent random variables. The comparative results are shown on Table 6-7. Across all EDPs, the changes in dispersion measure due to correlation in random variables ranged from -6% to +5%; thus, introducing positive correlation in model parameter uncertainties did not have a substantial impact in dispersion estimation.

However, studies by Haselton et al (2007) examined two cases of correlated random variables where correlation had a significant impact in collapse probabilities. In Haselton's study, two types of correlation were considered: Type A, where correlation was considered for random variables of a single element (for example, strength and stiffness of a material), and Type B, where correlation was considered for random variables in different elements. Correlation between elements at different story levels was not considered. Using Type A and B correlated random variables, collapse probabilities were studied for various designs of code-conforming 4-story reinforced concrete frame buildings. Results showed that correlated random variables significantly impacted predictions of collapse probabilities; for certain Type B correlation assumptions, the final uncertainty in collapse capacity changed by a factor of 2.0. Although Haselton's study was conducted in a different context, these are important findings,

and it would be important to further examine the impacts of correlated random variables in the future.

The dispersion values compared between 2D and 3D 30-story models were similar for most EDPs within tolerable variability. The main differences were in base shear, coupling beam rotations, and end boundary element compressive axial strains where the differences in dispersion were approximately $\pm 25\%$. The differences stemmed from a combination of different input ground motions used for 2D and 3D analyses, as well as different element and material models used.

6.5.1. Challenges in Opensees Analysis

The main challenge in implementing Monte Carlo simulations in Opensees analysis was overcoming issues of numerical convergence during nonlinear response history analysis. A non-convergence is generally encountered due to nonlinearity in element models, material degradation, or from dynamic analysis which can result in drifting of EDPs. This issue is particularly serious when Monte Carlo simulations are used, since the simulations can produce combinations of parameter values for which nonlinear response history analysis encounters severe convergence difficulties (Barbato et al, 2013).

The convergence rates were evaluated as ratios between converged simulations versus all attempted simulations. Convergence was counted when the full length of the earthquake record was successfully analyzed. The average convergence rates for the 20 and 30-story analyses were approximately 62% and 68%, respectively, as shown on Table 6-6. The implications of lower convergence rates were further examined by evaluating converged ground motions. When the 30 ground motions from either Suite C or D were randomly selected 1000 times through uniform

distribution, the mean frequency per ground motion was 33.3 (as shown in Figure 6-11), and there was an inherent dispersion, where $COV=0.19$. Since not all simulations converged, the first 1000 converged responses were utilized for 2D 20 and 30-story analyses, and the first 1000 converged ground motions were plotted against frequency as shown on Figure 6-12 and Figure 6-13. Subsequently, the errors resulting from lower convergence rates were measured by the increased dispersion (coefficient of variation), and they were approximately 0.13 and 0.07 for 20 and 30-story buildings, respectively.

Table 6-6. Summary of Opensees convergence rates

Model	Analysis Type	Random Variables	Converged Runs	Total Runs	Convergence Rate
20-Story	RTR	None (base model)	29	30	96.7%
	MCS	Independent	1131	1800	62.8%
		Correlated	1010	1670	60.5%
30-Story	RTR	None (base model)	28	30	93.3%
	MCS	Independent	1212	1800	67.3%
		Correlated	1081	1600	67.6%

Although the aforementioned errors provide an estimate of potential bias, it is difficult to quantify exactly how much the result may be biased from discarding non-converged solutions. Typically, non-converged realizations can further be distinguished as lack of convergence resulting from numerical issues or due to physical failure of the structure analyzed (Barbato et al, 2013); however, this quickly became a very time consuming task, and non-converged solutions were not analyzed any further. Overall, the 2D Monte Carlo simulations in Opensees were less time consuming to implement but there were crucial challenges in facing lower convergence rates.

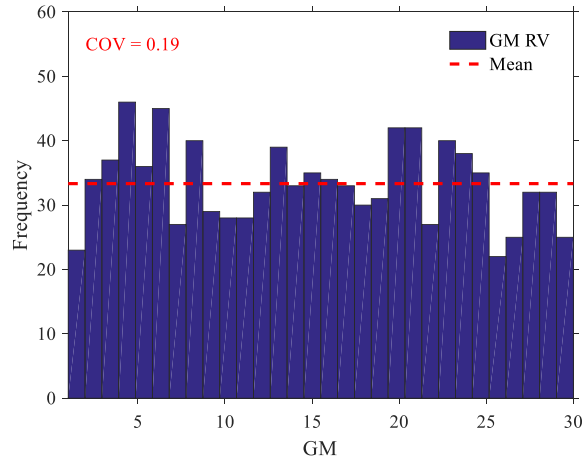


Figure 6-11. Frequency and dispersion in 30 ground motions randomly selected 1000 times through uniform distribution

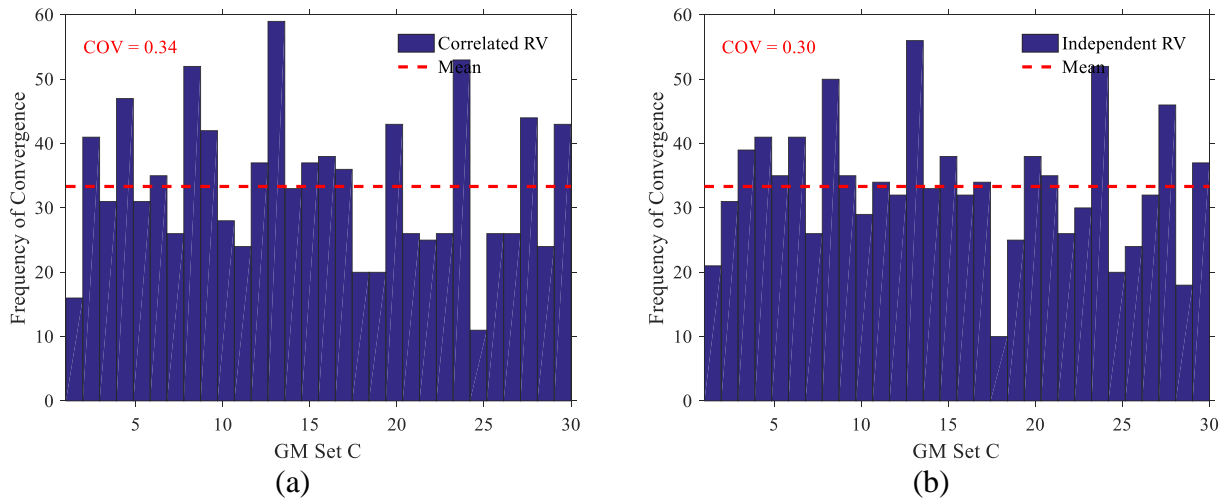


Figure 6-12. Frequency and dispersion in the first 1000 converged ground motions for the 20-story Opensees analyses using (a) correlated and (b) independent random variables

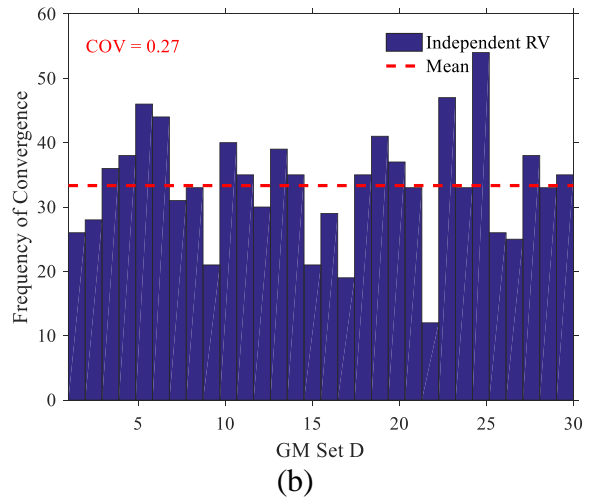
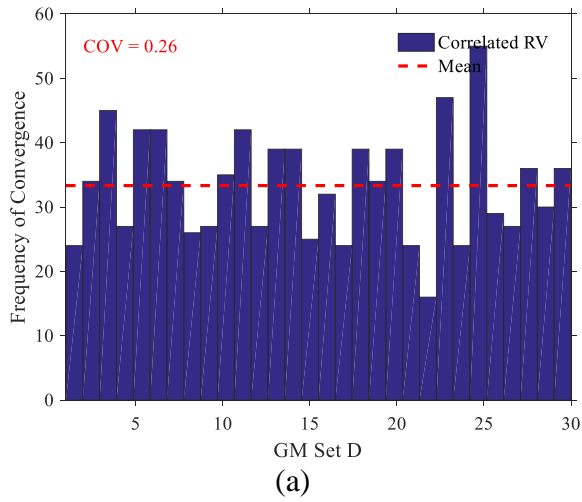


Figure 6-13. Frequency and dispersion in the first 1000 converged ground motions for the 30-story Opensees analyses using (a) correlated and (b) independent random variables

6.6. Summary of EDP Dispersion Values

For all EDPs, a summary of dispersion values are presented in Table 6-7. The total COV, ρ_{TOTAL} , represents total dispersion measured from Monte Carlo simulations and it incorporates record-to-record variability, model parameter uncertainties and design uncertainties. Record-to-record variability, ρ_{RTR} , was measured from nonlinear response history analyses subjected to 15 or 30 ground motions at all hazard levels. The model parameter and design COV, $\rho_{M\&D}$, was calculated as

$$\rho_{M\&D} = \sqrt{\rho_{TOTAL}^2 - \rho_{RTR}^2}$$

Because ρ_{TOTAL} was measured from Monte Carlo simulations with a specified tolerance, in certain cases ρ_{TOTAL} was less than ρ_{RTR} , up to 6.5%, 1.7%, and 24.7% for 30-story building 3D analysis, 30-story building 2D analysis and 20-story building 2D analysis, respectively. The 2D 20-story building analysis had the greatest error due to lowest convergence rates. Theoretically, ρ_{TOTAL} should always be greater since it encompasses both RTR variability and model parameter/design uncertainties. In these cases, ρ_{RTR} was capped at ρ_{TOTAL} and $\rho_{M\&D}$ was denoted as negligible. To mitigate these issues, more Monte Carlo simulations can be performed with a smaller tolerance in the future, provided that the computing power is available.

Table 6-7. Summary of EDP dispersion values

Hazard		SLE		DBE		MCE		MCE				OVE	
		25	43	(15)	(30)	(15)	(30)						
No. Stories		30	30	30	30	30	30	20	20	30	30	30	
Analysis		3D	3D	3D	3D	3D	3D	2D				3D	
RV		IND	IND	IND	IND	IND	IND	IND	COR	IND	COR	IND	
GM Suite		A	A	A	B	A	B	C	C	D	D	A	
Base Shear (H1 & H2)	Total	0.27	0.24	0.23	0.24	0.23	0.33	0.44	0.44	0.42	0.42	0.19	
	RTR	0.25	0.23	0.23	0.24	0.21	0.33	0.44	0.44	0.40	0.40	0.17	
	M&D	0.10	0.08	-	-	0.09	-	-	-	0.12	0.12	0.08	
Roof Drift (H1 & H2)	Total	0.20	0.22	0.30	0.39	0.31	0.39	0.41	0.42	0.35	0.36	0.26	
	RTR	0.20	0.22	0.28	0.36	0.28	0.39	0.41*	0.42	0.35	0.35	0.25	
	M&D	0.04	-	0.10	0.13	0.11	-	-	-	-	0.05	0.07	
CB Rotation (N & S & E & W)	Total	0.82	0.62	0.43	0.54	0.46	0.56	0.51	0.53	0.43	0.44	0.40	
	RTR	0.82	0.61	0.40	0.48	0.42	0.56	0.51*	0.53	0.41	0.41	0.38	
	M&D	-	0.11	0.17	0.24	0.19	-	-	-	0.14	0.16	0.11	
Corner BE	Tensile Strain	Total	0.60	0.48	0.38	0.39	0.43	0.57	0.48	0.49	0.49	0.49	0.47
		RTR	0.58	0.45	0.32	0.34	0.40	0.55	0.48*	0.49	0.49	0.49	0.46
		M&D	0.15	0.15	0.20	0.17	0.15	0.16	-	-	-	-	0.10
	Compr. Strain	Total	0.14	0.15	0.20	0.21	0.24	0.27	0.29	0.29	0.24	0.24	0.37
		RTR	0.13	0.14	0.18	0.20	0.24	0.27	0.29	0.29	0.22	0.22	0.37
		M&D	0.05	0.05	0.09	0.07	-	-	-	0.06	0.08	0.09	-
End BE	Tensile Strain	Total	0.52	0.40	0.37	0.38	0.40	0.52	0.74	0.74	0.56	0.56	0.51
		RTR	0.50	0.40	0.32	0.35	0.40	0.50	0.74	0.74	0.56	0.56	0.51
		M&D	0.16	0.08	0.18	0.16	0.07	0.16	-	-	-	-	-
	Compr. Strain	Total	0.17	0.17	0.24	0.27	0.29	0.43	0.73	0.71	0.53	0.53	0.40
		RTR	0.16	0.17	0.24	0.25	0.29	0.43	0.73	0.71*	0.53	0.53	0.40
		M&D	0.05	0.03	0.07	0.10	-	-	-	-	0.07	-	-

¹ IND – independent random variables

² COR – correlated random variables

³ M&D – model parameter and design uncertainties

* measured RTR variability is capped at total uncertainty

‘-’ indicates negligible COV

To summarize the aforementioned data, minimum and maximum dispersion values were tabulated on Table 6-8. The dispersion values were rounded up to the nearest 0.05, and the minimum and maximum values for the service levels were compared between SLE25 and SLE43. Furthermore, relative contributions from RTR variability versus model parameter/design certainties were noted. Across all hazard levels, the total dispersion values were between 0.20-0.45 for base shear and roof drift, 0.40-0.85 for coupling beam rotations, 0.40-0.60 and 0.15-0.40 for tensile and compressive axial strains at shear wall corner boundary elements, and 0.40-0.75 and 0.20-0.75 for tensile and compressive axial strains at shear wall end boundary elements. The dispersion in EDPs was the largest for coupling beam rotations and shear wall axial strains.

Relative contributions of various uncertainties were computed based on the squared ratios between ρ_{RTR} and $\rho_{\text{M\&D}}$. Relative contributions consisted of 72% to 98% from RTR variability and 2% to 28% from model parameter/design uncertainties. Thus, RTR variability was the dominant source of uncertainty, which is in agreement with findings from Porter et al (2002) and Lee and Mosalam (2005). Lee and Mosalam (2005) have also noted that the modeling/design uncertainties tend to reduce with increasing ground motion intensity; however, more simulations at higher intensities will need to be performed in the future to confirm these findings.

For moderate to high seismic structural reliability or collapse analyses, appropriate uses of dispersion measure from DBE, MCE, and OVE columns in Table 6-8 are recommended. In all cases, minimum values of 0.20 and 0.05 are recommended for RTR variability and model parameter/design uncertainties, respectively.

Table 6-8. Summary of minimum and maximum EDP dispersion values and relative percentage contributions from RTR variability and model parameter/design uncertainties

Hazard		SLE		DBE		MCE		OVE	
		MIN	MAX	MIN	MAX	MIN	MAX		
Base Shear (H1 & H2)	Total	0.25	0.30	0.25	0.25	0.25	0.45	0.20	
	RTR	0.25	0.30	0.25	0.25	0.25	0.45	0.20	
	M&D	0.10	0.10	0.00	0.00	0.10	0.15	0.10	
	% RTR	87%	89%	100%	100%	84%	92%	80%	
	% M&D	11%	13%	0%	0%	8%	16%	20%	
Roof Drift (H1 & H2)	Total	0.20	0.25	0.30	0.40	0.35	0.45	0.30	
	RTR	0.20	0.25	0.30	0.40	0.30	0.45	0.25	
	M&D	0.05	0.05	0.15	0.15	0.05	0.15	0.10	
	% RTR	97%	97%	88%	89%	87%	98%	92%	
	% M&D	3%	3%	11%	12%	2%	13%	8%	
CB Rotation (N & S & E & W)	Total	0.65	0.85	0.45	0.55	0.45	0.60	0.40	
	RTR	0.65	0.85	0.40	0.50	0.45	0.60	0.40	
	M&D	0.15	0.15	0.20	0.25	0.15	0.20	0.15	
	% RTR	97%	97%	81%	84%	83%	90%	92%	
	% M&D	3%	3%	16%	19%	10%	17%	8%	
Corner BE	Tensile Strain	Total	0.50	0.60	0.40	0.40	0.45	0.60	0.50
		RTR	0.50	0.60	0.35	0.35	0.40	0.60	0.50
		M&D	0.20	0.20	0.20	0.20	0.20	0.20	0.15
		% RTR	90%	94%	72%	80%	87%	92%	95%
		% M&D	6%	10%	20%	28%	8%	13%	5%
	Compr. Strain	Total	0.15	0.15	0.25	0.25	0.25	0.30	0.40
		RTR	0.15	0.15	0.20	0.25	0.25	0.30	0.40
		M&D	0.05	0.10	0.10	0.10	0.10	0.10	0.00
		% RTR	86%	90%	79%	88%	86%	96%	100%
		% M&D	10%	14%	12%	21%	4%	14%	0%
End BE	Tensile Strain	Total	0.45	0.55	0.40	0.40	0.45	0.75	0.55
		RTR	0.40	0.50	0.35	0.35	0.40	0.75	0.55
		M&D	0.10	0.20	0.20	0.20	0.10	0.20	0.00
		% RTR	91%	96%	76%	83%	90%	97%	100%
		% M&D	4%	9%	17%	24%	3%	10%	0%
	Compr. Strain	Total	0.20	0.20	0.25	0.30	0.30	0.75	0.40
		RTR	0.20	0.20	0.25	0.30	0.30	0.75	0.40
		M&D	0.05	0.05	0.10	0.10	0.10	0.10	0.00
		% RTR	91%	97%	87%	93%	-	98%	100%
		% M&D	3%	9%	7%	13%	2%	-	0%

6.7. Cumulative Distribution Functions

From 30-story analyses results (Suite A) presented in Chapter 6.4, a summary of means, standard deviations, and probability distributions are noted in Table 6-9. The detailed probability distributions for each EDP are graphically noted on Appendix C, whereas the probability distributions from the mean responses are shown on Table 6-9.

Using the means, standard deviations, and probability distributions (shown in Table 6-9), fitted cumulative distribution functions (CDF) were plotted for all EDPs. All CDFs are graphically presented on Figure 6-14 and Figure 6-15, whereas the values were tabulated and compared for all EDPs at standard z-score values at 0, ± 1 , and ± 2 , as shown on Table 6-10. These CDF plots and tables can be used as a reference guide, during performance-based design iterations. One way to use CDF tables is to compare EDPs among different hazards. For example, the 50 percentile normalized base shear demands (which corresponds to the mean, if data are normally distributed) at SLE43 and MCE hazard levels were 2.58 and 5.89, respectively. Thus, the MCE to SLE43 base shear ratio for this 30-story prototype building was approximately 2.3, which is in line with typical tall building designs. Another way to use the CDF tables is to estimate the variations in each EDP when a certain response, such as coupling beam rotations, is being calibrated to meet acceptance requirements. For example, at the MCE hazard level, when coupling beam rotations are reduced from 4.93% to 3.19% (corresponds to 84.1 percentile to 50 percentile), roof drifts reduce from 1.16% to 0.90% and normalized base shear demands reduce from 7.39 to 5.89. This corresponds to 54%, 29%, and 26% reduction in coupling beam rotations, roof drifts, and normalized base shear demands, respectively. As noted in the previous section, the coupling beams rotations had the greatest dispersion among all EDPs considered, and this is reflected in a larger reduction in responses compared to other EDPs. However, it is

important to note that this reference guide is based on a case-study 30-story building; it would be useful to expand this study to create a reference guide that contained information from a larger population of tall buildings.

Table 6-9. Summary of EDP means, standard deviations, and probability distributions

Hazard		SLE25	SLE43	DBE(15)	MCE(15)	OVE	
No. Stories		30	30	30	30	30	
Analysis		3D	3D	3D	3D	3D	
RV		IND	IND	IND	IND	IND	
GM Suite		A	A	A	A	A	
Normalized Base Shear (H1 & H2)	Mean	2.28	2.65	4.87	6.04	6.43	
	Std.	0.62	0.64	1.13	1.38	1.20	
	Distr.	LN	LN	N	LN	N	
Roof Drift (H1 & H2)	Mean	0.14%	0.18%	0.59%	0.90%	1.23%	
	Std.	0.03%	0.04%	0.18%	0.27%	0.32%	
	Distr.	N	N	N	N	N	
CB Rotation (N & E & S & W)	Mean	0.15%	0.30%	1.96%	3.50%	5.44%	
	Std.	0.12%	0.19%	0.85%	1.61%	2.16%	
	Distr.	LN	LN	LN	LN	N	
Corner BE	Tensile Strains	Mean	0.0002	0.0004	0.0017	0.0028	0.0037
		Std.	0.0001	0.0002	0.0006	0.0012	0.0018
		Distr.	LN	LN	LN	LN	LN
	Compr. Strains	Mean	-0.0006	-0.0007	-0.0011	-0.0014	-0.0015
		Std.	-0.0001	-0.0001	-0.0002	-0.0003	-0.0006
		Distr.	N	N	LN	N	N
End BE	Tensile Strains	Mean	0.0003	0.0005	0.0023	0.0040	0.0052
		Std.	0.0002	0.0002	0.0009	0.0016	0.0026
		Distr.	LN	LN	LN	LN	LN
	Compr. Strains	Mean	-0.0006	-0.0007	-0.0014	-0.0018	-0.0021
		Std.	-0.0001	-0.0001	-0.0003	-0.0005	-0.0008
		Distr.	LN	LN	N	LN	LN

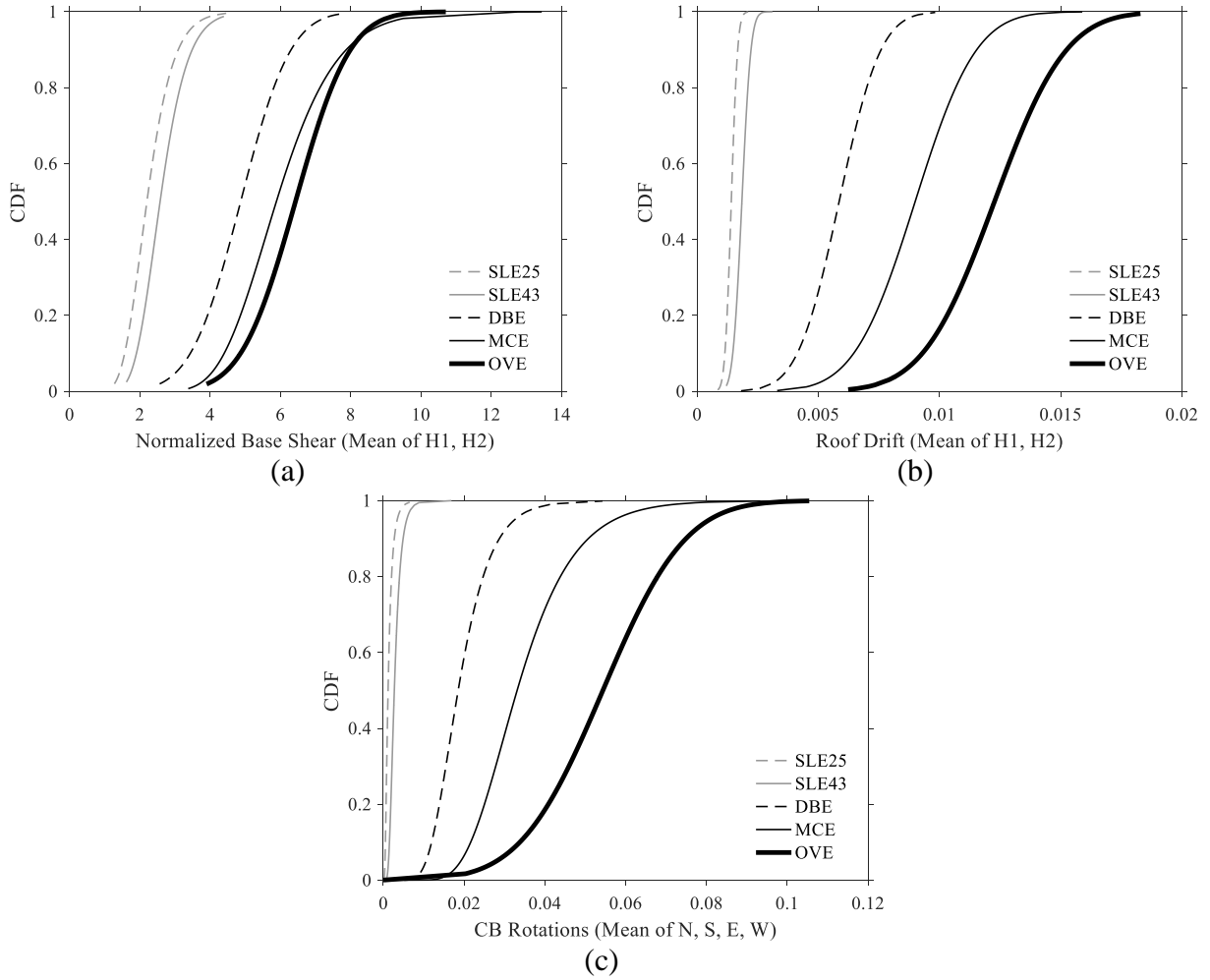


Figure 6-14. 30-story building Suite A analyses: cumulative distribution function for (a) normalized base shear, (b) roof drift, and (c) CB rotations

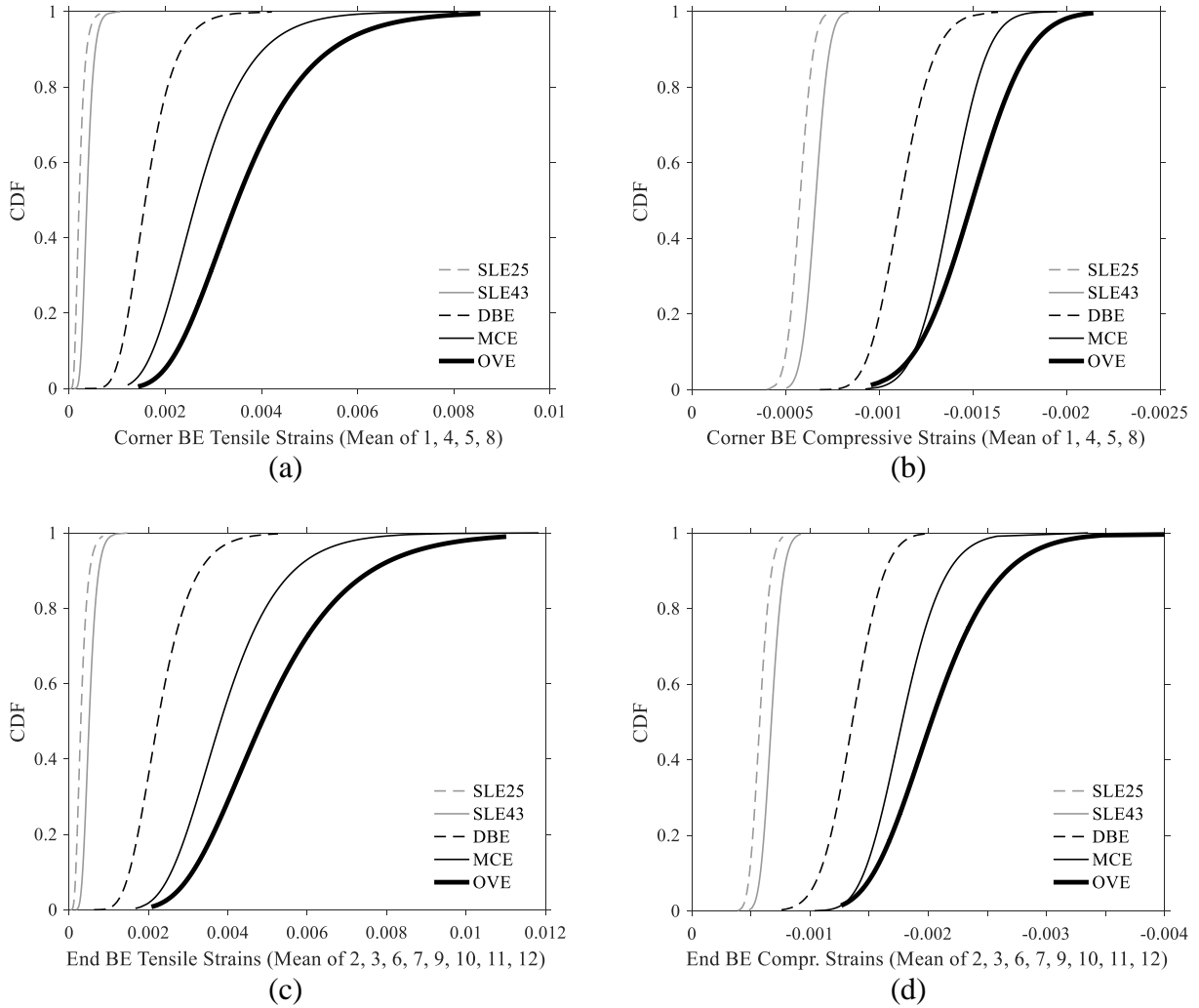


Figure 6-15. 30-story building Suite A analyses: cumulative distribution function for Corner BE (a) tensile strains and (b) compressive strains, as well as End BE (c) tensile strains and (d) compressive strains

Table 6-10. Summary of EDP values at standard z-scores 0, ± 1 , and ± 2 , for 30-story building Suite A analyses

Hazard (Suite A)	CDF (%)	z	Normalized Base Shear	Drift	CB Rotation	Corner BE		End BE	
						Tensile Strain	Compr. Strain	Tensile Strain	Compr. Strain
SLE25	2.3	-2 σ	1.30	0.09%	0.03%	0.0001	-0.0004	0.0001	-0.0004
	15.9	-1 σ	1.69	0.11%	0.06%	0.0001	-0.0005	0.0002	-0.0005
	50.0	0	2.20	0.14%	0.12%	0.0002	-0.0006	0.0003	-0.0006
	84.1	+1 σ	2.87	0.17%	0.24%	0.0004	-0.0007	0.0005	-0.0007
	97.7	+2 σ	3.78	0.20%	0.50%	0.0006	-0.0007	0.0008	-0.0008
SLE43	2.3	-2 σ	1.62	0.12%	0.08%	0.0001	-0.0006	0.0002	-0.0005
	15.9	-1 σ	2.04	0.15%	0.14%	0.0002	-0.0007	0.0003	-0.0006
	50.0	0	2.58	0.18%	0.26%	0.0004	-0.0007	0.0005	-0.0007
	84.1	+1 σ	3.28	0.22%	0.45%	0.0006	-0.0007	0.0007	-0.0008
	97.7	+2 σ	4.17	0.30%	0.87%	0.0010	-0.0007	0.0011	-0.0009
DBE(15)	2.3	-2 σ	2.64	0.18%	0.80%	0.0007	-0.0007	0.0011	-0.0008
	15.9	-1 σ	3.76	0.43%	1.20%	0.0011	-0.0009	0.0015	-0.0010
	50.0	0	4.87	0.59%	1.80%	0.0016	-0.0011	0.0022	-0.0014
	84.1	+1 σ	5.99	0.79%	2.72%	0.0022	-0.0013	0.0031	-0.0017
	97.7	+2 σ	7.11	0.90%	4.18%	0.0034	-0.0016	0.0045	-0.0020
MCE(15)	2.3	-2 σ	3.74	0.33%	1.35%	0.0012	-0.0009	0.0017	-0.0010
	15.9	-1 σ	4.70	0.67%	2.05%	0.0017	-0.0011	0.0025	-0.0013
	50.0	0	5.89	0.90%	3.19%	0.0026	-0.0014	0.0037	-0.0017
	84.1	+1 σ	7.39	1.16%	4.93%	0.0039	-0.0017	0.0055	-0.0023
	97.7	+2 σ	9.31	1.52%	7.73%	0.0060	-0.0020	0.0080	-0.0034
OVE	2.3	-2 σ	4.08	0.62%	2.03%	0.0014	-0.0010	0.0021	-0.0013
	15.9	-1 σ	5.21	0.93%	3.27%	0.0022	-0.0010	0.0029	-0.0013
	50.0	0	6.43	1.23%	5.44%	0.0034	-0.0015	0.0046	-0.0021
	84.1	+1 σ	7.65	1.58%	7.64%	0.0053	-0.0021	0.0075	-0.0029
	97.7	+2 σ	8.87	1.76%	9.82%	0.0086	-0.0021	0.0110	-0.0051

6.8. Conclusions

To assess seismic reliability of structural components or systems, it is essential that dispersions in EDPs are quantified. Thus, a methodology was developed to quantify dispersion in tall reinforced-concrete core wall building EDPs resulting from nonlinear response history analyses. Eleven input random variables were selected to represent RTR variability (resulting from 15 or 30 ground motions at five hazard levels), model parameter uncertainties, and design uncertainties. Given the means and COV of input variables, Monte Carlo simulations were utilized to estimate the means and COV of selected EDPs. For evaluation, shear demand was selected as the main EDP of interest for further reliability studies, roof drift was selected as a global EDP, and coupling beam rotations and shear wall boundary element tensile and compressive axial strains were selected as local EDPs. This methodology was applied to 30-story models developed in Perform 3D and Opensees and a 20-story model developed in Opensees. Based on the findings, the following conclusions were reached:

1. From both 3D (Perform 3D) and 2D (Opensees) Monte Carlo simulations, total dispersion for all EDPs were quantified as COV. Across all hazard levels, total dispersion ranged between 0.20-0.45 for base shear forces and roof drifts, 0.40-0.85 for coupling beam rotations, 0.40-0.60 and 0.15-0.40 for tensile and compressive axial strains at shear wall corner boundary elements, and 0.40-0.65 and 0.40-0.75 and 0.20-0.75 for tensile and compressive axial strains at shear wall end boundary elements. The dispersion in EDPs was the largest for coupling beam rotations and shear wall axial strains.

2. Probability distributions were either lognormal or normal for all EDPs at all hazard levels. For reliability or collapse analysis, investigating results from both probability distributions to determine a more conservative case is recommended at this time.
3. For structural reliability or collapse analyses, appropriate uses of dispersion measure from DBE, MCE, and OVE columns in Table 6-8 are recommended. In all cases, minimum values of 0.20 and 0.05 are recommended for RTR variability and model parameter/design uncertainties, respectively.
4. Relative contributions to total dispersion consisted of 72% to 98% from RTR variability and 2% to 28% from model parameter/design uncertainties. Thus, RTR variability was the dominant source of uncertainty which is in agreement with findings from Porter et al (2002) and Lee and Mosalam (2005).
5. Changes in dispersion measure due to positive correlation in model parameter random variables ranged from -6% to +5%; thus, introducing positive correlation in model parameter uncertainties did not have a significant impact in dispersion estimation.
6. As documented in Nowak et al (2008), expected concrete compressive strengths should be adjusted to $1.1 \cdot f'_c$ for high strength concrete compressive strengths ranging between 6ksi and 12ksi, unless project-specific material testing is conducted to justify a higher value. Current guidelines for the use of $1.3 \cdot f'_c$ per LATBSDC (2014) is more appropriate for normal strength concrete; the incorrect use of expected strength factors can result in inaccurate shear demands and capacities.
7. For all EDPs, CDF plots were presented and values were tabulated at standard z-scores 0, ± 1 , and ± 2 . The information from these plots can be used during performance-based design iterations to estimate the variations in each EDP when a certain criteria, such as

drifts or coupling beam rotations, are being calibrated to meet the acceptance requirements.

6.9. Limitations and Future Work

Limitations and future work are listed as follows.

1. In this study, Monte Carlo simulations were performed with a specified tolerance of 0.10 for COV of the dispersion measure. Thus, in some cases, total dispersion measured from Monte Carlo simulations carried errors, up to 6.5% for both 2D and 3D 30-story building analysis and up to 24.7% for the 2D 20-story building analysis. To mitigate this issue, more number of Monte Carlo simulations can be performed, provided that the necessary computing power is available. Currently, scripting to automate Perform 3D analyses is not available, thus, running more simulations was a challenge. When scripting or an open platform becomes available for Perform 3D, utilizing parallel computing for further studies is recommended. In such a case, (1) more number of simulations can be performed, reducing estimation errors and (2) simulations can be performed at other hazards levels, which can provide useful information for collapse, or to confirm findings that modeling/design uncertainties tend to decrease as ground motion intensities increase. Lee and Mosalam (2005) found this to be true for a case study of 7-story reinforced concrete shear wall building.
2. There were limitations and challenges in implementing Opensees models. Although the automated 2D analyses were less time consuming to implement and required less post-processing, the main drawback was having lower convergence rates. Convergence was counted when the full length of the earthquake record was successfully analyzed; the average convergence rates for the 20 and 30-story model analyses were approximately 62%

and 68%, respectively. Although other shear wall models, such as “ForceBeamColumn” and “SFI_MVLEM,” were tested rigorously for convergence, both models resulted in less convergence rates for tall coupled wall applications. Nevertheless, a new shear wall shell element, called “ShellMITC4” by Lu et al (2015) is shown to have better convergence rates for tall building applications; it is recommended that the new shear wall models continue to be studied and tested to advance tall building studies.

CHAPTER 7. UNCERTAINTIES IN STRUCTURAL WALL SHEAR CAPACITY

In this chapter, current procedures to calculate nominal shear strength for structural walls are presented and uncertainties in shear capacity are evaluated using experimental test results of shear-controlled walls.

7.1. Shear Capacity

Shear capacity of a structural wall is determined from the nominal shear strength equation as specified in ACI318-11:

$$V_n = A_{cv} [\alpha_c \lambda \sqrt{f'_c} + \rho_t f_y]$$

where A_{cv} is the cross-sectional area of shear wall, f'_c is the concrete compressive strength, ρ_t is the horizontal reinforcement ratio, f_y is the reinforcing steel yield strength, and α_c varies linearly from 3.0 for walls with aspect ratio h_w/l_w (height to length of walls) less than 1.5, to 2.0 for walls with aspect ratio greater than 2.0. Per ACI318-11, the maximum shear stress on any one wall is limited to $A_{cv} [10\sqrt{f'_c} Psi]$ and the average shear stress on all walls is limited to $A_{cv} [8\sqrt{f'_c} Psi]$.

Using the nominal shear strength equation, the expected shear strength ($F_{n,e}$) can be calculated using expected material properties. To examine how well the ACI318-11 nominal shear strength equation predicts actual strengths of walls, studies by Wallace et al (2013) are referenced in the following section.

7.2. Structural Wall Failure Modes and Shear Capacity

Wallace et al (2013) examined experimental test data from 40 walls with height to length aspect ratios between 1 and 3 that were closely designed to the current U.S. design standards. Relatively well-detailed walls were selected with area of boundary transverse reinforcement of at least half of that required by ACI318-11 and ratio of vertical hoop spacing to vertical boundary bar diameter of less than 8. The examined cross-sections were rectangular, flanged, barbell, and T-shaped. Compressive strengths ranged from 3.2ksi to 19.9ksi and reinforcing steel yield strengths varied between 62.3ksi and 205.9ksi.

For various wall failure modes, the ratios between the actual shear strength achieved by experimental tests (V_{max}) and the predicted shear strength using expected material properties ($V_{ne,ACI}$) were evaluated. The results are shown on Figure 7-1, represented by a relationship between $V_{max}/V_{ne,ACI}$ and curvature ductility. Curvature ductility was calculated as the ratio of ultimate curvature divided by yield curvature; this was used to categorize different wall failure modes as shear-controlled, flexure-controlled, and flexure-shear controlled. Shear-controlled walls are defined as walls with the least amount of ductility, generally less than 10. Shear failures are commonly characterized by sudden diagonal tension failures or crushing of concrete along diagonal compressive struts within the wall web. The mean $V_{max}/V_{ne,ACI}$ for shear-controlled walls is approximately 1.5 and it is evident that the current nominal shear strength equation per ACI318-11, using expected properties, under-predicts the actual shear strength. When walls fail in flexure, curvature ductility is typically greater than 10 and $V_{max}/V_{ne,ACI}$ is less than 1.0, as full shear capacity cannot be reached once the walls yield in flexure (for a quasi-static test with a single lateral point load). These walls are more ductile and the failures are characterized by concrete crushing followed by buckling and eventual fracture of boundary

vertical reinforcement. The transition region where curvature ductility is greater than 10 and $V_{\max}/V_{ne,ACI}$ greater than 1.0 is categorized as flexure-shear failure. The failure mechanism for these walls initially looks similar to flexure-controlled walls but shear resistance slowly degrades and the walls ultimately fail in shear (e.g, diagonal tension, diagonal compressive strut crushing, lateral instability due to high compression at the wall boundary).

It is important to note that although tall reinforced concrete shear walls are designed to fail in flexure, the $V_{\max}/V_{ne,ACI}$ values for flexure-controlled walls should not be used for shear design. This is because once the walls yield in flexure, the full shear capacity cannot be measured. Flexure-controlled wall tests are useful to obtain flexural capacity of walls but they do not provide information on ultimate shear capacity of walls. Thus, the mean overstrength for shear capacity should be obtained from tests where walls have failed in shear and have reached the full shear capacity.

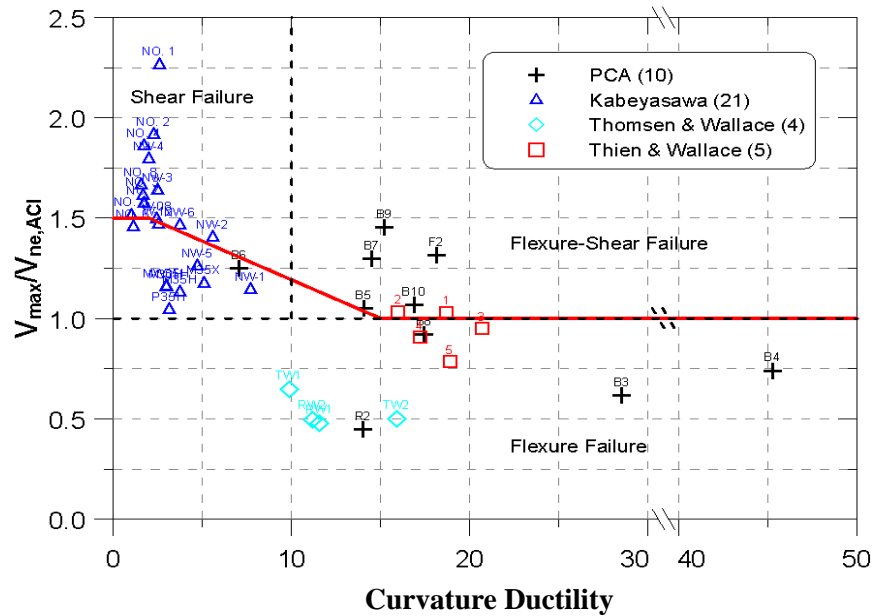


Figure 7-1. Structural wall shear capacity ($V_{\max}/V_{ne,ACI}$) versus curvature ductility, Wallace et al (2013)

7.3. Statistical Parameters for Shear Capacity

To examine statistical parameters for shear capacity, compilations of shear-controlled wall test results were referenced from Wallace (1998) and Wood (1990). Wallace (1998) examined 37 shear-controlled walls with concrete compressive strengths greater than 8ksi and Wood (1990) examined 143 shear-controlled walls with concrete compressive strengths between 2ksi and 8ksi.

7.3.1. Structural Walls with $f'_c \geq 8$ ksi

Wallace (1998) studied 37 wall specimens with height to length aspect ratios (h_w/l_w) less than 2.0 where all walls were expected to fail in shear. All specimens were constructed with high-strength concrete; concrete compressive strengths ranged from 7.9ksi to 19.9ksi and web reinforcing steel yield strengths ranged from 47ksi to 206ksi. Test specimens for high-strength concrete walls are relatively scarce and all 37 tests were conducted in Japan. This set includes the 21 shear-controlled walls previously presented in Figure 7-1.

It's important to note that some of the test results from these 37 wall specimens included web reinforcement ratios that significantly exceeded ACI318-11 recommendations. Per ACI318-11, the maximum average shear stress on all walls is limited to $V_{n,e} \leq A_{cv} [8\sqrt{f'_c} Psi]$ which sets an upper bound of $\rho_t \cdot f_y / f'_c$. To examine any potential bias associated with this data, the test results were further sorted into two bins, (1) $V_{n,e} \leq 1.1 \cdot A_{cv} [8\sqrt{f'_c} Psi]$ which is within ACI318-11 limits and (2) $V_{n,e} > 1.1 \cdot A_{cv} [8\sqrt{f'_c} Psi]$ which exceeds ACI318-11 limits. Since ACI318-11 limits $\sqrt{f'_c}$ to 100psi in shear strength calculations, the corresponding f'_c design limit is at 10ksi, and the 1.1 factor takes into account the expected strength properties of 10ksi

concrete. The mean and COV for the two bins, as well as for the entire set of data are shown in Table 7-1 and the results show that there is no significant bias.

Table 7-1. Shear-controlled wall tests separated into two bins by ACI318-11 limiting shear stress (Wallace et al, 2013)

Data	No. of Tests	$V_{\max}/V_{n,e}$		f'_c	
		Mean	COV	Mean (ksi)	COV
1. $V_{n,e} \leq 1.1 \cdot A_{cv} [8\sqrt{f'_c} Psi]$ (within ACI318-11 limits)	12	1.68	0.22	10.81	0.21
2. $V_{n,e} > 1.1 \cdot A_{cv} [8\sqrt{f'_c} Psi]$ (over ACI318-11 limits)	25	1.52	0.19	11.27	0.24
All	37	1.57	0.20	11.05	0.23

Overall, a plot of variations in ratio between maximum shear and nominal shear strength, $V_{\max}/V_{n,e}$, versus $\rho_t \cdot f_y / f'_c$ is shown on Figure 7-2(a). The limiting nominal shear strength was calculated as $V_{n,e} \leq A_{cv} [8\sqrt{f'_c} Psi]$. All 37 specimens had $V_{\max}/V_{n,e}$ between 1.0 and 2.5, with a mean $V_{\max}/V_{n,e}$ of 1.57 and coefficient of variation of 0.20. A histogram using 20 bins and a probability density function is plotted on Figure 7-3(a). The data are observed to follow normal distribution, and this assumption was tested on normal probability paper, as shown on Figure 7-4(a). The probability paper allows for a direct comparison between the cumulative density function and a model distribution by adjusting the scales so that the model distribution plots as a straight line. Detailed procedures for the use of probability paper are described in Chapter 7.3.3.

7.3.2. Structural Walls with $f'_c < 8\text{ksi}$

Wood (1990) studied 143 shear wall test specimens that were reported to have failed in shear. All test specimens were isolated walls that were either one or two stories high. The cross-sections were symmetric and the cross-sections were flanged, barbell, and rectangular.

Compressive strengths ranged from 1.9ksi to 7.1ksi and reinforcing steel yield strengths varied between 39.3ksi and 82.9ksi. Sixty-four wall tests were from Japan, and other wall tests were from Canada, Japan, New Zealand, and the United States.

A plot of the maximum average shear strength to the limiting nominal shear strength ratio, $V_{\max}/V_{n,e}$, versus $\rho_n f_y$ is shown on Figure 7-2(b). For 66% of the walls, $V_{\max}/V_{n,e}$ was between 1.0 and 2.0, and approximately 9% of the walls had maximum strengths less than the nominal shear strengths. Similar to Wallace (1998)'s trends, the maximum shear strengths of the walls were mostly high with a mean $V_{\max}/V_{n,e}$ of 1.67 and a coefficient of variation of 0.40. A histogram using 30 bins, overlaid with a probability density function is plotted on Figure 7-3(b). The data are observed to follow a lognormal distribution and this observation was tested using a lognormal probability paper as shown on Figure 7-4(b).

It is important to note that the dispersion (COV) measured from data presented by Wallace (1998) and Wood (1990) derives from a combination of uncertainties resulting from nominal shear strength prediction equation, material strengths including concrete compressive strengths and reinforcing steel yield strengths, construction quality, differences in testing approach, potential errors in test measurements, and other possible errors. Due to high quality measures required for tall building design and construction process through Seismic Peer Review Panels (LATBSDC, 2014) and stringent inspections enforced in the United States, no further dispersion was added to the measured values.

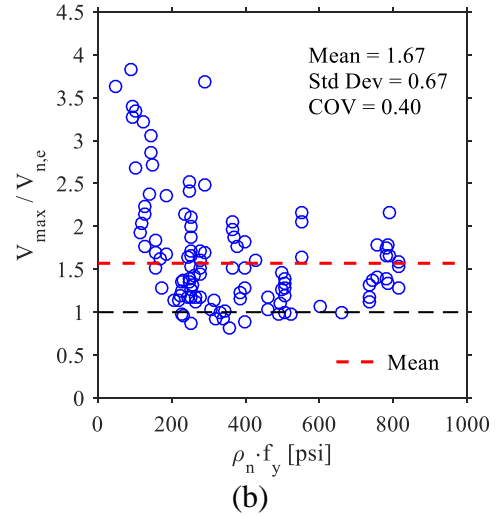
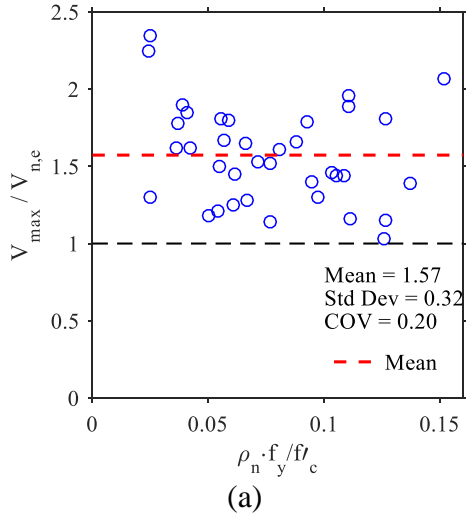


Figure 7-2. Variation in measured shear strength to nominal shear strength ratio versus reinforcement per (a) Wallace (1998) (b) Wood (1990)

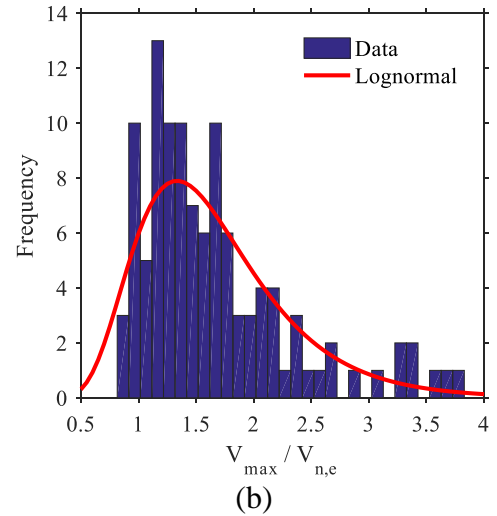
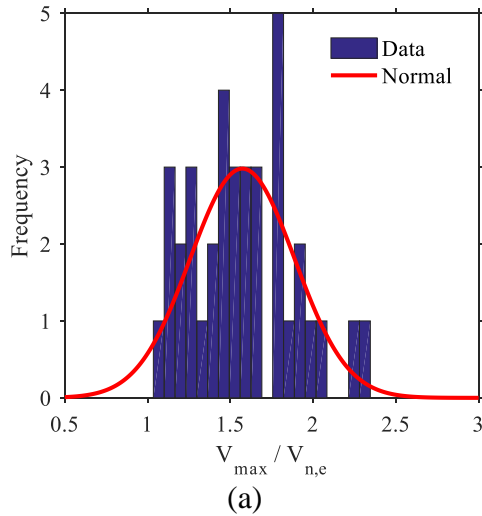


Figure 7-3. Histogram of $V_{max}/V_{n,e}$ using data by (a) Wallace (1998) (b) Wood (1990)

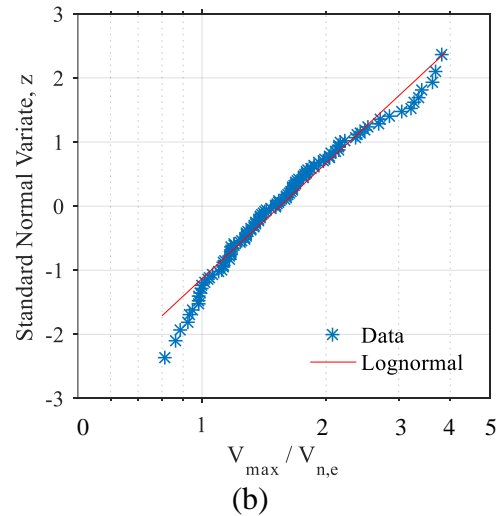
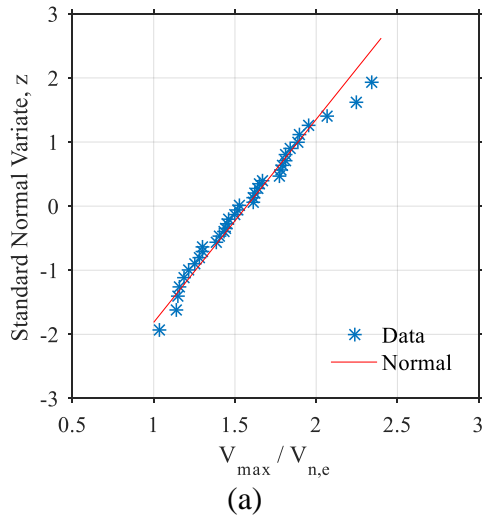


Figure 7-4. Probability distribution tests of $V_{max}/V_{n,e}$ using (a) Wallace (1998) (b) Wood (1990)

7.3.3. Probability Distribution Tests through Probability Papers

In a case where N values are obtained from a normally distributed random variable X , the values are denoted as $\{x\}$, and a brief description for the construction and use of normal probability paper are provided in the following (Nowak and Collins, 2000).

1. Sort values of $\{x\}$ in increasing order.
2. Calculate cumulative probability, p_i for each x_i .

$$p_i = \frac{1}{N+1}$$

3. For each p_i , determine standard normal variate, $z_i = \Phi^{-1}(p_i)$.

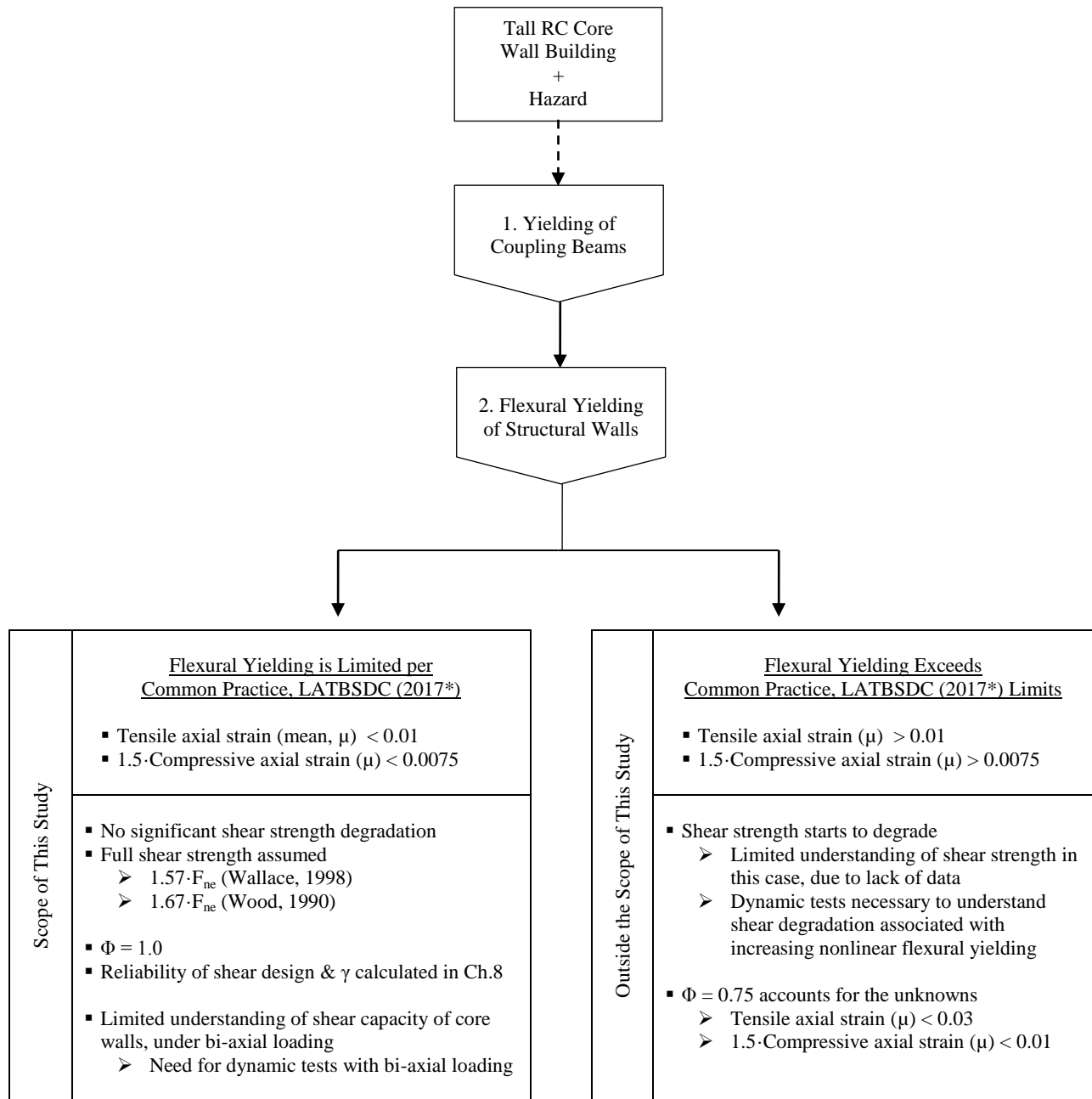
The calculated values of z_i are plotted on the y-axis, and values of $\{x\}$ are plotted on the x-axis. If the plot appears to follow a straight line, it is reasonable to conclude a normal distribution for X . From the normal probability paper plot, the values of mean and standard deviation can be read directly from the graph, where the mean, μ_X , is at $z=0$ and the standard deviation is the horizontal distance that spans between $1 \cdot z$ on the y-axis. For normal distributions, the best-fit line can be described as

$$best\ fit = \frac{x - \mu_X}{\sigma_X} = \left(\frac{1}{\sigma_X}\right)x + \left(\frac{-\mu_X}{\sigma_X}\right)$$

A similar procedure was used to prepare a lognormal probability paper, with data plotted on a lognormal x-axis scale.

7.4. Context in which Shear Controlled Wall Tests were Used

It is important to note the context in which the aforementioned shear controlled wall tests were used; a flowchart describing this process is shown on Figure 7-5. When a tall concrete core wall building undergoes a hazard, the coupling beams yield first and then the structural walls yield in flexure. Currently, it is common practice to limit the amount of flexural yielding in walls by restricting the mean tensile and compressive axial strains, as shown on Figure 7-5. When flexural yielding is limited, there is no significant shear degradation and full shear capacity can be assumed. This is the context in which shear controlled wall tests were used to conduct reliability studies in Chapter 8. On the other hand, when flexural yielding exceeds the axial strain limits set forth in Figure 7-5, shear capacity starts to degrade. Currently, there are limited test data that can quantify the rate of shear strength degradation associated with increasing nonlinear flexural yielding. Thus, further dynamic tests are needed to examine shear strength degradation with nonlinear flexural yielding including higher mode contributions. Moreover, core wall tests in biaxial loading would be helpful to understand how shear capacities may change due to varying shapes of the compressive zones. When flexural yielding exceeds recommendations provided in Figure 7-5, a lower $\phi=0.75$ is used to account for the uncertainties in shear capacity. These flexural yielding limitations will most likely be clarified in the 2017 edition of LATBSDC.



* Intentions of clarifying the flexural yielding limits in the 2017 edition of LATBSDC.

Figure 7-5. General sequence of tall reinforced concrete core wall building behavior during a hazard and the context in which shear controlled wall tests were used. All strain limits shown are for plastic hinge regions.

7.5. Conclusions

Structural wall shear capacities were examined using three sets of data. First, ratios between the actual shear strength achieved by experimental tests (V_{\max}) and the predicted shear strength using expected material properties ($V_{ne,ACI}$) were evaluated against curvature ductility for all wall failure modes: shear-controlled, flexure-controlled, and flexure-shear controlled. A total of 40 relatively well-detailed walls that were closely designed to the current U.S. design standards were examined. For shear-controlled walls, the mean $V_{\max}/V_{ne,ACI}$ was approximately 1.5 with curvature ductility less than 10. Flexure-controlled walls had mean $V_{\max}/V_{ne,ACI}$ less than 1.0 with curvature ductility greater than 10. The transition region (flexure-shear controlled walls) had $V_{\max}/V_{ne,ACI}$ greater than 1.0 and curvature ductility greater than 10. Subsequently, more test results were compiled for shear-controlled walls to establish statistical parameters for shear capacities. Shear-controlled walls were categorized into two bins according to concrete compressive strengths as $f'_c \geq 8\text{ksi}$ and $f'_c < 8\text{ksi}$. The data for the two bins were obtained from Wallace (1998) and Wood (1990), respectively. Based on the findings, the following conclusions were made:

1. For structural walls with $f'_c \geq 8\text{ksi}$, 37 shear-controlled wall tests were examined. Shear capacity had a mean overstrength of 1.57 with a coefficient of variation of 0.20. The data were observed to follow normal distribution.
2. For structural walls with $f'_c < 8\text{ksi}$, 143 shear-controlled wall tests were examined. Shear capacity had a mean overstrength of 1.67 with a coefficient of variation of 0.40. The data were observed to follow lognormal distribution.

3. The current nominal shear strength equation presented in ACI318-11 (shown below) is conservative by aforementioned overstrength factors.

$$V_{n,e} = A_{cv} \left[\alpha_c \lambda \sqrt{f'_c} + \rho_t f_y \right]$$

4. The dispersion (COV) measured from data presented by Wallace (1998) and Wood (1990) derives from variability and uncertainties in nominal shear strength prediction equation, material strengths including concrete compressive strengths and reinforcing steel yield strengths, construction quality, test setup, test measurement, and other possible errors. Due to high quality measures enforced for tall building design and construction through Seismic Peer Review Panels (LATBSDC, 2014) and required inspections, no further dispersion was added to the measured values.

7.6. Limitations and Future Work

Limitations and future work are listed as follows.

1. This study was conducted with the assumption that flexural yielding in structural walls was limited within LATBSDC (2014) recommendations; under these limitations, there is no significant shear strength degradation. Thus, full shear strength was assumed for structural wall shear designs. However, when there is increasing nonlinear flexural yielding, shear strength starts to degrade. Further dynamic tests are necessary to quantify the shear strength degradation associated with nonlinear flexural yielding. This is further explained in the following.
2. All tests documented from the two studies, Wallace (1998) and Wood (1990), were quasi-static wall tests performed on reduced-scale specimens under monotonic, repeated, or cyclic loads. Historically, these test procedures have been utilized to observe wall behaviors and determine strength equations. However, to evaluate structural behavior and capacity of reinforced concrete structural walls under high seismic events (when there is increased nonlinear flexural yielding), it will be necessary to perform more nonlinear dynamic tests in the future. Although dynamic tests tend to be more costly, (1) an assessment of interactions between various structural wall components, (2) quantifying shear degradation associated with increasing nonlinear flexural yielding, as well as (3) measuring initial, ultimate, and residual properties of structural walls during dynamic tests will be beneficial.
3. Shear capacities were calculated per ACI318-11 equations which were based on plane section structural walls. Further tests on L-shaped or core walls using bi-axial loading

will be necessary to understand how shear capacities in core walls may change with varying compressive zones during a strong ground shaking.

4. Currently, there are 5 large reinforced-concrete structural wall databases available. They consist of: (1) Network for Earthquake Engineering Simulation Hub (NeesHub), (2) American Concrete Institute (ACI) database, (3) Seismic Engineering Research Infrastructures for European Synergies (SERIES) by University of Patras, (4) University of California, Los Angeles (UCLA) database that comprises of 216 wall tests, and (5) University of Auckland (UoA) database that contains 144 wall tests. There are numerous wall tests that belong to all databases but there are also many wall tests that only belong to only one or a few databases. This makes it challenging to search for all relevant information available. Thus, there are joint efforts by the Virtual International Institute for Performance Assessment of Wall Systems (2015) to merge the databases and to request permission to access all test results. In this study, the shear controlled wall test results from Wallace (1998) were recovered from the UCLA database but it would be beneficial to access more shear controlled wall data and categorize them into different bins that are relevant to tall buildings (symmetric/asymmetric wall geometries, various axial load ratios $P/(A_g \cdot f'_c)$, etc) to further expand this study in the future.

CHAPTER 8. STRUCTURAL WALL SHEAR DESIGN RELIABILITY

This chapter reviews various component reliability methodologies and describes the procedures used to compute reliability of structural wall shear design for tall buildings. Reliability of structural wall shear design is presented for various risk categories and ground motion intensities.

8.1. Background

In United States, probability-based limit state design (PBLSD) is adopted in many material-specific codes to establish design acceptance criteria for structural components. PBLSD examines reliability of a structural component by calculating the probability of component failure due to demands exceeding the component capacity, $C < D$. Although the terminology used in PBLSD is based on load (Q) and resistance (R), load will be referred to as demand, resistance will be referred to as capacity, and limit states will be referred to as acceptance criteria to be consistent with capacity design terminology used in LATBSDC (2014). Per PBLSD, failure is defined as

$$P_f = P(C < D) = \int_{-\infty}^{+\infty} F_C(q_i) f_D(q_i) \cdot dq_i$$

where C is capacity, D is demand, F_C is cumulative probability distribution function of C and f_D is probability density function for D. In practice, rather than using the integral to compute probability of failure, probability of failure is calculated indirectly with a reliability index, β through a closed-form solution (Melchers, 1999, O. Ditlevsen and Madsen, 2005). For seismic events conditioned upon MCE level ground shaking, the anticipated reliability and corresponding reliability indexes per ASCE7-10 are summarized in Table 8-1.

Table 8-1. Anticipated reliability and corresponding reliability indexes, conditioned upon MCE level ground shaking

Risk Category	Anticipated Reliability	Probability of Failure, P_f	Reliability Index, β
I, II	90%	10%	1.28
III	94%	6%	1.56
IV	97%	3%	1.88

When closed-form solutions for probability of failure are not available, Monte Carlo methods can be utilized. Some of the key advantages of adopting Monte Carlo method are that there are no limitations on the random variable parameters (number of variables, probability distributions, etc), provided that the necessary computing power is available.

In the following sections, full distribution methods to compute probability of failure with β are briefly explained for the two cases where random variables C and D follow normal and lognormal distributions, and the Monte Carlo simulation techniques are explained.

8.2. Normal Distribution for Random Variables C and D

When random variables C and D are jointly normal, it is convenient to consider safety margin, which is defined as $F = C - D$. Since C and D are normal random variables and F is a linear combination the two, F is also a normal random variable. In this case, a closed-form solution can be used to calculate probability of failure, where $P_f[F \leq 0] = \Phi[-\beta]$ and the reliability index is defined as an inverse coefficient of variation of the safety margin:

$$\beta = \frac{\bar{F}}{\sigma_F} = \frac{\bar{C} - \bar{D}}{\sqrt{\sigma_C^2 + \sigma_D^2 - 2 \cdot \rho_{CD} \cdot \sigma_C \cdot \sigma_D}}$$

where, $\bar{F}, \bar{C}, \bar{D}, \sigma_F, \sigma_C, \sigma_D$ are expected values and standard deviations of safety margin, capacity, and demand, respectively, and ρ_{CD} is correlation between capacity and demand. In the case where the random variables C and D are statistically independent ($\rho_{CD} = 0$),

$$\beta = \frac{\bar{C} - \bar{D}}{\sqrt{\sigma_C^2 + \sigma_D^2}}$$

An equivalent representation of the reliability index can be expressed through an introduction of a demand factor and coefficient of variation for capacity and demand

$$\beta = \frac{1 - \left(\frac{1}{\gamma}\right)}{\sqrt{\rho_C^2 + \left(\frac{\rho_D^2}{\gamma^2}\right)}}$$

where demand factor and coefficient of variation for capacity and demand are defined as

$$\gamma = \frac{\bar{C}}{\bar{D}}, \rho_C = \frac{\sigma_C}{\bar{C}} \text{ and } \rho_D = \frac{\sigma_D}{\bar{D}}$$

To transform safety margin to a standard normal variable with expected value of 0 and variance of 1, a new variable U is introduced as

$$U = \left(\frac{f - \bar{F}}{\sigma_F} \right) = \left(\frac{f}{\sigma_F} \right) - \beta$$

where f is the outcome and F is the expected value of safety margin. The probability density function and cumulative distribution function of the standard normal variable are

$$p(f) = \frac{1}{\sigma_F \sqrt{2\pi}} \cdot \exp \left\{ -\frac{1}{2} \left(\frac{f - \bar{F}}{\sigma_F} \right)^2 \right\}$$

$$P_f[F \leq f] = \Phi \left(\frac{f - \bar{F}}{\sigma_f} \right)$$

where Φ represents standard normal cumulative distribution function. When failure occurs, $f=0$ and the probability of failure is

$$P_f[F \leq 0] = \Phi[-\beta]$$

Thus, when the reliability index is known, standard normal tables can be utilized to evaluate the probability of failure.

8.3. Lognormal Distribution for Random Variables C and D

When random variables C and D are jointly lognormal, it is convenient to consider safety factor, which is defined as

$$F = \frac{C}{D}$$

A random variable is defined to be lognormally distributed when its logarithm is normally distributed. Thus, new normal random variables, $X=\ln(C)$, $Y=\ln(D)$, and $Z=\ln(F)$, are introduced and safety factor can be expressed with a normal random variable Z, where

$$\ln(F) = \frac{\ln(C)}{\ln(D)}$$

$$Z = X - Y$$

In this case, a closed-form solution can be used to calculate probability of failure, where $P_f[Z \leq 0] = \Phi[-\beta]$ and the reliability index is expressed as inverse coefficient of variation of Z

$$\beta = \frac{\bar{Z}}{\sigma_Z} = \frac{\bar{X} - \bar{Y}}{\sqrt{\sigma_X^2 + \sigma_Y^2 + 2 \cdot \rho_{XY} \cdot \sigma_X \cdot \sigma_Y}}$$

where standard deviation of Z is $\sigma_Z = \sqrt{\sigma_X^2 + \sigma_Y^2 + 2 \cdot \rho_{XY} \cdot \sigma_X \cdot \sigma_Y}$. The expected values of X and Y are $\bar{X} = \ln(\bar{C}) - \left(\frac{\sigma_X^2}{2}\right)$ and $\bar{Y} = \ln(\bar{D}) - \left(\frac{\sigma_Y^2}{2}\right)$, and standard deviations of X and Y are $\sigma_X = \sqrt{\ln(1 + \rho_C^2)}$ and $\sigma_Y = \sqrt{\ln(1 + \rho_D^2)}$. Substituting for these values, reliability index can be rewritten as

$$\beta = \frac{\ln \left(\gamma \cdot \sqrt{\frac{1 + \rho_D^2}{1 + \rho_C^2}} \right)}{\sqrt{\ln(1 + \rho_C^2) + \ln(1 + \rho_D^2) - 2 \cdot \rho_{\ln C, \ln D} \sqrt{\ln(1 + \rho_C^2)} \sqrt{\ln(1 + \rho_D^2)}}$$

When random variables C and D are statistically independent,

$$\beta = \frac{\ln \left(\gamma \cdot \sqrt{\frac{1 + \rho_D^2}{1 + \rho_C^2}} \right)}{\sqrt{\ln(1 + \rho_C^2) + \ln(1 + \rho_D^2)}}$$

Again, when reliability index is known, standard normal tables can be utilized to find probability of failure as

$$P_f \left[\ln \left(\frac{C}{D} \right) \leq 0 \right] = \Phi \left(\frac{0 - \bar{Z}}{\sigma_Z} \right) = \Phi[-\beta]$$

8.4. Monte Carlo Simulations

The basic concept behind Monte Carlo simulation is described for the case where probability of failure is evaluated as demands exceeding the component capacity, $P_f(F = C - D < 0)$.

1. Select random variables C and D.
2. Establish probability distributions of selected random variables using previous test results.
3. Randomly generate values for all random variables.
4. Calculate $F = C - D$.
5. Repeat steps 1-4 until a sufficient number of samples have been generated and confirm that coefficient of variation for the Monte Carlo P_f estimator is within a specified tolerance.
6. Estimate probability of failure as

$$P_f = \frac{\text{number of times that } F < 0}{\text{total number of simulations}}$$

8.5. Component Reliability Methodology

The aforementioned methods were used to assess reliability of the current structural wall shear design criterion. Reliability of structural wall shear design was assessed in two ways, using closed-form solutions and Monte Carlo simulations. The process of using closed-form solutions is summarized in the flowchart shown on Figure 8-1. The process starts with establishing statistical parameters for shear demand and capacity. For shear demands, the following parameters were considered: (1) normal and lognormal probability distributions, (2) a series of demand factors, γ , varying from 1.0 to 2.0, and (3) coefficients of variation ranging between 0.20 and 0.60 for each γ . The mean shear demand of 1.0 was used, assuming that all design requirements per LATBSDC (2014) and ACI318-11 were satisfied. Shear capacity parameters were separated into two bins, for walls with $f'_c < 8\text{ksi}$ and $f'_c \geq 8\text{ksi}$, as described in Chapter 7. Once the demand and capacity statistical parameters were defined, closed-form solutions were used to compute probability of failure with the corresponding reliability index, β .

Additionally, Monte Carlo simulations were used to assess reliability of the current structural wall shear design criterion. The MCE level shear demands from Monte Carlo simulations (Chapter 6) were used; the demands were normalized by their means, and shear capacities were randomly generated using the statistical parameters described in Chapter 7. A total of 1000 simulations were performed. A summary of all reliability methodology and parameters used is provided in Table 8-2 below.

In Chapter 6, the total measured dispersion for shear demand ranged between 0.20 and 0.45 for all hazard levels. Thus, reliability results were recommended using a realistic shear dispersion value value of $\rho_D = 0.40$ and a conservative shear dispersion value of $\rho_D = 0.50$.

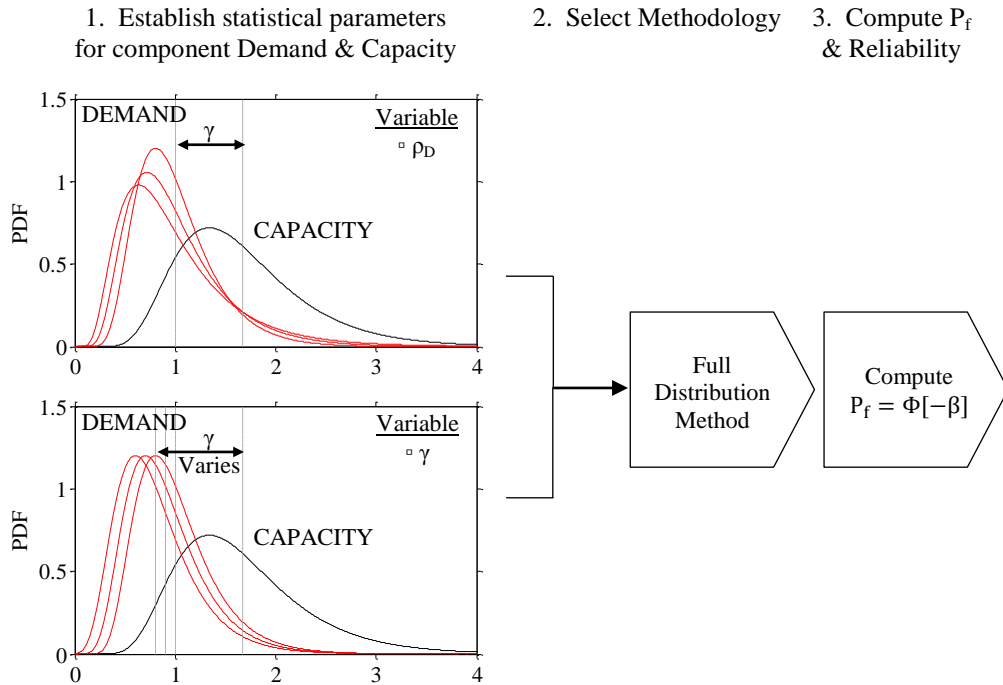


Figure 8-1. Flowchart of component reliability assessment using closed form solutions

Table 8-2. Summary of all reliability methodology and parameters considered

[Bin] Chapter	Methodology	Distribution	Demand Parameters	Capacity
[1] Ch. 8.6.1	Full Distribution Method (closed- form solutions)	Normal	$\gamma = 1.0$ ($\rho_D = 0.2$ to 0.6) ... to $\gamma = 2.0$ ($\rho_D = 0.2$ to 0.6)	$f'_c < 8\text{ksi}$ □ Wood (1990)
		Lognormal	$\gamma = 1.0$ ($\rho_D = 0.2$ to 0.6) ... to $\gamma = 2.0$ ($\rho_D = 0.2$ to 0.6)	□ Lognormal distribution □ Mean = 1.67 □ $\rho_C = 0.40$
	Monte Carlo Simulations □ 1000 runs	Actual (Chapter 6)	$\gamma = 1.0$ to $\gamma = 2.0$ $\rho_D = \text{actual}$ (Ch. 6)	
[2] Ch. 8.6.3	Full Distribution Method (closed- form solutions)	Normal	$\gamma = 1.0$ ($\rho_D = 0.2$ to 0.6) ... to $\gamma = 2.0$ ($\rho_D = 0.2$ to 0.6)	$f'_c \geq 8\text{ksi}$ □ Wallace (1998)
		Lognormal	$\gamma = 1.0$ ($\rho_D = 0.2$ to 0.6) ... to $\gamma = 2.0$ ($\rho_D = 0.2$ to 0.6)	□ Normal distribution □ Mean = 1.57 □ $\rho_C = 0.20$
	Monte Carlo Simulations □ 1000 runs	Actual (Chapter 6)	$\gamma = 1.0$ to $\gamma = 2.0$ $\rho_D = \text{actual}$ (Ch. 6)	

8.6. Shear Design Reliability | MCE Hazard Level

8.6.1. Structural Walls with $f'_c < 8\text{ksi}$

Shear design reliability was first assessed for structural walls with concrete compressive strengths less than 8ksi. Statistical parameters for shear capacity were held constant, as shown on Figure 7-2(b).

First, using closed-form solutions, the relationship between reliability and γ are plotted on Figure 8-2(a) for a range of ρ_D ; these were plotted upon examining normal and lognormal distributions for shear demands and the more conservative case was plotted for each combination of γ and ρ_D . As expected, to achieve the same level of reliability, demand factors increased as shear demand dispersion increased. Furthermore, when examining a fixed demand factor, reliabilities decreased with increasing shear demand dispersion. Using a realistic shear dispersion value ($\rho_D=0.40$), γ for 90%, 94%, and 97% reliabilities corresponded to approximately 1.25, 1.40, and 1.70, respectively. Using a conservative shear dispersion value ($\rho_D=0.50$), γ for 90%, 94%, and 97% reliabilities corresponded to approximately 1.30, 1.50, and 1.85, respectively. These values were rounded up to the nearest 0.05 and were summarized in Table 8-5. Next, reliability results computed directly from Monte Carlo simulations performed in Chapter 6 were compared to the closed-form solutions and results--see Figure 8-2(b). A summary of all Monte Carlo simulations used to compute reliability results are presented on Table 8-3. As it can be seen, results from Monte Carlo simulations provide a fairly close estimation, compared to the closed-form solutions. The differences in the closed-form solutions and Monte Carlo simulations resulted from two main reasons, where (1) the closed-form solutions were computed from worst-case scenarios resulting from shear demands following either normal or lognormal distributions, whereas shear demands from Monte Carlo simulations

were not fitted to any distributions, and (2) since Monte Carlo simulations were performed 1000 times, there was a variation in the Monte Carlo probability of failure estimator, and this is further discussed in the next section.

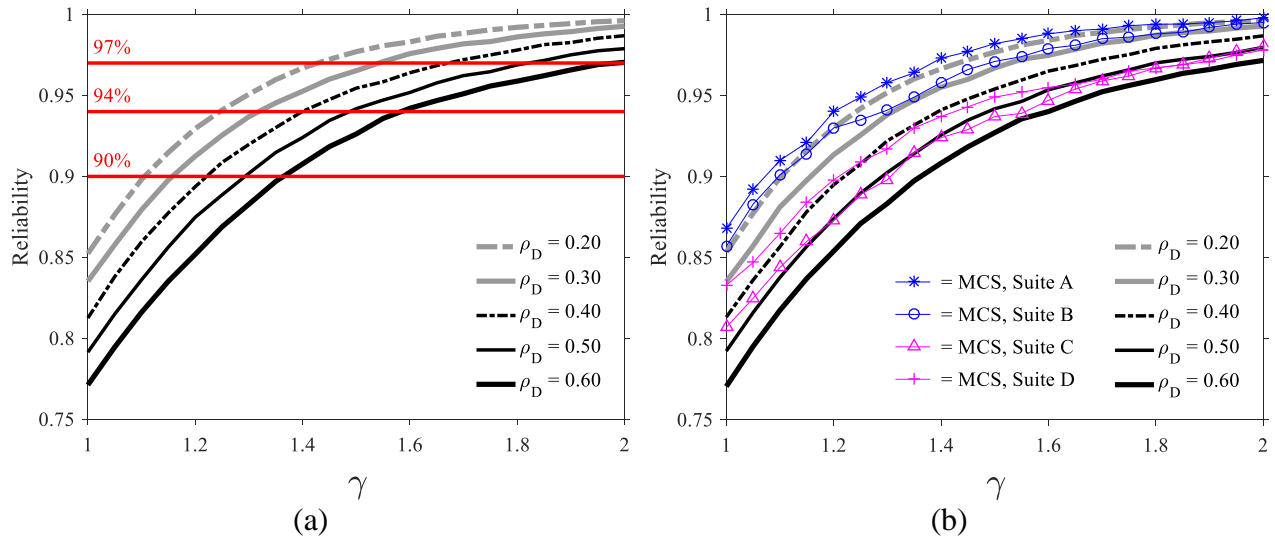


Figure 8-2. Shear design reliability | MCE hazard for structural walls with $f'_c < 8\text{ksi}$ (a) per closed-form solutions and (b) comparative results between closed-form solutions and Monte Carlo simulations

Table 8-3. Summary of MCE level Monte Carlo simulations

Analysis Type	Ground Motions	Software Platform	Model	RV used for Figure 8-2(b) and Figure 8-4(b)	Shear demand COV, ρ_D (Chapter 6)
Monte Carlo simulations	Suite A	Perform 3D	30-Story	Independent	0.23
	Suite B				0.33
	Suite C	Opensees	20-Story	Independent	0.44
	Suite D		30-Story		0.42

8.6.2. Variations in Monte Carlo Probability of Failure Estimator

Using the properties of the Monte Carlo probability of failure estimator, P_f (Nowak and Collins, 2000), the required number of samples can be calculated through

$$n = \frac{1 - P_f}{\delta^2 \cdot P_f}$$

where n is the required number of runs and δ is variation in P_f . This relationship is further depicted graphically in Figure 8-3. Since Monte Carlo simulations were performed 1000 times (as presented in Chapter 6), the variations in P_f was less than 0.10 when P_f was less than 0.10, whereas variations increased as smaller P_f was considered. For all risk categories, the variations in the Monte Carlo P_f are summarized in Table 8-4. For all reliabilities computed for risk categories I through IV, the variations were between approximately 0.10 and 0.18.

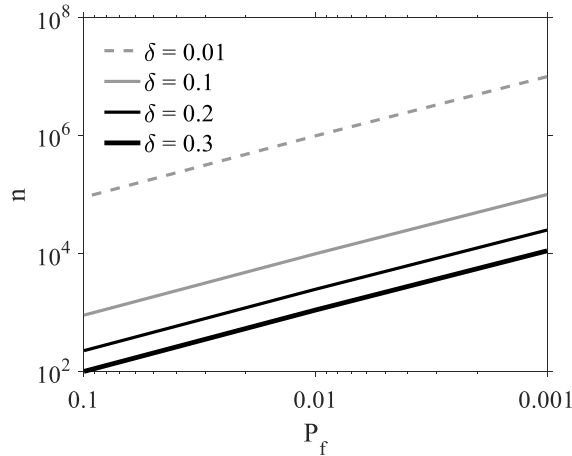


Figure 8-3. Variations in Monte Carlo probability of failure estimator versus required number of runs

Table 8-4. Summary of variations in Monte Carlo probability of failure estimator

Risk Category	P_f	n	δ
I and II	0.10	1000	0.095
III	0.06	1000	0.125
IV	0.03	1000	0.179

8.6.3. Structural Walls with $f'_c \geq 8\text{ksi}$

The procedures described in Chapter 8.6.1 were repeated to evaluate structural walls with $f'_c \geq 8\text{ksi}$. Statistical parameters for shear capacity were held constant, as shown on Figure 7-2(a). First, using closed-form solutions, the relationship between reliability and γ are plotted on Figure 8-4(a) for a range of ρ_D ; these were plotted upon examining normal and lognormal distributions for shear demands and the more conservative case was plotted for each combination of γ and ρ_D . Using a realistic shear dispersion value ($\rho_D=0.40$), γ for 90%, 94%, and 97% reliabilities corresponded to approximately 1.10, 1.25, and 1.40, respectively. Using a conservative shear dispersion value ($\rho_D=0.50$), γ for 90%, 94%, and 97% reliabilities corresponded to approximately 1.15, 1.35, and 1.55, respectively; these values are summarized in Table 8-5. The comparative results computed from Monte Carlo simulations and closed-form solutions are presented on Figure 8-4(b). The reliability results calculated from Monte Carlo simulations provide a fairly close estimation, compared to the closed-form solutions, and the sources of differences are described in Chapter 8.6.1.

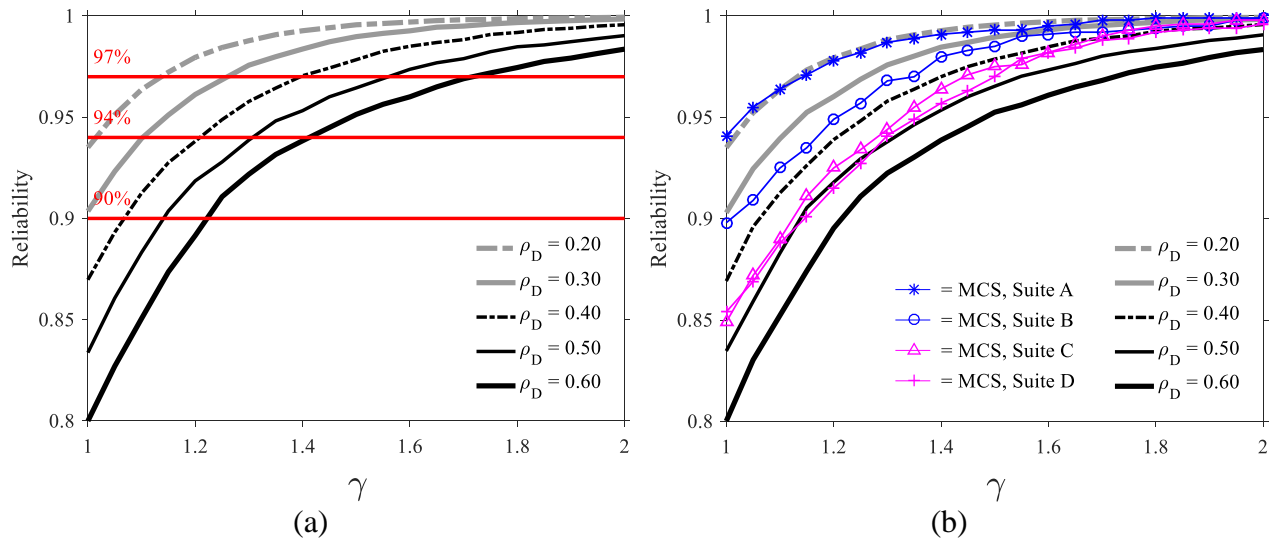


Figure 8-4. Shear design reliability | MCE hazard for structural walls with $f'_c \geq 8\text{ksi}$ (a) per closed-form solutions and (b) comparative results between closed-form solutions and Monte Carlo simulations

Table 8-5. Comparison of minimum required γ to achieve anticipated reliability versus current γ

Structural Wall f'_c	Risk Category	Reliability	Minimum required		Current ¹
			γ $\rho_D = 0.40$ (realistic)	γ $\rho_D = 0.50$ (conservative)	γ (empirical)
$f'_c < 8\text{ksi}$	I, II	90%	1.25	1.30	1.50
	III	94%	1.40	1.50	1.50
	IV	97%	1.70	1.85	-
$f'_c \geq 8\text{ksi}$	I, II	90%	1.10	1.15	1.50
	III	94%	1.25	1.35	1.50
	IV	97%	1.40	1.55	-

¹ LATBSDC (2014)

8.6.4. Summary

A summary of reliability results from Sections 8.6.1 and 8.6.3 are tabulated on Table 8-6. In addition to using measured ρ_C for shear capacity, reliability results from more conservative ρ_C values were computed for comparison. Linear interpolations of γ provide conservative estimates of shear design reliability and shaded regions indicate reliability less than 90%.

Table 8-6. Shear design reliability (%) | MCE hazard based on various values of γ , ρ_D , and ρ_C

Capacity COV, ρ_C	$f'_c < 8\text{ksi}$						$f'_c \geq 8\text{ksi}$						Capacity COV, ρ_C
	γ	ρ_D					ρ_D					γ	
		0.2	0.3	0.4	0.5	0.6	0.2	0.3	0.4	0.5	0.6		
0.40 (Measured)	1.0	85.3	83.4	81.4	79.2	77.2	93.6	90.4	86.7	83.3	80.1	1.0	0.20 (Measured)
	1.5	97.6	96.7	95.5	94.2	92.7	99.6	99.0	97.9	96.5	95.1	1.5	
	2.0	99.6	99.2	98.7	98.0	97.3	99.9	99.8	99.5	99.0	98.3	2.0	
0.50	1.0	79.3	78.3	76.8	75.3	74.0	86.7	84.4	82.0	79.3	77.4	1.0	0.30
	1.5	94.6	93.6	92.5	91.0	89.6	96.8	95.9	94.9	93.7	92.7	1.5	
	2.0	98.4	97.9	97.2	96.4	95.6	98.7	98.4	98.0	97.4	96.7	2.0	
0.60	1.0	73.7	73.2	72.5	71.7	70.7	80.6	79.5	77.8	76.3	74.4	1.0	0.40
	1.5	90.6	89.8	88.6	87.5	86.4	92.0	91.4	90.7	89.8	88.7	1.5	
	2.0	96.5	95.9	95.2	94.3	93.3	95.4	95.0	94.6	94.1	93.6	2.0	

8.7. Shear Design Reliability | All Hazard Levels

In addition to MCE hazard results, shear design reliability was computed at all hazard levels using mean shear demand ratios as shown on Table 6-9. Mean shear demand ratios for SLE25, SLE43, DBE, MCE and OVE hazard levels were 0.38, 0.44, 0.81, 1.0, and 1.07 (normalized at MCE level), respectively. Using these means, reliability values were computed and presented as a function of ground motion intensity, denoted as spectral acceleration at first mode period: $Sa(T_1)$. The results are presented on Figure 8-5. The blue single-hatched region indicates reliability using $\gamma=1.5$, the black speckled region indicates reliability using $\gamma=1.3$, and the red cross-hatched region indicates reliability using $\gamma=1.0$; all regions were computed with ρ_D between 0.20 and 0.60. The data points were fitted with maximum likelihood estimation method by Baker (2011). It is apparent that using the current recommendations of $1.5 \cdot F_{uc}$ for shear demand results in over 90% reliability for ground motion intensities up to $Sa(T_1) = 0.40$ and 0.50 for structural walls with $f'_c < 8\text{ksi}$ and $f'_c \geq 8\text{ksi}$, respectively. However, the values shown on Figure 8-5 were computed based on a case study 30-story building; further studies are necessary to normalize these results for tall reinforced-concrete core wall buildings.

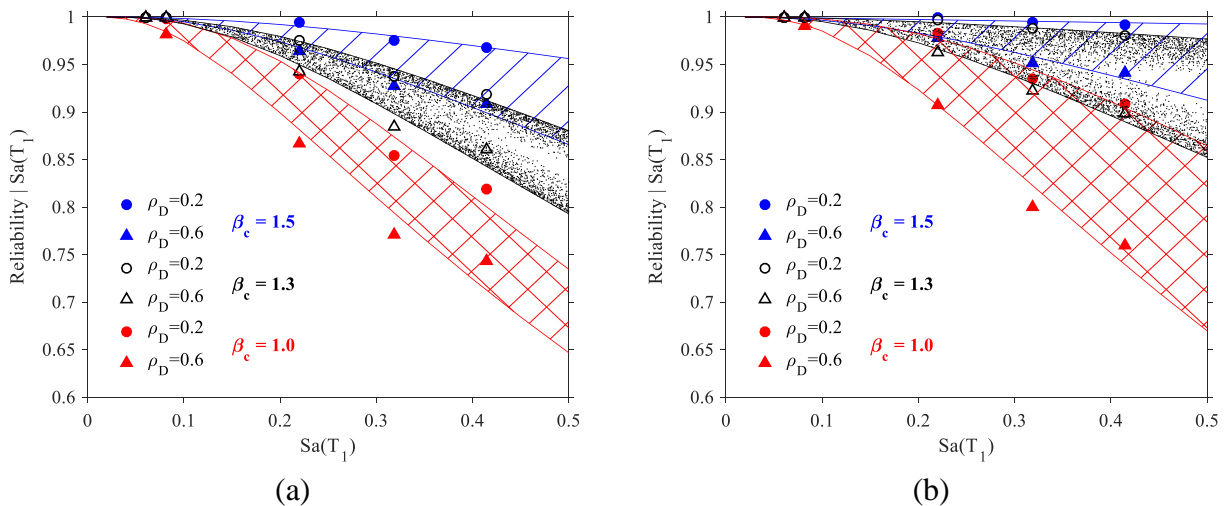


Figure 8-5. Shear design reliability at various ground motion intensities for structural walls with (a) $f'_c < 8\text{ksi}$ (b) $f'_c \geq 8\text{ksi}$

8.8. Conclusions

A methodology was developed to assess reliability of structural wall shear design for tall reinforced-concrete core wall buildings. Given statistical parameters for shear demand and capacity, closed-form solutions and Monte Carlo simulations were utilized to evaluate reliability of the current shear design acceptance criterion set forth by LATBSDC (2014). Reliabilities were computed with various parameters for shear demand and capacity. Based on the findings, the following conclusions were reached:

1. The current recommended shear design acceptance criterion, $\gamma \cdot F_{uc} \leq \kappa_i \cdot \phi \cdot F_{n,e}$ where $\gamma=1.5$, $\phi=1.0$, $\kappa_i=1.0$, and $\rho_D = 0.50$, resulted in 96.5% reliability for structural walls with $f'_c \geq 8\text{ksi}$ and 94.2% for structural walls with $f'_c < 8\text{ksi}$, conditioned upon MCE hazard level ground shaking, for the 20- and 30-story buildings studied.
2. For realistic reliability recommendations, $\rho_D = 0.40$ was used. For all ranges of f'_c considered, $\gamma=1.25$ is required to achieve 90% reliability, $\gamma=1.4$ is required to achieve 94% reliability, and $\gamma=1.7$ is required to achieve 97% reliability.
3. For conservative reliability recommendations, $\rho_D = 0.50$ was used. For all ranges of f'_c considered, $\gamma=1.3$ is required to achieve 90% reliability, $\gamma=1.5$ is required to achieve 94% reliability, and $\gamma=1.85$ is required to achieve 97% reliability.
4. Using the current recommendations of $1.5 \cdot F_{uc}$ for shear demand on a case study 30-story building resulted in over 90% reliability for ground motion intensities up to $Sa(T_1) = 0.40$ and 0.50 for structural walls with $f'_c < 8\text{ksi}$ and $f'_c \geq 8\text{ksi}$, respectively.

8.9. Limitations and Future Work

Limitations and future work are listed as follows.

1. The shear design reliabilities in this chapter were conducted using shear demand dispersion information from 20 and 30-story buildings at one project site. However, to recommend any changes in the governing building codes and tall building design guidelines, a reliability study including a large population of tall buildings is further needed to calibrate γ and ϕ factors.
2. This study focused primarily on reliability of structural wall shear design reliability. However, it would be worthwhile to expand this study to examine reliability of other components for tall reinforced-concrete core wall buildings. Examining reliability of deformation-controlled components, such as coupling beams and flexural capacity of structural walls, will provide useful information not only on component levels but also on how the performance of these components may contribute to the system level reliability.

CHAPTER 9. CONCLUSIONS

Reliability of structural wall shear design for tall reinforced-concrete core wall buildings was examined for various risk categories and ground motion intensities. Statistical parameters for shear demand were quantified through 20 and 30-story building nonlinear response history analyses performed through Monte Carlo simulations, and statistical parameters for shear capacity were measured through existing shear controlled wall test results. Given the statistical parameters for shear demand and capacity, closed-form solutions and Monte Carlo simulations were utilized to evaluate reliability of the current shear design acceptance criterion set forth by LATBSDC (2014):

$$F_{uc} \leq \kappa_i \phi F_{n,e}$$

where F_{uc} is 1.5 times the mean shear demand resulting from a suite of ground motions, $F_{n,e}$ is the nominal strength computed from expected material properties, ϕ is the uncertainty in $F_{n,e}$, taken as 1.0, and κ_i is the risk reduction factor, taken as 1.0 for the MCE level analysis. The 1.5 factor applied to the mean shear demand is referred to as the demand factor, γ . Reliabilities were computed with various statistical parameters for shear demand and capacity. It is important to note that these reliabilities were computed based on the assumption that flexural yielding in walls was limited by following all axial tensile and compressive strain requirements as noted in Figure 7-5. This ensures that there is no significant shear capacity degradation in structural walls. The following conclusions were drawn from the results:

Tall Building Modeling – Materials

1. As documented in Nowak et al (2008), expected concrete compressive strengths should be adjusted to $1.1 \cdot f'_c$ for high strength concrete compressive strengths ranging between 6ksi and 12ksi, unless project-specific material testing is conducted to justify a higher value. Current guidelines for the use of $1.3 \cdot f'_c$ per LATBSDC (2014) is more appropriate for normal strength concrete; the incorrect use of expected strength factors can result in inaccurate shear demands and capacities.

Tall Building Modeling – Systems

2. The use of Rayleigh versus modal damping in Perform 3D analysis resulted in notable differences for the 30-story reinforced concrete core wall building. Using Rayleigh damping generally resulted in underestimation of coupling beam rotations, up to 18%, underestimation of base shear demands, up to 14%, whereas it had minor effects (typically less than 5%) on interstory drifts.

Quantification of Dispersion in Various Engineering Demand Parameters

3. From both 3D (Perform 3D) and 2D (Opensees) Monte Carlo simulations, total dispersion for all EDPs were quantified as COV. Across all hazard levels, total dispersion ranged between 0.20-0.45 for base shear forces and roof drifts, 0.40-0.85 for coupling beam rotations, 0.40-0.60 and 0.15-0.40 for tensile and compressive axial strains at shear wall corner boundary elements, and 0.40-0.65 and 0.40-0.75 and 0.20-0.75 for tensile and compressive axial strains at shear wall end boundary elements. The dispersion in EDPs was the largest for coupling beam rotations and shear wall axial strains.

4. Probability distributions were either lognormal or normal for all EDPs at all hazard levels. For reliability or collapse analysis, investigating results from both probability distributions to determine a more conservative case is recommended at this time.
5. For structural reliability or collapse analyses, appropriate uses of dispersion measure from DBE, MCE, and OVE columns in Table 6-8 are recommended. In all cases, minimum values of 0.20 and 0.05 are recommended for RTR variability and model parameter/design uncertainties, respectively.
6. Relative contributions to total dispersion consisted of 72% to 98% from RTR variability and 2% to 28% from model parameter/design uncertainties. Thus, RTR variability was the dominant source of uncertainty which is in agreement with findings from Porter et al (2002) and Lee and Mosalam (2005).
7. Changes in dispersion measure due to positive correlation in model parameter random variables ranged from -6% to +5%; thus, introducing positive correlation in model parameter uncertainties did not have a significant impact in dispersion estimation.

Shear Capacity Mean and Dispersion

8. For structural walls with $f'_c \geq 8$ ksi, 37 shear-controlled wall tests were examined. Shear capacity had a mean overstrength of 1.57 with a coefficient of variation of 0.20. The data were observed to follow normal distribution.
9. For structural walls with $f'_c < 8$ ksi, 143 shear-controlled wall tests were examined. Shear capacity had a mean overstrength of 1.67 with a coefficient of variation of 0.40. The data were observed to follow lognormal distribution. The measured dispersion derives from variability and uncertainties in nominal shear strength prediction equation, material strengths including concrete compressive strengths and reinforcing steel yield strengths,

construction quality, variations in test setup and test instrumentation, and other possible errors.

10. The current nominal shear strength equation presented in ACI318-11 (shown below) is conservative by aforementioned overstrength factors.

$$V_{n,e} = A_{cv} \left[\alpha_c \lambda \sqrt{f'_c} + \rho_t f_y \right]$$

Reliability of Structural Wall Shear Design

11. The current recommended shear design acceptance criterion, $\gamma \cdot F_{uc} \leq \kappa_i \cdot \phi \cdot F_{n,e}$ where $\gamma=1.5$, $\phi=1.0$, $\kappa_i=1.0$, and $\rho_D = 0.50$, resulted in 96.5% reliability for structural walls with $f'_c \geq 8$ ksi and 94.2% for structural walls with $f'_c < 8$ ksi, conditioned upon MCE hazard level ground shaking, for the 20- and 30-story buildings studied.
12. For realistic reliability recommendations, $\rho_D = 0.40$ was used. For all ranges of f'_c considered, $\gamma=1.25$ is required to achieve 90% reliability, $\gamma=1.4$ is required to achieve 94% reliability, and $\gamma=1.7$ is required to achieve 97% reliability.
13. For conservative reliability recommendations, $\rho_D = 0.50$ was used. For all ranges of f'_c considered, $\gamma=1.3$ is required to achieve 90% reliability, $\gamma=1.5$ is required to achieve 94% reliability, and $\gamma=1.85$ is required to achieve 97% reliability.
14. Using the current recommendations of $1.5 \cdot F_{uc}$ for shear demand on a case study 30-story building resulted in over 90% reliability for ground motion intensities up to $Sa(T_1) = 0.40$ and 0.50 for structural walls with $f'_c < 8$ ksi and $f'_c \geq 8$ ksi, respectively.

APPENDIX A

Description of the 20-Story Building

The 20-story office building is located in Los Angeles, California. The building consists of centrally located shear walls with coupling beams that wrap the elevator core. It has a typical floor area of 8,464 square feet and a typical story height of 11-feet. The gravity system consist of 8-inch two-way, post-tensioned concrete slabs on level 1 through the roof level. Figure A-1 shows a typical plan view of levels 1 through roof. Figure A-2 shows an elevation view of the south core walls. The two-way slabs are supported on 24-inch by 24-inch concrete columns at the exterior of the building and concrete shear walls at the interior of the building. The lateral system consist of 24-inch thick concrete shear walls coupled with 36-inch deep, diagonally reinforced coupling beams. See Table A-1 for a summary of structural system and element sizes over the height of the building. The gravity loading criteria is the same as those specified for the 30-story building, as shown on Chapter 4.3.

Table A-1. Dimensions of structural members for 20-story building

Element	Level	Structural system & size
Shear walls	1-Roof	24-in. thick reinforced concrete
Coupling beams	1-Roof	24-in x 36-in. deep reinforced concrete
Slabs	1-Roof	8-in. thick post-tensioned concrete
Columns	1-Roof	24-in. x 24-in. reinforced concrete

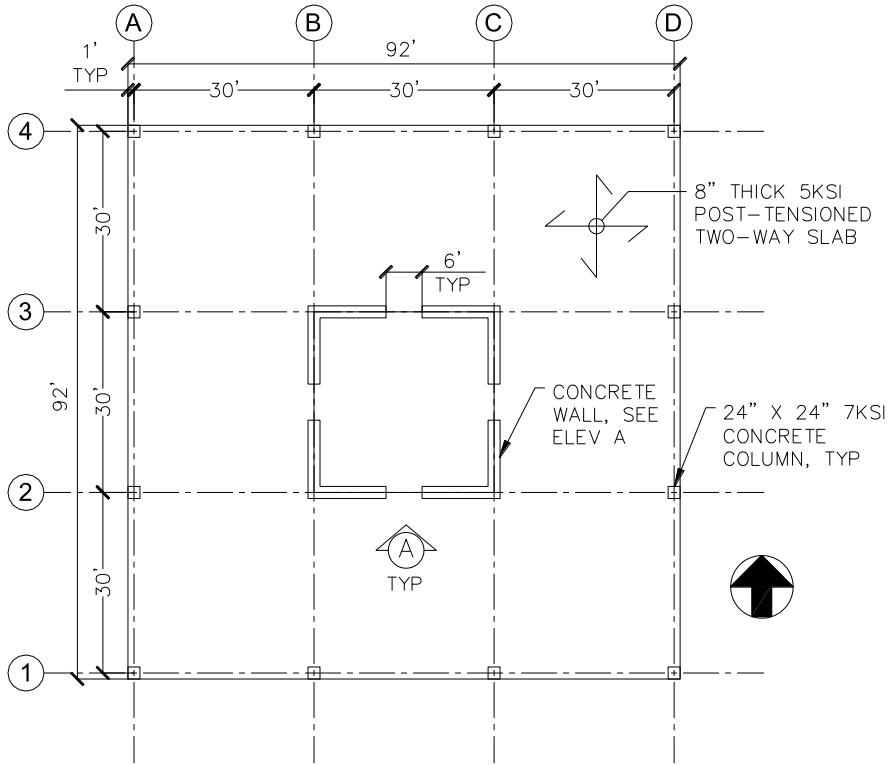


Figure A-1. 20-Story building, typical floor plan view

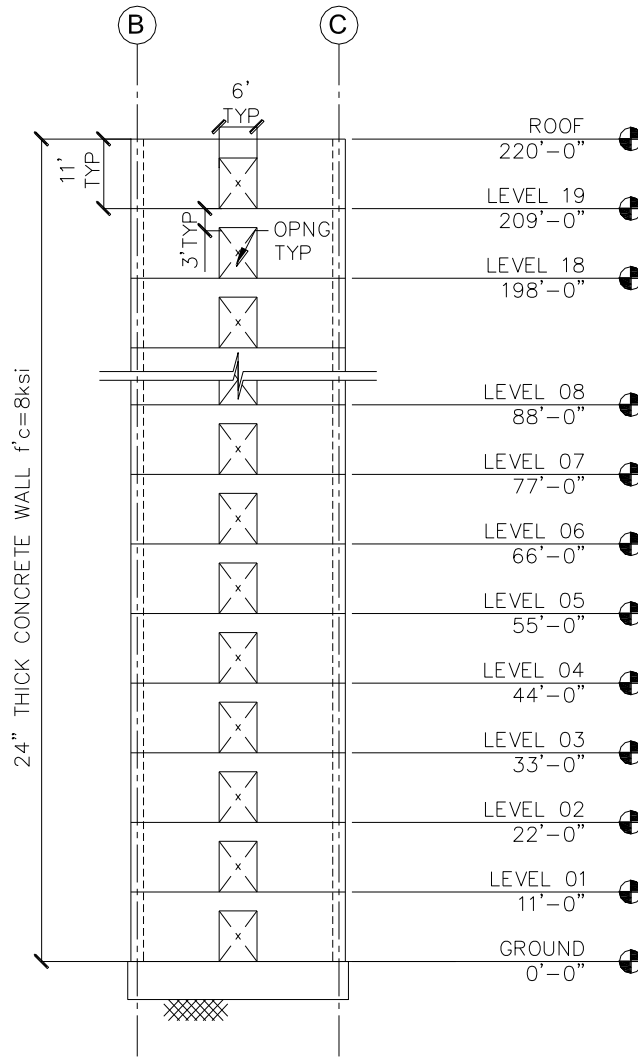


Figure A-2. 20-Story building, Elevation A of south wall

Strength and Stiffness Properties

The material strength and stiffness properties shown for the 30-story building in Chapter 4.5.2 were used to design the 20-story building. However, concrete properties shown on Chapter 5 were used for Monte Carlo simulations.

Coupling Beam and Structural Wall Designs

Diagonally reinforced coupling beams were designed with 6-#8 reinforcing per bundle and the strength-deformation parameters were calculated per procedures shown on Chapter 4. The structural walls were modeled with confined concrete for boundary elements and with unconfined concrete for web regions. The boundary elements were 48-inches in length and consisted of 3% reinforcing steel, and both web and transverse reinforcing steel ratios were specified at 0.41%. Other modeling procedures for structural walls were as shown on Chapter 4.5.3.

APPENDIX B

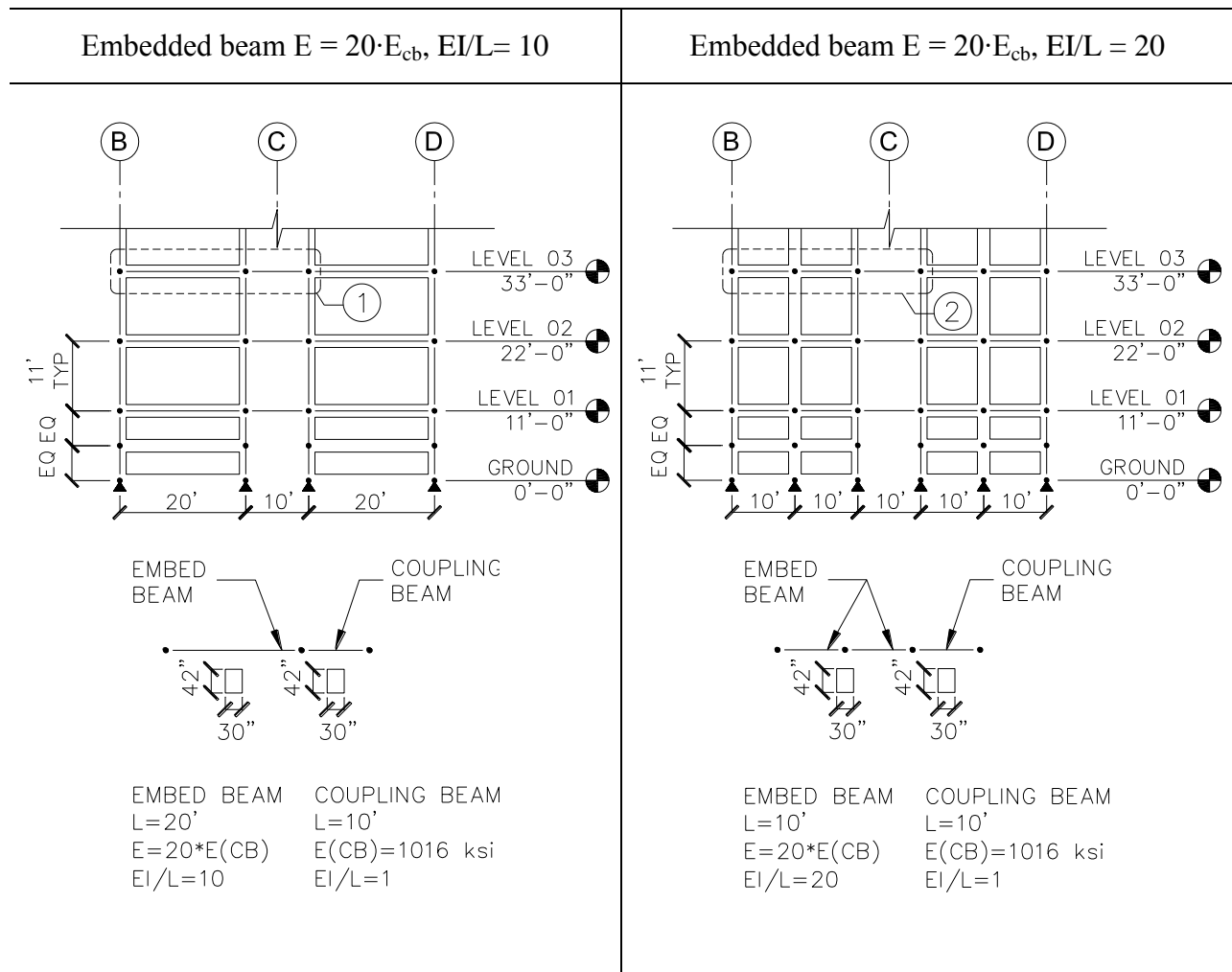
This section includes various sensitivity studies conducted from a 30-story reinforced-concrete core wall building. The basis of design from Chapter 4 was used to create a nonlinear model in Perform 3D. Although the design, modeling, and analysis procedures were very similar to the one demonstrated in Chapter 4, there were minor differences in design, such as shear wall and coupling beam thicknesses, and the amount of reinforcing in boundary elements and diagonally reinforced coupling beams. These small differences were deemed unimportant since relative values were evaluated in sensitivity studies. All sensitivity studies were conducted using 15 ground motions at the MCE level, except for the analysis of shear wall compressive zones, where MCE ground motion #14 was used. The following sensitivity studies are included in this Appendix:

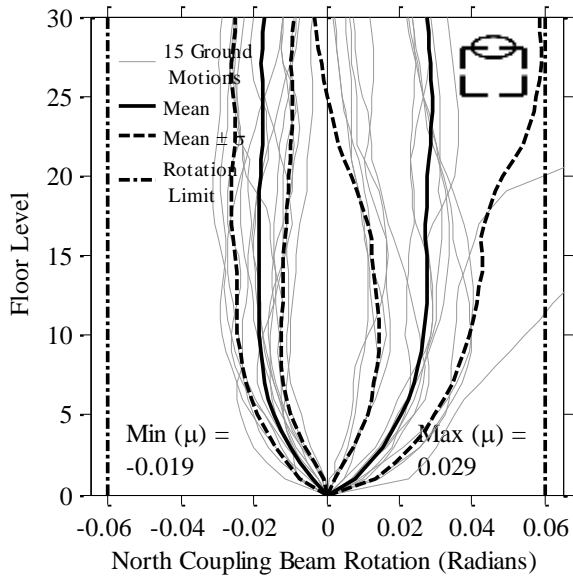
1. Embedded Beam Sensitivity Study
 - a. Embedded beam connected between 2 nodes ($EI/L=10$) versus 3 nodes ($EI/L=20$)
 - b. Embedded beam stiffness varied between 1, 5, 10, 20, 40 times E_{cb}
2. Rayleigh Damping versus Modal Damping
 - a. Interstory drifts
 - b. Coupling beam drifts
 - c. Shear demands
3. Shear Wall Axial Strains
4. Analysis of Core Wall Compressive Zones

1. Embedded Beam Sensitivity Study

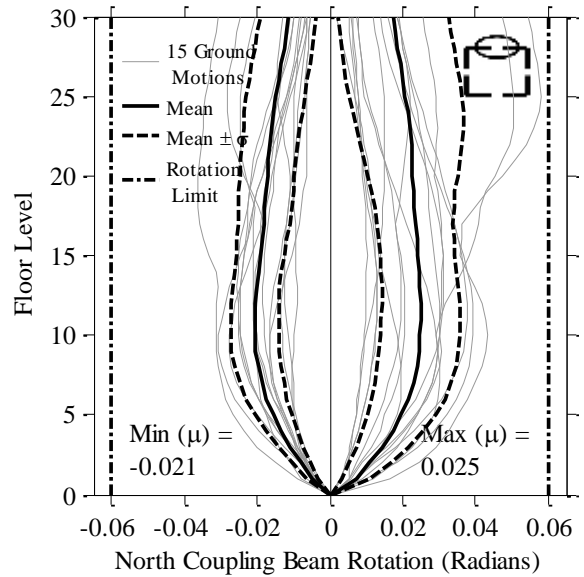
Embedded beams are generally recommended to be modeled with 20 times the stiffness of the coupling beams (Powell, 2007). However, when the shear walls are significantly longer than the coupling beams, 20·E may not be stiff enough to capture the correct rotational values of coupling beams. In this section, the differences between the two cases, when (1) the shear walls are twice as long as coupling beams versus when (2) the shear walls are the same length as coupling beams, are explored.

- a. Embedded beam connected between 2 nodes ($EI/L=10$) versus 3 nodes ($EI/L=20$)

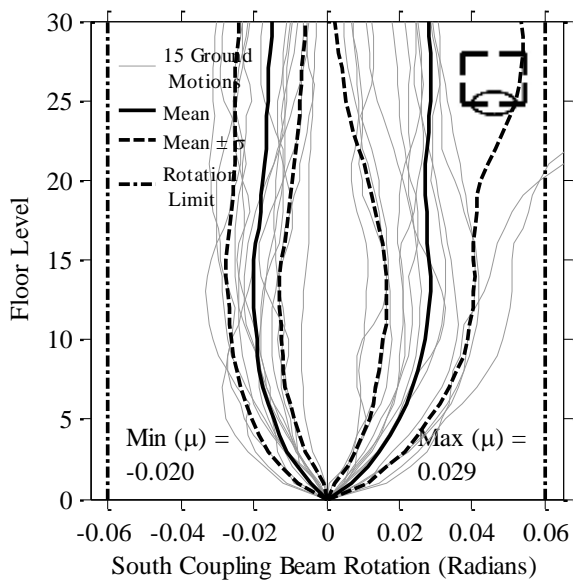




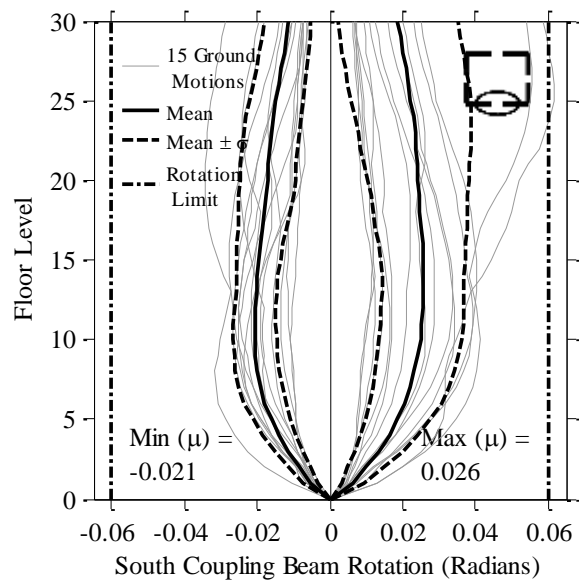
(a)



(a)



(b)



(b)

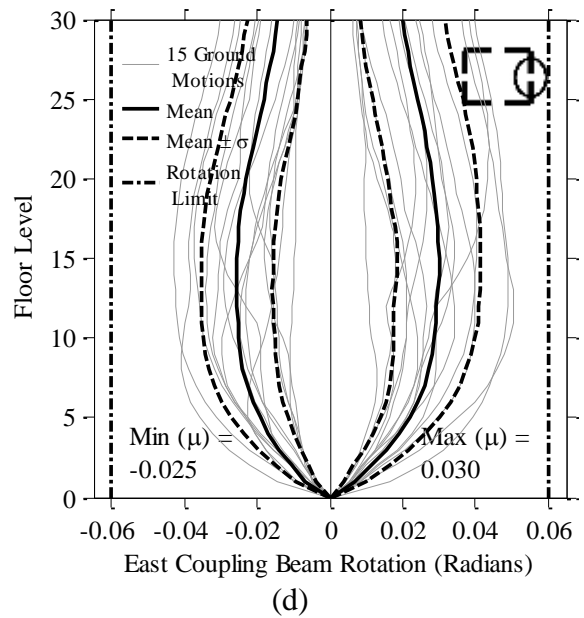
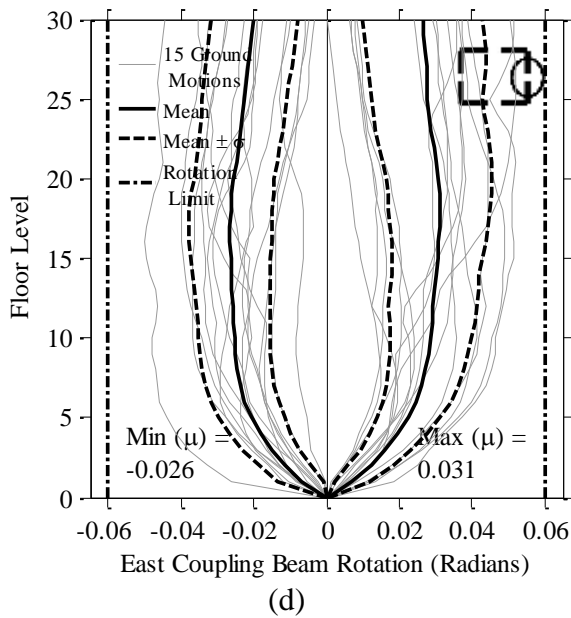
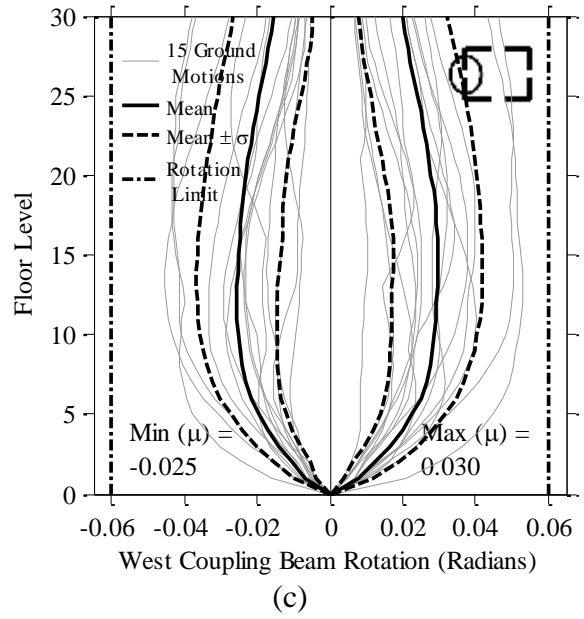
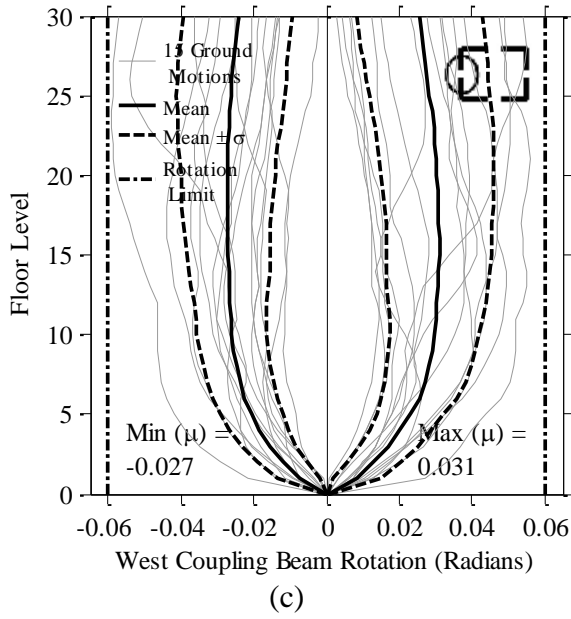


Figure B-1. Embedded beams with a stiffness of $E = 20 \cdot E_{cb}$ and $EI/L = 10$ for coupling beams (a) North (b) South (c) West (d) East

Figure B-2. Embedded beams with a stiffness of $E = 20 \cdot E_{cb}$ and $EI/L = 20$ for coupling beams (a) North (b) South (c) West (d) East

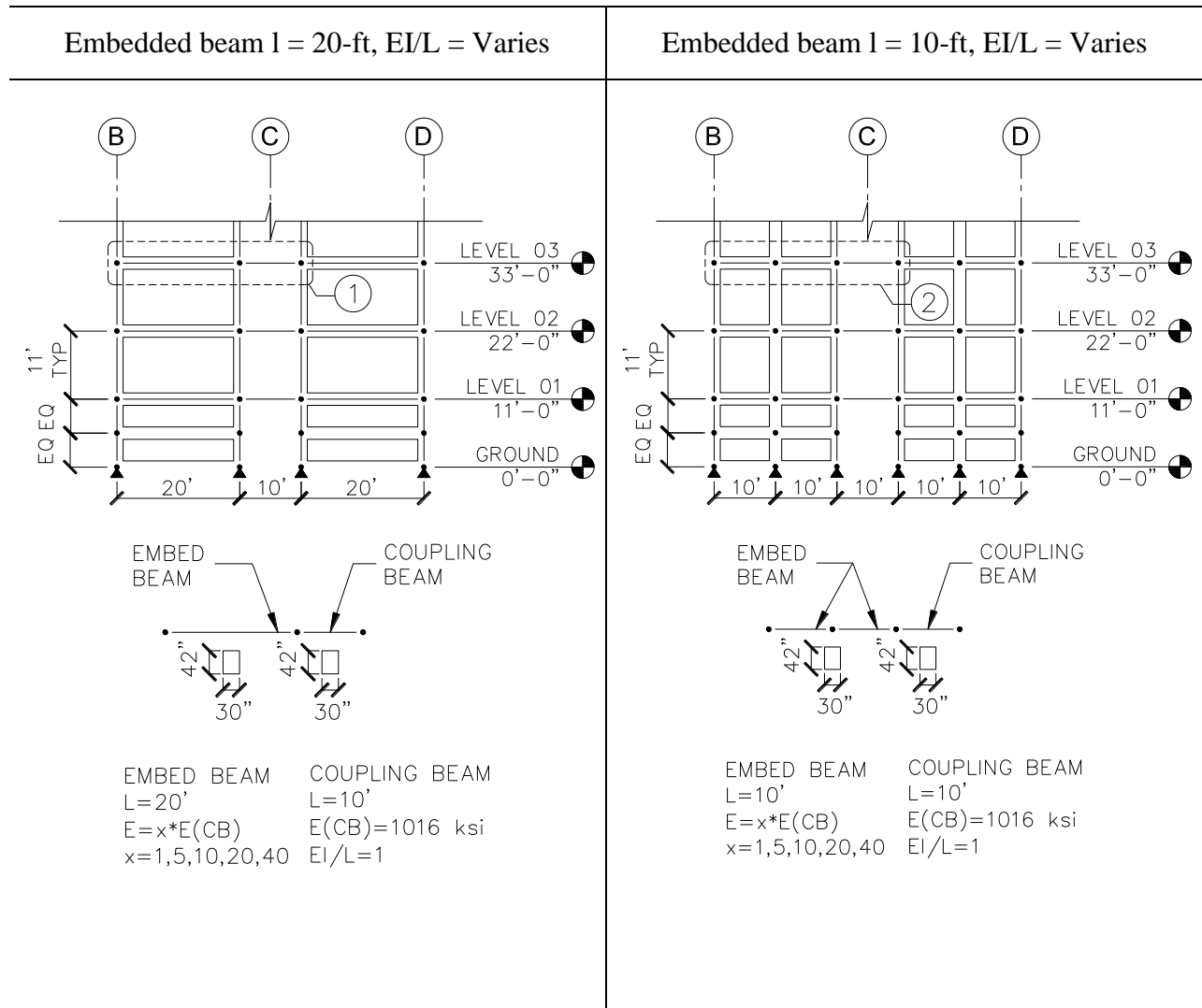
Table B-1. Summary of coupling beam rotations and errors for EI/L=10 and 20

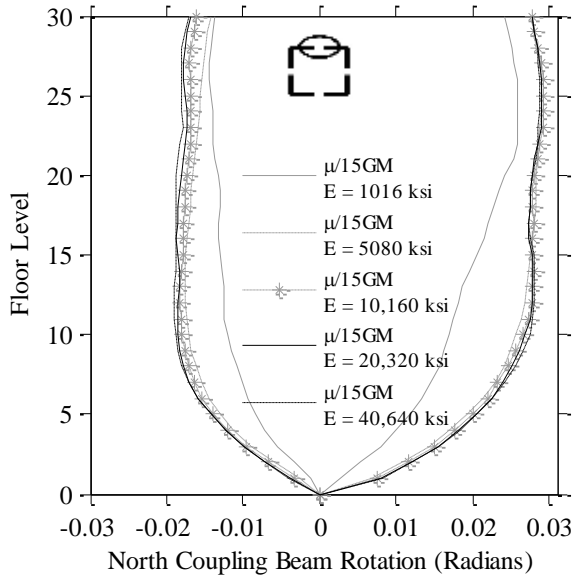
Mean Values	EI/L	North	South	West	East
+ Rotations	10	0.029	0.029	0.031	0.031
	20	0.025	0.026	0.030	0.030
	% difference	16%	12%	3.3%	3.3%
- Rotations	10	-0.019	-0.020	-0.027	-0.026
	20	-0.021	-0.021	-0.025	-0.025
	% difference	-9.5%	-4.8%	8%	4%

It can be seen from Table B-1 that the differences in coupling beam rotations due to softer embedded beams ($EI/L = 10$) can vary between approximately -10% and 16%. To avoid these errors, shear walls should be meshed to similar lengths as the coupling beams.

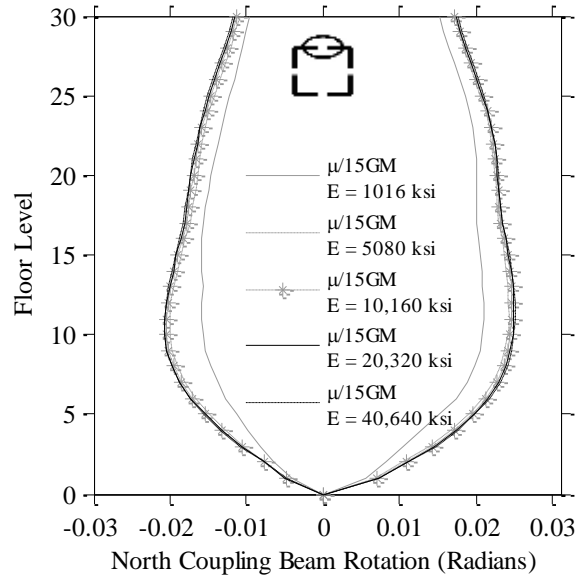
In the following section, the two cases, where embedded beams are 1, 5, 10, 20, and 40 times the stiffness of coupling beams, are explored.

b. Embedded beam stiffness varied between 1, 5, 10, 20, 40 times E_{cb}

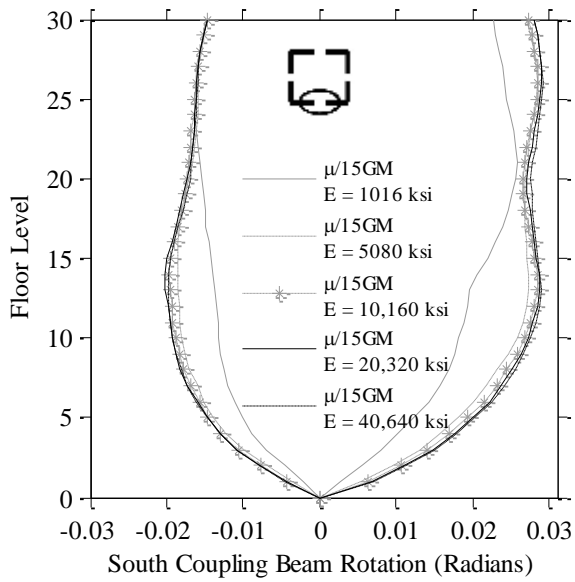




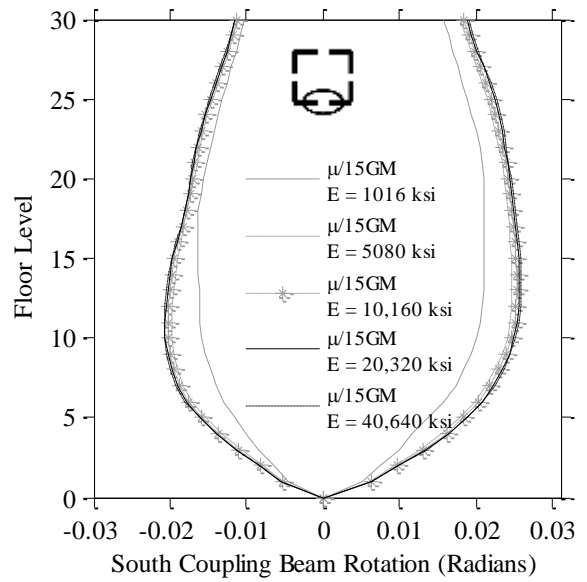
(a)



(a)



(b)



(b)

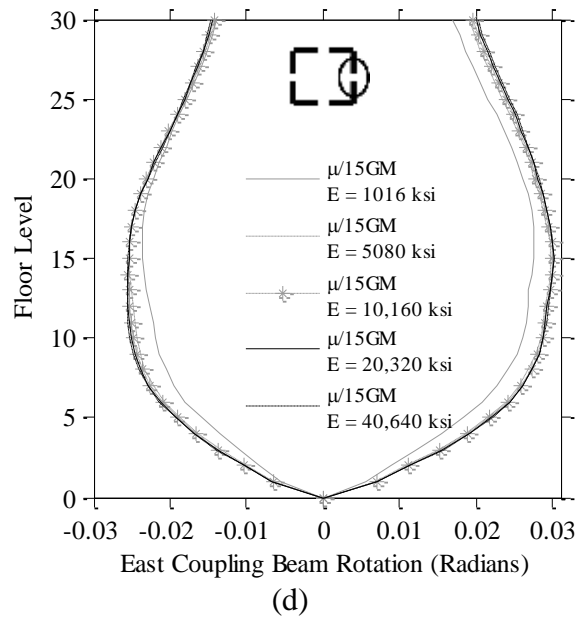
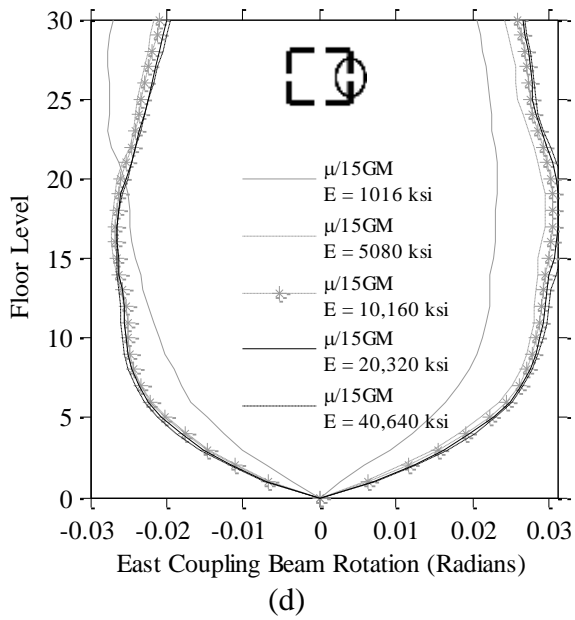
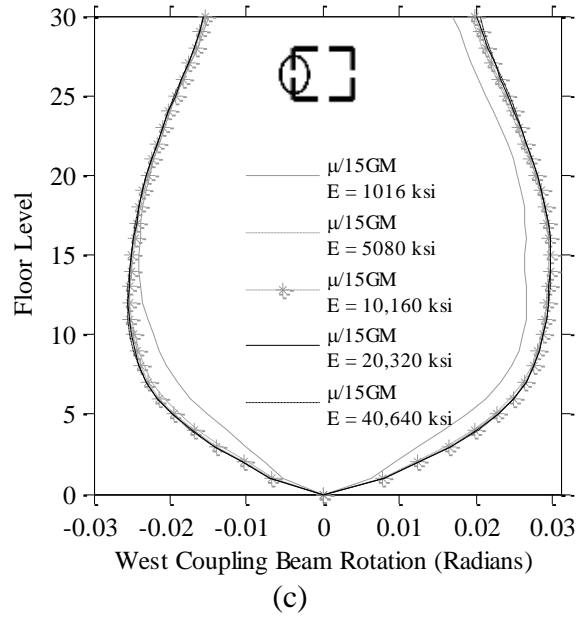
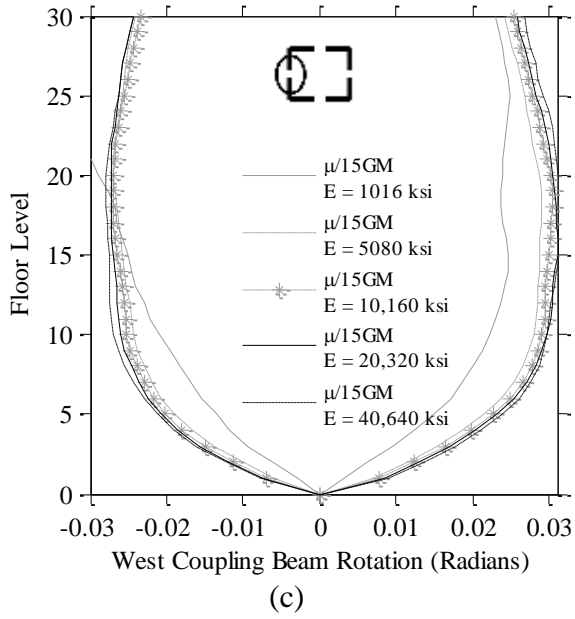


Figure B-3. Varied stiffness values for embedded beams with span of 20ft for coupling beams (a) North (b) South (c) West (d) East

Figure B-4. Varied stiffness values for embedded beams with span of 10ft for coupling beams (a) North (b) South (c) West (d) East

In both cases, the solutions start to converge above $10 \cdot E$, as shown on Figure B-3 and Figure B-4. In Figure B-4, the results from $20 \cdot E$ and $40 \cdot E$ are almost identical. In Figure B-3, more dispersion (error) among the five cases are noted, due to the use of softer embedded beams.

2. Rayleigh Damping versus Modal Damping

For the case of coupled shear walls, the use of Rayleigh versus modal damping can result in notable differences due to the way damping is implemented. When Rayleigh damping is used, the βK damping coefficient for coupling beams is based on the initial elastic bending and shear stiffness values, which can be large. When the coupling beams yield, although the ductility ratios are usually substantial, the βK damping coefficients stay constant; this can overestimate the βK energy dissipation and underestimate the deformations of the coupling beams (CSI, 2011). For modal damping, this is not a potential issue.

However, when modal damping is used, damping matrix is only based on the modes where mode shapes have been calculated. Since in a real structure, the number of degrees of freedom is much larger than the number of modes generally considered in analysis, many displaced shapes will be undamped. Thus, a small amount of Rayleigh damping is used in conjunction with modal damping to ensure that the higher modes are damped.

In the following subsections, the differences in interstory drifts, coupling beam rotations, and shear demands are presented from the two models where (1) 3% damping at $0.33 \cdot T_1$ and $1.5 \cdot T_1$ was assigned for Rayleigh damping, which resulted in approximately 2.5% damping at the first mode period (noted as RD) and (2) 2.4% modal damping (noted as MD) in conjunction with 0.1% Rayleigh damping was used. The differences in structural responses were calculated as:

$$\% \text{ Difference} = \frac{(\text{MD} - \text{RD})}{\text{RD}} \times 100\%$$

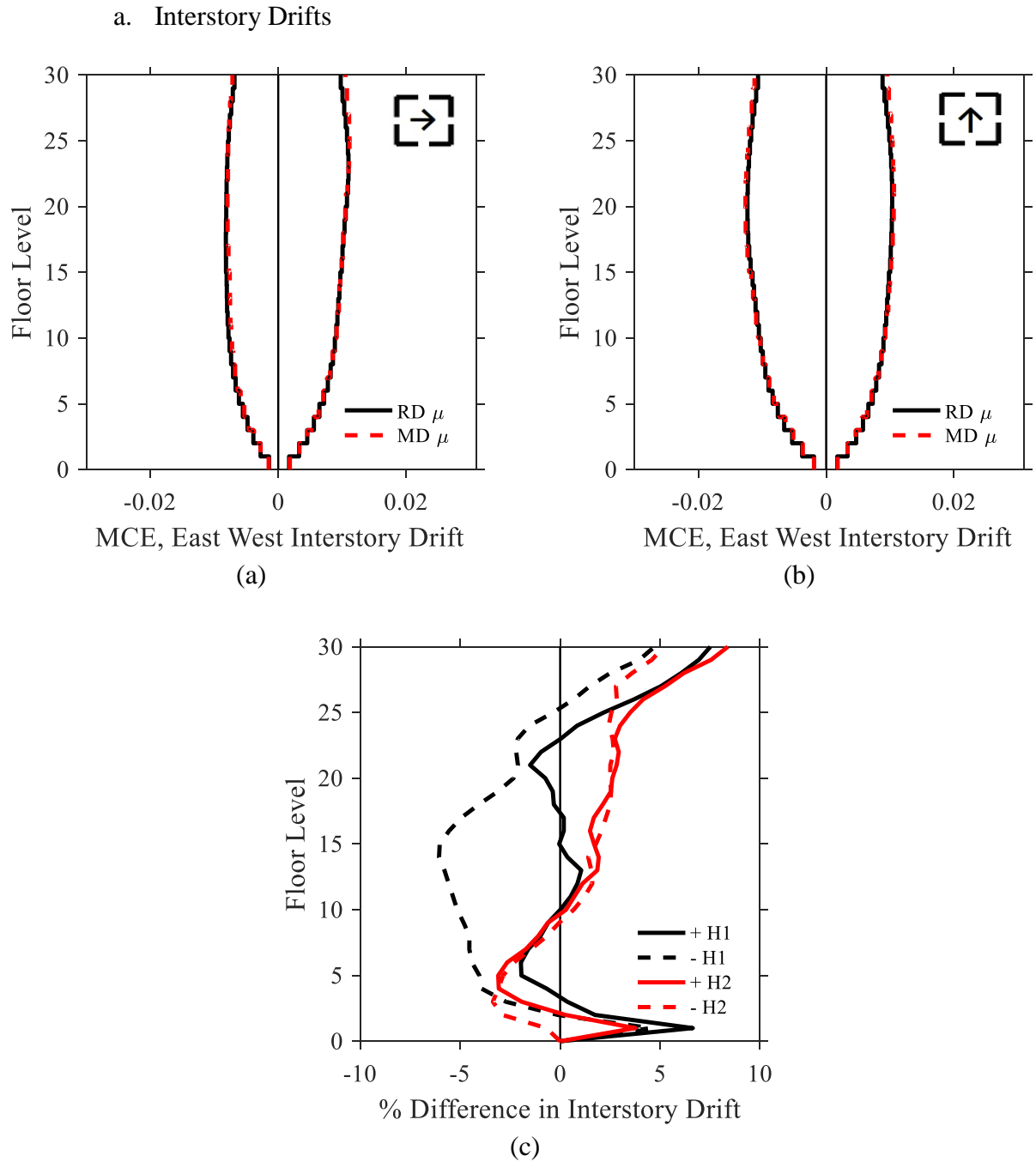


Figure B-5. 30-story building interstory drift comparison between Rayleigh damping and modal damping for (a) H1 direction (b) H2 direction and (c) % difference

b. Coupling beam rotations

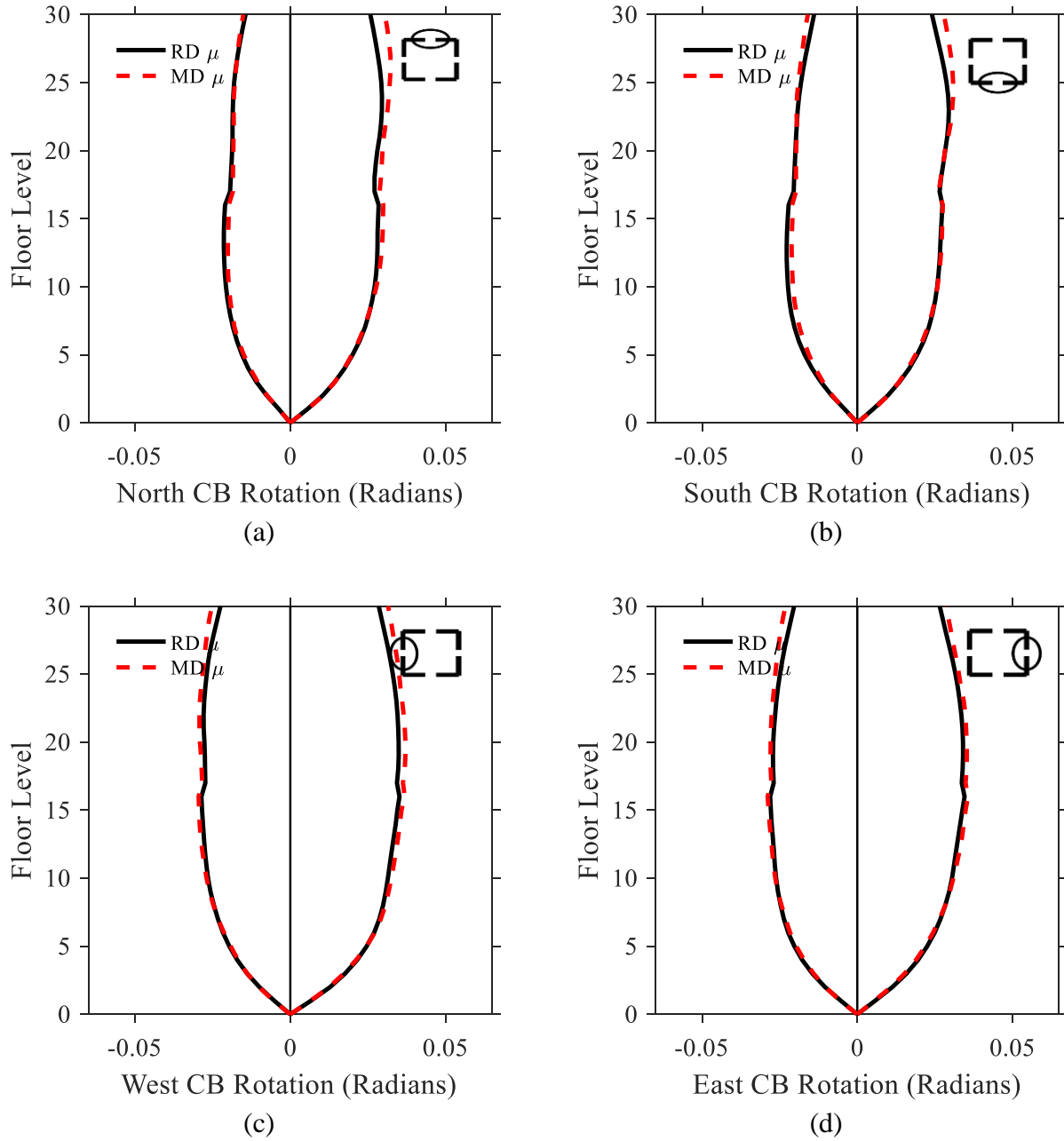


Figure B-6. 30-story building coupling beam rotations comparison between Rayleigh damping and modal damping for (a) North (b) South (c) West and (d) East coupling beams

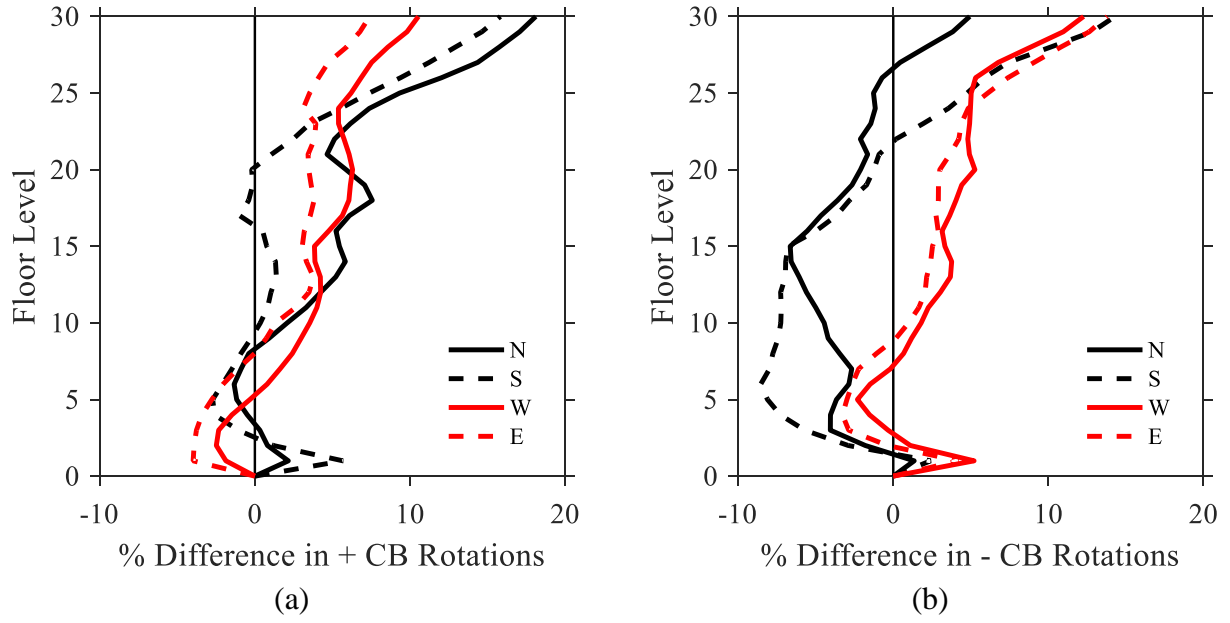


Figure B-7. 30-story building coupling beam rotations comparison (% difference) between Rayleigh damping and modal damping in (a) positive rotations and (b) negative rotations

c. Shear demands

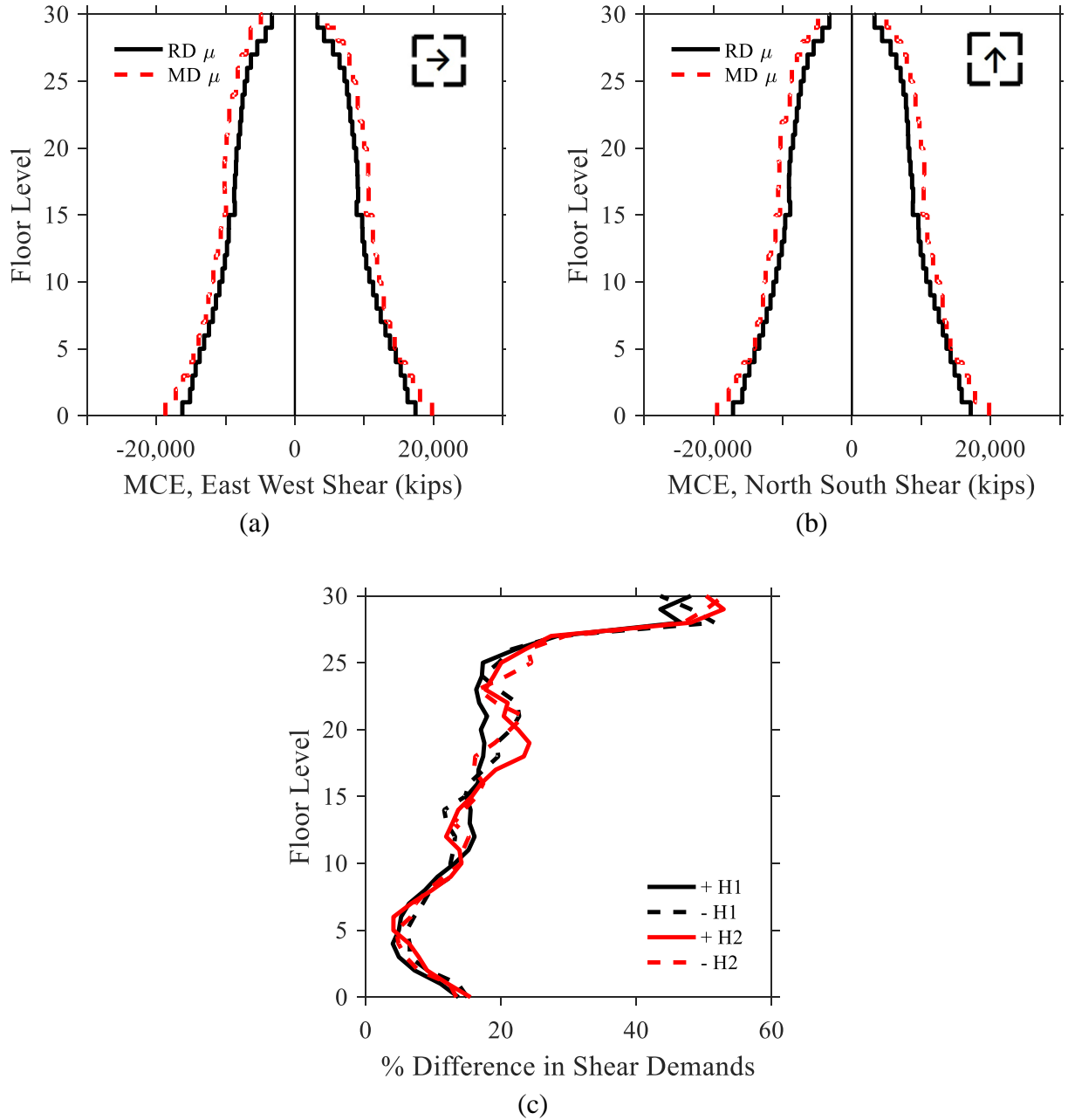


Figure B-8. 30-story building base shear comparison between Rayleigh damping and modal damping for (a) H1 direction (b) H2 direction and (c) % difference

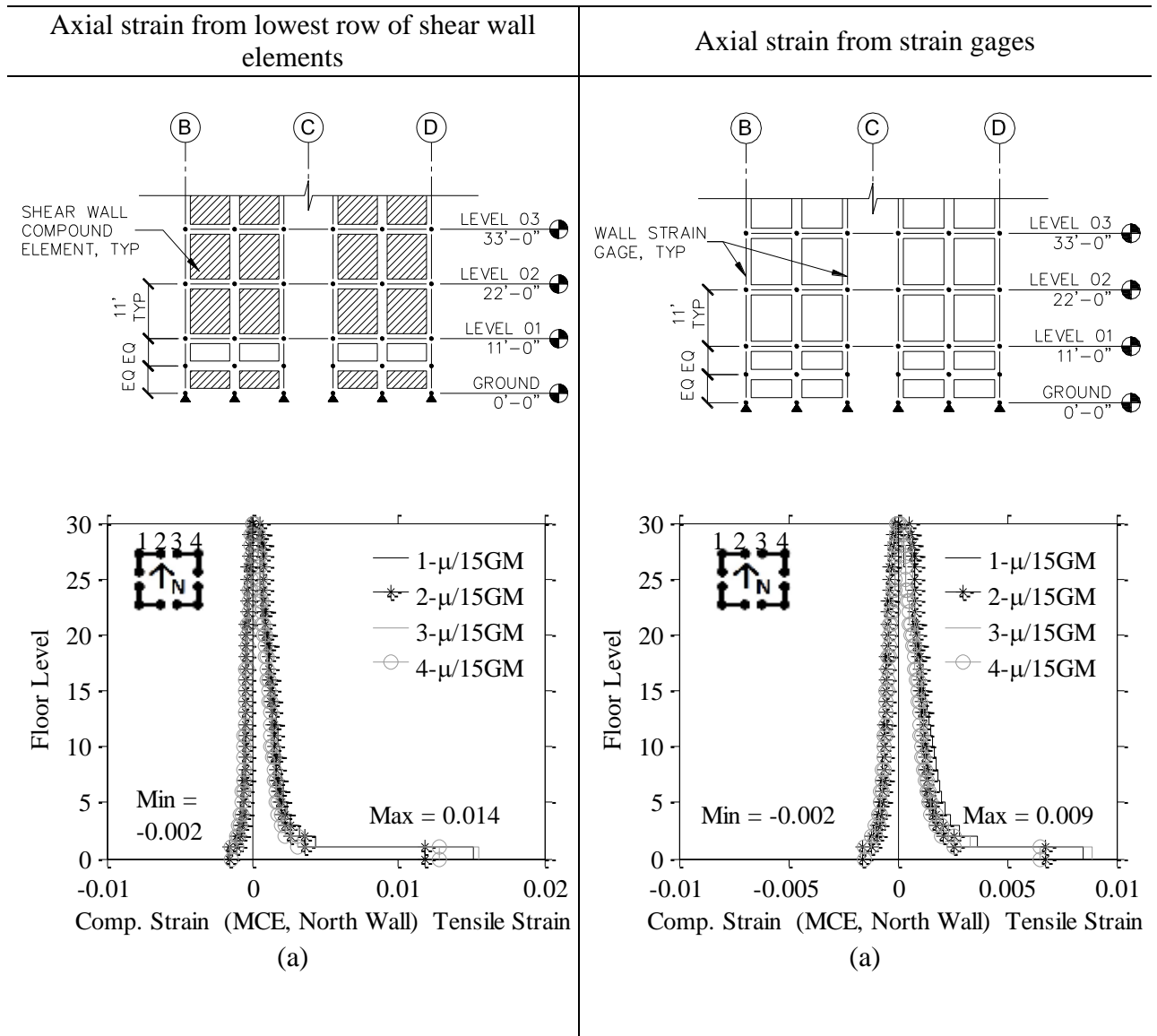
The changes in interstory drifts due to the two different damping methods were minor, as shown on Figure B-5. For most levels, the changes were less than 5% and the maximum difference was reflected on the +H2 direction interstory drift, on the roof level, at 8.4%.

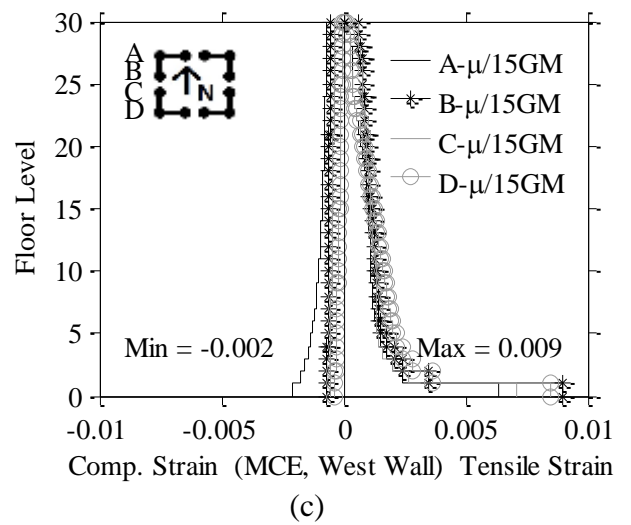
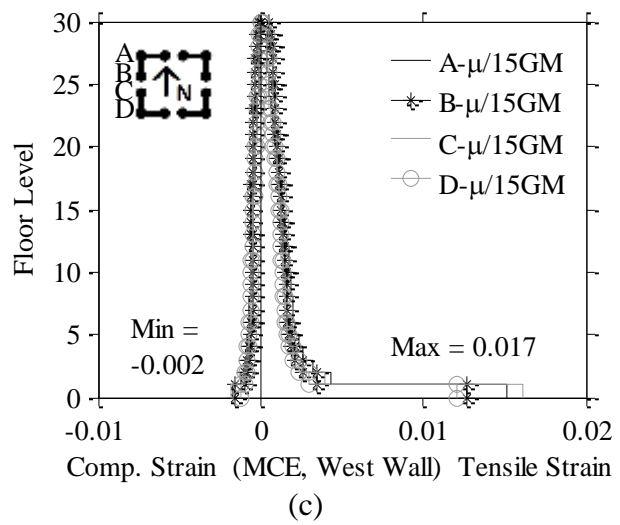
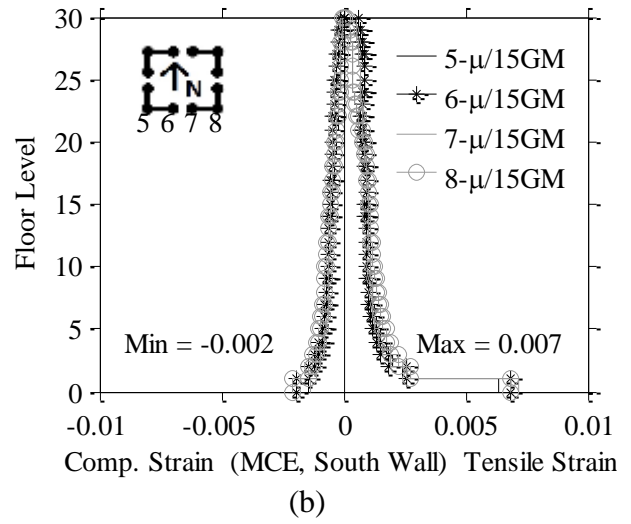
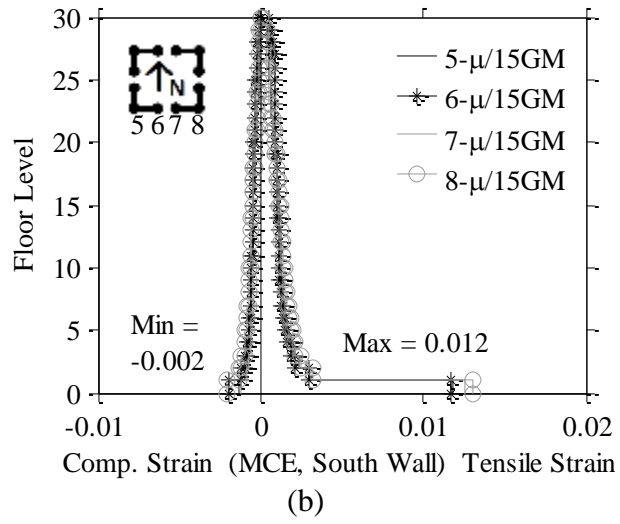
As expected, the rotations in the coupling beams were mostly underestimated with Rayleigh damping, as shown on Figure B-6. The modal damping responses generally higher with an upwards trend with increasing height (refer to Figure B-7). The maximum differences were shown from the positive rotations in the North coupling beam, at 18.1%. The exception to this trend was shown for negative responses in the North and South coupling beams, where modal responses were lower by up to 8.5%.

With the use of Rayleigh damping, the yielding of coupling beams was delayed which in turn delayed the onset of yielding for the shear walls. Thus, the underestimation in coupling beam rotations resulted in underestimation in shear forces. This is clearly shown on Figure B-8. Modal damping base shear responses were on average 14.4% greater than base shear responses from Rayleigh damping. The differences in base shear were smallest around level 5 and had an upwards trend with increasing height. The greatest differences were shown for both positive and negative direction H2 shear forces, towards the roof, at 52.9%.

3. Shear Wall Axial Strains

When several shear wall elements are modeled within the plastic hinge length (story height in this case), the plastic hinge rotations will tend to be concentrated in the lowest row of elements. Thus, strain gages are generally modeled to compute average axial strains over the plastic hinge length. A comparative study is demonstrated below; on the left, axial strains are plotted from shear wall elements from the lowest row of elements, whereas on the right, axial strains are plotted from strain gages over the height of each story.





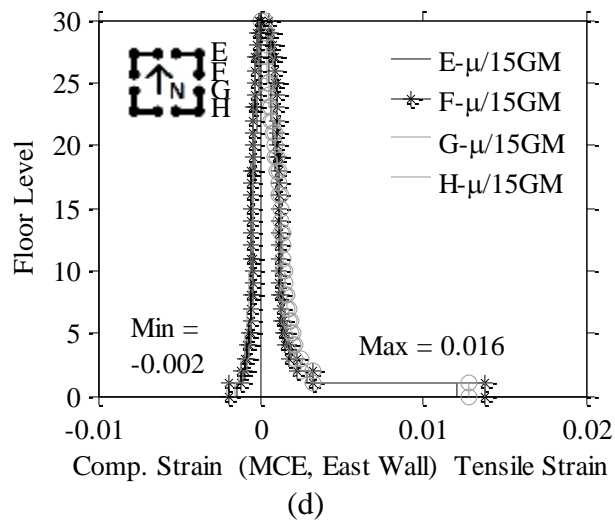


Figure B-9. Axial strains are plotted from the lowest row of shear wall elements.

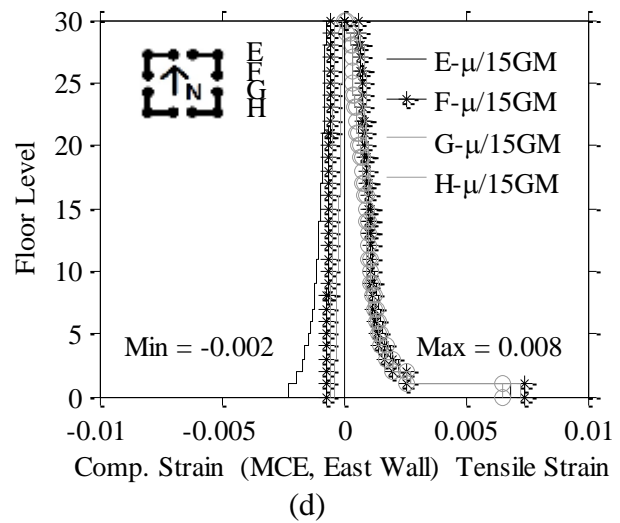


Figure B-10. Axial strains are plotted from strain gages over the height of each story.

Table B-2. Summary of tensile and compressive axial strains and errors

Mean Values	Method	North Wall PH ¹	South Wall PH	West Wall PH	East Wall PH
Tensile strains	Elements	0.014	0.012	0.017	0.016
	Strain gage	0.009	0.007	0.009	0.008
	% difference	55.6%	71.4%	88.9%	100%
Compressive strains	Elements	-0.002	-0.002	-0.002	-0.002
	Strain gage	-0.002	-0.002	-0.002	-0.002
	% difference	0%	0%	0%	0%

¹ plastic hinge

As shown on Table B-2, the tensile axial strains were concentrated in the lowest row of elements, and the mean strains were higher by approximately 56% to 100%, in comparison to the tensile axial strains that were averaged over the plastic hinge lengths. Thus, modeling strain gages over the plastic hinge lengths are recommended to capture the correct axial strains.

4. Analysis of Core Wall Compressive Zones

Shear wall axial strains were examined at 5 locations per L-shaped core walls (refer to Figure B-12) to study compressive zones. Understanding compressive zones is important to define the areas of confinement within boundary elements. Strain values from ground motion #14 were plotted at various times corresponding to peak displacement values, specifically at 8.4, 10.1, 12.4, 14.0, 18.0, 19.3, 29.7, and 31.3 seconds. The results are shown on Figure B-12; per each selected time step, time history plots are shown for displacements in X and Y directions, and shear wall axial strains are plotted. Similar studies can be conducted using all MCE level ground motions to examine compressive zones within limiting confinement strains and to determine boundary element lengths. On the other hand, it is common practice to provide nominal confinement (along with cross ties at every longitudinal reinforcement) in the entire core wall area within plastic hinge locations, as well as in the stories above, or to establish minimum confinement areas as shown on Figure B-11.

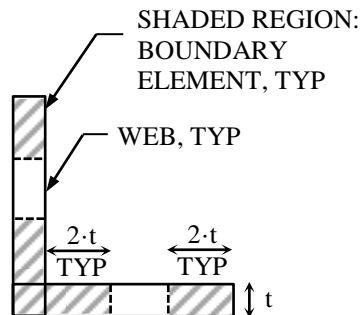
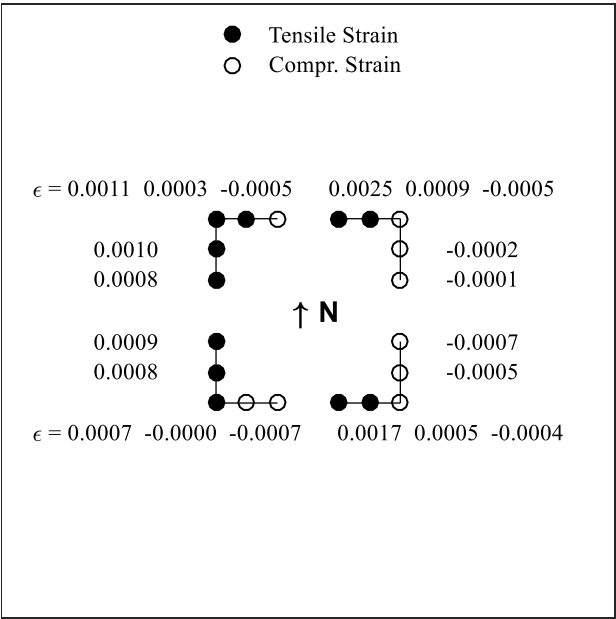
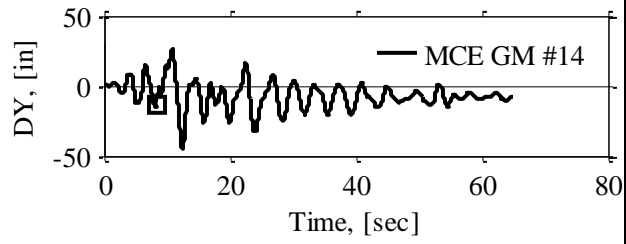
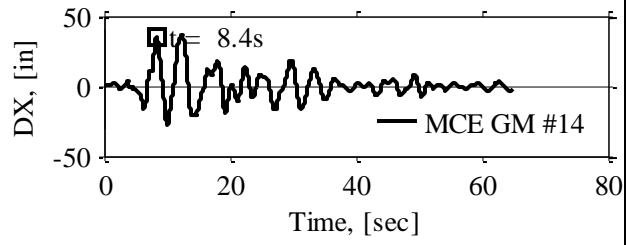
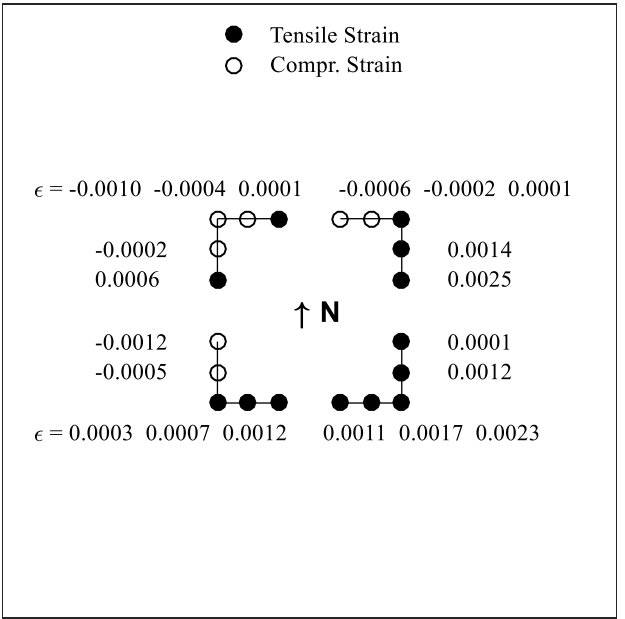
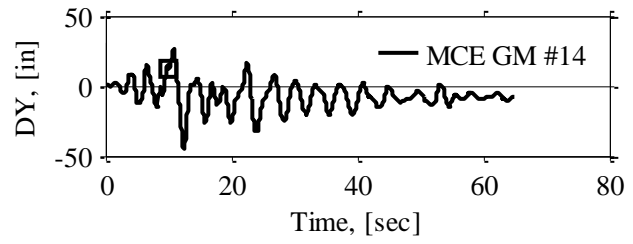
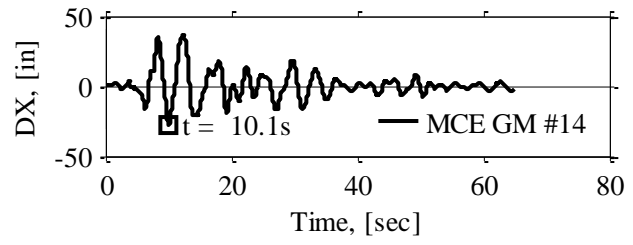


Figure B-11. Minimum core wall boundary element lengths, per common practice

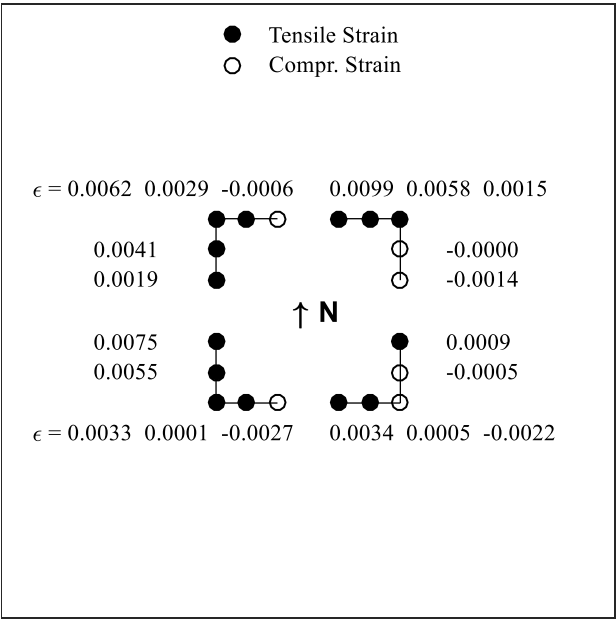
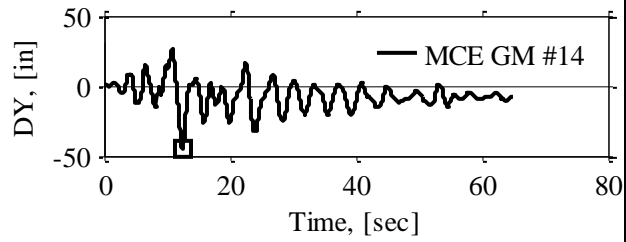
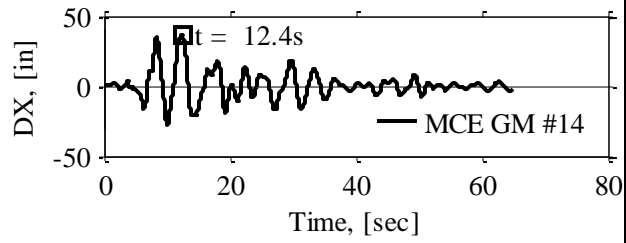
1. t = 8.4 seconds



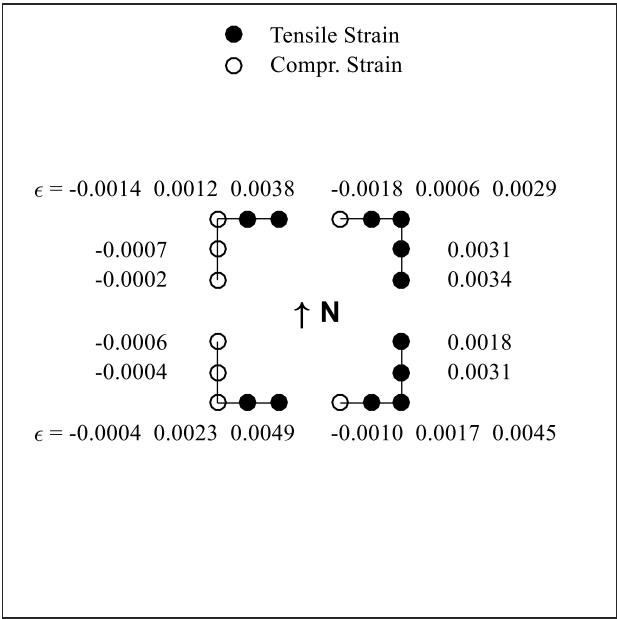
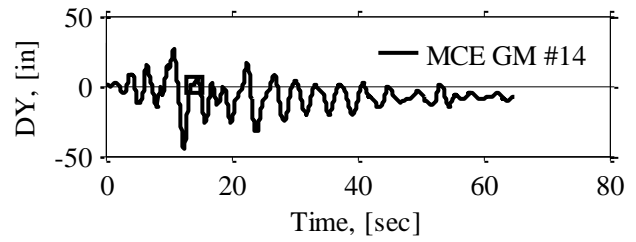
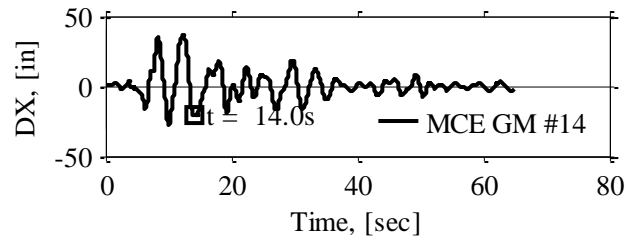
2. t = 10.1 seconds



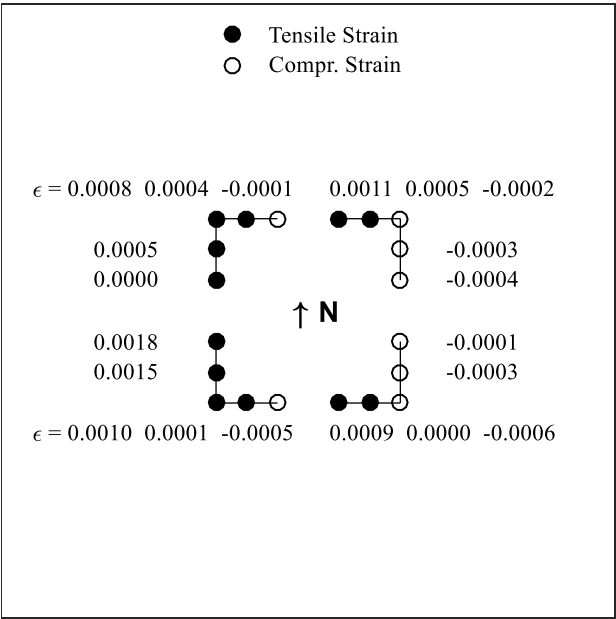
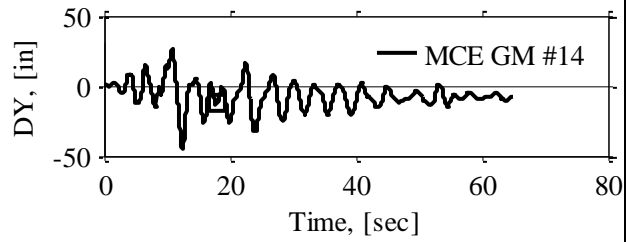
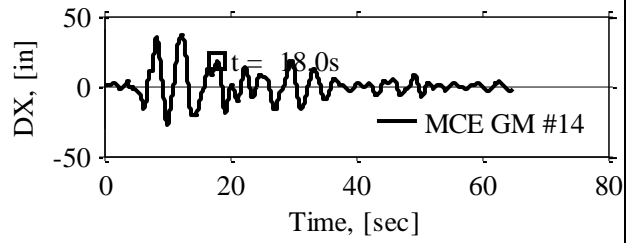
3. t = 12.4 seconds



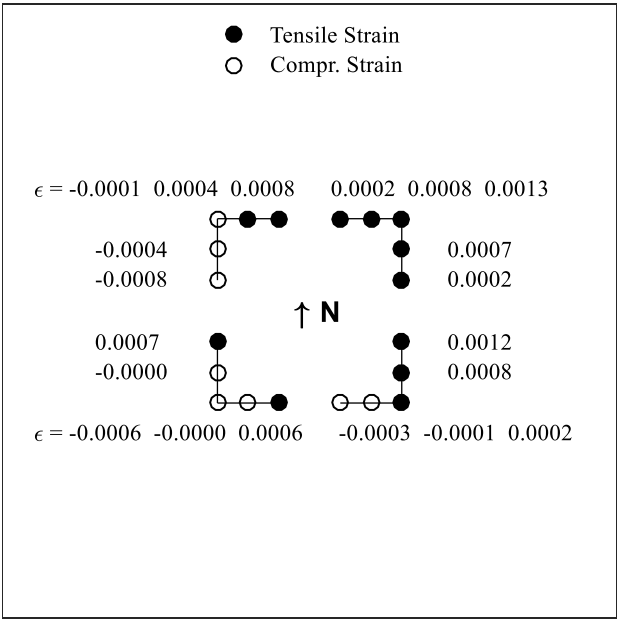
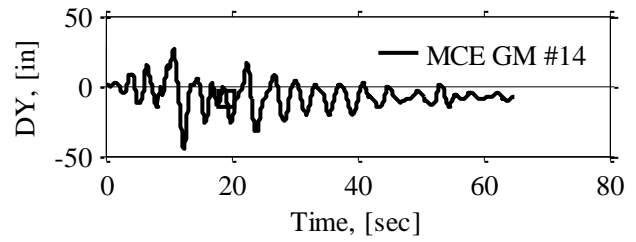
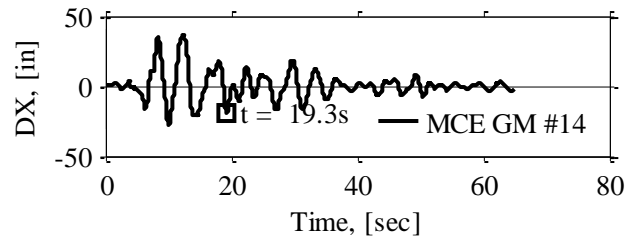
4. t = 14.0 seconds



5. t = 18.0 seconds



6. t = 19.3 seconds



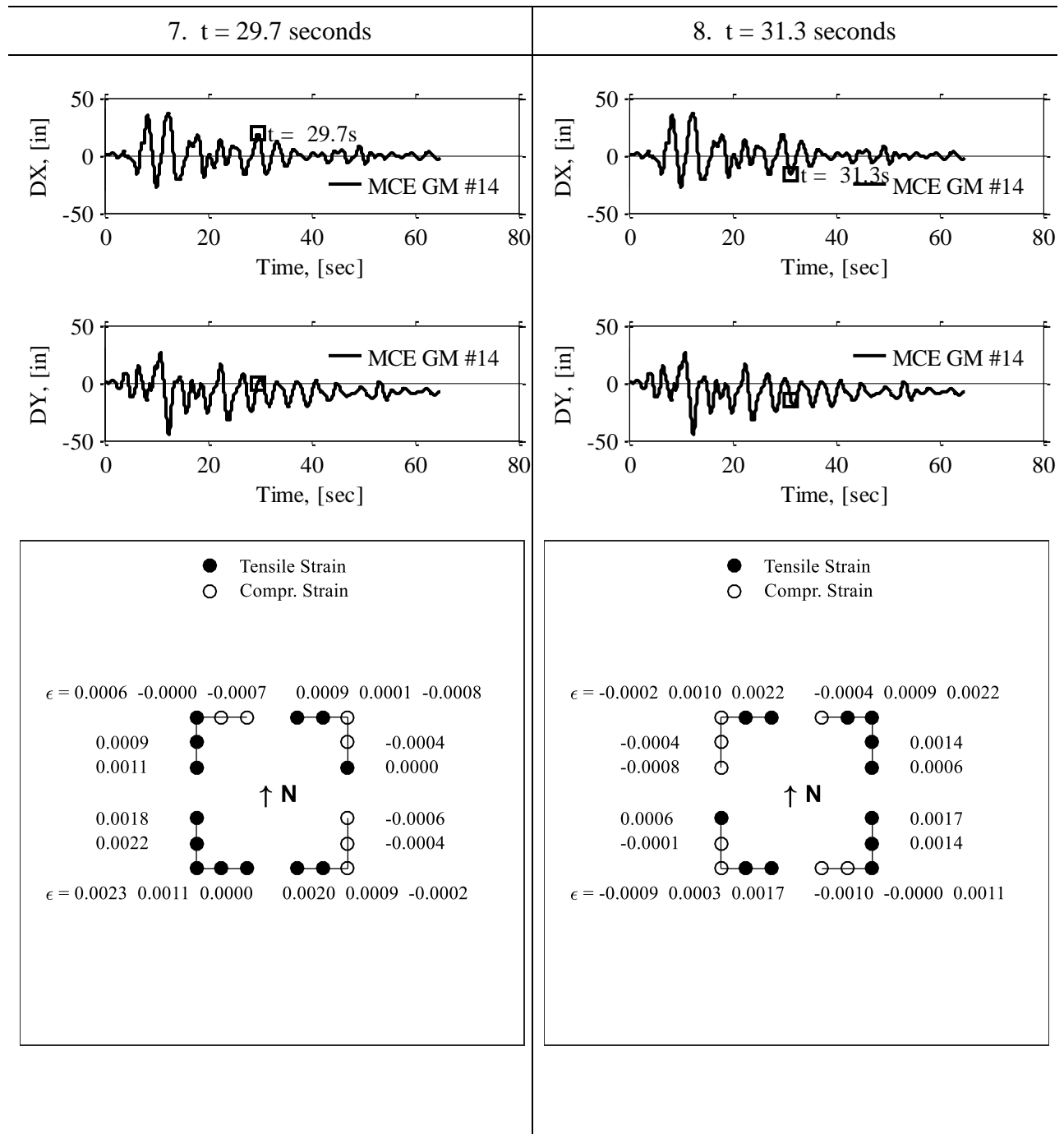


Figure B-12. Core wall axial strains plotted for GM #14 at 8.4, 10.1, 12.4, 14.0, 18.0, 19.3, 29.7, and 31.3 seconds.

APPENDIX C

A comprehensive set of dispersion plots are presented for all engineering demand parameters explored in Chapter 6.

Base Shear Force

See Chapter 6.4.1 for base shear dispersion plots in H1 and H2 directions and Chapter 6.4.2 for convergence plots for the dispersion measure in both directions. Histograms overlaid with probability distributions for each hazard level in both directions are presented in this section.

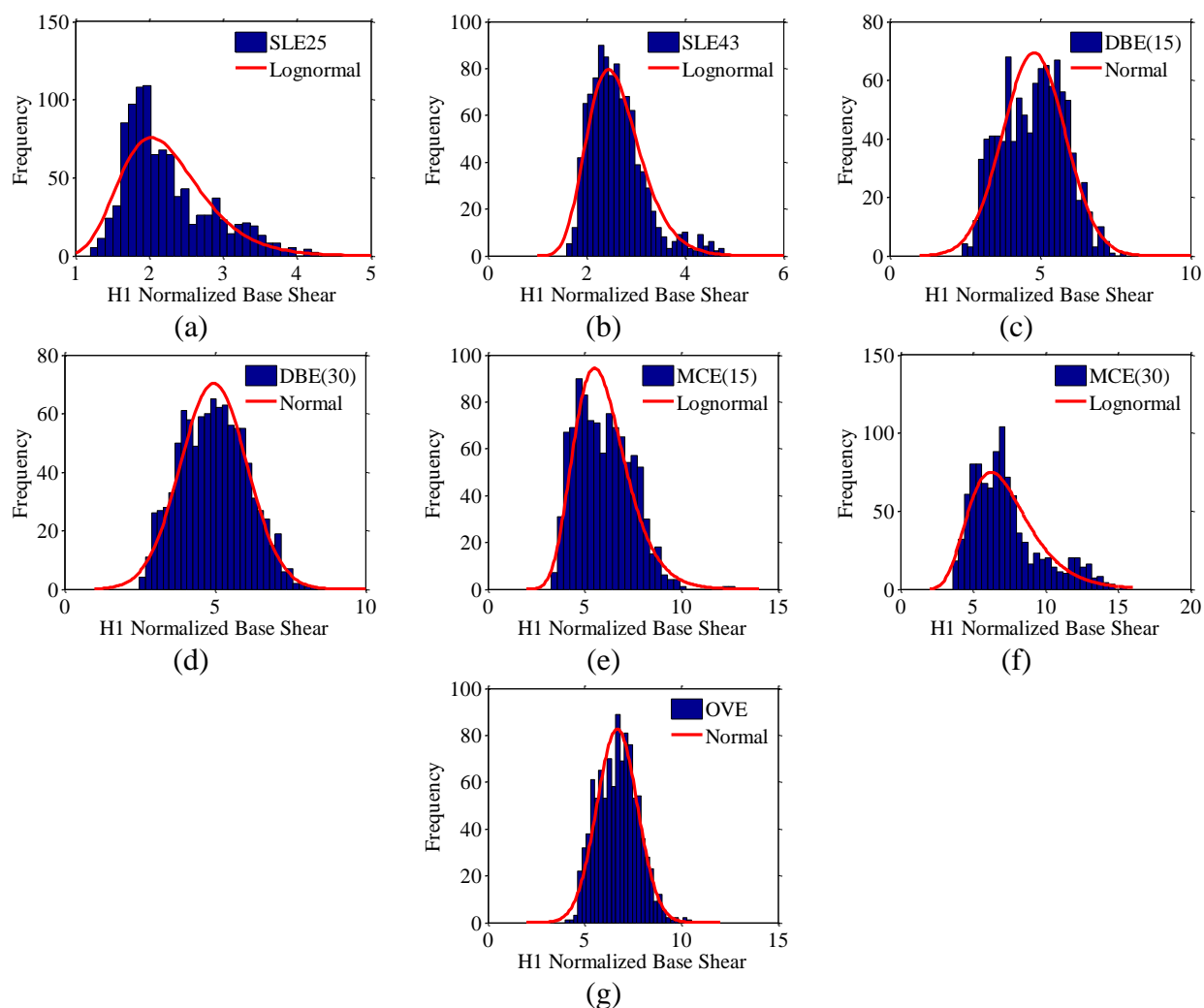


Figure C-1. Normalized base shear histogram and fitted distribution for H1 direction (a) SLE25 (b) SLE43 (c) DBE(15) (d) DBE(30) (e) MCE(15) (f) MCE(30) and (g) OVE hazard levels

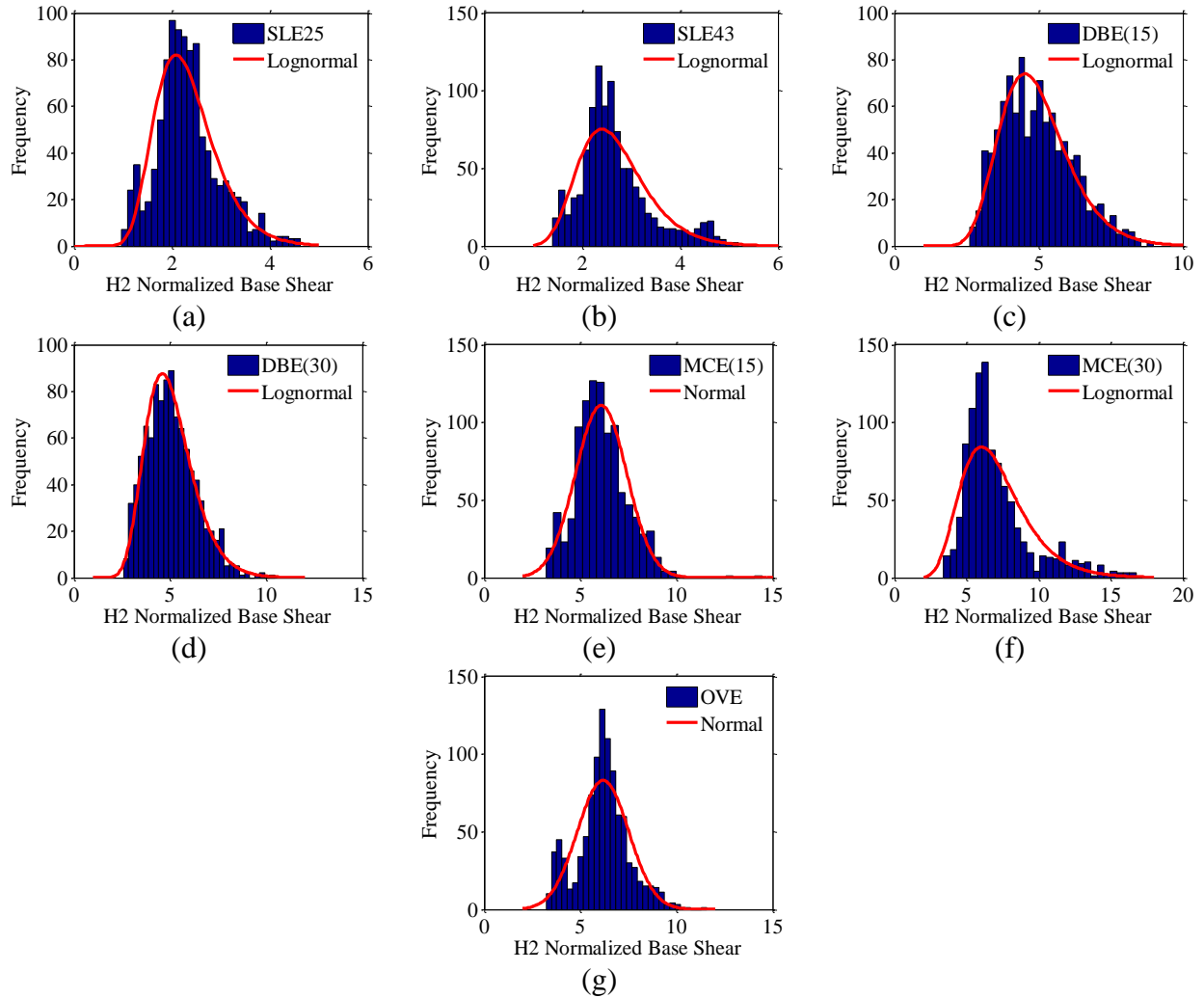


Figure C-2. Normalized base shear histogram and fitted distribution for H2 direction (a) SLE25 (b) SLE43 (c) DBE(15) (d) DBE(30) (e) MCE(15) (f) MCE(30) and (g) OVE hazard levels

Roof Drifts

See Chapter 6.4.3 for roof drift dispersion plots in H1 and H2 directions. Convergence plots for the dispersion measure in H1 and H2 directions, as well as histograms overlaid with probability distributions for each hazard level in both directions are presented in this section.

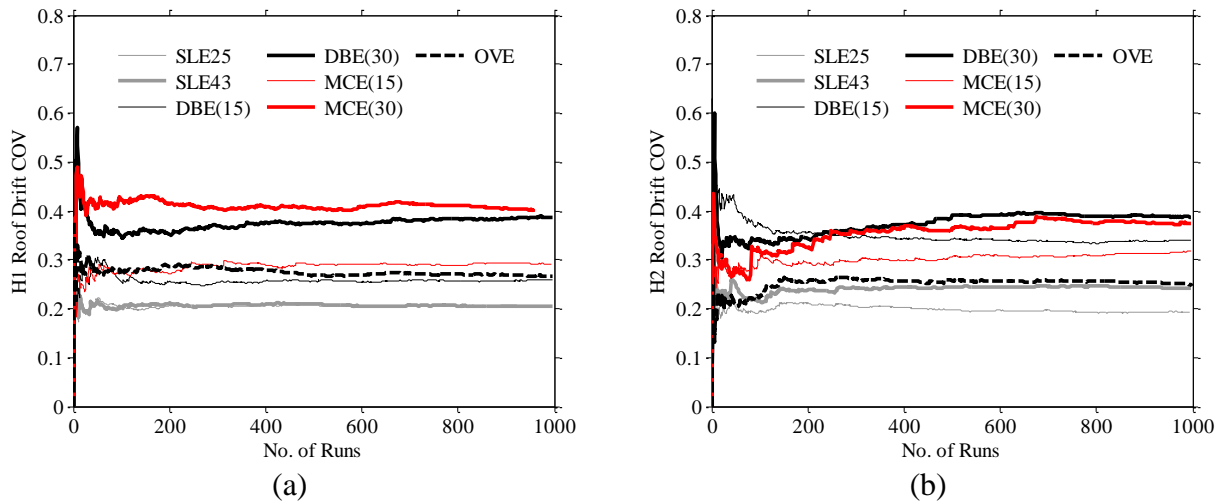


Figure C-3. Convergence test for dispersion measure: COV versus number of runs for roof drifts, in (a) H1 and (b) H2 directions

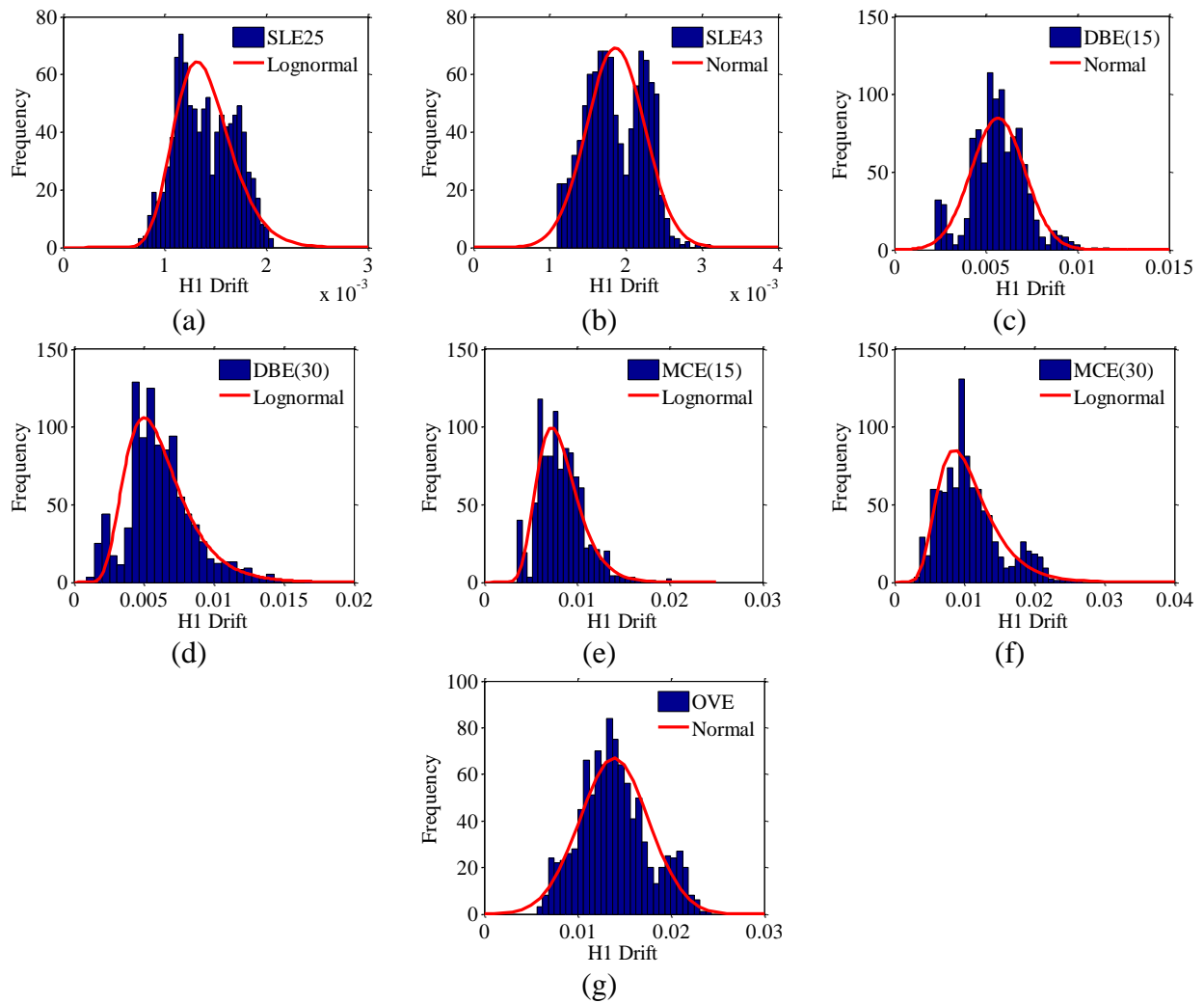


Figure C-4. Roof drift histogram and fitted distribution for H1 direction (a) SLE25 (b) SLE43 (c) DBE(15) (d) DBE(30) (e) MCE(15) (f) MCE(30) and (g) OVE hazard levels

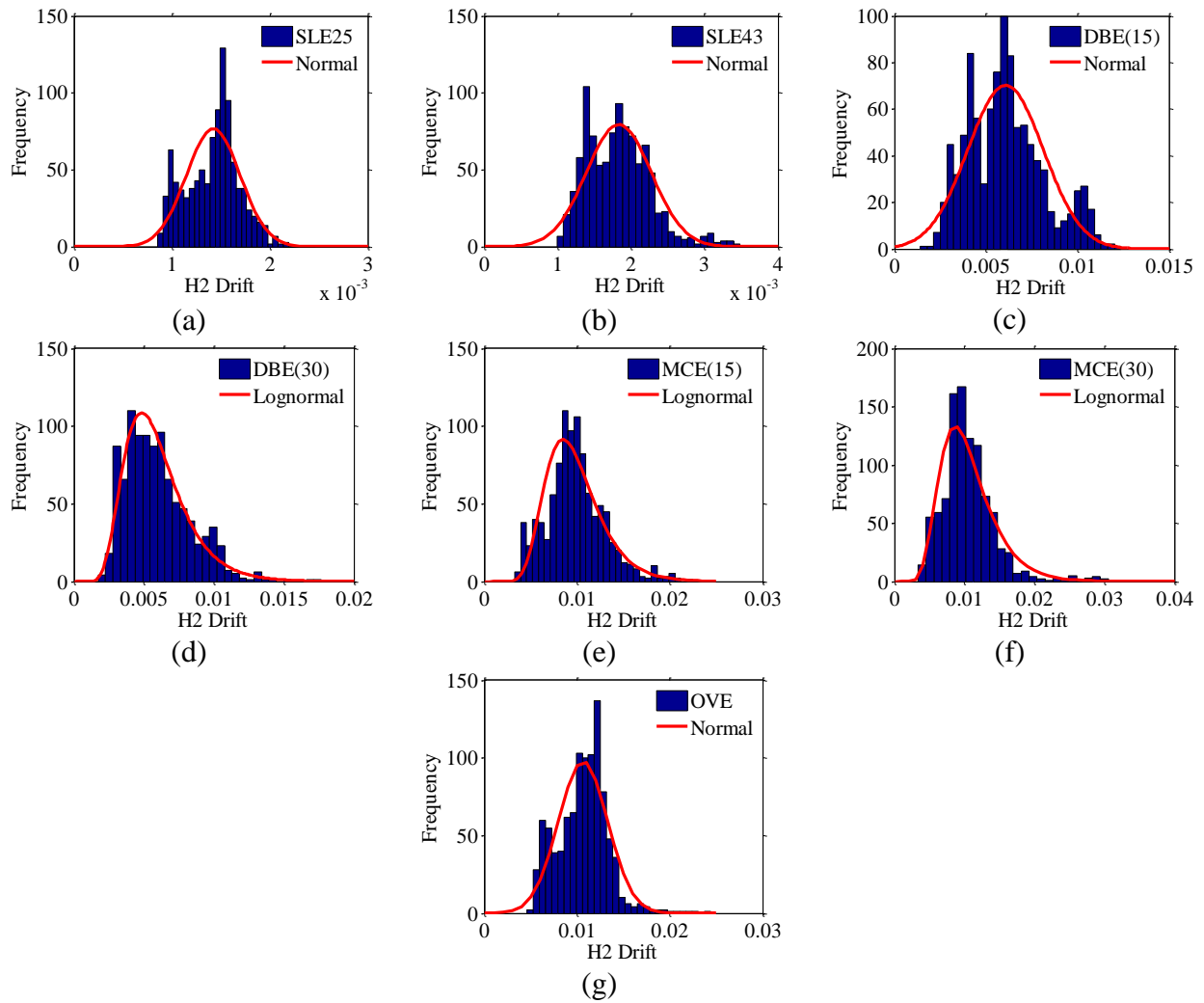


Figure C-5. Roof drift histogram and fitted distribution for H2 direction (a) SLE25 (b) SLE43 (c) DBE(15) (d) DBE(30) (e) MCE(15) (f) MCE(30) and (g) OVE hazard levels

Coupling Beam Rotations

The following plots are presented for coupling beam rotations: dispersion for North, East, South, and West coupling beams on the 20th floor, convergence for the dispersion measure for the four coupling beams, and histograms overlaid with probability distributions for each hazard level, for the four coupling beams.

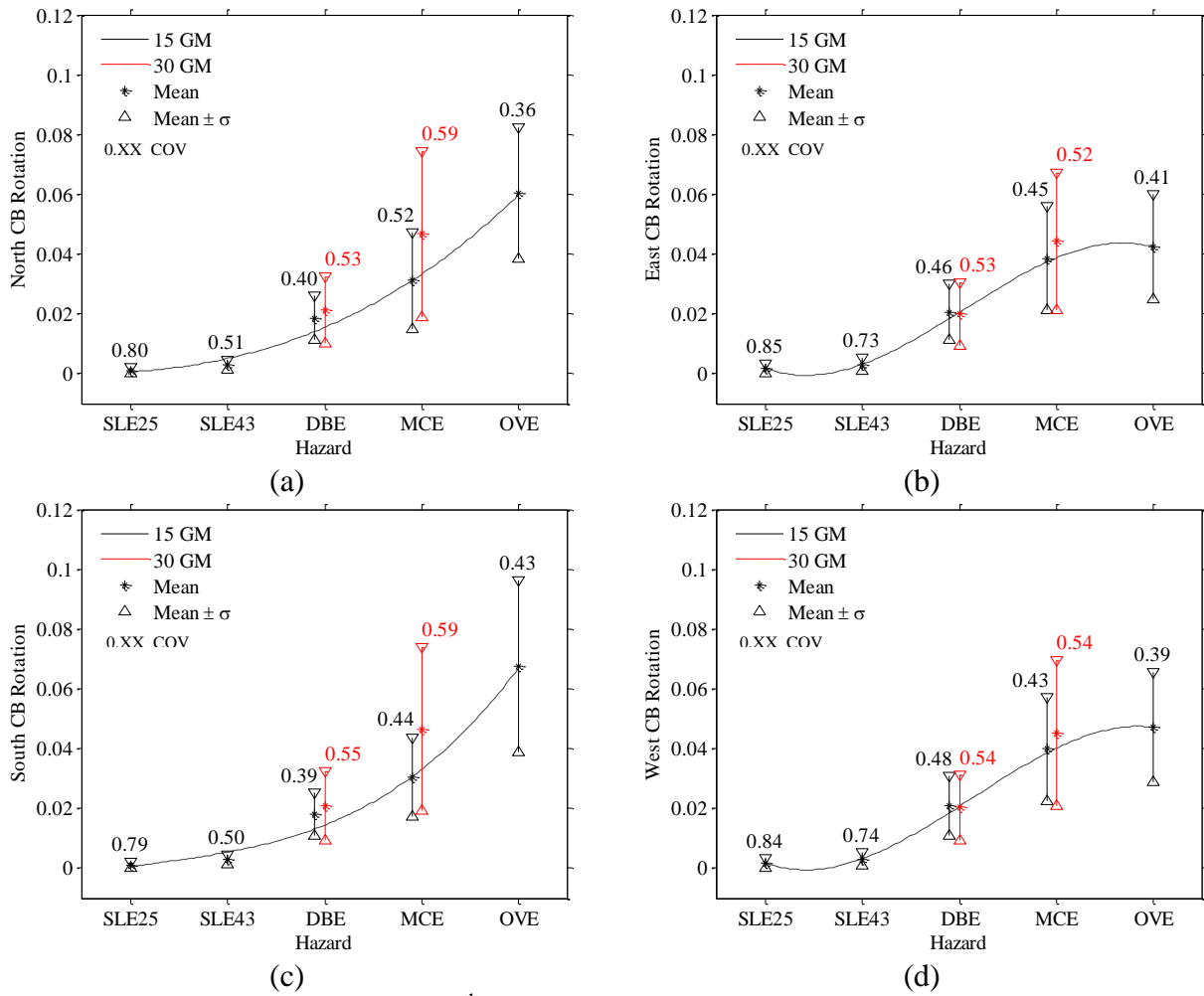


Figure C-6. 30-Story building 20th floor coupling beam rotations, mean and dispersion at 5 hazard levels for (a) North (b) East (c) South and (d) West coupling beams

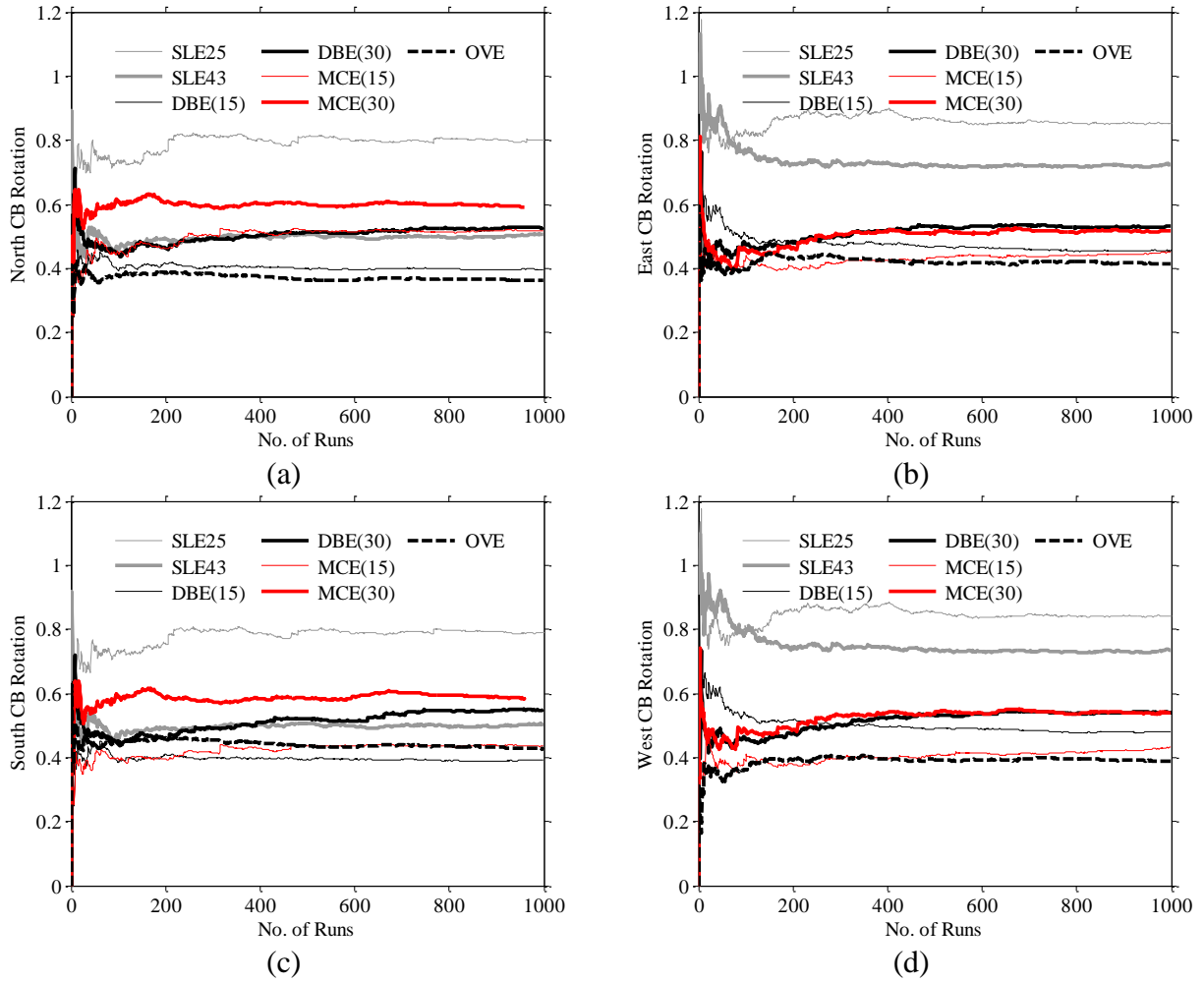


Figure C-7. Convergence test for dispersion measure: COV versus number of runs for (a) North (b) East (c) South and (d) West coupling beams

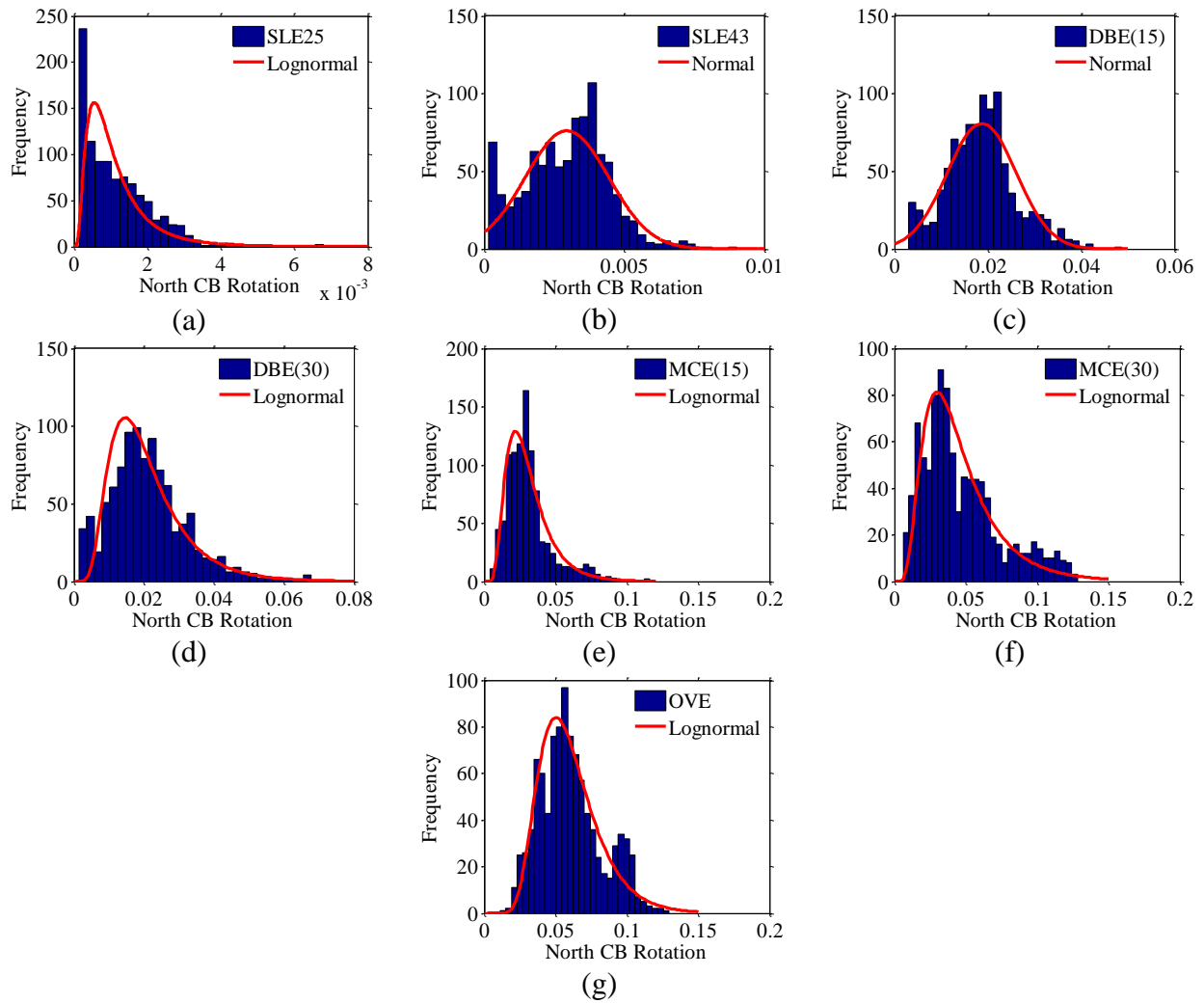


Figure C-8. North coupling beam histogram and fitted distribution for (a) SLE25 (b) SLE43 (c) DBE(15) (d) DBE(30) (e) MCE(15) (f) MCE(30) and (g) OVE hazard levels

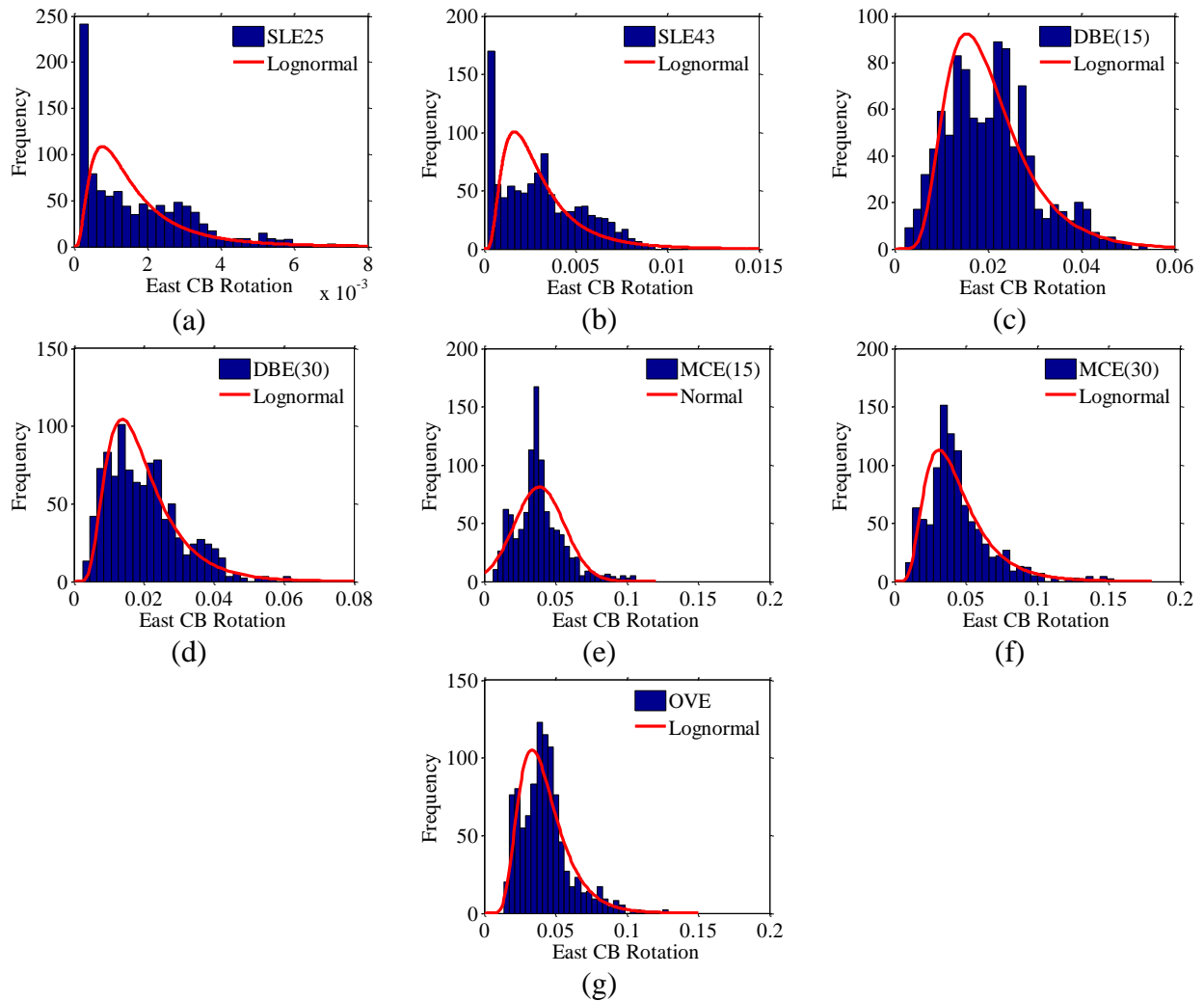


Figure C-9. East coupling beam histogram and fitted distribution for (a) SLE25 (b) SLE43 (c) DBE(15) (d) DBE(30) (e) MCE(15) (f) MCE(30) and (g) OVE hazard levels

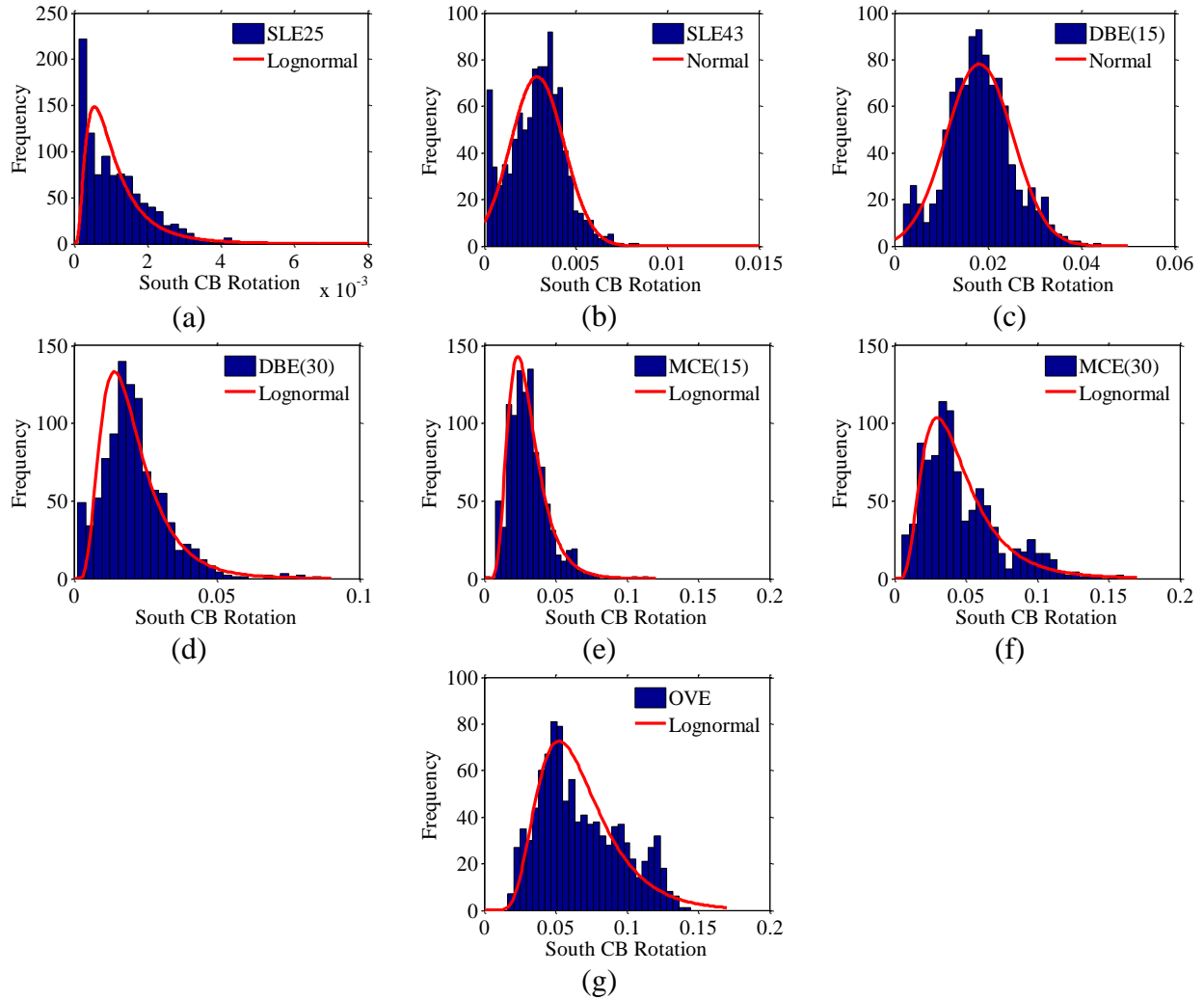


Figure C-10. South coupling beam histogram and fitted distribution for (a) SLE25 (b) SLE43 (c) DBE(15) (d) DBE(30) (e) MCE(15) (f) MCE(30) and (g) OVE hazard levels

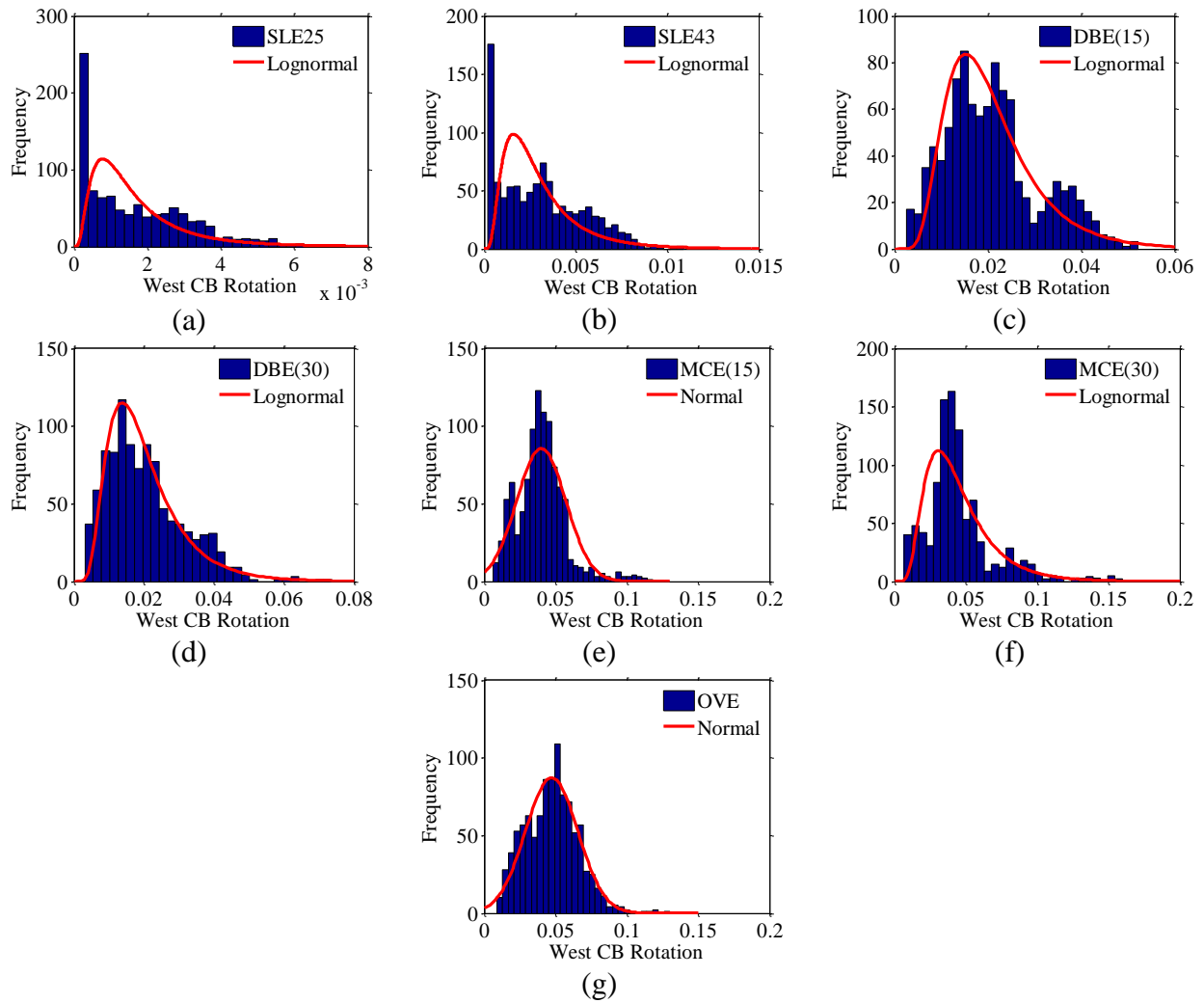


Figure C-11. West coupling beam histogram and fitted distribution for (a) SLE25 (b) SLE43 (c) DBE(15) (d) DBE(30) (e) MCE(15) (f) MCE(30) and (g) OVE hazard levels

Tensile Axial Strains

The following plots are presented for tensile axial strains: dispersion for boundary element locations #1 through #16 (as shown on Figure 6-9) and histograms overlaid with probability distributions.

Corner Boundary Element Locations

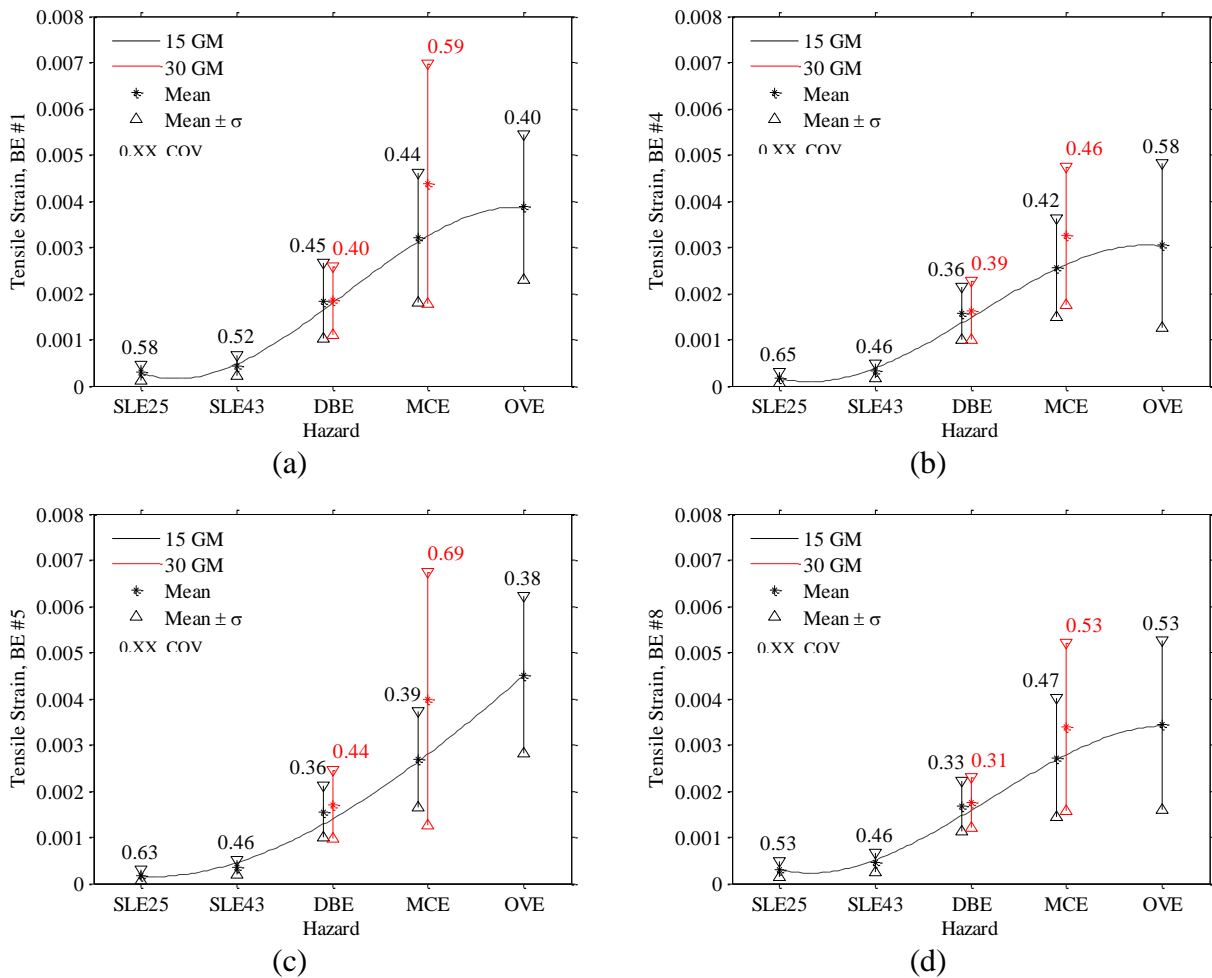


Figure C-12. 30-Story building structural wall boundary element tensile axial strains, mean and dispersion at 5 hazard levels for BE (a) #1 (b) #4 (c) #5 and (d) #8

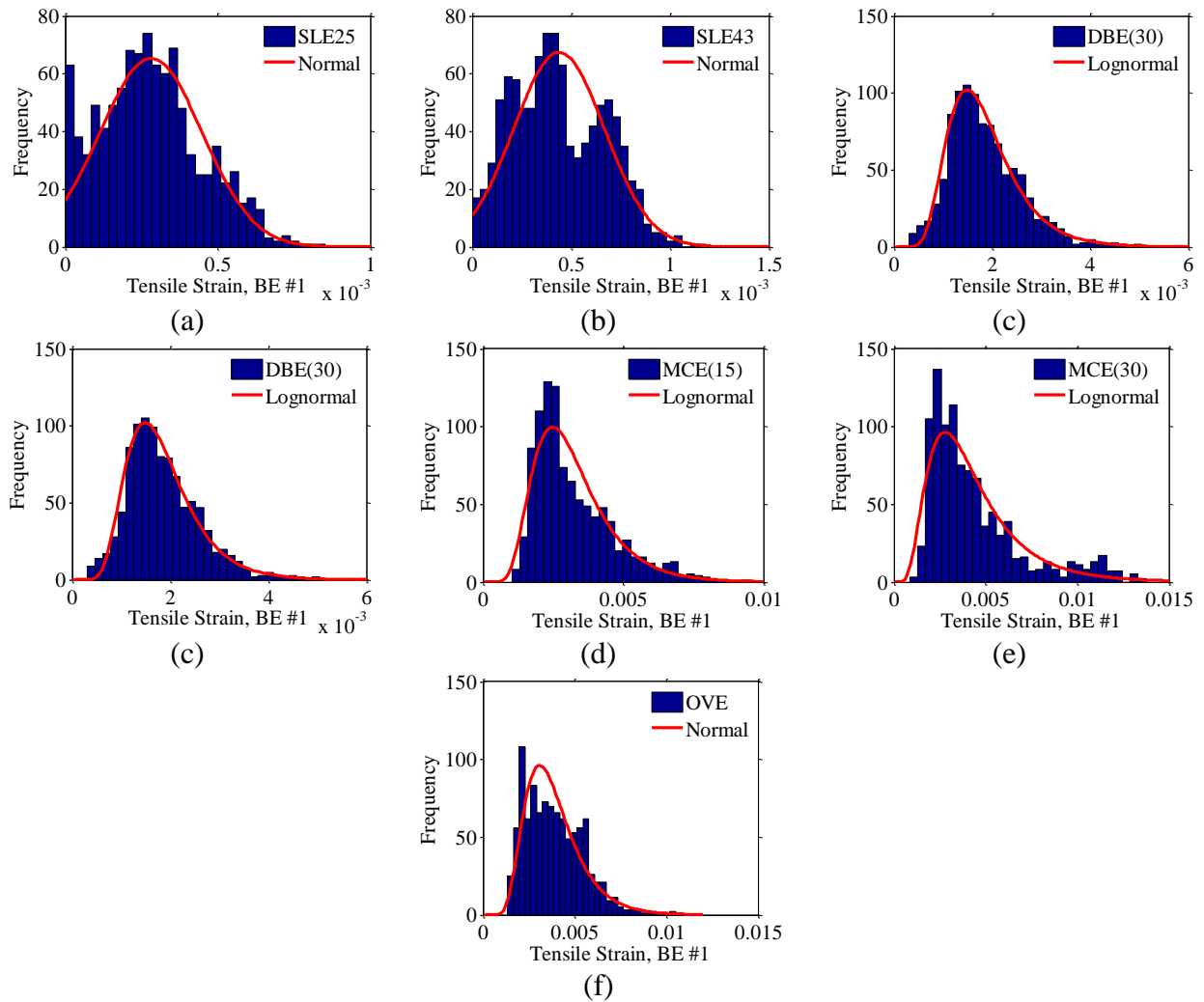


Figure C-13. Boundary element tensile axial strain (#1) histogram and fitted distribution (a) SLE25 (b) SLE43 (c) DBE(15) (d) DBE(30) (e) MCE(15) (f) MCE(30) and (g) OVE hazard levels

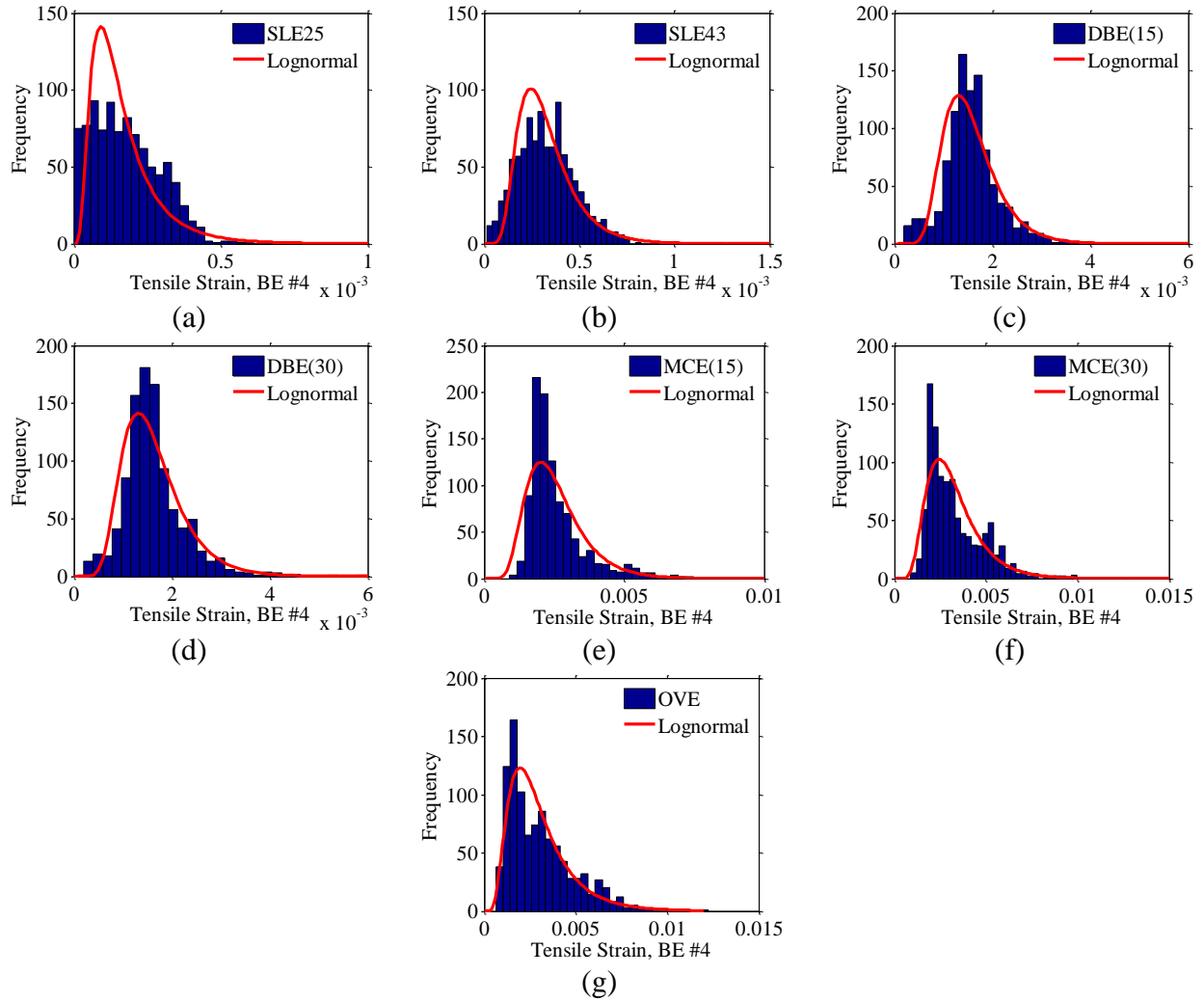


Figure C-14. Boundary element tensile axial strain (#4) histogram and fitted distribution (a) SLE25 (b) SLE43 (c) DBE(15) (d) DBE(30) (e) MCE(15) (f) MCE(30) and (g) OVE hazard levels

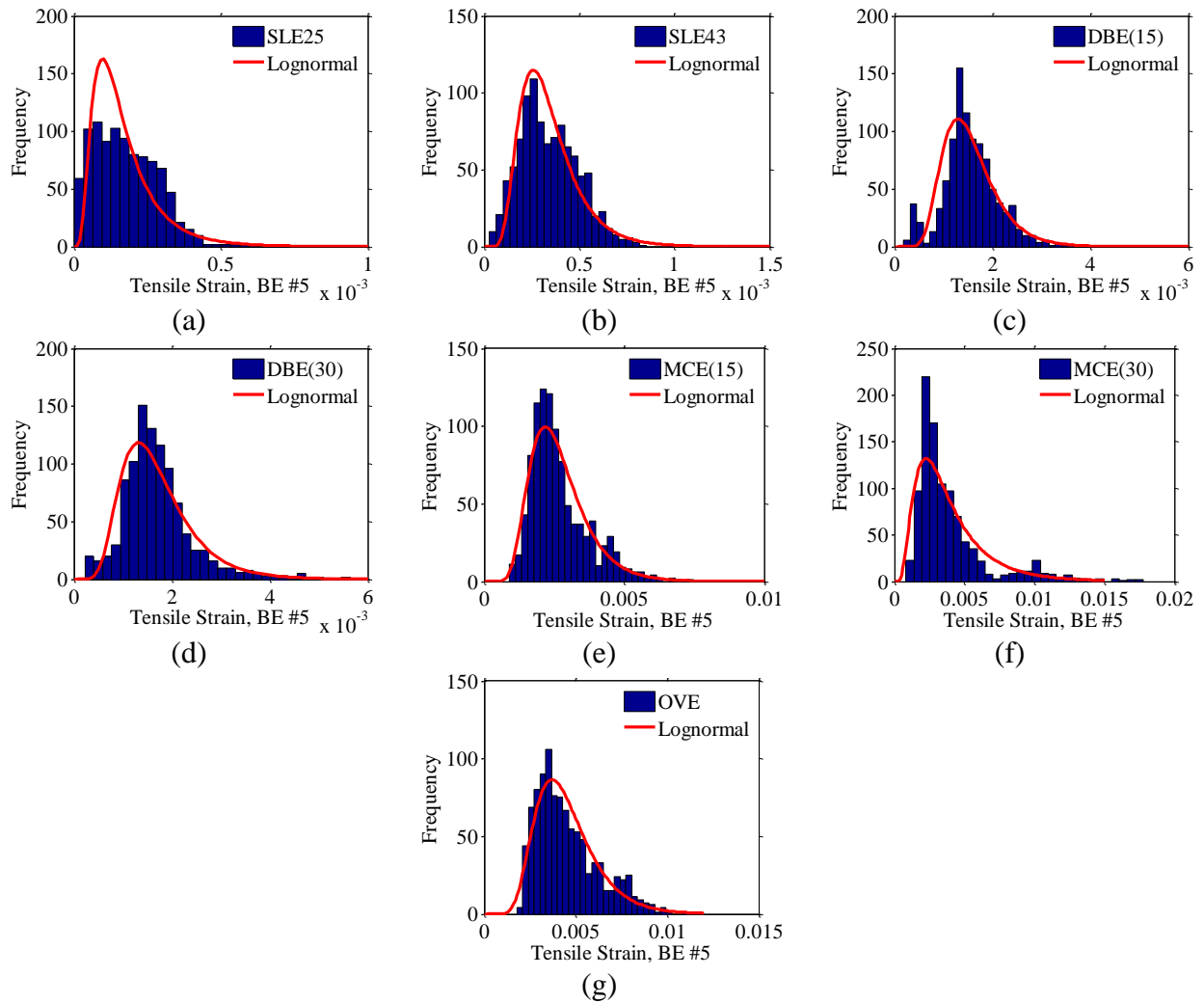


Figure C-15. Boundary element tensile axial strain (#5) histogram and fitted distribution (a) SLE25 (b) SLE43 (c) DBE(15) (d) DBE(30) (e) MCE(15) (f) MCE(30) and (g) OVE hazard levels

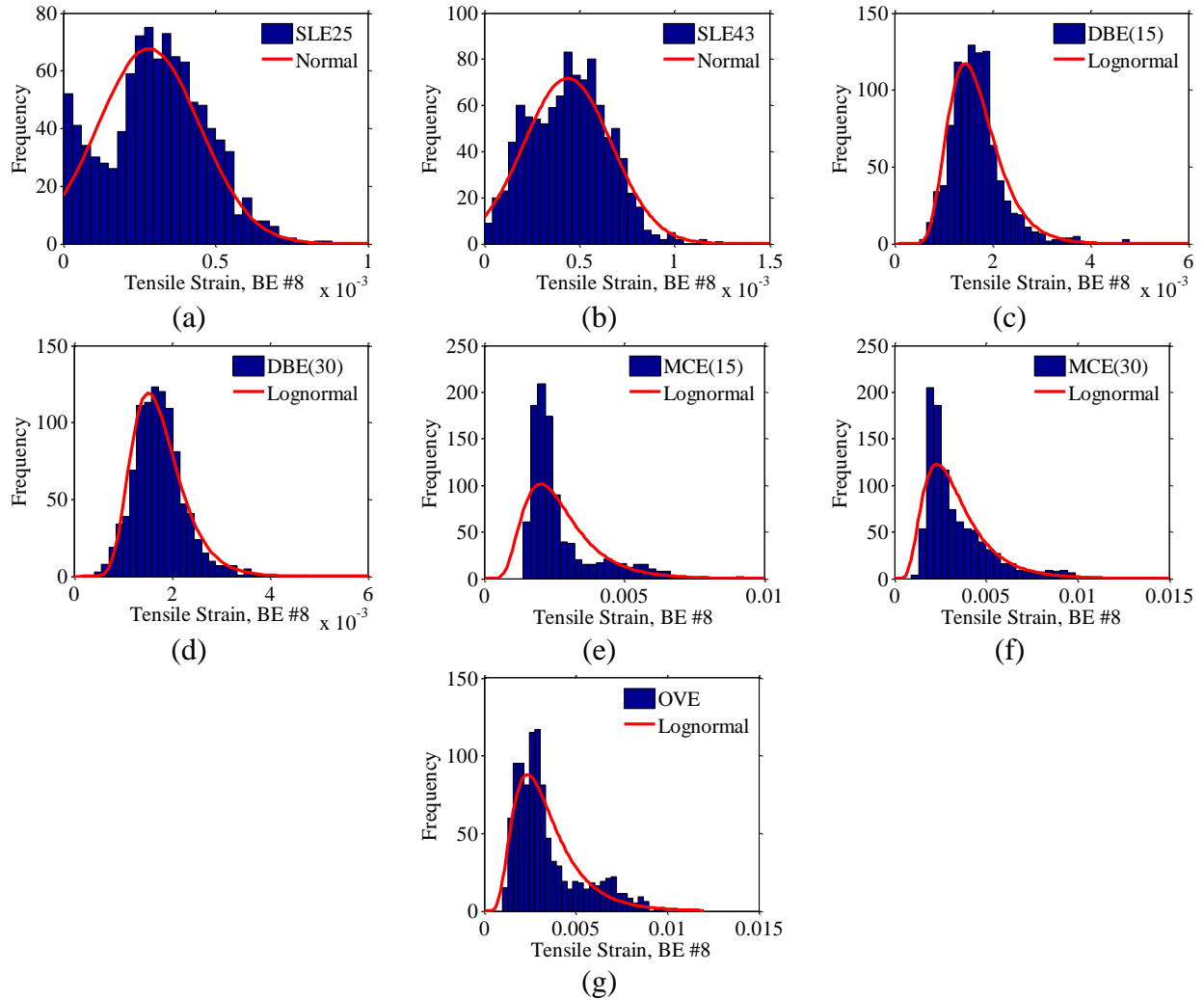
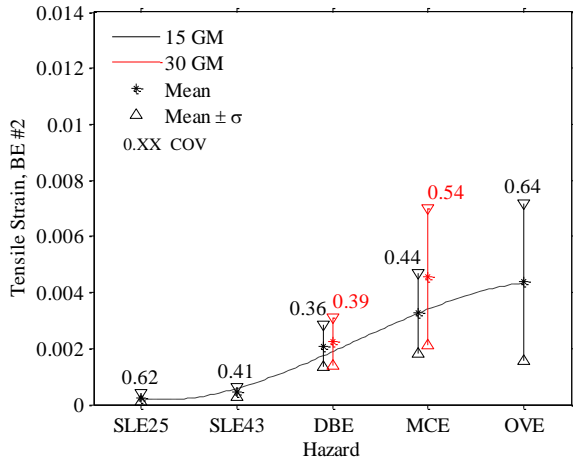
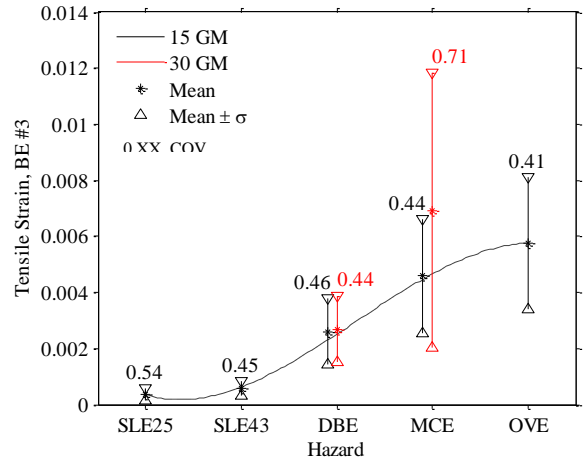


Figure C-16. Boundary element tensile axial strain (#8) histogram and fitted distribution (a) SLE25 (b) SLE43 (c) DBE(15) (d) DBE(30) (e) MCE(15) (f) MCE(30) and (g) OVE hazard levels

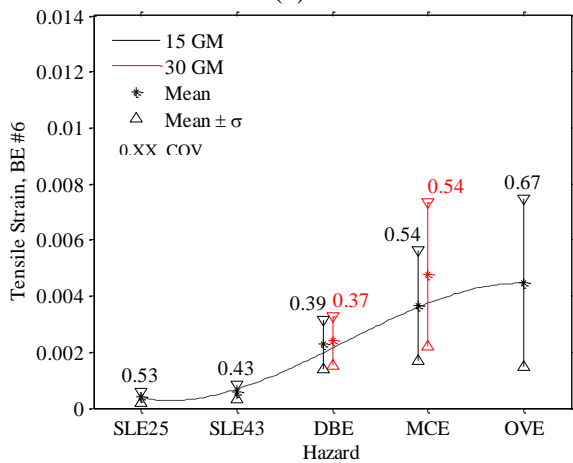
End Boundary Element Locations



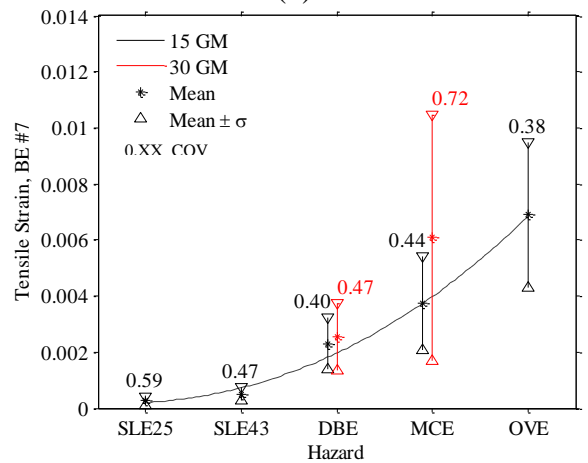
(a)



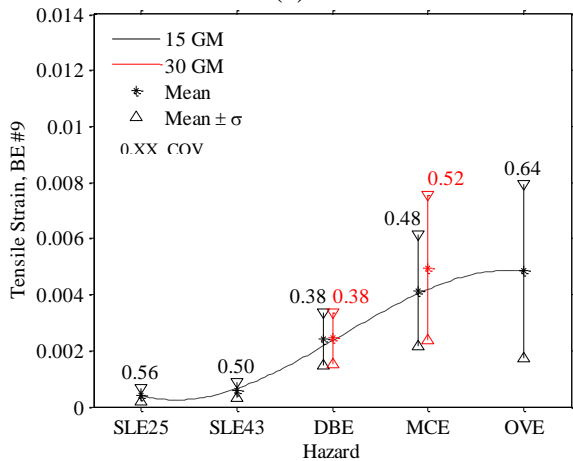
(b)



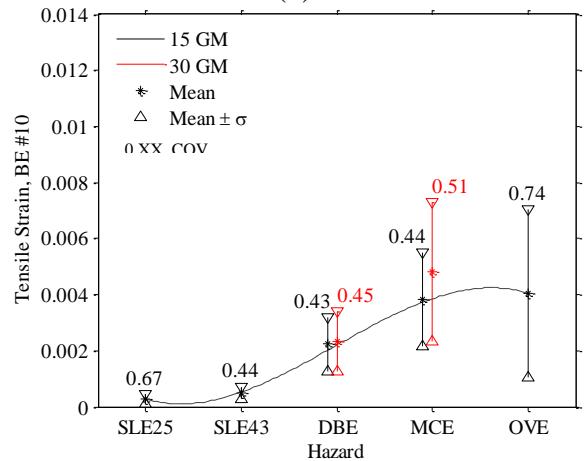
(c)



(d)



(e)



(f)

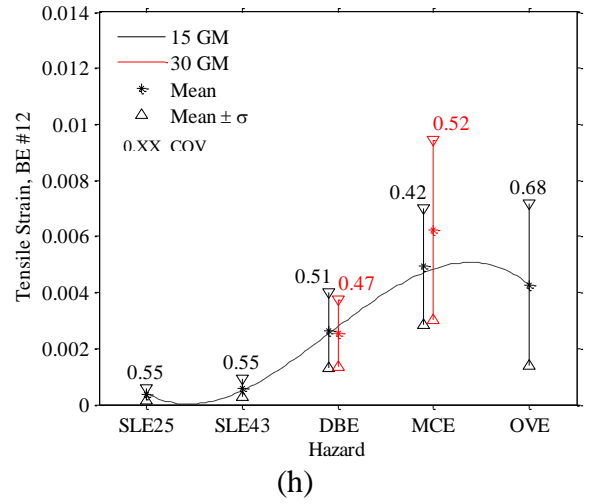
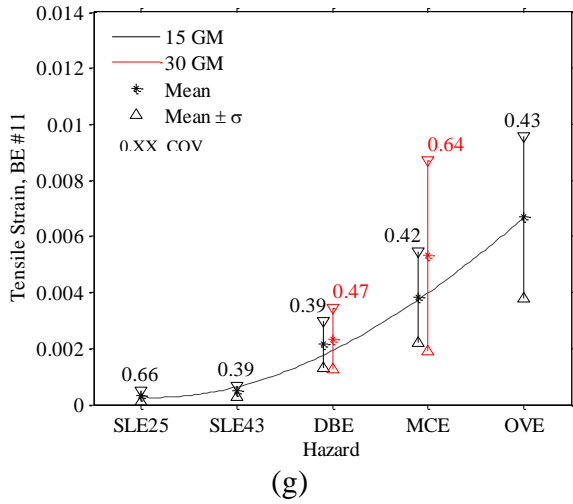


Figure C-17. 30-Story building structural wall boundary element tensile axial strains, mean and dispersion at 5 hazard levels for BE (a) #2 (b) #3 (c) #6 (d) #7 (e) #9 (f) #10 (g) #11 and (h) #12

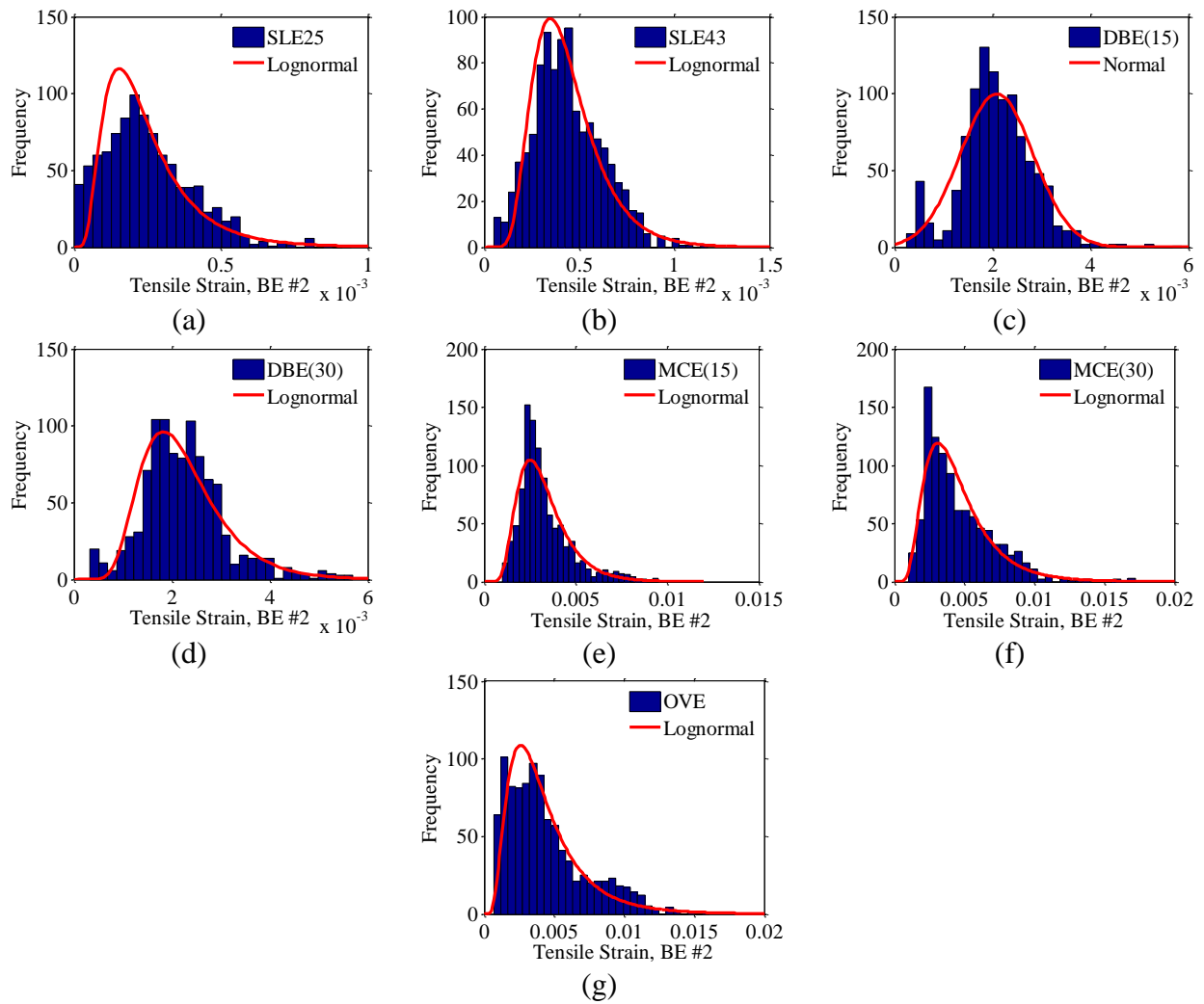


Figure C-18. Boundary element tensile axial strain (#2) histogram and fitted distribution (a) SLE25 (b) SLE43 (c) DBE(15) (d) DBE(30) (e) MCE(15) (f) MCE(30) and (g) OVE hazards

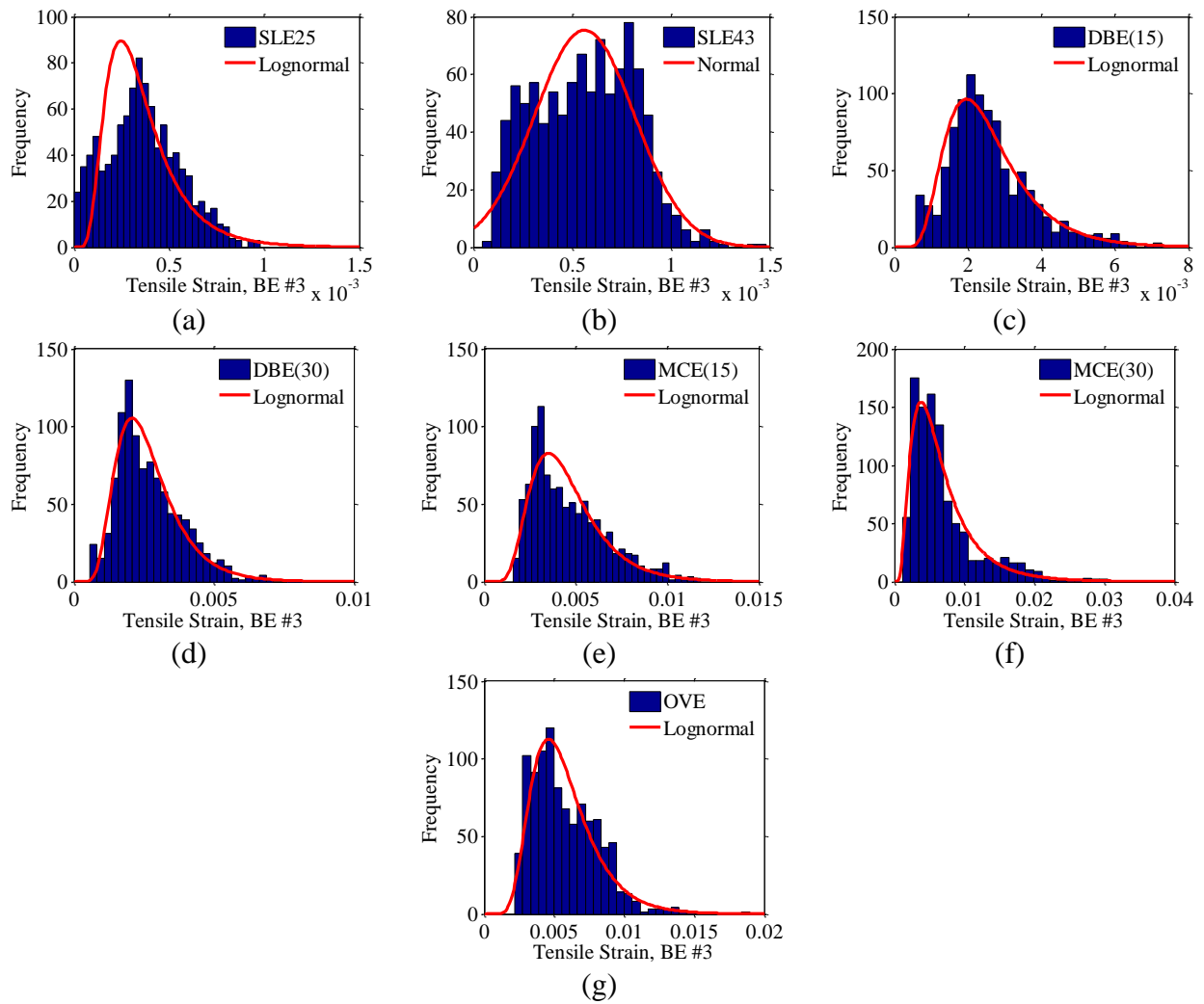


Figure C-19. Boundary element tensile axial strain (#3) histogram and fitted distribution (a) SLE25 (b) SLE43 (c) DBE(15) (d) DBE(30) (e) MCE(15) (f) MCE(30) and (g) OVE hazard levels

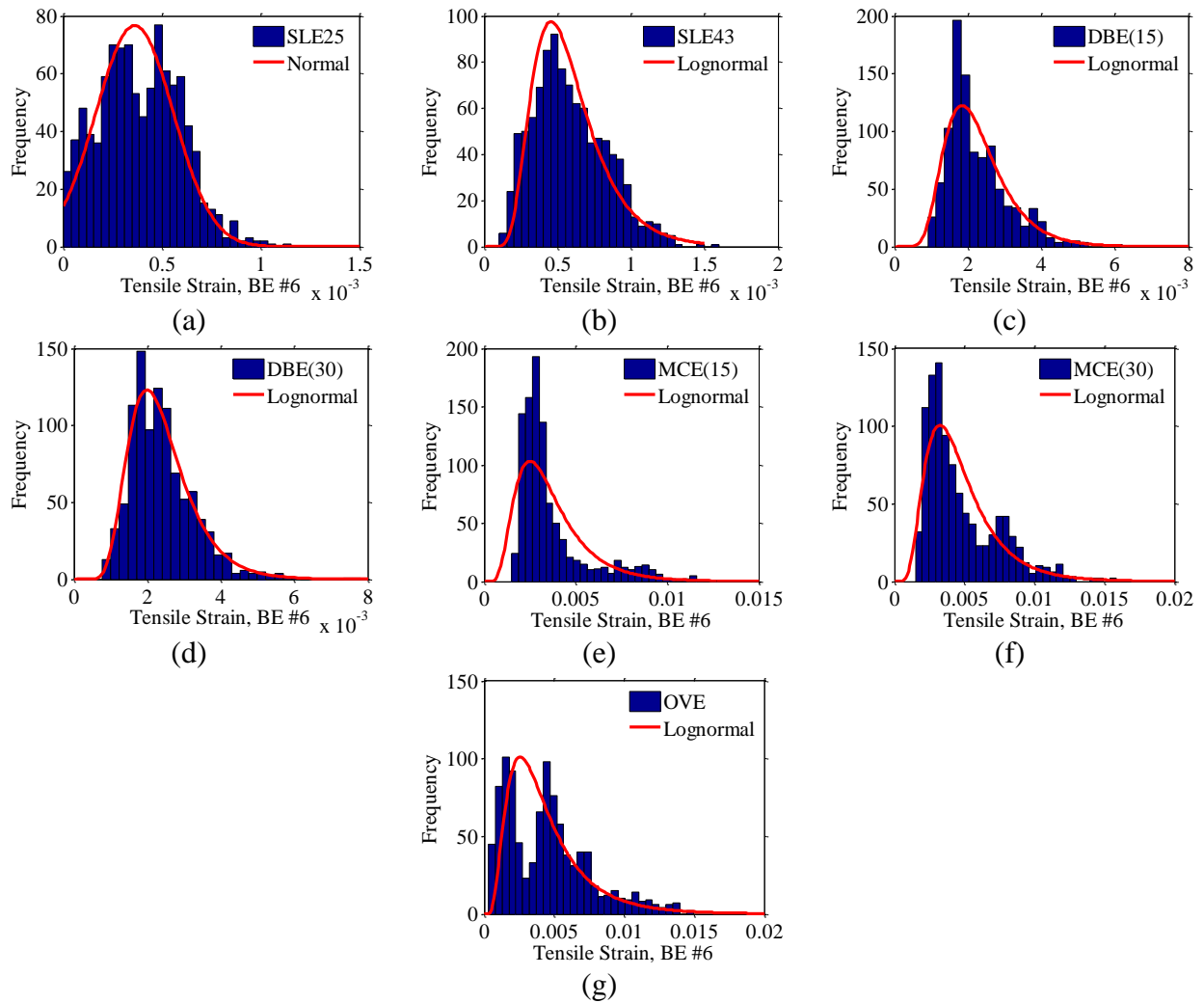


Figure C-20. Boundary element tensile axial strain (#6) histogram and fitted distribution (a) SLE25 (b) SLE43 (c) DBE(15) (d) DBE(30) (e) MCE(15) (f) MCE(30) and (g) OVE hazard levels

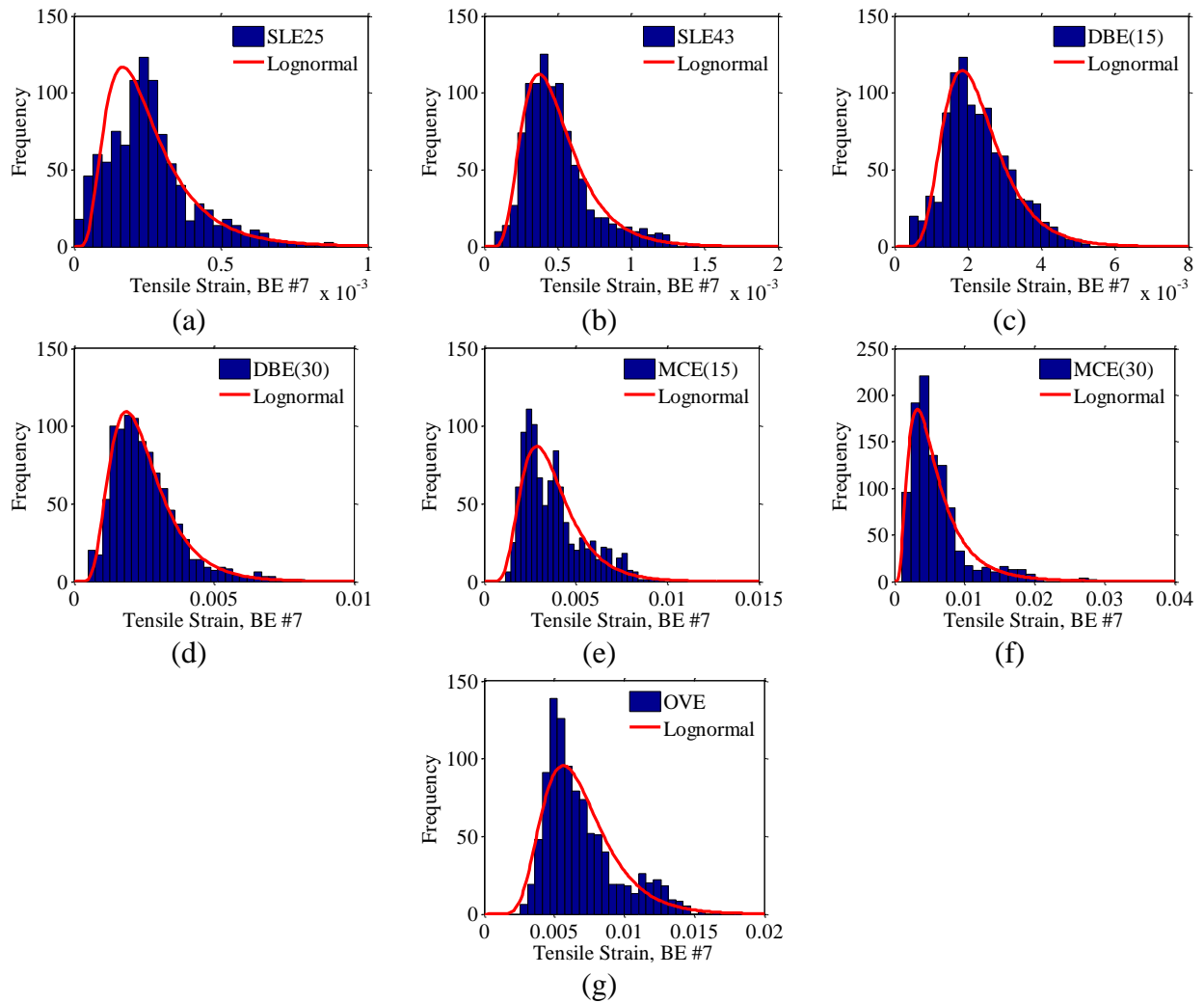


Figure C-21. Boundary element tensile axial strain (#7) histogram and fitted distribution (a) SLE25 (b) SLE43 (c) DBE(15) (d) DBE(30) (e) MCE(15) (f) MCE(30) and (g) OVE hazard levels

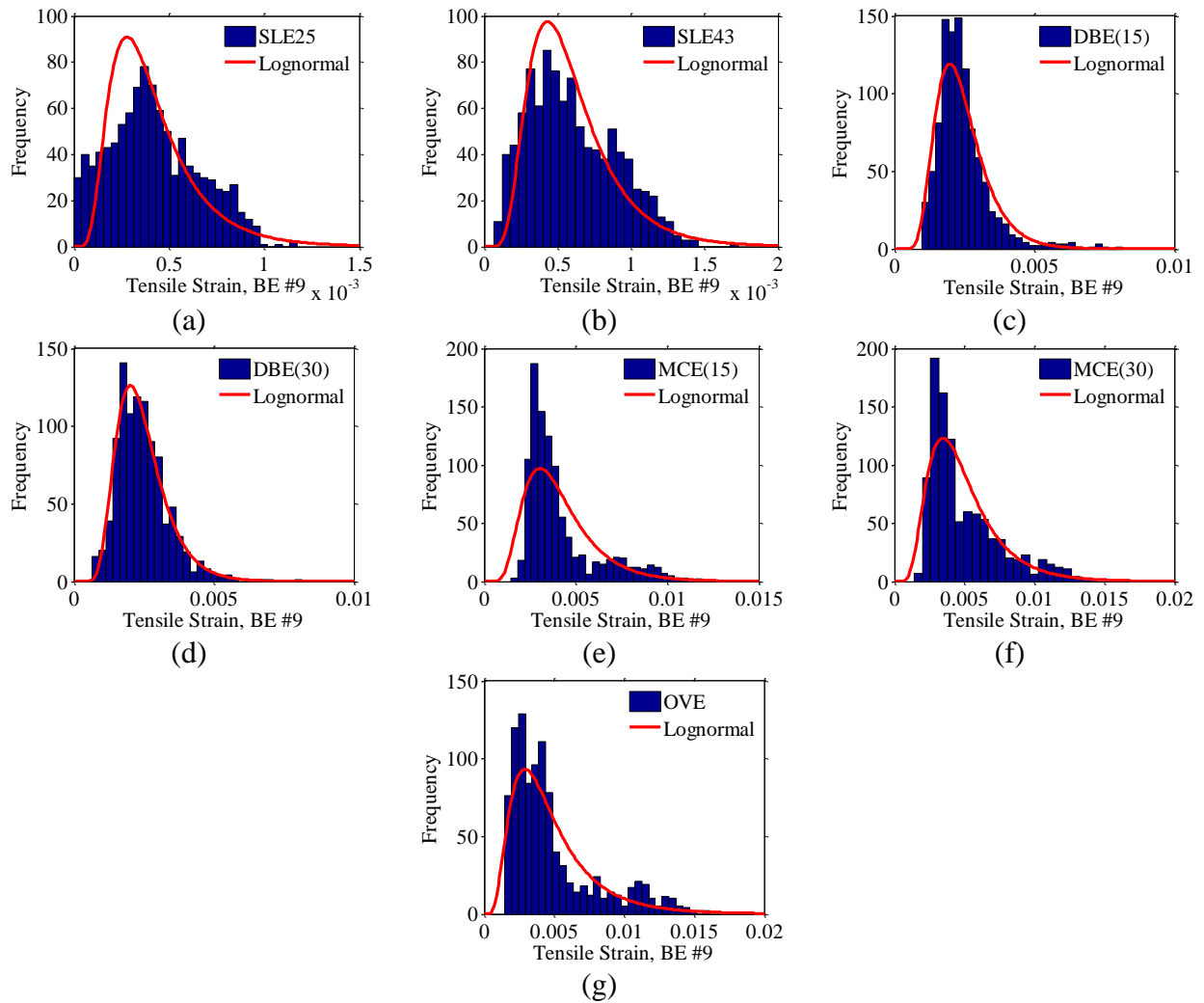


Figure C-22. Boundary element tensile axial strain (#9) histogram and fitted distribution (a) SLE25 (b) SLE43 (c) DBE(15) (d) DBE(30) (e) MCE(15) (f) MCE(30) and (g) OVE hazard levels

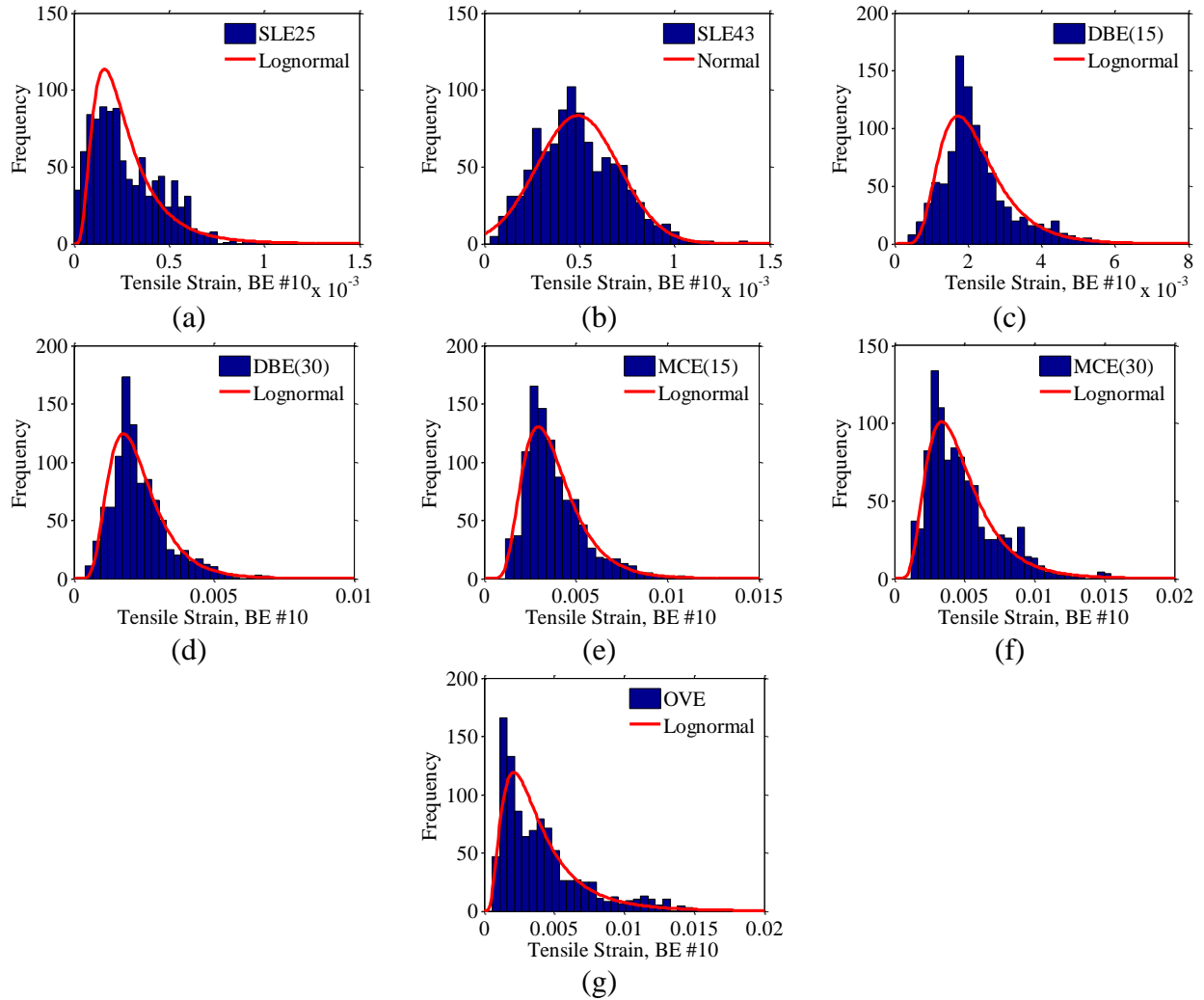


Figure C-23. Boundary element tensile axial strain (#10) histogram and fitted distribution (a) SLE25 (b) SLE43 (c) DBE(15) (d) DBE(30) (e) MCE(15) (f) MCE(30) and (g) OVE hazard levels

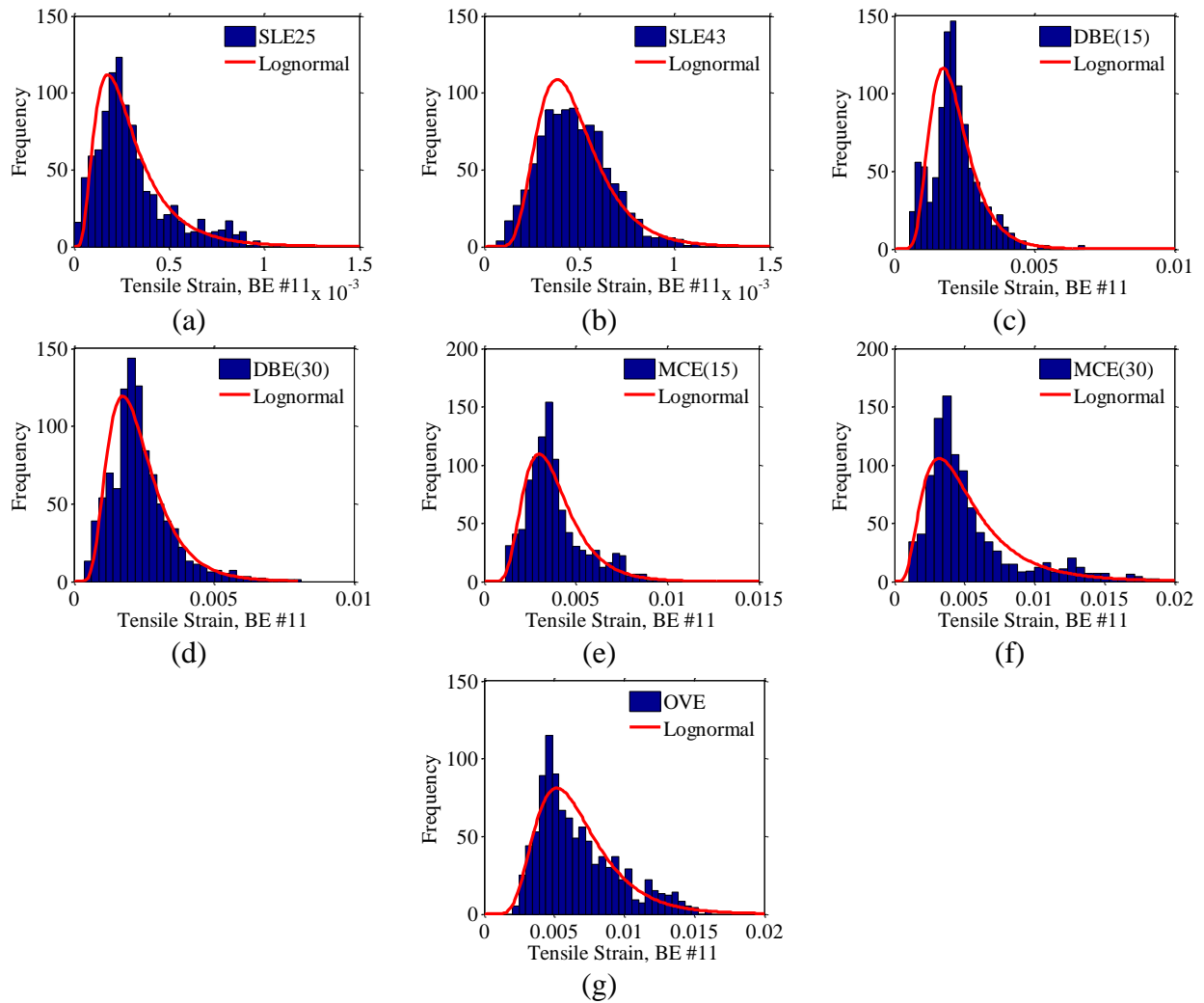


Figure C-24. Boundary element tensile axial strain (#11) histogram and fitted distribution (a) SLE25 (b) SLE43 (c) DBE(15) (d) DBE(30) (e) MCE(15) (f) MCE(30) and (g) OVE hazard levels

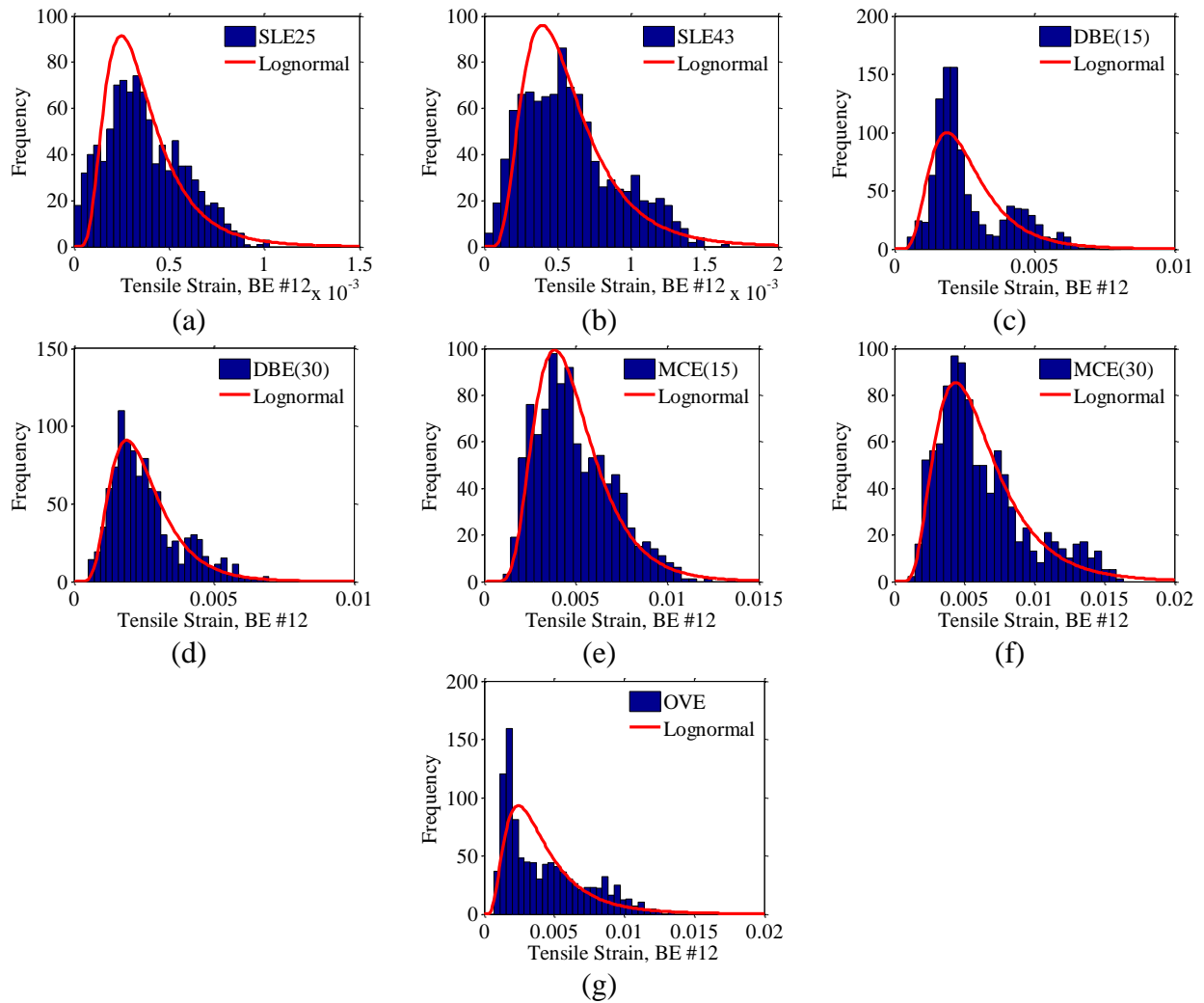


Figure C-25. Boundary element tensile axial strain (#12) histogram and fitted distribution (a) SLE25 (b) SLE43 (c) DBE(15) (d) DBE(30) (e) MCE(15) (f) MCE(30) and (g) OVE hazard levels

Compressive Axial Strains

Compressive axial strain dispersion plots for structural boundary element locations #1 through #16, as shown on Figure 6-9, are presented in this section.

Corner Boundary Element Locations

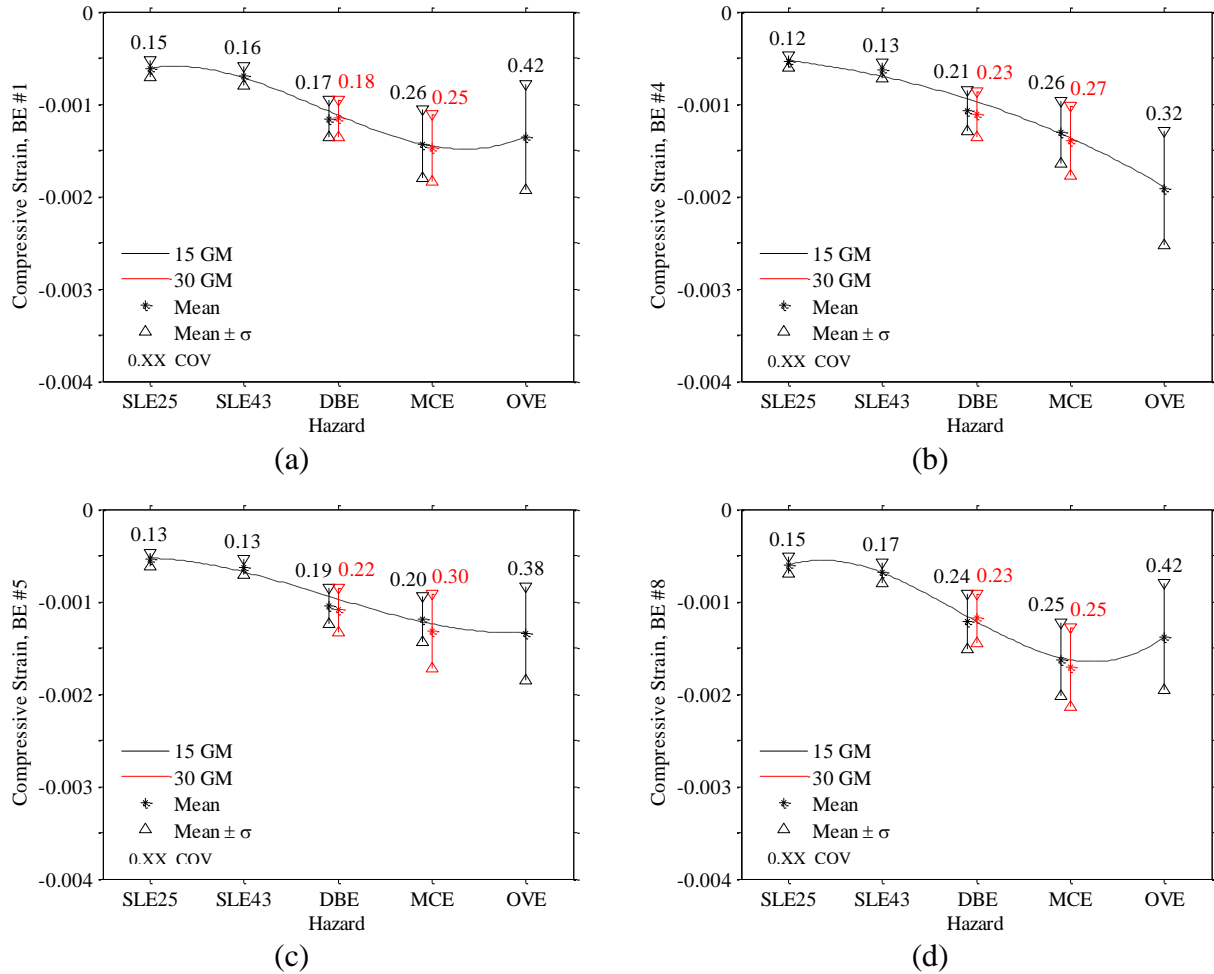
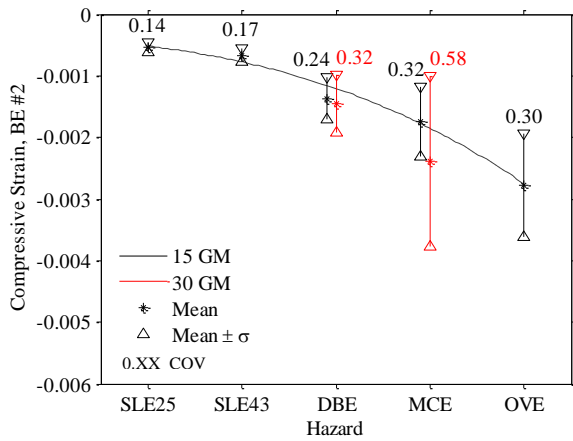
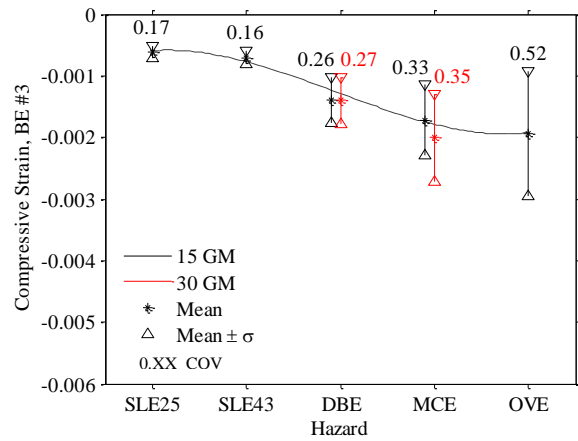


Figure C-26. 30-Story building structural wall boundary element compressive axial strains, mean and dispersion at 5 hazard levels for BE (a) #1 (b) #4 (c) #5 and (d) #8

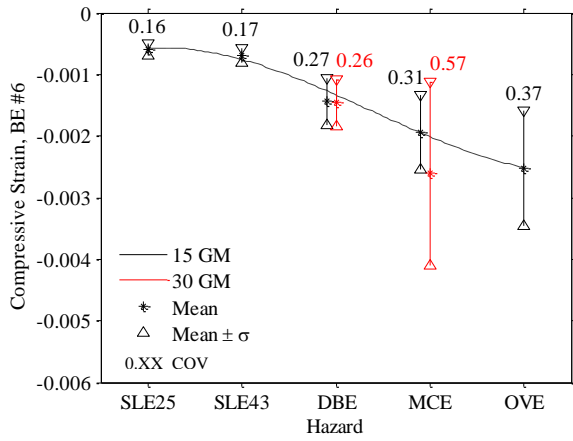
End Boundary Element Locations



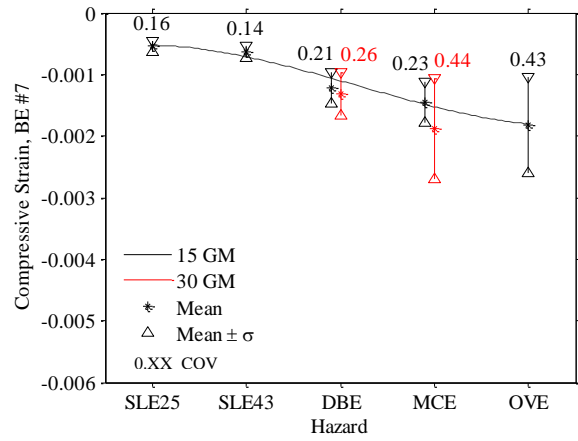
(a)



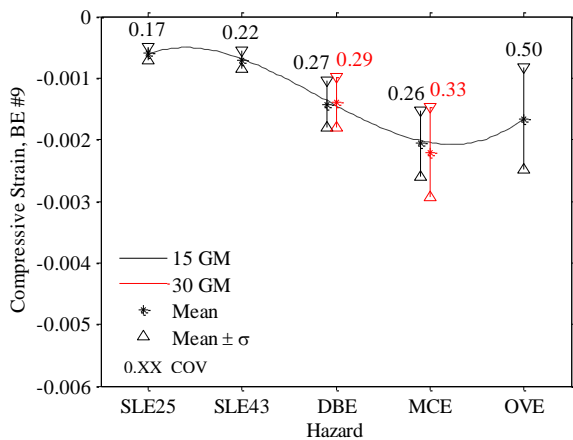
(b)



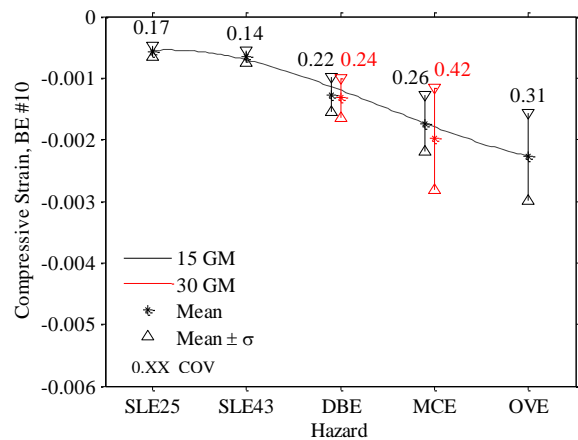
(c)



(d)



(e)



(f)

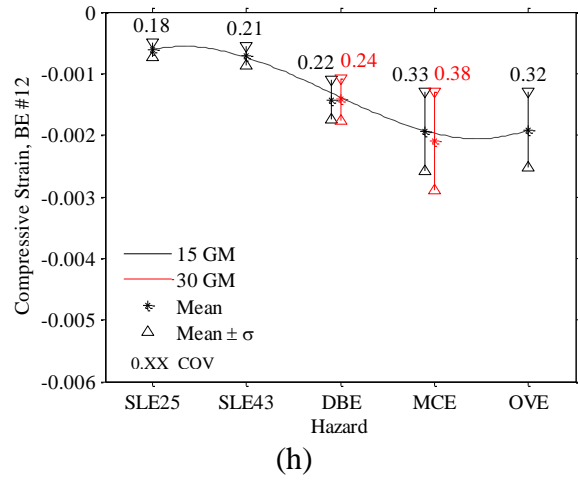
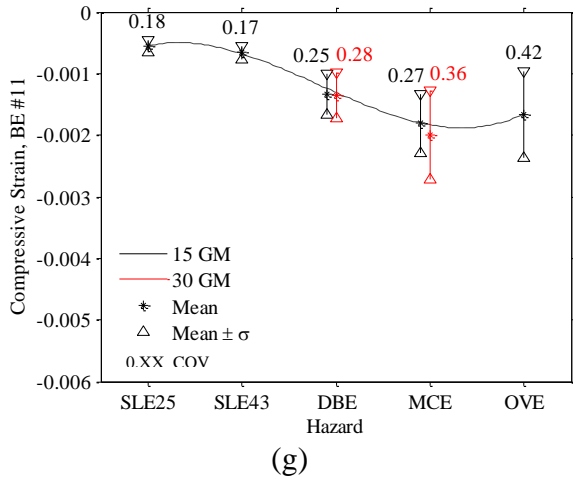


Figure C-27. 30-Story building structural wall boundary element compressive axial strains, mean and dispersion at 5 hazard levels for BE (a) #2 (b) #3 (c) #6 (d) #7 (e) #9 (f) #10 (g) #11 and (h) #12

REFERENCES

1. Abrahamson, N., and Al Atik, L., (2010). "An Improved Method for Nonstationary Spectral Matching," *Earthquake Spectra*, V.26, No.3. pp.601-617.
2. ACI318 (2011). "Building Code Requirements for Structural Concrete and Commentary," American Concrete Institute, Farmington Hills, MI.
3. ASCE7 (2010). "Minimum Design Loads for Buildings and Other Structures," American Society of Civil Engineers, Reston, VA.
4. ASCE7 (2016). "Minimum Design Loads for Buildings and Other Structures," Unpublished document.
5. ASCE41 (2013). "Seismic Evaluation and Retrofit of Existing Buildings," American Society of Civil Engineers, Reston, VA.
6. Baker, J.W. (2011). "Conditional Mean Spectrum: Tool for ground motion selection," *Journal of Structural Engineering*, 137(3), 322-331.
7. Baker, J. W. (2011). "Fitting Fragility Functions to Structural Analysis Data Using Maximum Likelihood Estimation." [http://web.stanford.edu/~bakerjw/fragility/archived_versions/Baker_\(2011\)_fragility_fitting.pdf](http://web.stanford.edu/~bakerjw/fragility/archived_versions/Baker_(2011)_fragility_fitting.pdf) Web. April 06, 2016.
8. Barbato, M., Zona, A., and Conte, J. P. (2013). "Probabilistic Nonlinear Response Analysis of Steel-Concrete Composite Beams," *ASCE Journal of Structural Engineering*, 10.1061/(ASCE)ST.1943-541X.0000803, 04013034-1.
9. Bazzurro, P., Luco, N. (2006). "Do Scaled and Spectrum-Matched Near-Source Records Produce Biased Nonlinear Structural Responses?," 8th U.S. National Conference on Earthquake Engineering, San Francisco, CA, USA, April 18-22, 2006.
10. Bournonville, M., Dahnke, J., and Darwin, D. (2004). "Statistical Analysis of the Mechanical

Properties and Weight of Reinforcing Bars,” The University of Kansas Structural Engineering and Materials Laboratory, Lawrence, KS.

11. CBC (2013). “California Building Code,” California Building Standards Commission, Sacramento, CA.
12. Chang, G. A., and Mander, J.B. (1994), “Seismic Energy Based Fatigue Damage Analysis of Bridge Columns: Part I – Evaluation of Seismic Capacity,” NCEER Technical Report No. NCEER-94-0006, State University of New York, Buffalo.
13. CSI Perform 3D Version 5.0.0. (2011). “Nonlinear Analysis and Performance Assessment of 3D Structures,” Computers and Structures Inc, Berkeley, CA.
14. CSI. (2011). “User Guide Perform 3D, Nonlinear Analysis and Performance Assessment of 3D Structures,” Computers and Structures Inc, Berkeley, CA.
15. Corotis, R. B., and Doshi, V. A. (1977). “Probability Models for Live-Load Survey Results,” Journal of the Structural Division, ASCE Vol. 103, No. ST8, Proc. Paper 13109, August 1977, pp. 1551-1560.
16. Ditlevsen, O., and Madsen, H. O. (2005). “Structural Reliability Methods,” Internet Edition 2.2.5 <http://www.mek.dtu.dk/staff/od/books.htm>. July, 2005.
17. Ellingwood, E., Galambos, T., MacGregor, J. G., and Cornell, C. A. (1980). “Development of a Probability Based Load Criterion for American National Standard A58,” National Bureau of Standards Special Publication 577, Washington, D.C.
18. English, J. (2013). “Nonlinear Modeling of Reinforced Concrete Core Walls in Tall Buildings – Analyzing Shear Demands and Amplification Factors,” University of California, Los Angeles.

19. FEMA P695 (2009). "Recommended Methodology for Quantification of Building System Performance and Response Parameters (prepared for the Federal Emergency Management Agency)," Applied Technology Council, Redwood City, CA.
20. Filippou F.C., Popov, E.P., and Bertero, V.V. (1983). "Effects of Bond Deterioration on Hysteretic Behavior of Reinforced Concrete Joints". Report EERC 83-19, Earthquake Engineering Research Center, University of California, Berkeley.
21. Hamburger, R. (2011). "Reliability Shear Wall Design," Personal Communication. July 22, 2011.
22. Haselton, C. B., Goulet, C. A., Mitrani-Reiser, J., Beck, J. L., Deierlein, G. G., Porter, K. A., Stewart, J. P., and Taciroglu, E. (2007). "An Assessment to Benchmark the Seismic Performance of a Code-Conforming Reinforced Concrete Moment-Frame Building," PEER Report 2007/12, Pacific Earthquake Engineering Research Center, University of California, Berkeley, CA.
23. Hognestad, E., Hanson, N. W., and McHenry, D. (1955). "Concrete Stress Distribution in Ultimate Strength Design," Journal of the American Concrete Institute, Vol. 27, No.4, pp. 455-481.
24. Ibarra, L., and Krawinkler, H. (2005a). "Effect of uncertainty in system deterioration parameters on the variance of collapse capacity," Proceedings, ICOSSAR 2005, Rome, Italy, pp. 3583-3590, Millpress, Rotterdam, ISBN 90 5966 040 4.
25. Ibarra, L., and Krawinkler, H. (2005b). "Global Collapse of Frame Structures Under Seismic Excitations," PEER Report 2005/06, and John A. Blume Earthquake Engineering Center Technical Report No. 152, Department of Civil Engineering, Stanford University, Stanford,

CA.

26. IBC (2012). "International Building Code," International Code Council, Falls Church, VA.
27. Kang, T.H-K., and Wallace, J.W. (2005). "Dynamic responses of flat plate systems with shear reinforcement," *Structural Journal, ACI*, Vol. 102, No.5, pp. 763-773.
28. Kim, S., and Wallace, J.W. (2014). "Shear Demands of Structural Walls," 10th U.S. National Conference on Earthquake Engineering, Alaska, USA, July 21-25, 2014.
29. Klemencic, R., Fry, J.A., Hurtado, G., and Moehle, J.P. (2006). "Performance of Post-Tensioned Slab-Core Wall Connections," *PTI Journal*, V.4, No.2. pp.7-23.
30. Kolozvari, K., Orakcal, K., and Wallace, J. W. (2015a). "Modeling of Cyclic Shear-Flexure Interaction in Reinforced Concrete Structural Walls. I: Theory," *ASCE Journal of Structural Engineering*, V. 141, No. 5, 04014135.
31. Kolozvari, K., Orakcal, K., and Wallace, J. W. (2015b). "Modeling of Cyclic Shear-Flexure Interaction in Reinforced Concrete Structural Walls. II: Experimental Validation," *ASCE Journal of Structural Engineering*, V. 141, No. 5, 04014136.
32. Kolozvari, K., and Wallace, J.W. (2016). "Practical Nonlinear Modeling of Reinforced Concrete Structural Walls," *ASCE Journal of Structural Engineering*, 10.1061/(ASCE)ST.1943-541X.0001492, G4016001.
33. LATBSDC (2014). "An Alternative Procedure for Seismic Analysis and Design of Tall Buildings Located in the Los Angeles Region." Los Angeles Tall Buildings Structural Design Council, Los Angeles, CA.
34. Lee, T. H., and Mosalam, K. M. (2005). "Seismic demand sensitivity of reinforced concrete

- shear-wall building using FOSM method,” *Earthquake Engineering and Structural Dynamics*, Vol. 34, pp.1719-1736.
35. Lehmer, D. H. (1951). “Mathematical Methods in Large-Scale Computing Units,” *Annals of the Computation Laboratory of Harvard University*, Vol. 26.
36. Lignos, D.G., and Krawinkler, H. (2012). “Development and Utilization of Structural Component Databases for Performance-Based Earthquake Engineering,” *Journal of Structural Engineering*, Vol. 139, No. 8, pp.1382-1394.
37. Lu, X., Xie, Linlin, Guan, H., Huang, Y., and Lu, X. (2015). “A shear wall element for nonlinear seismic analysis of super-tall buildings using Opensees,” *Finite Elements in Analysis and Design*, Vol. 98, pp.14-25.
38. Matlab, v. R2016a (2016). The MathWorks, Inc., Natick, MA.
39. Melchers, R. E. (1999). “Structural Reliability Analysis and Prediction,” John Wiley and Sons, Inc., New York, NY.
40. Menegotto, M., and Pinto, P.E. (1973). “Method of Analysis of Cyclically Loaded RC Plane Frames including Changes in Geometry and Non-Elastic Behavior of Elements under Normal Force and Bending,” *Preliminary Report IABSE*, Vol. 13.
41. Moehle, J.P., Bozorgnia, Y., Jayaram, N., Jones, P., Rahnama, M., Shome, N., Tuna, Z., Wallace, J.W., Yang, T.Y., and Zareian, F. (2011). “Case studies of the seismic performance of tall buildings designed by alternative means,” *Task 12 Report for the Tall Buildings Initiative (PEER TBI Task 12)*, Pacific Earthquake Engineering Research Center, University of California, Berkeley, CA.
42. Moehle, J., Bozorgnia, Y., and Yang, T.Y. (2007). “The Tall Buildings Initiative,” SEAOC

2007 Convention Proceedings, Squaw Creek, California, USA, September 26-29, 2007.

43. Naeim, F., Tileylioglu, S., Alimoradi, A., and Stewart, J.P. (2010). “The Real Deal on Soil-Foundation-Structure Interaction (SFSI),” SEAOC 2010 Convention Proceedings, Indian Wells, CA.
44. Naish, D., Fry, A., Klemencic, R., and Wallace, J.W. (2013a). “Reinforced Concrete Coupling Beams--Part I: Testing,” ACI Structural Journal, Vol. 110, No. 6, pp. 1057-1066.
45. Naish, D., Fry, A., Klemencic, R., and Wallace, J.W. (2013b). “Reinforced Concrete Coupling Beams--Part II: Modeling,” ACI Structural Journal, Vol. 110, No. 6, pp. 1067-1076.
46. Nowak, A., and Collins, K. R. (2000). “Reliability of Structures,” McGraw-Hill, New York, NY.
47. Nowak, A., Szerszen, M. M., Szeliga, E. K., Szwed, A., and Podhorecki, P. J. (2008). “Reliability-Based Calibration for Structural Concrete, Phase 3,” Portland Cement Association and Precast/Prestressed Concrete Institute, Skokie, IL.
48. Orakcal, K., Conte, J.P., and Wallace, J.W. (2004). “Flexural Modeling of Reinforced Concrete Structural Walls – Model Attributes,” ACI Structural Journal, Vol. 101, No. 5, pp. 688-698.
49. Orakcal, K., Masson, L. M., and Wallace, J.W. (2009). “Shear Strength of Lightly Reinforced Wall Piers and Spandrels,” ACI Structural Journal, Vol. 106, No. 4, pp. 455-466.
50. Orakcal, K., and Wallace, J.W. (2006). “Flexural Modeling of Reinforced Concrete Walls – Model Calibration,” ACI Structural Journal, Vol. 103, No. 2, pp. 196-206.
51. Opensees, v. 2.4.6 (2015). “Open System for Earthquake Engineering Simulation.” Pacific

Earthquake Engineering Research Center, University of California. Berkeley, CA.

52. PEER TBI (2010). "Guidelines for Performance-Based Seismic Design of Tall Buildings," PEER-2010/05, Pacific Earthquake Engineering Research Center, University of California, Berkeley, CA.
53. PEER/ATC 72-1 (2010). "Modeling and Acceptance Criteria for Seismic Design and Analysis of Tall Buildings," Applied Technology Council, Pacific Earthquake Engineering Research Center, University of California, Berkeley, CA.
54. Porter, K. A., Beck, J. L., and Shaikhutdinov, R. V. (2002). "Sensitivity of Building Loss Estimates to Major Uncertain Variables," *Earthquake Spectra*, Volume 18, No. 4, pp. 719-743.
55. Powell, G. H. (2007). "Detailed Example of A Tall Shear Wall Building," Computers & Structures, Inc.
56. Razvi, S. and Saatcioglu, M. (1999). "Confinement Model for High-Strength Concrete," *Journal of Structural Engineering*, V.125, No.3. pp.281-289.
57. SEAOC Blue Book (2008). "Seismic Design Recommendations," Seismology Committee, Structural Engineers Association of California, Sacramento, CA.
58. Virtual International Institute for Performance Assessment of Wall Systems (2015). "2nd Workshop," Santa Barbara, CA, August 16-19, 2015.
59. Wallace, J. W. (1998). "Behavior and Design of High-Strength RC Walls," *ACI Structural Journal*, SP-176, American Concrete Institute, Farmington Hills, MI, pp. 259-279.
60. Wallace, J.W., Segura, C., and Tran, T. (2013). "Shear Design of Structural Walls," 10th International Conference on Urban Earthquake Engineering, Tokyo Institute of Technology,

Tokyo, Japan, March 1-2, 2013.

61. Wood, S. L. (1990). "Shear Strength of Low-Rise Reinforced Concrete Walls," *ACI Structural Journal*, Vol. 87, No. 1, pp. 99-107.
62. Vulcano, A., Bertero V. V., and Colotti, V. (1988). "Analytical Modeling of RC Structural Walls," *Proceedings, 9th World Conference on Earthquake Engineering*, V.6, Tokyo-Kyoto, Japan, pp. 41-46.
63. Zareian, F. (2006). "Simplified Performance-Based Earthquake Engineering," Ph.D. Dissertation, Department of Civil and Environmental Engineering, Stanford University, Stanford, CA.